NAM Nederlandse Aardolie Maatschappij B.V.

Technical Addendum to the Winningsplan Groningen 2013

Subsidence, Induced Earthquakes and Seismic Hazard Analysis in the Groningen Field

Date: November 2013

Contents

0 Executive Summary

0.1 Background

This report provides technical support for the update of the Groningen Winningsplan of 1st December 2013 and contains details of the analysis of subsidence and earthquakes induced by gas production from the Groningen field. This report presents the significant study progress on:

- Results of geomechanical and seismological studies into induced earthquakes in the Groningen field based on the historical earthquake record with forecasts of future seismicity
- Results of the analysis of compaction of the reservoir rock and subsidence with forecasts of future subsidence
- Impact of different depletion scenarios and the application of pressure maintenance on the seismic hazard

In a letter to Parliament (11th February 2013 reference TK 2012-2013 33529, no. 2), the Minister of Economic Affairs initiated a number of studies on induced earthquakes in the Groningen area. Study number 5 addresses "research into the maximum strength of earthquakes associated with the Groningen gas field". Study number 6 addresses "research into different production methods to reduce the number and magnitude of earthquakes". A Technische Begeleidingscommissie Ondergrond (TBO; Technical Guidance Committee Sub-surface) and Steering Committee were set up by the Minister of Economic Affairs to oversee this study work and ensure quality and independence. The results of these studies 5 and 6 have been summarised in this report.

0.2 Introduction

Although considerable progress was made in the understanding of the seismic hazard, uncertainty remains at present. Note that the uncertainty range around the seismic hazard (and hence predictions around the maximum) is not constant but instead grows in the future (even in the next 5 to 10 years). This increasing uncertainty, however, is intended to be balanced by an overall programme to further calibrate and validate assumptions and to take appropriate preventive measures, where acceptable limits may be exceeded.

The scientific knowledge and uncertainty range described in this report reflects the current level of understanding, but not necessarily the true physical uncertainty. Consequently, predictions of the seismic hazard range are believed to be conservative. To reduce the uncertainty NAM has initiated a further data acquisition programme to obtain additional field data, as well as a studies programme. Once the uncertainty is reduced, the conservatism and related preventive measures may be scaled down accordingly. The execution of the field data acquisition plan and the integration of data in the studies program will be secured in the monitoring protocol as addendum to the Winningsplan (the "Beheersprotocol voor Borging van het Seismisch Risico binnen grenzen", (Ref. 1)). This protocol and associated monitoringsplan contain a proposal on how to validate, update and report the risk assessment and related key assumptions on an annual basis. This is expected to result in a continuous improvement and more constrained assessment of the seismic hazard over the coming years.

0.3 Historical Seismicity in the Groningen field

Since the early nineties, relatively small earthquakes have occurred in the vicinity of the Groningen gas field. It is recognized that these events are induced by the production of gas from the field. In 1993, a geophone monitoring network, operated by KNMI, was installed in the field. This was extended several times and has a detection limit of M_L=1.5 since 1996. Several cases of earthquakes induced by gas production have been recorded in literature. A possible analogue for larger earthquakes in the Groningen area is the 2004 earthquake of magnitude M_L =4.4 in the Rotenburg gas field (Germany), which also produces from the Rotliegend.

The earthquake in the Huizinge area on the August 16th, 2012 was the strongest event recorded to date in the Groningen Province with magnitude M_L =3.6 and caused damage to buildings and raised significant public concerns and subsequent feelings of fear.

Following this event the minister of EZ initiated an extensive study program to better understand the occurrence and magnitude of the earthquakes induced by the production of gas from the field and to assess the hazard these impose. NAM's study and data acquisition plan at that stage was merged into this program. Early 2013, the Minister of Economic Affairs installed the Technische Begeleidingscommissie Ondergrond (Technical Guidance Committee Sub-Surface) and the Steering Committee to oversee, advise on and assure these studies. The results and insights gained with the sub-surface studies are presented by NAM in two reports, which have been issued to the TBO.

0.4 Results of Seismological Studies based on the historical seismic record

The Groningen gas field is one of the largest gas fields in the world and has been producing since late 1963. Currently, the gas is produced through 20 processing locations (clusters), consisting of 8 to 12 wells each, gas treatment facilities and compressors. The production from the field causes the reservoir pressure to decline. This results in compaction of the reservoir rock, which leads to subsidence at surface and strain build-up in the reservoir rock. It is believed that accommodation of (a fraction of) this compaction strain by seismogenic fault slip is the source of the observed seismicity. If this fraction were invariant with production, the maximum magnitude of a future event is expected to be M_L =4.5 with a 95% upper bound of M_L =5.5. However, the fraction of induced strain accommodated by earthquakes is likely to be increasing with on-going reservoir compaction and this explains the observed distribution of earthquakes in time and over the Groningen area. Table 0.1 shows the modeling results based on a statistical analysis of the current earthquake 'catalogue', combined with first-order geomechanical assumptions, i.e. de-emphasizing the role of individual faults in the reservoir.

Period	Maximum Magnitude			Maximum PGA		
	P_{50}	P_{10}	P_2	P_{50}	P_{10}	P_2
2013 - 2016	3.4	4.1	4.6	0.02g	0.12g	0.30g
2013 - 2018	3.6	4.4	4.9	0.03g	0.18g	0.42g
2013 - 2023	3.9	4.8	5.3	0.06g	0.33g	0.67g

Table 0.1: Summary of the maximum magnitude and maximum PGA values with 50%, 10% and 2% chances of exceedance over three different time periods of assessment according to the current production plan, the time-decay compaction model and the modified Akkar et al. (2013) GMPE.

0.5 Assessment of the Hazard

To characterise the seismic hazard in a manner that is relevant to the potential impact of the earthquake on the built environment, it is necessary to quantify the hazard in terms of the nature of the ground shaking produced at any given surface location. The simplest and most widely-used of these parameters is the maximum amplitude on the acceleration time series, the peak ground acceleration (PGA). Using collections of ground-motion recordings, empirical equations have been developed, relating PGA to variables like the magnitude and the distance between the earthquake and the site of recording. These relationships are generally called ground-motion prediction equations, or GMPEs. Existing appropriate GMPEs derived from recordings of tectonic earthquakes in Europe and the Middle East, adjusted to provide a good fit to the Groningen data at smaller magnitude levels, were adopted for the prediction of PGA.

A Monte-Carlo approach to Probabilistic Seismic Hazard Assessment (PSHA) was identified as being best suited to the analysis of the Groningen field's induced seismicity. Guided by Eurocode 8 interpreted for non-stationary seismicity, maps of ground motion equivalent to the 475 year return period have been calculated.

0.6 Uncertainty in the Hazard Assessment

The most prominent uncertainty affecting the calculated hazard is the large uncertainty in the coupling coefficient relating seismic moment budget to the volumetric strain due to compaction (the partitioning factor).

Also, the choice of model relating reservoir pressure decline to compaction introduces significant uncertainty in the longer term. The uncertainty range in the compaction was estimated by using three different compaction models. These were the bi-linear model, the time-decay model and the linear isotach model. For the bi-linear and time-decay models a reduced rock compressibility was used, while for the isotach model both the rock compressibility measured on core material and the reduced compressibility were used to obtain a fit with historically measured subsidence data.

Sensitivity tests showed that the selection of a suitable ground motion prediction equation (GMPE) and the future production period chosen for calculating the annualised hazard had a considerable influence on the resulting hazard estimates. Comparing these results with those for tectonic earthquakes is problematic, also because tectonic earthquakes typically have a longer duration and occur at greater depth.

More detailed geomechanical modeling with an emphasis on the role of faults is in progress, and utilizes explicit modeling of faults within a multi-scale geomechanical modeling framework. This work has the potential to physically constrain the partitioning factor, thereby reducing uncertainty of model predictions. Currently, applications of all geomechanical models are hampered by the paucity of relevant field data, leaving room for multiple geomechanical explanations. A higher resolution of more field parameters is required to make a step forward in a better understanding of geomechanical behavior. A further data acquisition campaign is in progress, including logging of geomechanical rock properties and installation of geophones in two deep observation wells. The data obtained with the geophones in the deep wells will be shared as stipulated in the borgingsprotocol (Ref. 1). Additionally, the existing monitoring network of shallow geophones and accelerometers will be extended.

Advances in geomechanical modeling combined with the new field data will be used to improve the understanding of the fault slip behavior and when validated by the observed seismicity, this has the potential to reduce the currently large uncertainties. Explicit geomechanical / fault movement modeling is showing insightful results. This should lead to a more robust geomechanical workflow for use in seismic hazard analysis to enable subsurface stress management as a tool to reduce the hazard. An important example are the ongoing geomechanical studies, that explicitly model faults in the reservoir, of which it is expected that it will be able to demonstrate an absolute upper bound to the maximum magnitude.

0.7 Alternative Production Strategies

0.7.1 Depletion

The Groningen field is currently produced by a depletion mechanism. Effort is made to maintain, given the production level, the pressure differences in the main area of the field as small as possible. Several measures have been investigated that could potentially reduce induced seismicity:

- An alternative production philosophy is to preferentially produce the southern part of the field, which (up till now) is less earthquake prone, in an attempt to keep the reservoir pressure in the area around Loppersum relatively high. This would reduce compaction around Loppersum, which potentially has a temporary beneficial impact on local seismicity. As a negative consequence the pressure difference between northern and southern part of the field will increase.
- Reduction of the production level of the field is another potential measure to reduce seismicity. Lower production levels will lead to longer production times to produce the reserves and will therefore reduce the number of earthquakes over a time period (e.g. during a year), but not necessarily the total number of earthquakes during the production life of the field.
- In the western periphery of the field, the reservoir pressure in a number of poorly drained blocks remains higher than in the main area of the field. Depletion of these blocks to reduce the pressure difference with the main area of the field has the potential to reduce seismicity.
- Maintaining the reservoir pressure by injecting fluid/gas volumes to balance the gas withdrawal also has the potential to reduce seismicity. This requires extensive and costly redevelopment of the field, including the construction of large new facilities on a substantial industrial scale, which will have a large impact on the surroundings (Ref. 3).

To investigate the impact of the different measures on the seismicity and the hazard, production forecasts and the corresponding reservoir pressure development for different production scenarios have been prepared. For these different production scenarios the resulting compaction (contour maps and associated volumes) was estimated as input into the seismic hazard analysis. This analysis showed that the difference in compaction, resulting from the different depletion scenarios over the period 2013 – 2023 is smaller than the spread from using the different compaction models. For the different production scenarios the incremental compaction volume over this 10 year period ranges from 50 to 58 mln m^3 using the time decay model. However, for the base case production scenario the incremental compaction volume over this 10 year period ranges from 58 to 76 mln m^3 for different compaction models. This illustrates that the uncertainty introduced by the different compaction models is larger than the spread introduced by the different production scenarios.

0.7.2 Pressure Maintenance

Currently, the Groningen field is planned to be produced under a depletion drive mechanism. Low abandonment pressures are required to reach the highest ultimate gas recovery from the field, which is part of effective recovery (as included as a principle in the Dutch mining regulations). Consequently, this also leads to highest compaction, subsidence and the resulting seismic activity. Maintaining the reservoir pressure in the Groningen field at a level above the abandonment pressure will, after a certain delay period, halt depletion-induced compaction and subsidence. Therefore, it has the potential to reduce induced seismicity in the field.

A study was carried out to establish the feasibility and contours of pressure maintenance projects in the context of Groningen, and to assess the impact on seismicity. Initially, different injection media were screened (nitrogen carbon dioxide, flue gas, water). Based on its abundant presence, relatively inert behaviour and tolerance for presence in the sales gas, nitrogen was chosen as the optimal injection medium to conduct a screening study. Use was made of the reservoir model of the Groningen field, the experience with gas-gas displacement and gas-mixing from the Grijpskerk and Norg underground gas storage projects, and the nitrogen injection project in De Wijk.

This study aims to provide a first:

- outline of the project scope, and
- assessment of the effectiveness to reduce the frequency and magnitude of earthquakes.

Reservoir processes for nitrogen injection are more complex and fundamentally different from the current depletion drive process. Breakthrough of nitrogen in producer wells is expected to materially reduce Groningen gas reserves. The large electricity consumption required for the production of nitrogen further reduces the gas volume available for sales.

The scope of the project is beyond current global experience (estimated to be 5 – 7 times larger than the largest similar nitrogen injection project ever installed). Although the scope and dimensions of a pressure maintenance project have been defined, feasibility of the project has not yet been established.

Nitrogen injection takes at least 5 years to first injection and some 10 years to ramp up to full capacity. The total cost of the project is estimated to be between 6 and 10 bln €. The project will carry a material environmental footprint, with extensive land use and electricity consumption. Societal support for a large-scale nitrogen injection project is therefore considered a key determining factor. Alternative approaches for reducing the magnitude and frequency of earthquakes will have to be assessed.

Results presented herein reflect an early stage assessment of the nitrogen injection gas recovery concept. Scope has been identified for optimization in a number of areas.

Pressure maintenance is expected to arrest reservoir compaction, and hence to reduce the seismic hazard. However, to what extent is yet to be established through further geomechanical modelling. Especially, the impact on seismicity when injecting into or close to a fault needs to be addressed.

0.8 Hazard Analysis of Alternative Production Strategies

Using a Monte Carlo method (NAM, 2013), the Akkar et al (2013) ground motion prediction equation modified to be consistent with ground motion data from the Groningen Field and the earthquake record of at least magnitude 1.5 events for Groningen, the following PSHA results were obtained for the base production scenario:

- For the 10 years from 2013 to 2023 based on the time-decay reservoir compaction model the PSHA indicates a 50%, 10% and 2% probability of peak ground acceleration, PGA, exceeding 0.06*g*, 0.33*g* and 0.67*g* respectively, where *g* is the standard acceleration of gravity (9.81 m/s^2).
- For a 5-year assessment period from 2013 to 2018 the corresponding results are a 50%, 10% and 2% probability of PGA exceeding 0.03*g*, 0.18*g* and 0.42*g* respectively. Similarly for a three year assessment period from 2013 to 2016, there is a 50%, 10% and 2% chance of PGA exceeding 0.02*g*, 0.12*g* and 0.30*g* respectively.

It is important to point out that the 2% over 10 years hazard results listed above should not be considered equivalent to the 10% chance over 50 years stipulated by Eurocode 8, because induced seismicity within the Groningen Field varies with time and is not modelled as a Poisson process.

Epistemic uncertainty characterises uncertainty in the values of parameters which are fixed but either unknown or known only to within a certain precision. Significant epistemic uncertainties exist in the seismic hazard assessment for the Groningen Field; these are primarily associated with strain partitioning, the GMPE and reservoir compaction. A logic-tree approach, in which each branch of the logic-tree represents a distinct scenario of a particular model and associated parameter values, was used to explore the impact of the key epistemic uncertainties on the estimated hazard. It was found that the strain partitioning uncertainty has the largest impact of those considered. The epistemic uncertainty attributed to strain partitioning will in some part be due to random (aleatory) variability, representing the stochastic nature of the earthquake process. The relative contribution of epistemic and aleatory uncertainties to the overall uncertainty in strain partitioning is still unknown. Further earthquake, surface acceleration, and subsidence monitoring within the Groningen Field in combination with additional geomechanical studies will provide more information that may help to better constrain these uncertainties and therefore reduce conservatism in the assessment of their consequences. .

Probabilistic seismic hazard assessments from 2013 to 2023 were conducted for 19 distinct scenarios that form a representative sample of the different geological, compaction, development, and production scenario elements. The results obtained indicate all these depletion scenarios yield similar seismic hazard estimates with the exception of the emergency stop scenario, which reduces the maximum PGA with a 2% chance of exceedance to 0.41*g*. This represents a 38% reduction compared to 0.67*g* for the current case (SN STD).

In the emergency stop scenario, the linear isotach compaction model predicts significant rates of compaction will persist until long after 2080. There is no analogue field evidence to support such behaviour. Equally, laboratory measurements are unable to constrain the isotach model behaviour on the multi-decadal time-scale exhibited here. For these reasons, the reliability of this particular isotach model with a high compressibility coefficient is doubtful. Using a lower compressibility coefficient gives compaction results comparable to the results of the time decay model and is considered to be a more realistic representation.

0.9 Results of Geomechanical Studies

Geomechanical studies to increase our understanding of the physical fault slip process have also been extended. A first series of analyses has been carried out aimed at identifying potential fault slip mechanisms and the impact of various modelling options and their associated parameters on the simulated geomechanical response. A two-dimensional modelling environment is chosen to allow a wide range of modelling options and parameters to be evaluated relatively quickly.

Geomechanical models cannot directly predict radiated seismic energy; however, more detailed models that explicitly capture fault slip behavior could provide an advanced methodology to better predict the

evolution of seismic fault slip and related radiated energy. Advanced multi-scale mechanical modeling combined with a geomechanics-seismicity relationship might provide a suitable framework to better understand seismic fault slip behavior and assess future seismicity via a physically-constrained strain partitioning (i.e., partition factor). This will be the subject of future study work, which will aim to establish a workflow leading to a robust integration between 3D explicit fault modelling and the existing Seismological Modeling to reduce seismic uncertainty. This work may help to constrain the uncertainty in the partitioning factor.

Some relevant insights have been gained into the potential fault slip mechanisms that might be responsible for the recorded seismic events in the Groningen field. Three different responses have been found based on the formation offset along an existing fault plane, namely for down-thrown formations with an offset smaller and larger than the thickness of the depleting reservoir and for up-thrown reservoir formations. The difference in response is expressed in term of the depletion level at the onset of fault slip, the number of slip sections, the total length of the slip sections, the maximum Relative Shear Displacement and the dissipated energy by slip along the fault plane. The reported values for the mentioned response parameters are not representative for the Groningen field conditions at this stage.

These new insights open the opportunity to look for seismic fingerprints to 1) determine if slip along existing faults is indeed the root cause of the recorded seismic events, and 2) to discriminate between different slip mechanisms, constrained by available structural information. Further studies are underway to evaluate the impact of other modelling options.

The geomechanical / fault movement Finite Element Analysis (FEA) models may provide the capability to reduce the uncertainty in partitioning factor calculations. A number of these models have shown good agreement with field measurements and because they explicitly account for faults (a subset of faults interpreted from seismic data was included in the model), this is a promising approach to provide a physically meaningful basis for relating compaction strain energy with energy exerted during fault slip (dissipated energy).

Results illustrate the potential advantages of this approach:

- Temporal evolution of fault energy dissipation from geomechanical models correlates reasonably well with observed radiated energy from seismic events
- As a first step the partitioning or scaling factor that relates radiated energy with dissipated energy was assumed to stay constant within the analyzed period (1996-2012).
- Predicted energy dissipation is significantly different in different regions of the field in agreement with observed seismicity

While the comparison is encouraging, further improvement may be established by enhancing the representation in the FEA models of the faults, fault behaviors (e.g., slip / velocity weakening), compaction physics (e.g. non-linear, rate-dependent compaction), etc. Also the full range of models consistent with the historic seismicity data accounting for the stochastic variability due to finite sample effects within the earthquake catalogue should be assessed. By providing a "physics-based" constraint on the relationship between compaction strain energy and fault dissipated energy, these models could reduce the variability in partitioning factors that had previously been calculated based on models without explicit consideration of faults.

0.10 Studies Programme

The logic tree analysis showed that the uncertainty in the partitioning factor is the largest epistemic contribution to the uncertainty in the hazard. Reducing this uncertainty is the prime objective of continued data gathering in the field in combination with continued geomechanical studies. The geomechanical modelling in combination with additional data from geophones in deep wells and near surface is expected to be able to reduce the uncertainty in the partitioning factor and therefore also the uncertainty in the hazard. A continuation of the study program is therefore planned. The main elements of the study and data acquisition plan continuing in 2014 include: investigations to improve subsidence prediction, extensive geomechanical modelling, monitoring of earthquakes in the Loppersum area with geophones

located in deep wells, field-wide monitoring of earthquakes with geophones and ground accelerations with accelerometers.

References:

1 Beheersprotocol voor Borging van het Seismisch Risico binnen grenzen, NAM, November 2013.

0.11 Independent Review

The technical work presented in this report has been assured using internal assurance processes. The Internal assurance is supplemented by independent (external) assurance. For the petroleum engineering work SGS Horizon has been contracted to perform an independent review of the sub-surface models (Geology and Reservoir Engineering).

The geomechanical and seismological studies have been reviewed by Professor of Seismology and Rock Physics, Ian Main of the University of Edinburgh. Professor Main's areas of expertise are: processes that lead up to failure events, from earthquakes, rock fracture, and volcanic eruptions to failure of building materials and bridges, and in quantifying the resulting hazard.

The study work documented in this report was presented to Prof Main in two sections. These correspond to the two TBO report (studies 5 and 6). He prepared two separate reviews, which have been included in this report.

0.12 Independent review of 'Report to the Technical Guidance Committee (TBO) on Subsurface Aspects of Induced Earthquakes in the Groningen Field' (part 1)

Review by Ian Main, University of Edinburgh, Oct 7 2013.

Recommendations by the reviewer are given in italics below.

This is a comprehensive and very well written report which comes to some clear conclusions on (a) characterising the current level of seismic hazard associated with future production of gas from the Groningen field, and (b) making projections for future levels of hazard associated with the planned production scenario, both using best practice as far as possible at this stage. All of the major conclusions and caveats listed are reasonable in the light of current knowledge (see e.g. Ellsworth, 2013), as are the plans in going forward with outstanding work to reduce the remaining uncertainties further.

As an external reviewer I was really impressed by the speed of assimilation of my previous suggestions into the document in terms of new work additional work done, the effect these changes have already made in the knock-on conclusions, and in conditioning the plans for future work, the most important of which are the planned borehole passive seismic monitoring, the characterisation of the ground motion site response and the full 3D geo-mechanical simulation characterisation and validation.

All of the authors and project managers should be commended for completing such a comprehensive and professional piece of work to get to such a point in such a short time frame. I was also impressed by the use of competing hypotheses, both in fitting current data and in making forecasts for future behaviour, in addition to applying the formal error analysis provided.

The report squarely addresses the major question 5: "What is the largest induced earthquake that can be expected in the Groningen area?", but does this as part of a more comprehensive and appropriate analysis of events of all sizes and probabilities. From this is clear that the main hazard is likely to come from intermediate-sized events, and I agree with the authors that maximum magnitude itself is not the best way to characterise the overall hazard. However, the analysis has not yet so far been coupled with an analysis of vulnerability and hence it is not yet known what likely magnitude range constitutes the biggest risk or impact to society.

Further work outside the scope of the current document will be needed to quantify and calibrate the site response and its variability, and to assess the exposure, vulnerability and risk per se, for example along the lines of the 'Cat' modelling community in the Insurance industry, using GIS data bases likely accessible to the regulators. Perhaps this is better addressed in the report summarising the response to question 6, although I note this question also focuses explicitly on hazard.

It was good finally to see all of the various studies aimed at addressing question 5 brought together for the first time, and especially the geo-mechanical modelling now made explicit in chapter 9. I also liked the explicit section on 'what we don't know' – always a good question. As acknowledged by the report:

The initial geo-mechanical model needs to be developed further, especially by more characterisation of the constitutive rules for laboratory samples as well as field-scale or well tests and then to integrate the 3D model into the seismic hazard analysis.

In addition I recommend in future work plotting the actual and geo-dynamically modelled stress state positions relative to the strength envelope at the present time and the start of production, as well as any other available snapshot times, to get an idea both of the current stress state and the trajectory for different parts of the reservoir. It will be interesting to see if there is a correlation between the seismic to aseismic partition coefficient and the proximity to the critical state curve along this stress trajectory, for example illustrated as contours of the partition coefficient on the critical state diagram. Looking forward this may provide a simple visual 'dashboard' for stress state monitoring and management.

While it is good to see finite size effects used as a constraint on maximum magnitude, the very high aspect ratio of 60km by 300 m (200:1) is way above the average of 2:1 for rupture dimensions of small and intermediate-magnitude events, though some large strike slip earthquakes that break the surface can have larger ratios of ~10:1.

More work will be needed in future to determine the actual aspect ratio of the source ruptures, e.g. using the aftershock area, and to determine the extent to which the overlying salt layer might resist the propagation of dynamic slip. This is important because it will place constraints on the likelihood of surface rupture. The new borehole seismic network will help greatly with this, in particular by reducing uncertainty in source depth estimation.

Finally, it is clear from the report that understanding and constraining the partitioning coefficient between seismic and total deformation and its evolution is still an issue. I have separately made some technical suggestions on how to address this source of uncertainty as part of the on-going study, and note Shell have already organised a much broader workshop on the issue.

Reference:

1 Ellsworth, W. (2013) Injection-induced earthquakes, Science 341, no. 6142, DOI: 10.1126/science.1225942)

0.13 Independent review of 'Report to the Technical Guidance Committee (TBO) on alternative production measures and hazard analysis' (part 2)

Review by Ian Main, University of Edinburgh, 14 November 2013.

This report addresses the question of how the stress state in the subsurface may be managed to reduce the hazard from future seismicity induced by gas production from the Groningen field. It is written at quite a high level and is also quite dense, so it is not possible to check all of the details leading to a particular conclusion. Nevertheless the conclusions are based on a large body of previous work, and there are many significant new findings and recommendations. The report acknowledges many remaining sources of uncertainty in calculating the future hazard, as well as summarising strategies to reduce the uncertainty in terms of passive monitoring of the field and in better characterisation of the material properties in going forward. Some of this uncertainty will reduce with additional data from the planned monitoring programme, but a significant amount will remain.

The report explicitly considers the likely response of the reservoir to several potential scenarios aimed at reducing the hazard by planned stress state management, including an 'emergency stop' and full pressure support by injection of nitrogen as end-member strategies. The likely response of the reservoir and associated hazard is complex and hard to predict exactly, as clearly acknowledged in the report. It may depend on structural detail that cannot be resolved at present within the seismic resolution, or on model

parameter uncertainty that can be addressed by more work on the materials concerned, conditioned on a large programme of monitoring of the field, including new seismic data to be acquired from borehole sites. One of the biggest sources of uncertainty is the strong effect of different models for compaction, which has a greater effect than the differences in the different mitigation strategies.

The predicted hazard is expressed sensibly by a range of measures rather than a single number, enabling risk management to be done with a sensible spread of possible outcomes. This is done by assuming a non-stationary Poisson process with a hazard rate that increases in time, conditioned on past behaviour. The effect of different sources of uncertainty in hazard forecasting is estimated using a logic tree analysis of the outcome of work conducted earlier in the programme. Overwhelmingly the main source of uncertainty that emerges is the partition coefficient between seismic and aseismic (elastic and plastic) strain, and the degree to which this may change in time. This is very sensibly identified as a priority in planning future work.

Two major new studies have been carried out using 2D and 3D geo-mechanical models, conditioned on the structural and mechanical properties of the field, supported by a technical appendix. This is a necessary and impressive contribution to stress state management for hazard mitigation. The appendix shows that a good body of field-specific data is available to condition the geo-mechanical models, though more needs to be done as acknowledged, including better characterisation of materials outside the reservoir horizon, and a study of the scaling properties of the relevant parameters. Despite this the models already provide a good history match to past data, albeit likely with a large number of parameters that are to some extent tuneable, and falsifiable forecasts of reservoir response are made for different model parameters within the reasonable range. The forecasts will in time help discriminate between the competing models as new data are collected.

The 2D modelling study predicts a maximum displacement within the reservoir of 0.5 m or so. This is consistent with a maximum possible magnitude of around 6.5 in TBO report 5, based on the assumption there of a 100% partition coefficient. Typically a magnitude 6 will produce 1m or so of slip, and the modelled slip on a single fault in the present report is less than this. This may indicate the main hazard is from smaller but more common events, consistent with the conclusion reported in TBO report addressing question 5. By having such slip on many faults, and considering the potential for reactivated slip to propagate or indeed nucleate in the surrounding layers this may resolve the problem of unrealistic aspect ratios in the previous report (see also Table 6.1).

The report points out that even the 'emergency stop' scenario is not without risk – as demonstrated recently in a real case in a geothermal energy context in Basel, Switzerland, showing that transient or time-dependent effects do need to be taken into account, as considered explicitly here. Similarly maintaining 100% pressure in the reservoir may also require intrusive surface installations and workflows. In this case it is important to acknowledge the possibility of hysteresis, i.e. recovering pressure fully will not be an absolute guarantee of zero risk.

The executive summary presents a very good overview of the outcomes of the work programme so far, given such a dense and technical report. It is also a fair summary of the state of knowledge at present and presents sensible ways of moving forward, when taken in conjunction with the comprehensive list of recommended further work in Table 6.1. This work in progress highlights the operational fact that risk management will be a learning process, informed by feedback in the light of new data and the actual outcomes.

My main general comments are as follows.

1. It might have been useful to provide a more extended discussion of the rationale for the production scenarios considered in the part 1 report. (The petroleum engineering aspects are considered separately in part 2, but a brief summary of the broad rationale and explicit cross-reference to the relevant sections might also be useful in part 1).

2. All of the scenarios are long-term 'smoothed' scenarios for the population of induced events. It may be useful also to examine and plan for adjustments to production as individual felt events occur, and

to develop protocols in advance for hazard mitigation during such transients. Even at this stage it seems quite plausible that a temporary 'emergency stop' might turn out to be sub-optimal.

3. This and previous reports highlight a structural problem in the regulatory framework for seismic hazard in Europe as a whole, not just in the Netherlands, i.e. its current basis in a stationary Poisson model as a basis for probabilistic seismic hazard assessment. Here the hazard is both non-stationary and probably non-linear in time. As such the current report is very much placed at the research frontier in terms of seismic hazard forecasting.

Non-stationary models are being developed in other contexts, and some new techniques may emerge from the literature as time goes on (for natural as well as induced seismicity). For now the approach taken is reasonable given the state of the art and the lack of clear guidelines on time-dependent hazard in Europe. It is particularly strong both in identification and assessment of uncertainties, and in making specific plans for reducing these. Much more work needs to be done of course, and there is likely an irreducible element to the uncertainty which will need to be considered in risk management and communication, but many of the key building blocks for stress state management to underpin this future effort are now in place.

1 Introduction

This report provides technical support for the update of the Groningen Winningsplan of 1st December 2013 and contains additional details of the analysis of subsidence and earthquakes induced by gas production from the Groningen field. This report presents study progress on:

- Results of geomechanical and seismological studies into induced earthquakes in the Groningen field based on the historical earthquake record with forecasts of future seismicity
- Results of the analysis of compaction of the reservoir rock and subsidence with forecasts of future subsidence
- Impact of different depletion scenarios and the application of pressure maintenance on the seismic hazard

In a letter to parliament (11 February 2013 reference TK 2012-2013 33529, no. 2), the Minister of Economic Affairs initiated a number of studies on induced earthquakes in the Groningen area. Study number 5 addresses "research into the maximum strength of earthquakes associated with the Groningen gas field". Study number 6 addresses "research into different production methods to reduce the number and magnitude of earthquakes". A Technische Begeleidingscommissie (TBO; Technical Guidance Committee Sub-surface) and steering committee were set up to oversee this study work and ensure quality and independence. The results of these studies have been incorporated in this report.

The research was carried out by experts from NAM, Shell Research Centre in Rijswijk and the ExxonMobil Upstream Research Centre in Houston with support from external experts with relevant knowledge. The report is contains 12 chapters (including this introductory chapter), which are briefly introduced below:

2. This introduction to the document (1) is followed by an introduction into the geology of the Groningen field. This section also contains historical background information relevant to induced earthquakes, which will be referred to in later sections. The section concludes with a history of induced seismicity in the Groningen field and a description of the current (2012) seismic network.
3. This section includes a discussion of the depletion philosophy for the Groningen field. An alternative philosophy aiming to reduce earthquakes in the Loppersum area is introduced. The impact of production curtailment and depletion philosophy on the reservoir pressure is considered.
4. Compaction of the reservoir rock in response to gas production plays a crucial role in the process of inducing earthquakes. Section four explains the process and future trends expected in the compaction and subsidence.
5. Induced earthquakes are not only experienced in the Groningen field, but in several other fields in the world. Section five gives an overview of other fields, where earthquakes induced by gas production earthquakes have been reported.
6. Section six on the release of energy by earthquakes is the core of this document. Starting with the historical earthquake record, a statistical and geomechanical analysis is given of the frequency of occurrence and magnitude of induced earthquakes and the expected future trend of the seismicity.
7. Once the earthquake has occurred, the released energy moves to the surface and causes movement of the ground. This constitutes the hazard. Section seven describes this process and methods to assess the ground movement based on the released energy.
8. In section eight, the insights into the induction of earthquake are combined with the method to assess ground motions to provide hazard maps. It starts with a discussion of the hazard for limited time periods (3, 5 and 10 years in the future) and an analysis of the uncertainty in the hazard analysis using a logic tree approach. Based on compaction forecasts using different compaction models, the seismic hazard for the current production plan and different production scenarios is estimated.
9. A review of the geomechanical studies into the role of faults is given in section nine. Geomechanical modelling based on 2D fault geometries to gain fundamental insights into potential fault slip mechanisms and of 3D full field and sub-models for regions of the field is described in this section of the report.
10. Based on the current data the substantial uncertainties remain. Plans for additional data acquisition activities to reduce the uncertainty in the earthquake parameters are laid out in section ten. A study

and data acquisition plan to reduce the remaining uncertainty in the hazard is summarized in this section.

11. The methodology used in the 3D geomechanical modelling of the sub-models is summarized in this appendix.
12. This appendix describes the option for pressure maintenance. In this selection of the injection medium for pressure maintenance, several fluids are considered. Nitrogen is selected as the most suitable option. The modelling of the displacement and mixing of the injected nitrogen and the indigenous natural gas is described. Production forecasts and reserves estimates are prepared for a base case development concept. The surface facilities required for a field development on the basis of pressure maintenance through nitrogen injection is also sketched.
13. Conclusions and final Insights have been included in Section 13.

2 Introduction to the Geology and Seismicity in the Groningen field

2.1 Regional Geology and Conceptual Structural Model

2.1.1 Structural setting

The reservoir rocks of the Groningen field are dissected by a large number of natural faults. Some of these natural faults are thought to play an important role in the creation of earthquakes. They represent zones of weakness along which movement of volumes of reservoir rock can take place. Hence, it is key to understand the distribution and character of the natural faults in the subject area. More detailed accounts on the relation between earthquakes and natural faults are given elsewhere in this document. This section describes the development of the fault system through time and its main geometrical characteristics.

The Groningen field is located on the Groningen High that has been a tectonically stable block since the late Kimmerian uplift. The current depth of the Rotliegend reservoir, around 2600-3200 mTVD (true vertical depth), reflects the maximum burial depth. The Groningen High is surrounded in the east by the Ems Graben and Lower Saxony Basin and in the west by the Lauwerszee Trough (Figure 2.1). The Groningen field is mainly fault-closed in all directions with dip closures present only locally. Top seal of the Groningen field is provided by the overlying Zechstein salt. Figure 2.2 shows a seismic line from NW to SE illustrating these features.

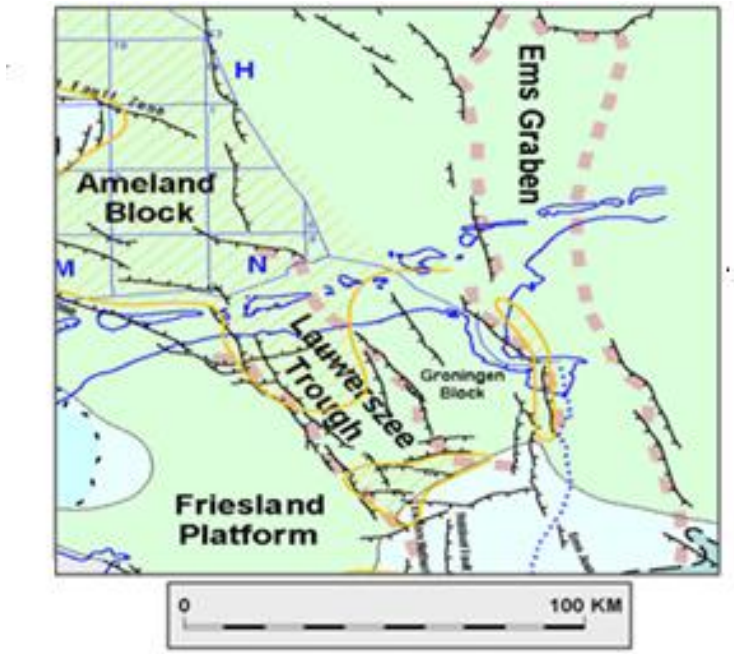

Figure 2.1 Main structural elements in the northern Netherlands

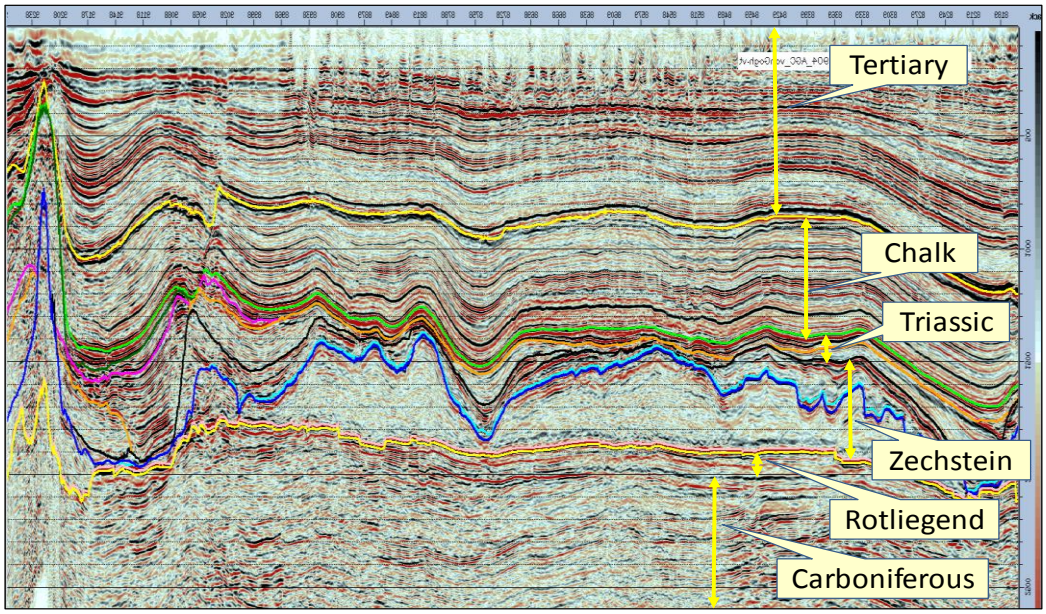

Figure 2.2 Seismic cross-section through the Groningen field (see Figure 2.4 for detailed interpretation)

The Ems Graben and Lauwerzee Trough are results of a Late Carboniferous / Early Permian rifting phase (extensional). The Groningen High was formed by the development of large North to West trending faults. Initiation of these faults started prior to the Saalian erosional event which marks the Carboniferous-Permian boundary across the region.

Most of these faults have been reactivated by two major tectonic events. The first was a period of SE-NW extension which began during the Triassic and continued into the Late Jurassic. An inversion stage followed during the late Jurassic-early Cretaceous (Kimmerian). Movement of the Zechstein salt also took place in Cretaceous times. With the onset of the Alpine orogeny the area underwent a period of N-S compression, lasting into the early Tertiary. This resulted in a second period of reactivation, evidenced in some areas by transpressive skinny grabens and pop-up structures.

Detailed analysis of fault orientations, timing and kinematics has enabled to subdivide different structural domains (SD1 to SD9 in Figure 2.3). Note that only a selection of the most important faults is included in the structural model. Moreover, not all faults present in the subsurface are necessarily identified in the seismic interpretation. SD1 in the South-Western periphery of the Groningen field is the most complex and intensely faulted domain. It has experienced the most pronounced shortening and inversion, mainly along NW- and E-trending faults, and manifested by pop-up structures.

SD5 in the Zeerijp area is another structurally complex domain. It is interpreted to be a depressed graben feature bounded by two NNW-oriented oblique slip faults, which originated from a deep-seated older fault zone. The difference in orientation between this fault zone and the Triassic-Jurassic stress field led to strike-slip movement along the graben boundary faults, and to rotation of fault blocks within the graben.

SD6 in the North-East is an example of a structurally quiet domain. E-W trending faults are branching from a deeper-seated fault system, probably as a result of Jurassic extension and without evidence for later-stage inversion.

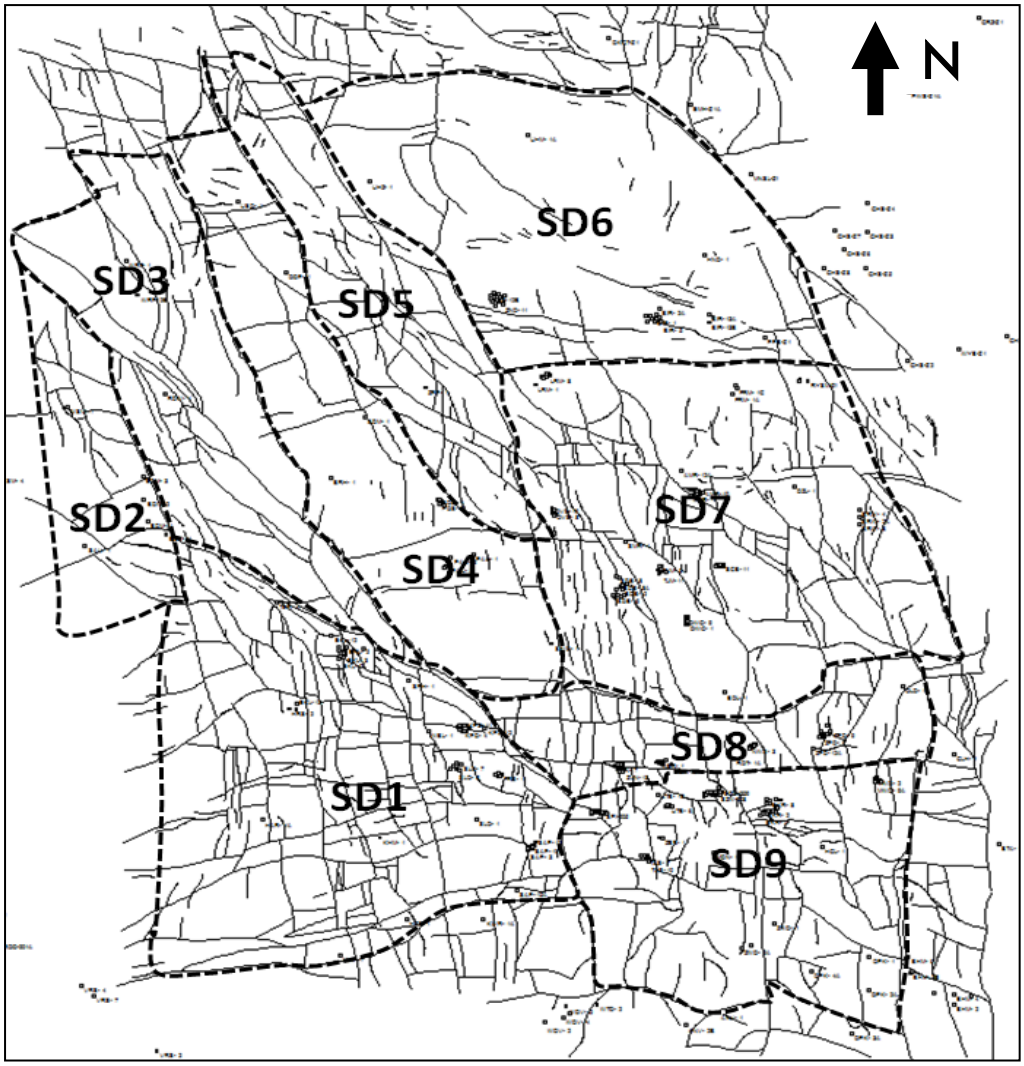

Figure 2.3 Structural domains in the Groningen field (total area ~ 40 x 40 km); faults shown are at Top_Rotliegend level

2.1.2 Stratigraphy and depositional setting

A second important factor in the study of induced earthquakes, next to the structural model described above, is the distribution of rock properties in the reservoir. For example: the higher its porosity, the higher is the potential for the rock to compact as a result of gas production (the key role of compaction induced seismicity is described in section 4). Porosity is high in sandstone rock and low in claystones. The depositional processes that formed the sandstones are also important in the sense that rocks formed by wind action (aeolian sediments) generally have higher porosities than those formed by river currents (fluvial sediments). In the following, an overview is given of the important rock formations present in the subsurface of Groningen.

The gas-bearing interval in the Groningen field comprises both Upper Rotliegend Group (Permian) and Limburg Group (Carboniferous) sediments, separated by the Saalian Unconformity.

The Carboniferous sediments range in age from Westphalian-A to Westphalian-D. They represent lower to middle delta plain deposition under humid, subtropical conditions. The Carboniferous strata have been tilted and eroded during the Variscan orogeny (Figure 2.4). This created a depositional relief that was gradually filled by the Rotliegend.

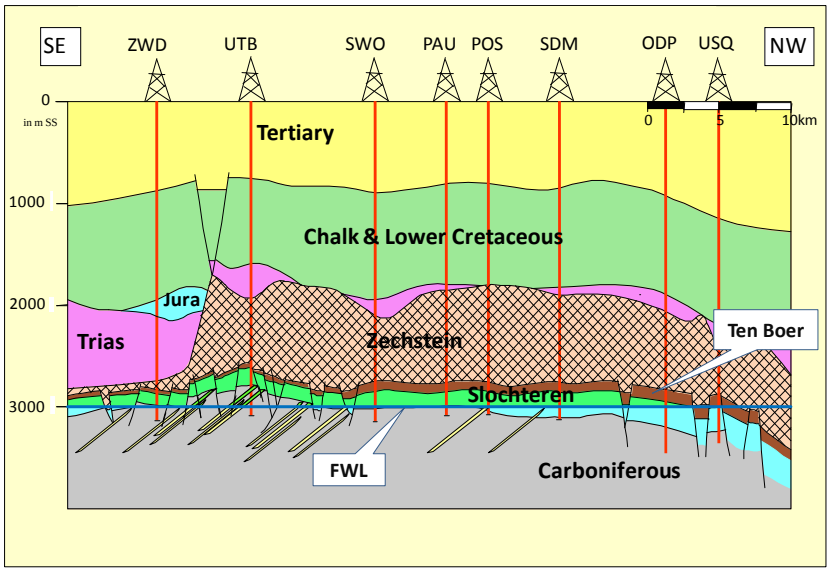

Figure 2.4 Schematic cross-section through the Groningen field indicating the main stratigraphic intervals. FWL indicates the free water level.

The Upper Rotliegend Group comprises the Silverpit and Slochteren Formations. These are subdivided into the following lithostratigrahic members (top to bottom): Ten Boer Claystone (ROCLT, heterolithic shale/silt/sand), Upper Slochteren Sandstone (ROSLU, mainly sand), Ameland Claystone (ROCLA, heterolithic shale/silt/sand) and the Lower Slochteren Sandstone (ROSLL, mainly sand).

Table 2.1 Lithostratigraphic Subdivision

Time	Group	Formation	Member	REGEO CODE
Permian	Zechstein			ZE
Permian	Upper Rotliegend	Silverpit	Ten Boer Claystone	ROCLT
		Slochteren	Upper Slochteren Sandstone	ROSLU
		Silverpit	Ameland Claystone	ROCLA
		Slochteren	Lower Slochteren Sandstone	ROSLL
Carboniferous	Limburg			DC

The Silverpit- and Slochteren Formations form a wedge of continental sediments that is onlapping southwards onto the Carboniferous relief, and thickening towards the northwest (Figure 2.5). Rotliegend sediments were deposited under arid, desert climate conditions. In the south of the Groningen area, along the basin margin, the sediments consist of mixed alluvial/braided river deposits. These grade northwards into mixed fluvial-aeolian deposits (Lower and Upper Slochteren Sandstone Members) and ultimately into lake margin and desert lake fines (the Ten Boer and Ameland Claystone Members.

Figure 2.5 Lithostratigraphic subdivision of the Rotliegend in the Groningen area

The Ameland and Ten Boer Claystone Members are characterized by silty to shaly wet sandflat deposits, representing lake level highstands of regional scale as a response to climatic variations. The Ameland Claystone can be clearly distinguished as a separate lithological unit in the northern half of the field, but pinches out towards the South. Total thickness of Rotliegend sediments ranges from 140 m in the SSE to 300 m in NNW.

The Rotliegend is overlain by the sediments of the Zechstein interval. The Zechstein is dominated by evaporate deposits, mainly halite, which forms a perfect seal for Rotliegend reservoirs. The lowermost part of the Zechstein comprises a very competent and high-density carbonate/anhydrite interval which is referred to as the Basal Zechstein. It is present throughout the greater Groningen area with a remarkably constant thickness (~50 m in average). The large acoustic impedance contrast between the Basal Zechstein and the overlying halite package creates a very strong seismic reflector, which is well-suited for mapping the structural features described in section 2.1.1. The interval may also play an important role in the transmission of seismic signals from a deeper source area to the surface. This is treated elsewhere in this document.

2.1.3 Reservoir model and rock properties

The Rotliegend interval has been subdivided into the five Slochteren reservoir zones, four Slochteren heterolithic zones, and three Ten Boer zones. A further vertical refinement was made by dividing the zones into thinner layers. The resulting static framework consists of 12 reservoir zones, 203 layers and a total of nearly 6 million grid cells. Approximately 90% of all grid cells have a thickness between 1 and 2 m.

Models to describe the distribution of reservoir properties in the Groningen field are based on the extensive database of wireline log and core data. The modeling methodology applied is Sequential Gaussian Simulation (SGS), supported by trend maps that reflect the regional depositional trends.

The mean Net-to-Gross for the Ten Boer Claystone ranges between 8 and 15%, but is typically larger than 95% for the Slochteren reservoir zones. The thin heterolithic zones separating the reservoir zones still have mean NtG values as high as 75 - 80%. The distribution of porosity shows comparable trends, with mean values of 6 – 10% for sandy interbeds in the Ten Boer Claystone, 15 - 18% for the reservoir zones, and only slightly lower mean values for the sandy parts of the heterolithic intervals.

Best reservoir quality is seen in the central parts of the field where aeolian processes have played an important role. Properties decrease towards the southern margin of the field, and towards the north. This is in line with depositional trends of becoming more clay-rich towards the north, and more fluvial-dominated or conglomeratic towards the south. as an example gives the porosity distribution of one of the reservoir zones.

The mean permeability of the reservoir zones ranges from tens to hundreds of milliDarcies, gas saturation ranges from 60 to 80%.

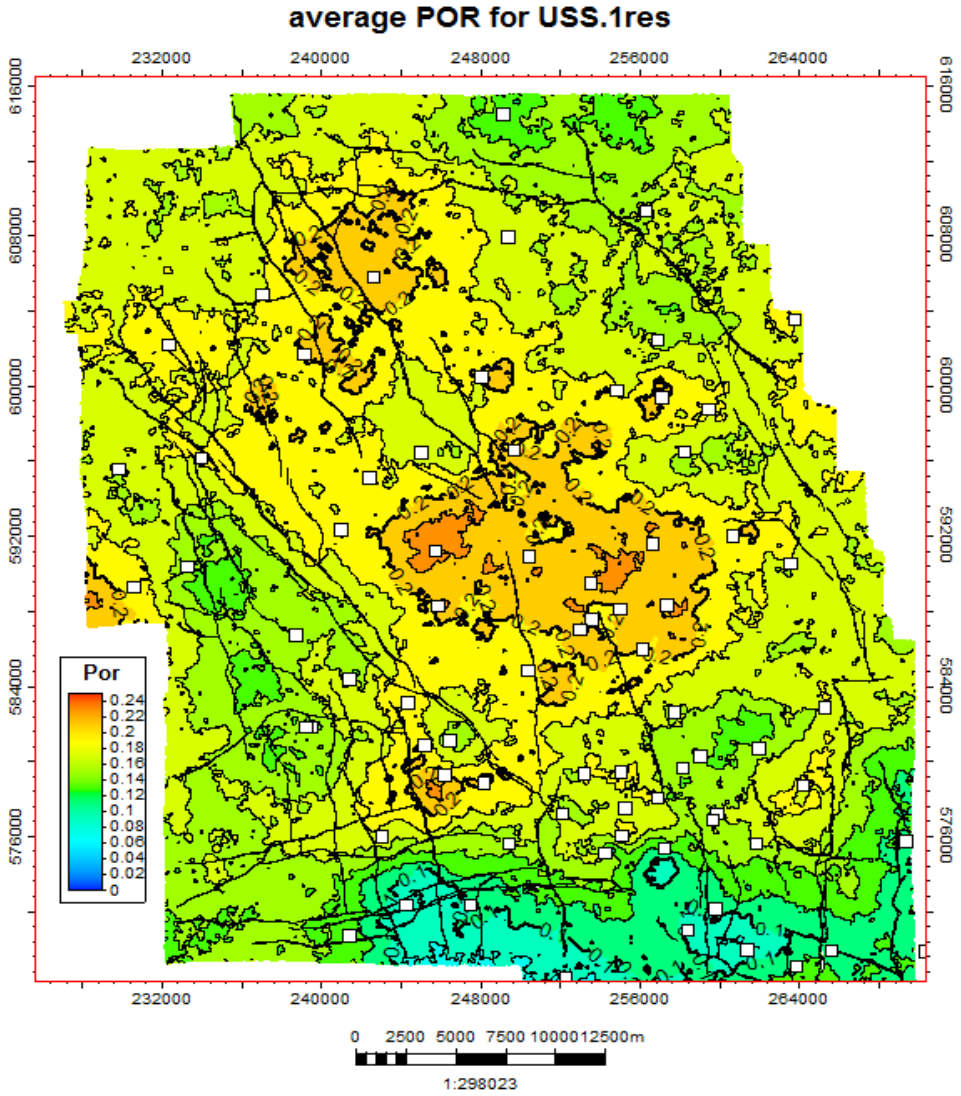

Figure 2.6 Average porosity of one of the Upper Slochteren Sst reservoir zones

2.2 Current Monitoring Network and Historical Seismicity in the Groningen Field

Since 1986 relatively small earthquakes have occurred in the vicinity of producing gas fields in the northern Netherlands. These events occasionally caused feelings of unease amongst residents. Some of these earthquakes in excess of a certain magnitude and intensity also caused damage to buildings, be it mostly non-structural.

A multidisciplinary study, initiated by the Ministry of EZ and guided by a Supervisory Committee (BOA, 1993), analyzed the relationship between gas production and earthquakes, concluding that based on the seismic pattern, the hypocenter locations, difference with historical seismicity and the frequency-magnitude distribution, the earthquakes were of non-tectonic origin and most likely induced by reservoir depletion (i.e. gas production). Following an agreement with the Royal Dutch Metereological Institute, KNMI, a borehole seismometer network was installed in 1995 in Groningen to detect earthquakes, measure their epicenters and quantify their magnitude. Accelerometers were also installed to measure ground motions in areas where earthquakes frequently occurred.

The earthquake near Huizinge (16/8/2012) with magnitude M_L=3.6 was experienced by witnesses as more intense and with a longer duration of ground motion than previous earthquakes in the same area, and certainly led to more emotions. Significantly more incidents of building damage were reported than for previous earthquake events. Together with the general observation that seismicity in the Groningen area seems to be increasing over the last years, and on instigation by SodM, the issue of gas production induced seismicity in Groningen has become the subject of new studies and data acquisition.

2.2.1 Previous Work

After the BOA study, multiple studies were published on the mechanisms of induced seismicity (TNO, TU-Delft) and statistics and analysis of recorded events (KNMI). Studies using numerical computer models showed that pressure depletion resulting from gas production lead to a stress change on existing faults, resulting in reactivation of these faults and consequently the occurrence of earthquakes. This is currently accepted by both operators and governmental bodies as the mechanism that best explains the earthquakes. Based on the recorded events, KNMI developed peak ground acceleration / peak ground velocity (PGA/PGV) maps for a certain return period assuming a stationary model.

2.2.2 Seismic Monitoring Network

Prior to 1989, the lower detection limit for earthquakes was a magnitude of 2.5. Extension of the network in Assen lowered this limit to 2.3, while the installation of a borehole seismometer station in Finsterwolde further reduced the detection limit in the Groningen Field to 1.5 (De Crook et.al, 1998). In 1995, the KNMI network was extended with 8 shallow boreholes all equipped with 3 component geophones at 4 levels (50 – 100 – 150 – 200 mTV depth). This monitoring network has been extended since;

1. in 2006, an accelerometer network with 8 accelerometers was installed,
2. in 2010 an additional 6 boreholes spread over the Northern Netherlands were added

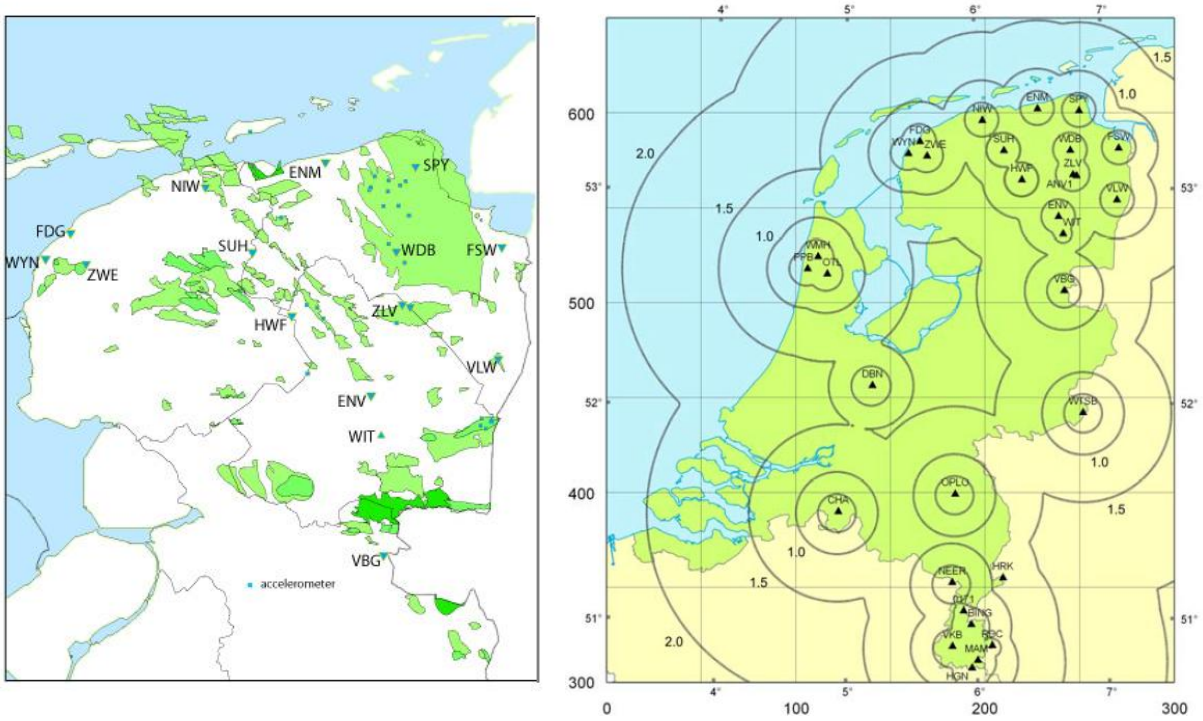

Figure 2.7 *Left: an overview of the KNMI network, triangles indicate locations of the borehole stations; squares the locations of the accelerometers. Right: Detections limits of earthquake magnitude (Dost et. al., 2012).*

The detection limit of the present network is magnitude M=1, with a number of limitations described in Eck et al (2004) and Dost et al (2012). The uncertainty in the location of the hypocenters is relatively large; laterally 500m and vertically several kilometers. Additional to the borehole seismometers 12 accelerometers are in place. This network is being upgraded with replacement of 5 older accelerometers and the installation of additional 6 accelerometers. This will improve measurement of lateral movement at surface and the location of earthquake hypocenters. Further extension of the seismometer network is planned for 2014, for details see section 10.2.3.

2.3 Earthquake Statistics

Around 220 earthquakes with magnitude ≥ 1.5 were registered in the period from 1991 till July 2013 in the Groningen area. Before 1991, no earthquakes were reported from the Groningen area, but earthquakes did occur in areas around Assen and Purmerend. It therefore seems plausible to assume that no humanly perceptible events in the Groningen area occurred before 1991. Figure 2.8 shows the surface projections (epicenters) of the recorded earthquakes, with in red the M=3.6 Huizinge event. More information about this event can be found in Dost and Kraaijpoel (2013).

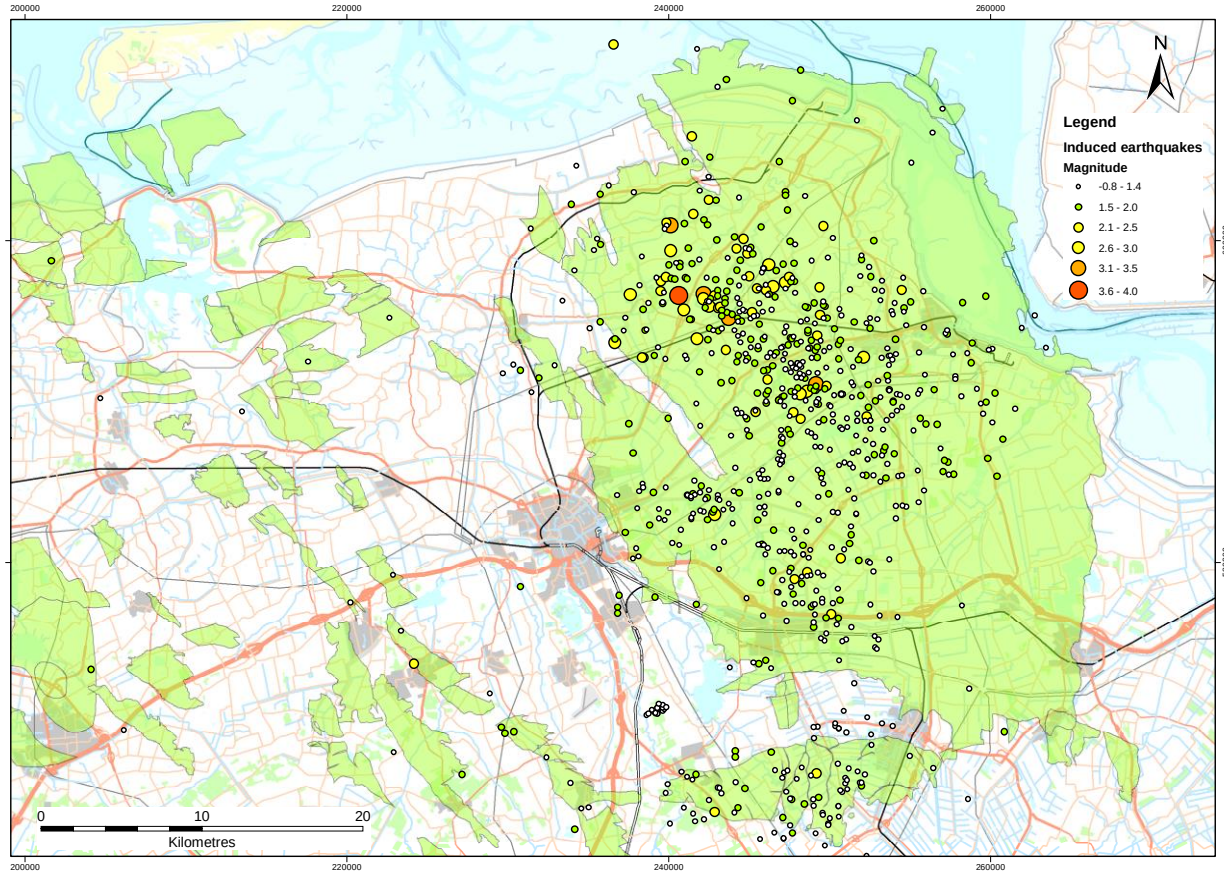

Figure 2.8 Epicenters of the registered earthquakes by the KNMI (till July 2013)

The earthquake data published by KNMI are filtered using a threshold $M_l \geq 1.5$ to avoid interference from network changes. This threshold is valid since August 1995, making 1996 the first year with a complete dataset. Figure 2.9 shows the yearly number of earthquakes categorized by magnitude intervals. From this we conclude that on average the annual number of earthquakes has been increasing since 2003.

A comparison can also be made between gas production (variation) and the number of earthquakes. Due to the relatively small amount of earthquakes with $M_l \geq 1.5$ in Groningen, only correlations between *annual* production (or production over a larger time interval) and earthquakes are relevant. Figure 2.10 shows the relationship between the cumulative energy released by the earthquakes and the amount of produced gas. The seismic energy can be calculated with the equation used by the KNMI (Van Eck et al. 2004). It is based on the relation published by Ahorner & Pelzing (1985) between released seismic energy (E_s in Joule) and local magnitude (M_l):

$$Log E_s = 3{,}81 + 1{,}64 \mathrm{M_l}$$

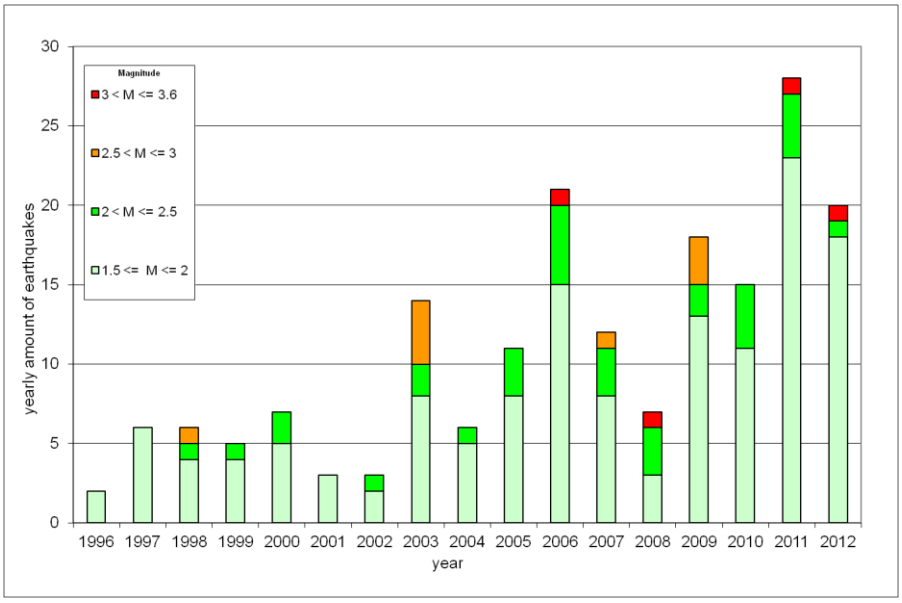

Figure 2.9 yearly amount of earthquakes since 1996, grouped by magnitude class

The production of gas leads to a decrease of the pressure in the reservoir, which is regarded to be the largest driving force behind the earthquakes. The first earthquake ($M_l \geq 1.5$) was observed at a cumulative production of around 1300 billion Nm^3. A slight increase of the slope is visible at a production of around 1700 billion Nm^3. This is further discussed in section 6.2.

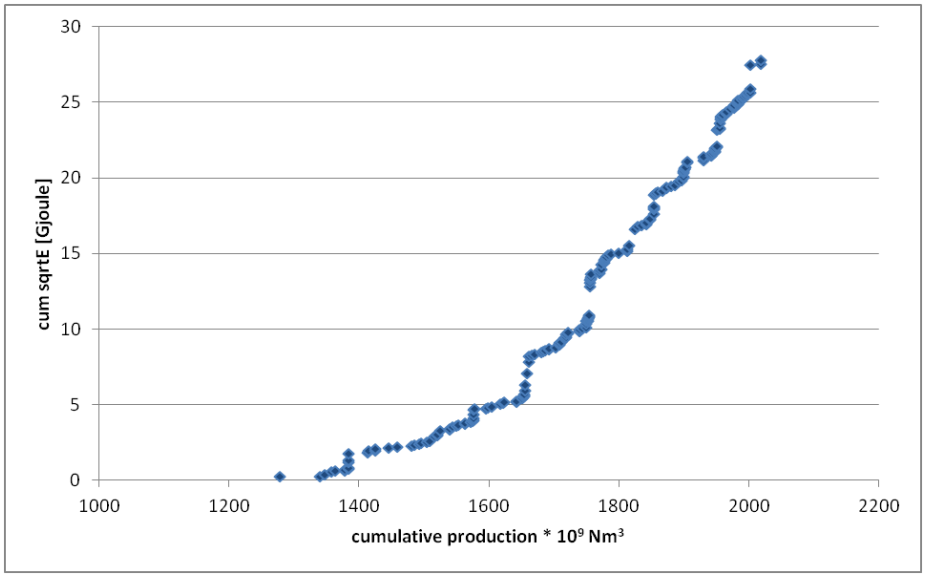

Figure 2.10 Cumulative square root of seismic energy versus cumulative production of gas in the Groningen field

2.4 Compaction and Seismicity

An initial review of the location of highest seismicity with various reservoir parameters was carried out. The distribution of earthquake epicenters was compared to incremental stress, bulk reservoir volume change density (compaction) and fault density (Figure 2.11). The observed epicenters conformance is most closely with the volume change density.

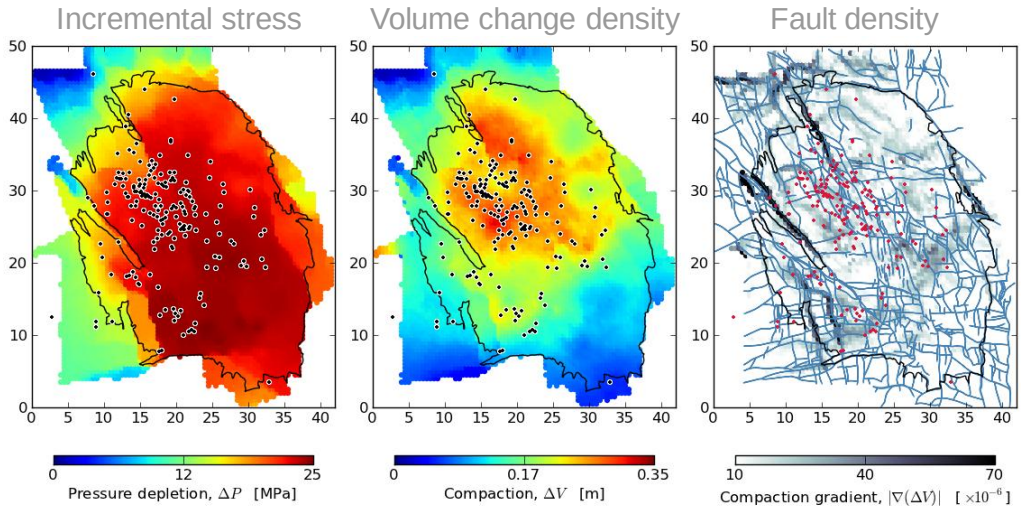

- Critical stress necessary but insufficient for observable seismicity
- Observed earthquakes conform with reservoir volume changes
- Fault reactivation is a likely mechanism[1] - but which faults?

[1] *E.g.* Lacq, Yibal, Ekofisk, Valhall, Fashing

Figure 2.11 Observed seismicity concentrates around the center of the field. This is also the area of largest volume change density. Pressure depletion is largest in the south of the field away from this area of high observed seismicity, while fault density is also high in areas with less observed seismicity.

Conformance between the observed seismicity and reservoir compaction is also apparent when the observed earthquakes are plotted against the compaction at the epicenter and origin time of each earthquake (Figure 2.12). Most earthquakes occurred after local compaction exceeded 18 cm (90%). The same effect is apparent again by plotting maps of cumulative earthquake epicenters and the 18 cm reservoir compaction contour as they develop through time (Figure 2.13). Seismicity is mostly observed inside this compaction contour, while outside this contour, compaction appears to be almost aseismic.

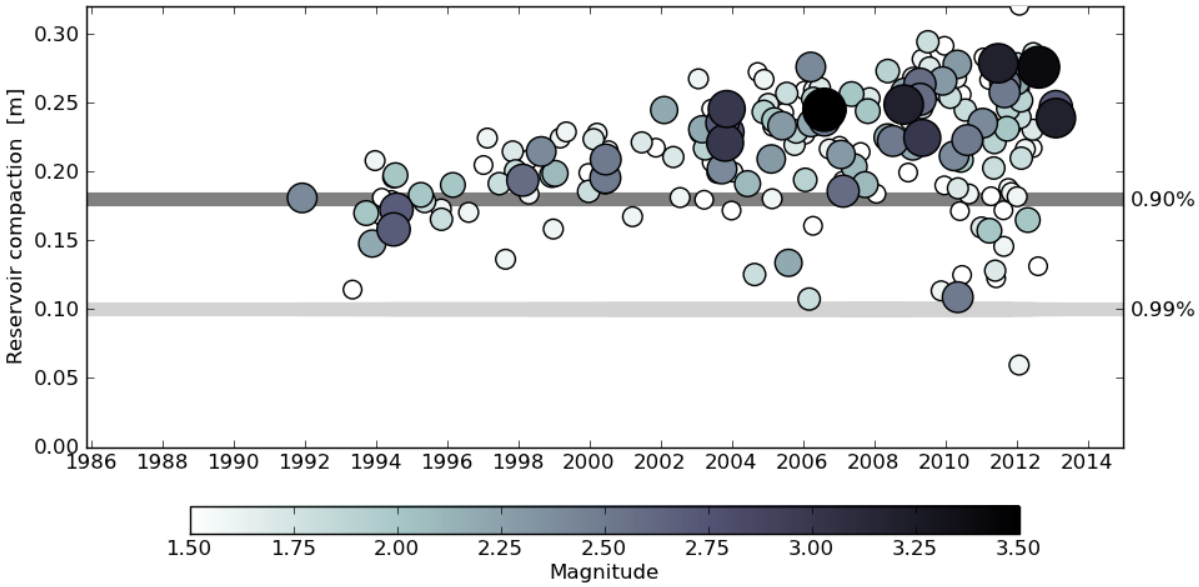

Figure 2.12 The observed earthquakes plotted for reservoir compaction against time. The size and color of the marker indicate the magnitude of the earthquake.

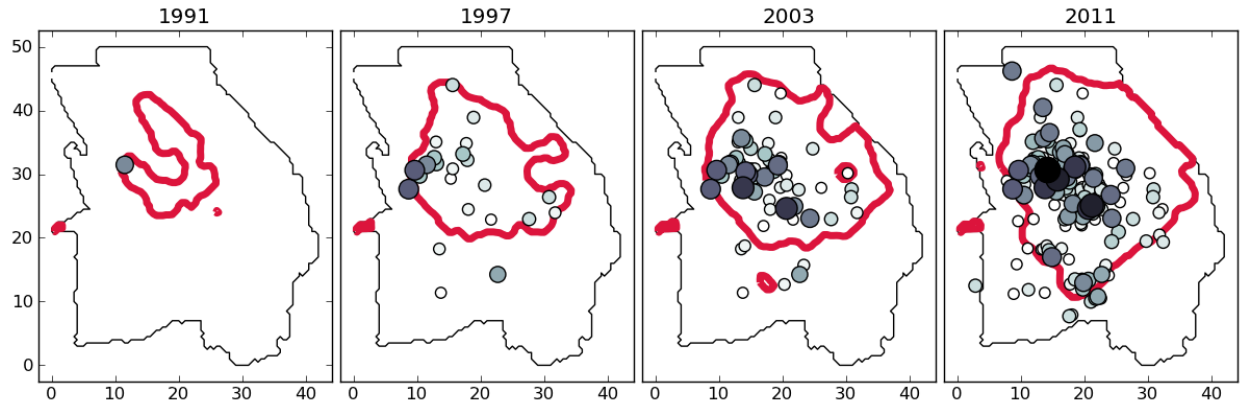

Figure 2.13 The observed earthquakes plotted on the map of the field together with the 18 cm compaction contour for four years (1991, 1997, 2003 and 2011).

2.5 References

Ahorner, L., Pelzing, R. (1985) The source characteristics of the Liège earthquake on November 8, 1983, from digital recordings in West Germany. In: P. Melchior (ed), Seismic activity in Western Europe. D. Reidel, Dordrecht, pp. 263-289.

BOA (1993) Eindrapport multidisciplinair onderzoek naar de relatie tussen Gaswinning en Aardbevingen in Noord-Nederland; Begeleidingscommissie Onderzoek Aardbevingen, 1993

De Crook, Th., H.W. Haak & B. Dost (1998). Seismich risico in Noord-Nederland.KNMI (Koninklijk Nederlands Meteorologisch Instituut), Techn. Rep., De Bilt, Netherlands.

Dost, B. and Kraaijpoel, D. (2012) The August 16, 2012 earthquake near Huizinge (Groningen). KNMI report, KNMI De Bilt, 2013.

Dost, B., Goutbeek, F., van Eck, T., Kraaijpoel, D. (2012) Monitoring induced seismicity in the North of the Netherlands: status report 2010. WR 2012-03.

Van Eck, T., Goutbeek, F., Haak, H., Dost, B. (2004) Seismic hazard due to small shallow induced earthquakes. WR 2004-01.

3 Gas production from the Groningen field

3.1 Historical production

The Groningen field was discovered by well SLO-1 in 1959. After this discovery, a public-private partnership - between the NAM, its shareholders, DSM (now EBN) and the Dutch government - was set up. Its objective was, and is, to pursue a joint policy in order to explore and exploit the gas accumulations within the boundaries of the Groningen concession to maximize economic reserves.

The partners in this venture had a sense of urgency in the development and marketing of the Groningen gas, as it was estimated that there was only a limited window of opportunity for the selling of this resource. It was generally thought that nuclear energy would replace fossil fuel within the near future.

The field was developed by several production clusters in the Southern part of the field. At the time, the full extent of the field was not known and it was thought that the entire field could be produced through these Southern clusters. However, additional appraisal drilling in the Northern part of the field proved that the Groningen gas volumes were larger than previously assumed. Furthermore, pressure measurement in these appraisal wells indicated that, as the Northern part was declining in pressure with a significant delay (Figure 3.1), additional production clusters in the North were required. A detailed description of the facilities in the Groningen field can be found in the Groningen winningsplan.

In the early seventies, rapid development of the field continued with several production clusters in the Northern part of the field.

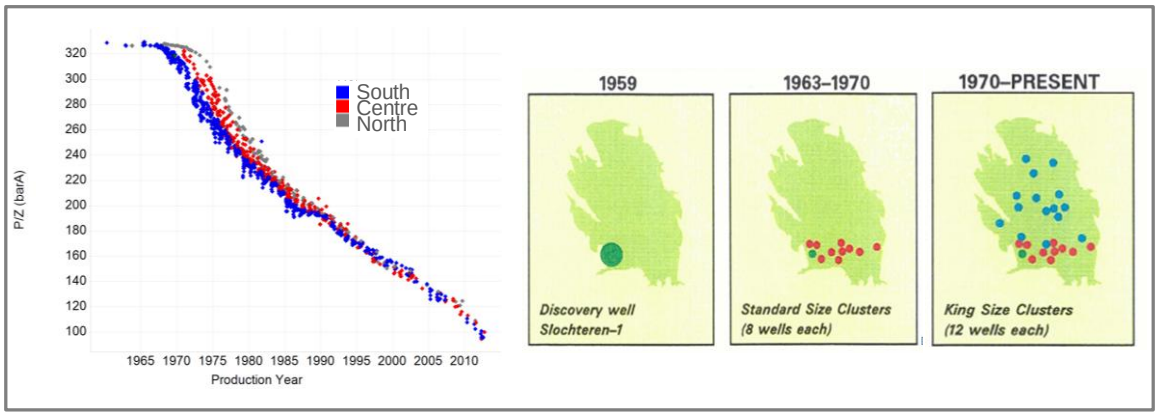

Figure 3.1 Phased development of Groningen field and historical pressures

After the first oil crisis in 1973, it became clear to the Dutch government that nuclear energy would not replace fossil fuels and the rapid development of the Groningen field was not considered desirable any longer. Therefore, the Small Field Policy was introduced. The Small Field Policy is intended to stimulate the exploration and development of smaller gas reservoirs onshore and offshore in The Netherlands. Any gas found can be offered to GasTerra, who has the obligation to purchase the gas at reasonable terms and conditions. For oil and gas companies this means that small fields can be developed attractively, no separate commercial development is required in case of small finds, and these fields can be operated without disruptions due to fluctuations in gas demand.

The overcapacity of the Groningen field made the Small Field Policy possible; the Groningen field would be the swing provider ('sluitpost') between small fields' production and customer demand. This role demanded good co-operation between NAM and GasTerra in order to ensure market demand and supply were matched and that NAM made its investment on the Groningen field in an optimum manner. The success of the Small Fields Policy is illustrated in Figure 3.2.

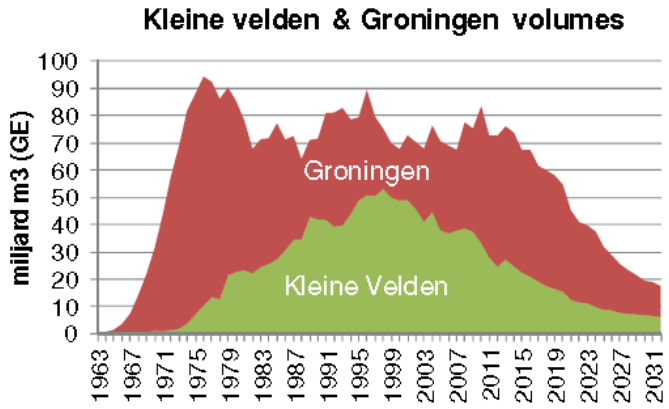

Figure 3.2 Annual gas demand and relative gas production of the Groningen field and small gas fields ("kleine velden")

With the introduction of the Small Fields Policy, a production philosophy has been introduced that balances the production from the field to keep pressure differences between the North and South of the field at low levels. In practice, this means that the clusters in the North of the field, where the cluster density is lower and therefore in-place volumes per cluster are larger, are produced preferentially. The clusters in the South of the field are only produced when required (i.e. mostly in winter). Exceptions to this are the relatively small peripheral blocks in the South-Western part of the field. In these blocks, the reservoir pressure lags behind the pressure in the main area of the Groningen field. Dedicated production wells are planned in these areas (see section 2.2.2).

At the end of the 1980's, with the continuous production of the Groningen field, it became clear that compression at production clusters was required in order to reduce the suction pressure at the wells. In addition, the predictions at the time indicated that in the summer months the small fields' gas production would be larger than the market demand, even with Groningen at its minimum flow.

This resulted in a decision to delay the installation of compression on the Groningen clusters and to develop three Under Ground Storages: two by NAM - Norg and Grijpskerk, and one by BP (currently TAQA) in Alkmaar. These UGSs are considered part of the Groningen system and are an extension of the Groningen main field. They were built with the following requirements: high production capacity (security of supply in winter) and large volume shifting capacity (i.e. increased demand in summer). This is illustrated in Figure 3.3.

In recent years, the gas demand has increased whilst the contribution of the small gas fields is steadily declining (also Figure 3.3). As a result, Groningen production has increased and the UGS fields have been used more frequently. Therefore, in 2012 the decision was made to expand the Norg UGS. This will be followed by the installation of 2nd stage compression later this decade. Future development plans for meeting the gas demand in the Groningen field are described in section 2.2.2.

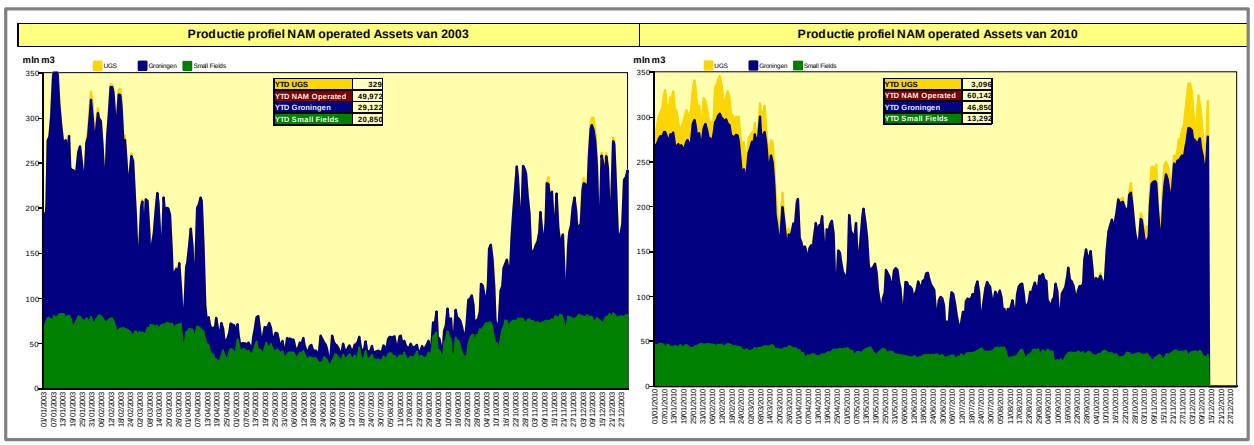

Figure 3.3 Intra-year production of NAM, 2003 versus 2010. (Small gas fields in green, Groningen main field in blue and the UGSs in yellow)

3.2 Pressure development in the field over time

The current production philosophy aims to balance the production from the field and keeps pressure differences low between the North and South. In some peripheral parts of the field, where the reservoir pressure is lagging behind, there are opportunities for further development (see section 2.2.2 for more detail). Figure 3.4 shows that the measured pressure lag in the gas in North West is relatively small (i.e. maximum of some 20 bar). The measured pressure lag in the gas in the South West is larger (i.e. close to 100 bar). Note: The Harkstede block has been put in production through the Eemskanaal-13 well and is preferentially produced as a result of the implemented production philosophy.

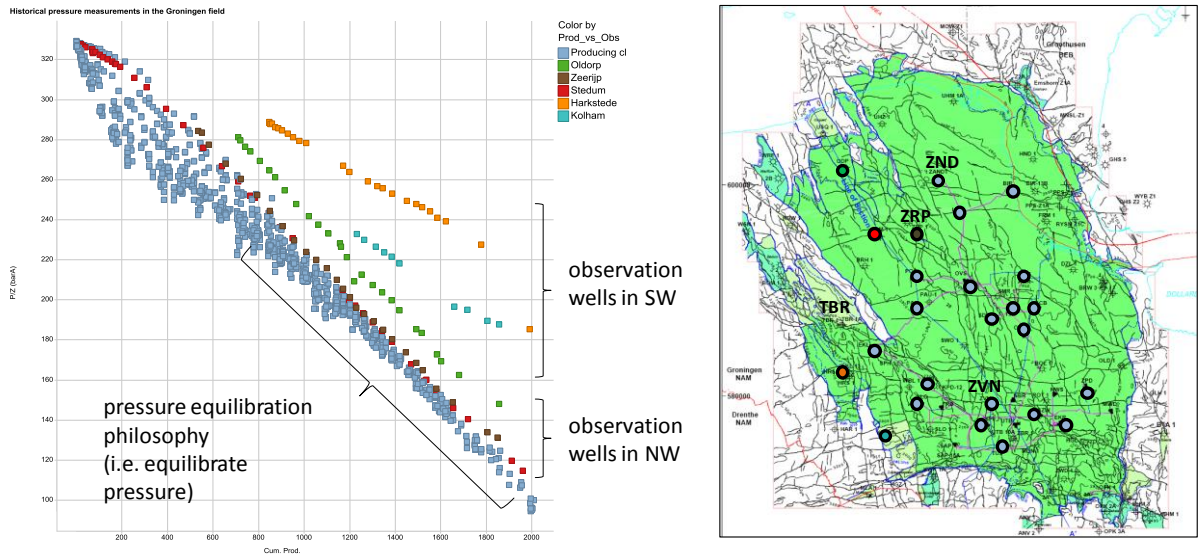

Figure 3.4 Pressure difference in the field (in bar)

Due to declining reservoir pressure and subsequently a reduction in production capacity, the current production philosophy will become more difficult to maintain. In other words: in order to meet demand, all production locations in the field need to produce more frequently. As a result it is expected that the pressure difference between North and South under the current production scenario will start to increase again to some 20-25 bar. Figure 3.5 shows the forecasted pressure decline based on current estimated market demand. Two production clusters are shown, 't Zandt (ZND) in the North and Zuiderveen (ZVN) in the South. The pressure in ZVN clearly shows the pressure response of preferential production during the winter. These fluctuations, of as much as 10 bar, cannot be seen at Zeerijp where a steady and constant yearly pressure decline is observed and forecasted (i.e. a pressure pulse originating from the South of the field has no noticeable pressure effect in the North of the field). The annual pressure depletion of the field in the period 2005-2015 and 2010-2020 is slightly less than 5 bar/year based on the imposed maximum production cap of 425 bcm per decade (ignoring yearly fluctuations). This translates to 1 bar pressure depletion for every 8 to 9 bcm produced.

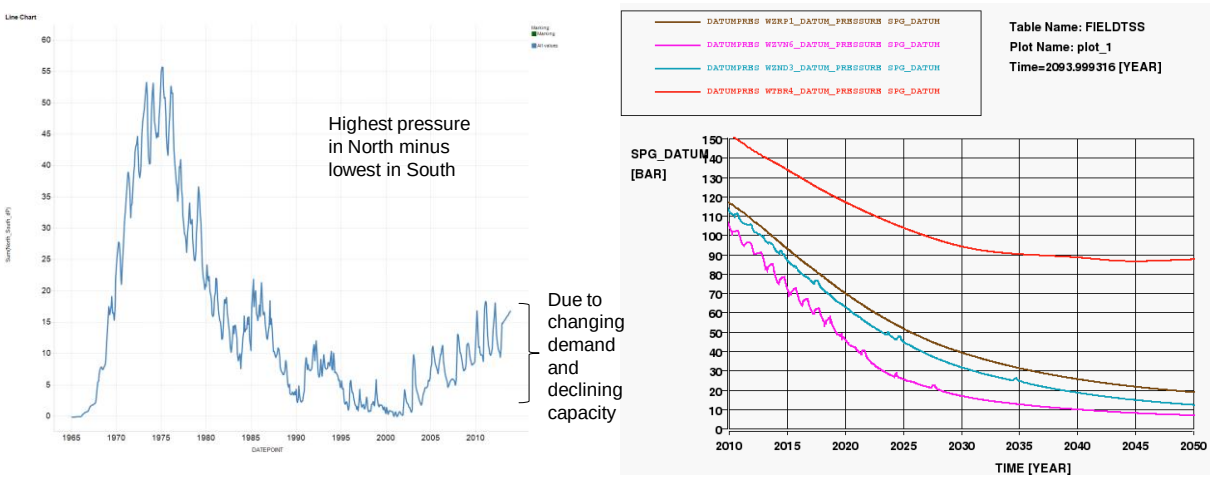

Figure 3.5 *North-South Pressure differential (left pane) and forecasted pressure decline (right pane) based on current estimated market demand. (pink = Zuiderveen, blue = 't Zandt, Brown = Zeerijp, red = Ten Boer)*

The reservoir model (Section 3.2) which is used for forecasting, is calibrated with more than 50 years of production and pressure data. The model was history matched against more than 1700 down hole pressure measurements. A good quality history match has been obtained with a relative small root-mean-square error of only 1.77 bar. Figure 3.6 illustrates the quality of the match by showing four production clusters in different parts of the field as an example.

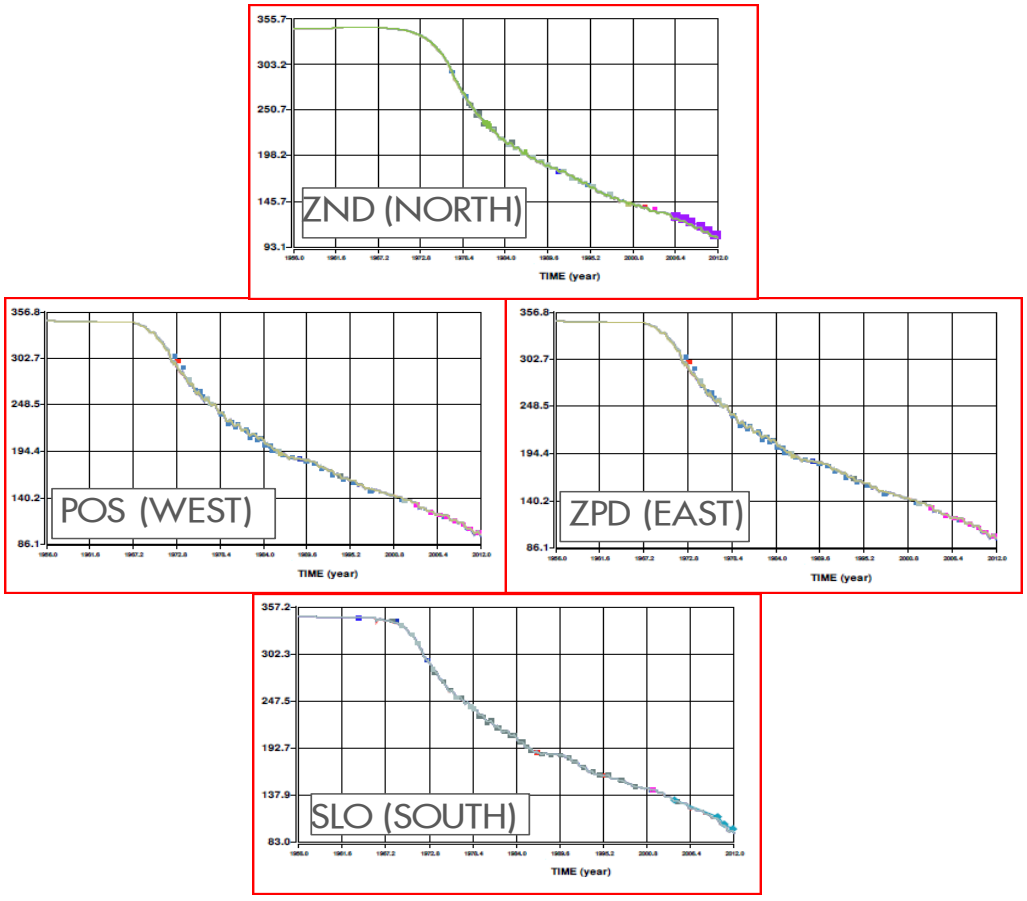

Figure 3.6 *Historical production/pressure measurement (markers) versus simulated pressure (lines) for four production clusters. Pressure is shown in Bar.*

3.3 Development projects

With the increasing level of pressure depletion in the Groningen field, it becomes increasingly more difficult to provide the contractually agreed capacity and gas volumes. A number of projects have been initiated (Figure 3.7) in order to mitigate the decline in production capacity. These projects can be put into two different categories; installation of additional compression capacity and drilling new development wells.

3.3.1 Compression

With continued depletion and reduction of reservoir pressure, additional compression stages will need to be applied together with inter-stage cooling in order to reduce the tubing head pressure (THP) at the wellhead and subsequently the pressure in the reservoir (Pres). Note that each bar of pressure depletion relates to about 8 to 9 bcm of additional recovery for the Groningen field.

At present the first stage compressors in the field are being modified for lower suction pressure and lower production rates. Also currently, the technical concept for second stage compression is being tested on the Schaapbulten cluster. If technically successful, the concept will be applied to most of the other clusters. A modeling study on the optimal phasing and implementation of second stage, and also later third stage compression will be completed early 2014. This will determine at which clusters, and at what point in time, installation of additional compression stages will be most optimal.

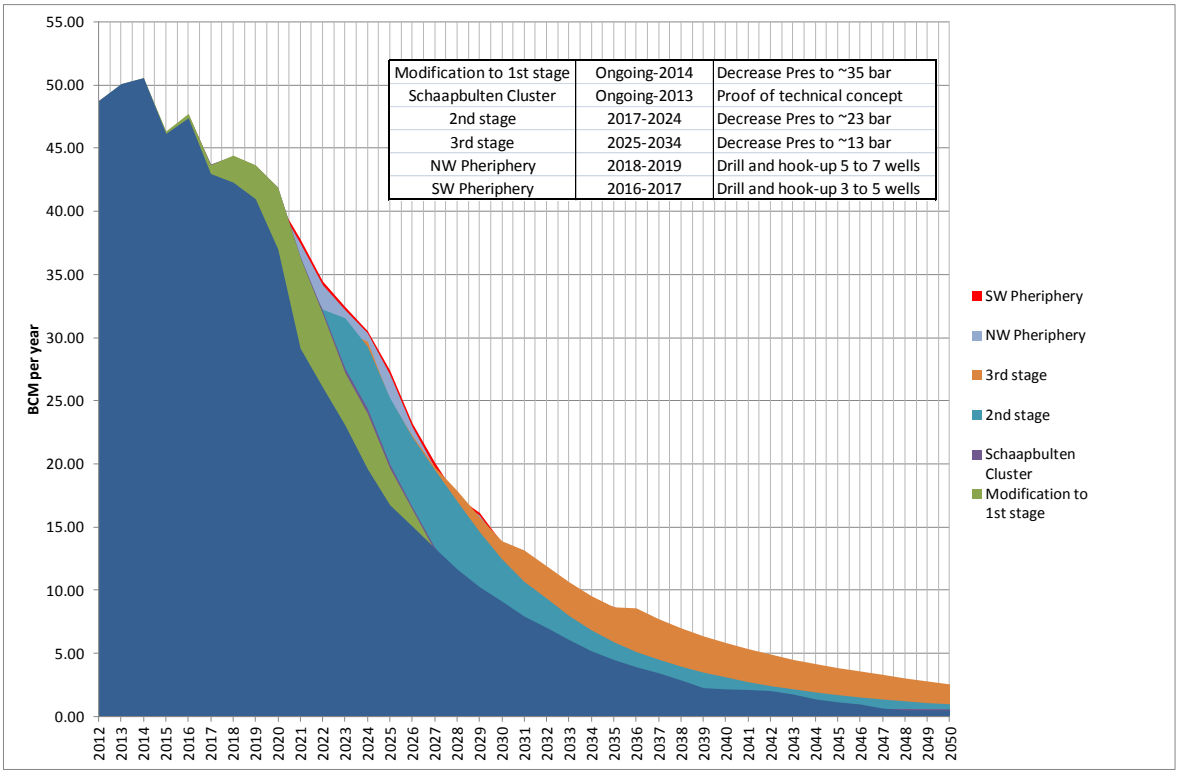

Figure 3.7 Production forecast for the main development projects (as used for 2012 reserves submission). Stages refer to compression stages.

3.3.2 New development wells

Based on the results of a major model refinement and update in 2012, an inventory has been made of remaining infill opportunities in the Groningen field. These opportunities are mainly located in the peripheral parts of the field where the reservoir pressure is known or expected to be lagging behind with respect to the central parts.

3.3.3 Development of the North-Western periphery

This is the area of the existing observation wells Barnheem-1, Stedum-1 and Zeerijp-1 (see Figure 3.8). The expected additional recovery in the area is estimated around 5 bcm of gas. The notional development plan for this area consists of the following elements:

- Construction of a production pipeline to an existing cluster (either Leermens, 't Zandt or Ten Post).
- Drilling additional wells.
- Modification and extension of existing installations.
- Potential construction of a new drilling site and production satellite.

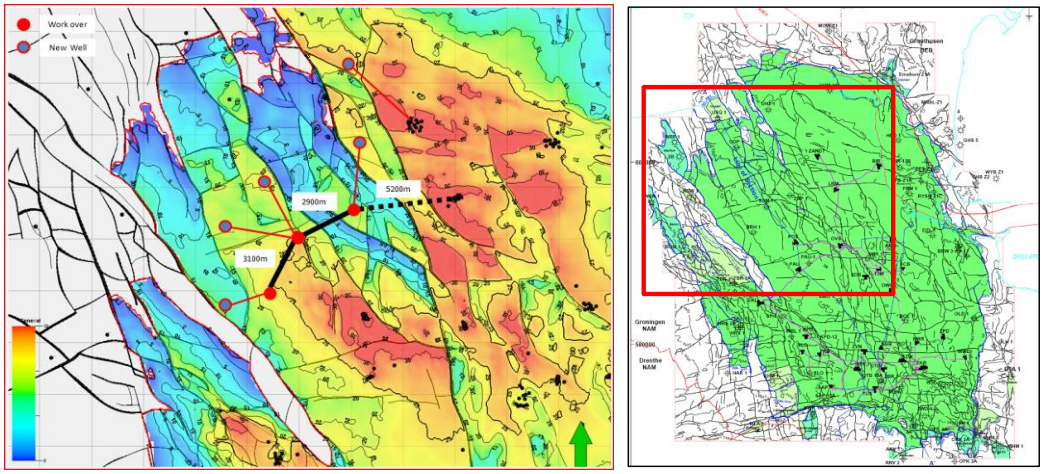

Figure 3.8 Notional lay-out of NW development project.Notional future wells indicated by red (surface)and blue (reservoir level) dots. Black lines indicate the gas evacuation route to the Leermens cluster.

3.3.4 Development of the South-Western periphery

This is the area of the existing production clusters Eemskanaal, Kooipolder and Froombosch, and the observation wells Kolham-1, Harkstede-2A and Ten Boer-4 (see Figure 3.9). The expected additional recovery in the area is about 4 bcm. The development plan for this area include the following elements:

- Drilling wells from the existing Ten Boer and Kolham locations.
- Construction of a new drilling location, including a pipeline to a nearby production cluster.
- Drilling of new wells from this new location.
- Drilling of additional wells from the existing production clusters (Eemskanaal, Kooipolder, Froombosch).

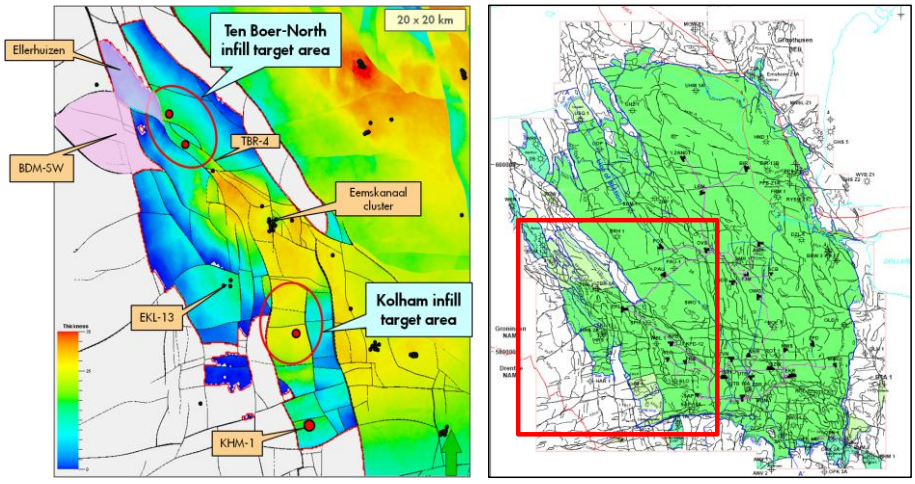

Figure 3.9 Notional lay-out of SW development project

3.3.5 Development of gas from the Carboniferous below the Groningen field

Recent studies have demonstrated that the development of gas-bearing Carboniferous sandstone reservoirs faces serious technical and economic challenges, for instance drilling through the already depleted Rotliegend formation into potentially undepleted Carboniferous sands. Its feasibility will depend on the availability of new drilling and completion technologies in the future. Experiences in the coming years from Carboniferous fields in other parts of the country may lead to new insights.

3.4 Depletion of the Groningen Field

This section of the report described the current depletion plan for the Groningen field and introduces an alternative depletion philosophy. Apart from production to satisfy market demand, curtailment is considered. In a separate report (Ref. 1) production based on a pressure maintenance philosophy is described. Based on the different development options and off take policies a number of scenarios are presented. In section 3 the compaction volumes for these scenarios will be assessed and in section 4 the seismic hazard.

3.4.1 Depletion behaviour under the current production philosophy

Since the introduction of the Small Fields Policy in the seventies, a production philosophy has been introduced that balances the production from the Groningen field to minimise the pressure differences between the North and South of the field. In practice, this means that the clusters in the North of the field, where the cluster density is lower and therefore in-place volumes per cluster are larger, are produced preferentially. The clusters in the South of the field are only produced when required (i.e. mostly in winter). The effectiveness of the introduced production philosophy is shown in Figure 3.10, by the narrow pressure band-width of some 10-25 bar for the majority of pressure measurements, after 1,000 Bcm was produced. Exceptions to this are the relatively small peripheral blocks in the South-Western peripheral part of the field.

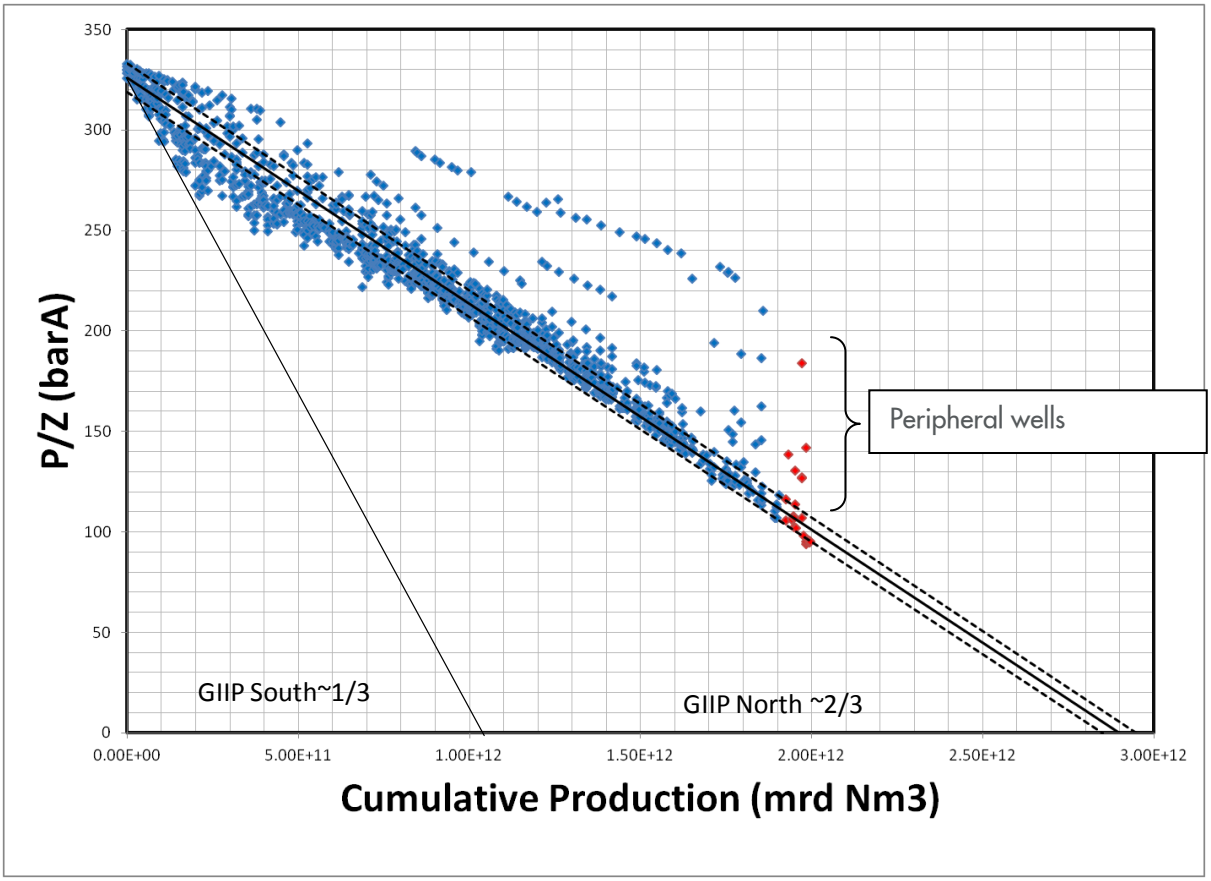

Figure 3.10 The P/Z plot for the Groningen field shows he decline in reservoir pressure with decreasing production.

In Figure 3.11 the results of several production curtailment scenarios and the impact on the Groningen 2nd and 3rd stage projects is shown. With a lower production limit, the timing at which Groningen drops of plateau is delayed and subsequently the installation of compression is also delayed. This figure shows the technical optimal timing for the base case model. For different sub-surface realisations this timing can be slightly different.

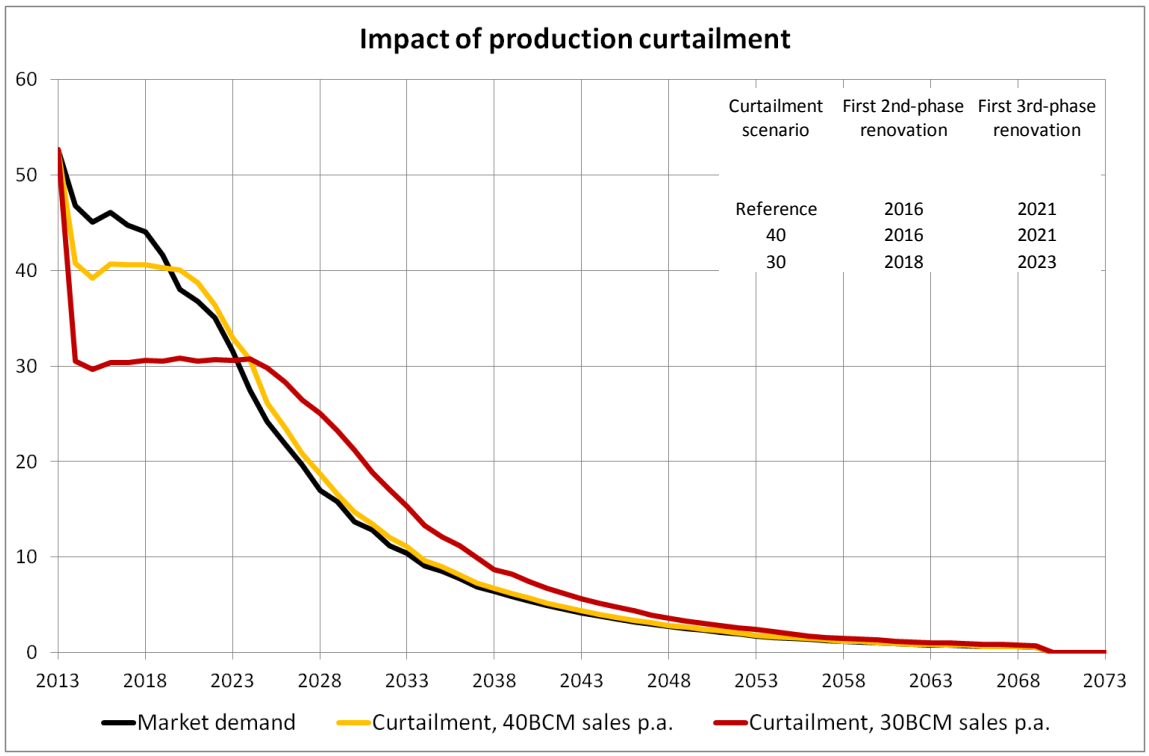

Figure 3.11 The impact of curtailment scenarios on gas production in Bcm/year and on the timing of the compression projects. The reference scenario is based on expected market demand.

Figure 3.12 shows for different curtailment scenarios the forecasted pressure of two production clusters, 't Zandt (ZND) in the North and Zuiderveen (ZVN) in the South. From the figure the following observations can be made:

- Depletion in 2012-2014 was some 6 bar/year.
- Under the current implemented production philosophy, curtailment has the largest impact on clusters in the South of the field. The pressure decline for clusters in the North of the field is less affected. This effect is most noticeable before 2025. After 2030, the pressure decline rates for the various curtailment scenarios converge.
- 30 Bcm/year curtailment reduces depletion in the South to almost 2 bar/yr and in the North to 4 bar/yr in the period 2014-2020. These numbers are very consistent with the earlier discussed general depletion trends per region based on P over Z plot (4*6+2*3=30 Bcm/yr).

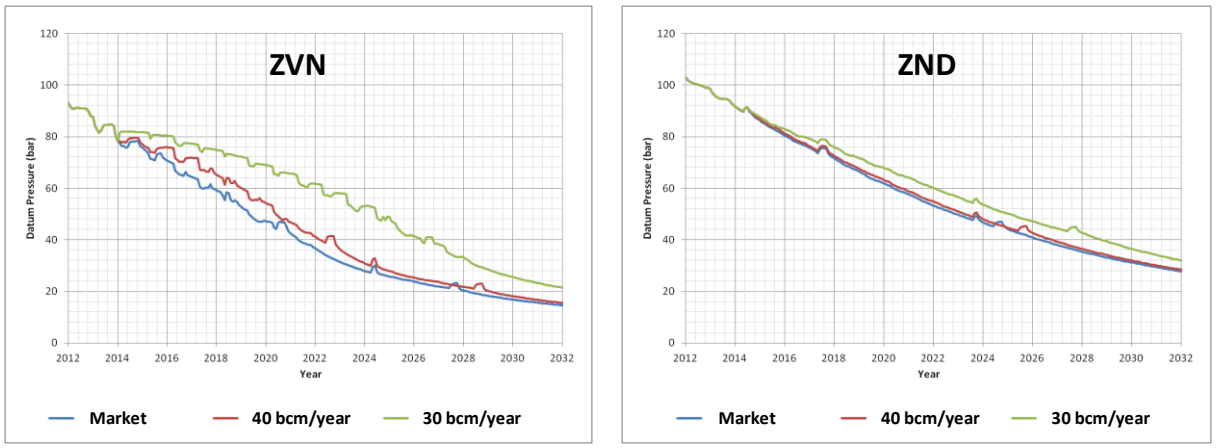

Figure 3.12 Effect of curtailment on pressure depletion with the current production philosophy.

Under a production philosophy based on equalisation of pressure over the field, curtailment has its largest impact on the pressure in the South of the field. Under reduced offtake scenarios the pressure is higher in the South of the field.

3.4.2 Depletion behaviour under an alternative production philosophy

An alternative objective of curtailment could be the reduction of the annual depletion in areas where earthquakes occur more frequently. In Figure 3.13, the field is divided in three areas with different seismicity. The alternative production philosophy could be implemented by preferentially producing the clusters in the area with no or only infrequent earthquakes (Area 1). In periods with increased demand, also clusters in the area with occasional earthquakes are taken into production (Area 2). The clusters in the area with frequent earthquakes (Area 3) are only taken into production during periods with high demand. As a negative consequence the pressure difference between northern and southern part of the field will increase.

The Eemskanaal-cluster is an exception, as it produces gas of a different quality. This gas is blended with normal Groningen gas and hence the amount of gas produced from the Eemskanaal cluster is determined by how much the other clusters produce. In practice, the Eemskanaal cluster produces at a below average rate (<40%).

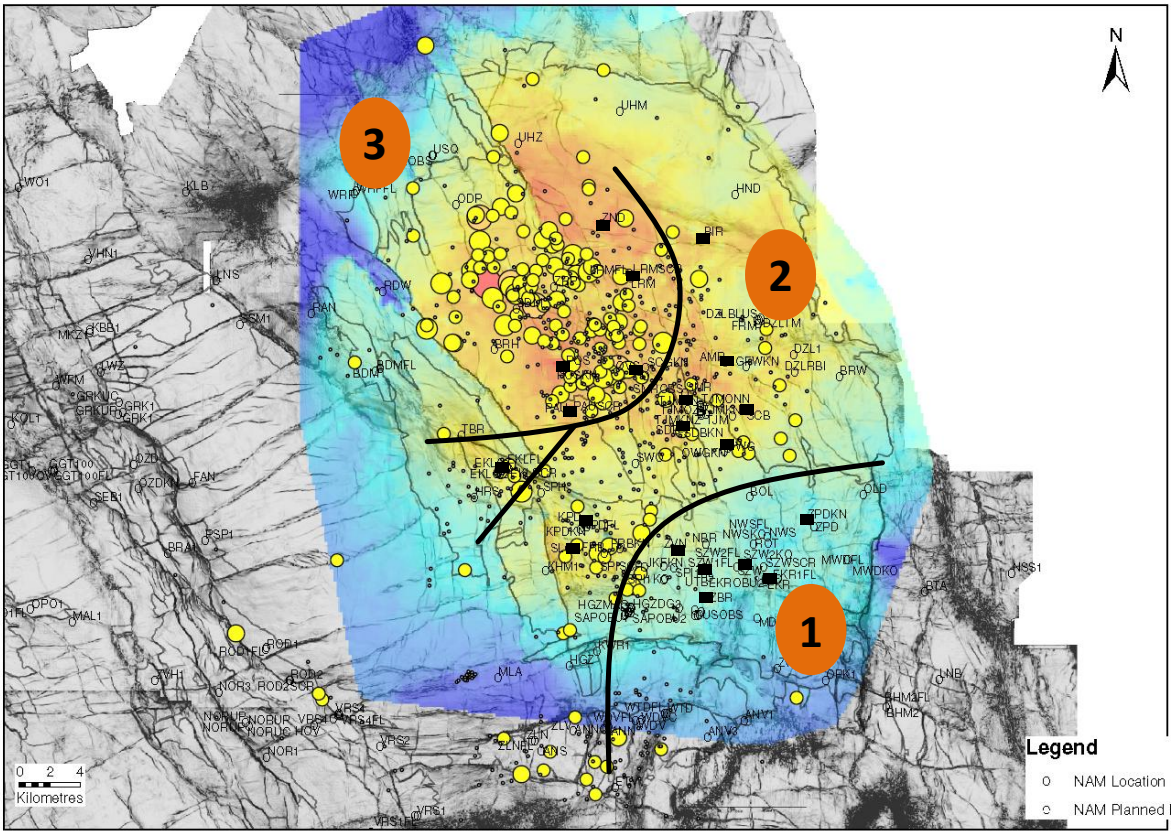

Figure 3.13 *Three areas of the Groningen field with different levels of seismicity. The alternative production philosophy aims to reduce the pressure drop (and therefore compaction) in the earthquake prone areas of the field (area 3) and preferentially produce the areas which are less susceptible to earthquakes (area 1).*

The forecasted pressure response to the alternative production philosophy for different curtailment scenarios is shown in Figure 3.14. The two production clusters, 't Zandt (ZND) in the North and Zuiderveen (ZVN) in the South respond very differently. From the figure the following observations can be made:

- Depletion in 2012-2014 was some 6 bar/year.
- Under the implementation of the alternative production philosophy, curtailment has the largest impact on clusters in the North of the field, while the pressure decline for clusters in the South of the field is less affected. This effect is most noticeable before 2025. After 2030, the various pressure decline rates converge.
- A 30 Bcm/year curtailment reduces depletion in the North to some 2 bar/yr and in the South to some 4 bar/yr in the period 2014-2020. The reduction in the depletion in the North of the field is only temporary as beyond 2020 the depletion stabilises to some 4 bar/yr.
- The pressure difference between North and South will increase to some 30-35 bar (see Figure 3.15).

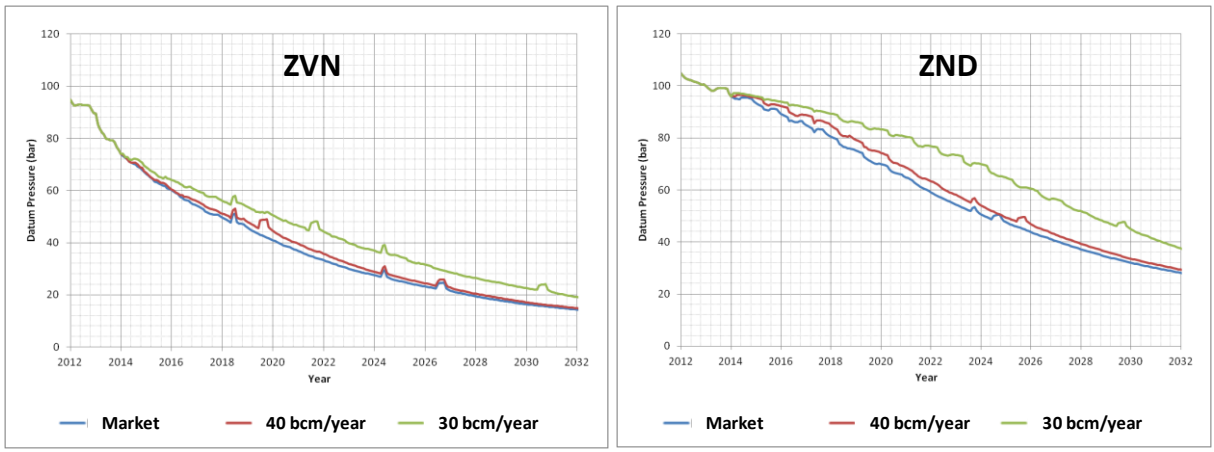

Figure 3.14 Effect of curtailment on pressure depletion under the alternative production philosophy.

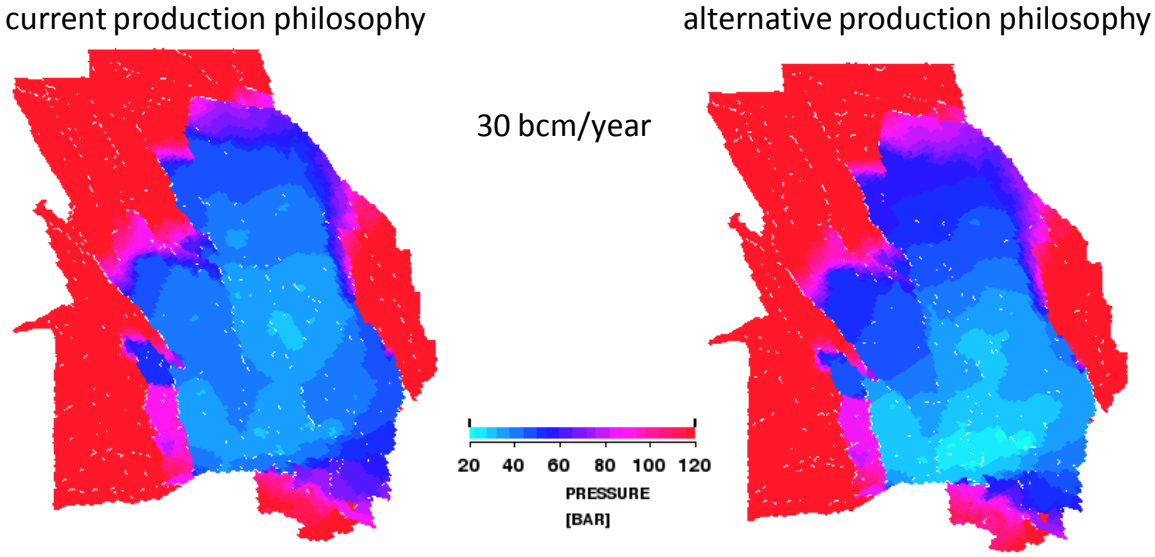

Figure 3.15 Pressure difference in the field for the 30 Bcm/year curtailment scenario assuming the current (left) and the alternative production philosophy (right).

The alternative production philosophy will also impact the timing of the future development projects, more specifically the installation of additional compressors. In Figure 3.11 the results of several production curtailment scenarios and the impact on the Groningen 2nd and 3rd stage compression projects are shown. A consequence of the alternative production philosophy is that compression is required earlier in the South. However, in the North the requirement for compression is delayed. In practise, this means that instead of an implementation schedule based on 3 clusters per year an implementation schedule of 2 clusters per year is required.

The effect of the different production philosophies under a 30 Bcm/year curtailment scenario is most clearly demonstrated by Figure 3.18. With the current production philosophy the pressure difference between the North and the South of the field is reduced. The initial excess capacity in this scenario makes the pressure difference drop to close to zero. After 2023 the pressure difference increases again due to the reduced production flexibility, when the capacity has declined to the curtailment level.

The alternative production philosophy shows the opposite effect. Following from this philosophy, the pressure in the North is maintained high while the pressure difference with the South increases to some 30 bar. The pressure difference remains at this level for about ten years and then declines as the field off take declines.

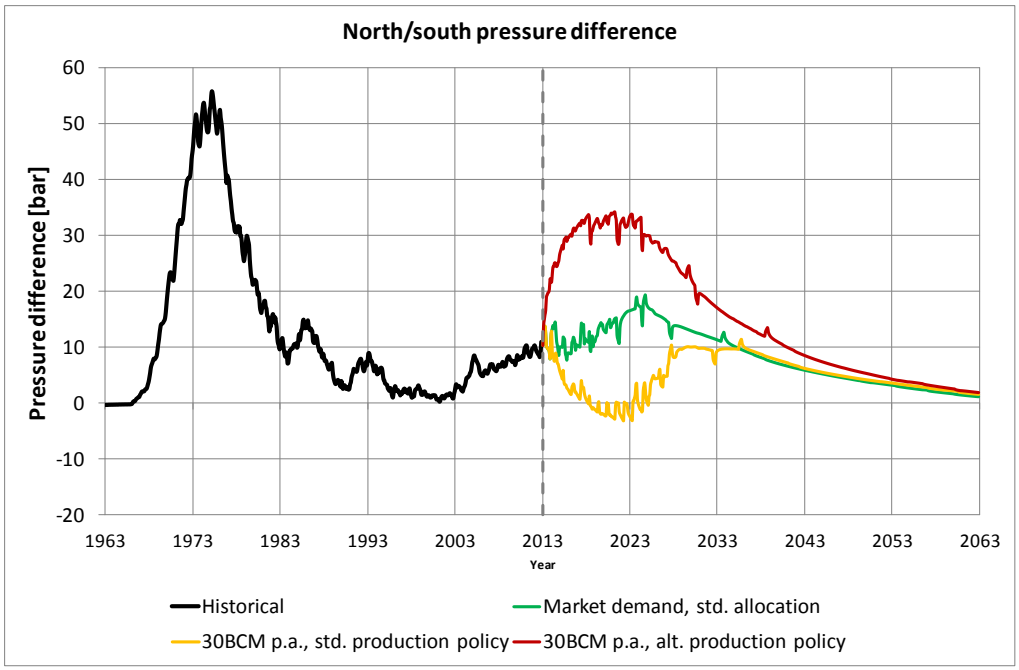

Figure 3.16 Development of the pressure difference between the north and the South of the Groningen field for different production philosophy's with a 30 Bcm/year curtailment. The market scenario (green), 30Bcm/year curtailment using the current depletion philosophy (yellow) and the 30Bcm/year curtailment using the alternative depletion philosophy (red) are shown.

3.4.3 Effect of subsurface uncertainty on depletion behaviour

In general with stronger aquifer support of the gas reservoir, the pressure decline in the aquifer will be less, but felt in a larger area of the area of the aquifer. This will impact the compaction of the aquifer rock. The uncertainty in the aquifer behaviour therefore impacts compaction and subsidence predictions.

In the history matching process the reservoir model is conditioned to reproduce the measured pressure data throughout the production history. A very extensive data set of more than 1700 pressure measurements in the gas column is available. The history matching process results in a well-conditioned model, which can serve to predict future reservoir pressure with confidence. The ability to reproduce the measured pressure data is expressed in the RMS (Root Mean Square) of the difference between measured and simulated pressure data. For the best model realisation this is some 1.7 bar, while in practise models with a RMS< 3 bar are considered to be acceptable matches. Thanks to the large pressure data set, the pressure match and pressure prediction in the gas column of the field is reliable over the larger part of the field.

The reservoir pressure in the gas column is well understood, but the pressure in the water leg is poorly constrained. This is mainly due to the lack of data from the water leg. Such data (e.g. from repeat formation tests) can only be acquired immediately after drilling of the reservoir section of a well. As over the last decennia only a few wells have been drilled, most of the available RFT data is from the seventies and eighties. In Figure 3.17 an example of available RFT data is shown.

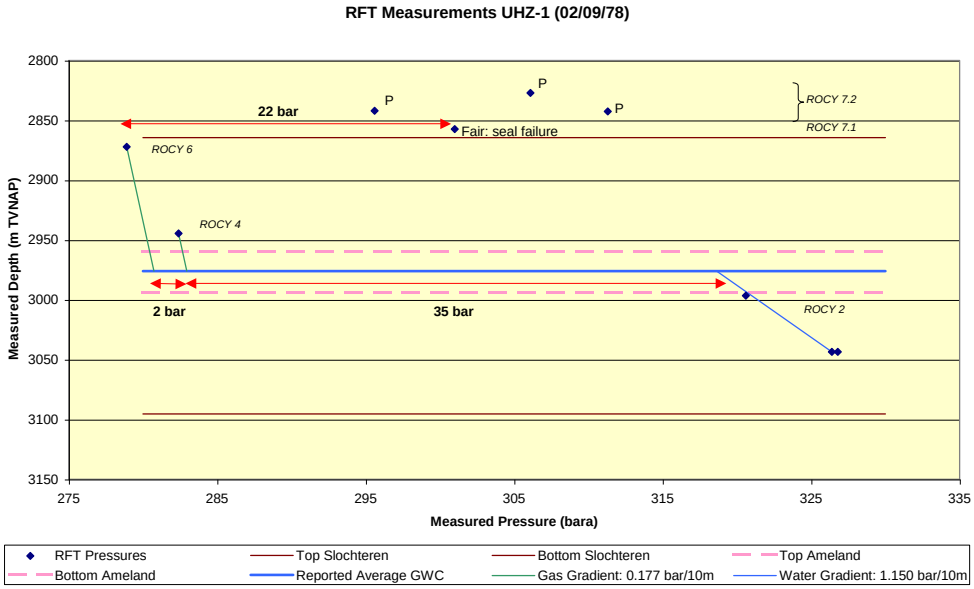

Figure 3.17 Example of RFT data from well Uithuizen-1 showing a pressure difference between the gas- and water leg.

The uncertainty in the pressure behaviour of the aquifer is particularly large in the North-West periphery where only a few observation wells are located (see Figure 3.18).

A good pressure match with historical pressure data in this area can be obtained with different levels of pressure support from the aquifer. This can have a significant influence on the future pressure prediction in this area (Figure 3.19). In other parts of the field, the well density is larger and hence the uncertainty is smaller.

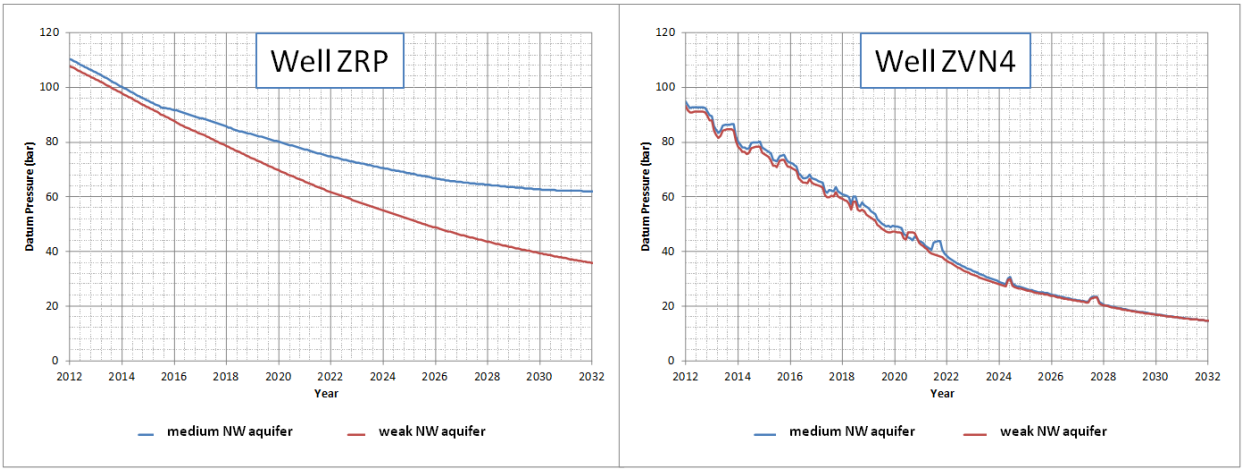

Figure 3.18 Pressure prediction based on market demand assuming different NW aquifer strengths for a well in the NW (ZRP) and a well in the South (ZVN4) of the field.

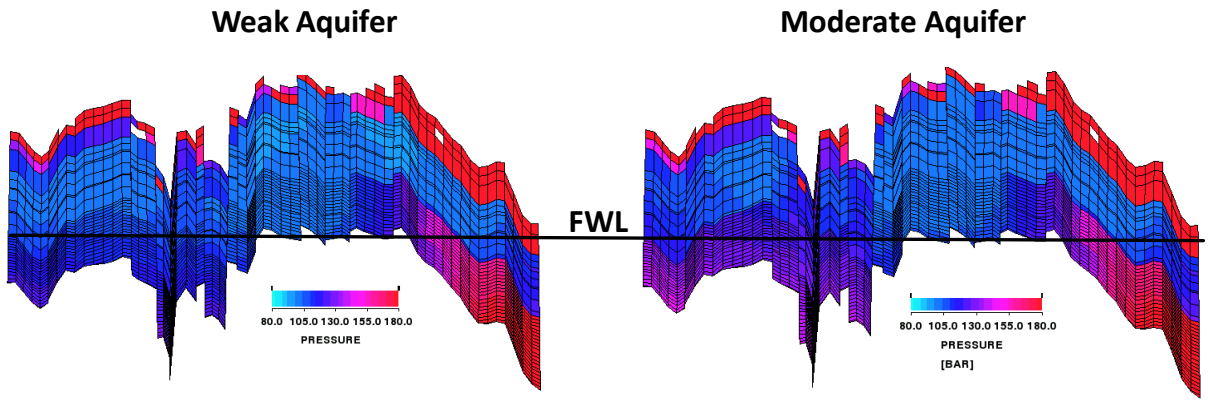

Figure 3.19 East-West Cross section through well Zeerijp showing different pressure realisations. The colours indicate reservoir pressure in bar(red 350 bar and light blue 95 bar). With a moderate aquifer the reservoir pressure in the water leg is higher by some 20 bar.

3.5 Pressure Maintenance

Pressure maintenance as a general concept is based on reinjection of a volume equal to the gas volume production from the reservoir. By balancing the injected and produced volume, the pressure in the gas reservoir can be stabilised. Since compaction is thought to be a key factor in the creation of seismicity, this would also reduce seismic activity in the Groningen area. Pressure maintenance is expected to arrest reservoir compaction, and hence to reduce the seismic hazard. However, to what extent is yet to be established through further geomechanical modelling. Especially the impact on seismicity of injection into or close to a fault is a concern. The current insights have mainly been obtained with the geomechanical sub-models and are described in section 9.

A description of a base case re-development of the field for pressure maintenance is included in this report as appendix 12. This shows the dimensions and impact of such a re-development of the Groningen field. Here we include only a short summary.

Based on its abundant presence, relatively inert behaviour and tolerance for presence in the sales gas, nitrogen was chosen as the optimal injection medium. Pressure maintenance using injection of nitrogen has been studied, supported by a base case development concept and production forecast. Analyses have been based on the Groningen reservoir model, and on the experience in modelling of gas–gas displacement and mixing in the reservoir in the underground storage projects of Norg and Grijpskerk, but the remaining uncertainty in the production forecasts and recovery is large.
Breakthrough of nitrogen in producer wells as a consequence of pressure maintenance is expected to significantly reduce Groningen gas reserves compared to continued depletion of the reservoir. Large electricity consumption further reduces the gas volume available for sales.
The scope of the project is far beyond the scale of current global experience (5 – 7 times larger than the largest similar project ever installed). Although the contours and main dimensions of a Pressure Maintenance Project have been sketched, technical feasibility of the project has not yet been established. Installation of nitrogen injection takes at least 5 years to first injection and some 9 years to ramp up to full capacity. Cost of the project is estimated at 6 to 10 bln EUR.
The project carries a material environmental footprint, with significant land use and electricity consumption. Societal support for a large-scale nitrogen injection project is expected to be a key risk.
This study is in an early stage assessment of the pressure maintenance recovery concept. Optimization is still possible for a number of aspects. Injection of water is not considered a feasible and reliable pressure maintenance option to reduce seismic activity.

3.6 Scenarios

A number of scenarios have been investigated, combining different geological realizations, development plans and production options (Table 3.1).

Two geological models were used, i.e. the best history matched model based on reservoir pressure (G1) and a model with additional changes in the porosity and aquifer strength in the northwest of the field to improve the match of the modelled subsidence with the measured subsidence data (G2).

The development scenarios are based in incrementally adding well drilling projects. The base development includes the compression projects and the hook-up of a single well in the Kolham area of the field (D1). In the next two cases the development of the north western area of the field (D2) and the south western area of the field (D3) are successively added.

The curtailment scenarios investigated are the market driven production scenario (C1) and curtailment of gas production to 40 Bcm/year (C2) and 30 Bcm/year (C3). A production case where the production is ceased (C4) is also included. This case is sometime referred to as the "emergency stop scenario".

Within the curtailment levels the different production philosophies are implemented. The current philosophy is based on maintaining the reservoir pressure differences in the main area of the field as small as possible (A1). The alternative philosophy to keep reservoir pressure preferentially higher in the north than in the south by managing the gas offtake from these areas (A2) is also included. The development of the field for implementation of pressure maintenance based on injection of nitrogen (A3) is described in a separate report (Ref. 1).

For the modelling of compaction and subsidence three compaction models were used: the time-decay model (S1), the isotach (1st cycle) model (S2) and the bi-linear model (S3). This is further described in section three of this report.

Table 3.1 *Different geological, development and production cases used in the preparation of the different scenarios for assessment of subsidence and seismic hazard.*

	Geological Realisations
G1	Model realization with Moderate NW aquifer
G2	Model realization with Weak NW aquifer
	Development Scenarios
D1	KHM1 hook-up, 2nd & 3rd stage compression
D2	D1 + North Western Periphery development
D3	D2 + South Western Periphery development
	Curtailment Scenarios
C1	Market Demand
C2	40 bcm/year
C3	30 bcm/year
C4	No production
	Alternative Philosophy
A1	Current Production Philosophy
A2	Alternative Production Philosophy
A3	Pressure Maintenance
	Subsidence Model
S1	Time decay
S2	Isotach (1st cycle)
S3	Bi-linear

Table 3.2 *Scenarios for which pressure development in the reservoir, compaction at reservoir level and seismic hazard has been assessed.*

	Petroleum Engineering				Subsidence
Nr	Geo R	Dev Sc	Curt	Alt Phil	Compaction Models
1	G1	D1	C3	A1	S1/S2/S3
2	G1	D1	C2	A1	S1/S2
3	G1	D1	C1	A1	S1/S2/S3
4	G1	D2	C1	A1	S1/S2
5	G1	D3	C1	A1	S1/S2
6	G1	D1	C3	A2	S1/S2
7	G1	D1	C2	A2	S1/S2
8	G1	D1	C1	A2	S1/S2
9	G1	None	C2	A3	S1/S2
10	G1	No	C4	None	S1/S2

Based on the different cases in terms of geology, development, production and subsidence model, a number of scenarios were prepared (Table 3.2). For each of these scenarios the pressure development in the reservoir, the compaction at reservoir level (Section 4) and seismic hazard (Section 8) are assessed.

3.7 Conclusion

- Two different production philosophies lead to different pressure distributions over the field. The effects on seismicity will be addressed in Section 4.
- Reservoir pressure predictions in the gas column are well constrained by the historical pressure data and the reservoir model. Closer to the water leg the uncertainty in the reservoir pressure is generally larger. This is expressed in larger local uncertainty in the reservoir compaction and seismicity.

4 Historical compaction / subsidence and future trends

4.1 Summary

For the Groningen subsidence calculations three compaction models were investigated: the bi-linear, time decay and isotach model. The bi-linear model was the preferred compaction model in NAM until 2011 and has been used in subsidence forecasts to calculate the subsidence for the Groningen winningsplan of 2007. When updating the Ameland winningsplan in 2010 it became apparent that the bi-linear model could not describe the ongoing subsidence observed above this field (Winningsplan Ameland, 2011) with decreasing depletion rates. This ongoing subsidence was the reason to develop the time decay model,which showed a good fit between measured and modelled subsidence, with only a small number of reasonably well constrained parameters. The time-decay model for Ameland gives a good fit with the subsidence measurements whilst applying a Cm-porosity trend line based on the Cm values from laboratory data (Cm-lab) taken from the Slochteren Formation.

The same approach was followed to match the subsidence above the Groningen field. In this case, however, the same Cm-porosity trend line could not be used directly. To match the subsidence above Groningen, a multiplication factor of about 0.5 to this trend line had to be applied.

A third model was adopted from TNO (Pruiksma et al. 2013) called the linear isotach model. This model provides a good match with the historical subsidence data but contains more degrees of freedom. It also allows for a history matched scenario with implementation of the laboratory base Cm-porosity trend line. This scenario leads to an even more extensive continuation of subsidence and is considered at the moment as a worst case scenario.

Reservoir pressures from the Groningen MoReS model have been used as input for the compaction model. The distribution of reservoir porosity and thickness were taken from the static Petrel model and upscaled with the condition that the upscaled compaction is equal to the sum of the compaction of the individual layers.

A RMS method was used to check the "goodness-of-fit" between modelled and measured historic subsidence.

4.2 Introduction

The Groningen field was discovered in 1959 and gas production started in 1963. Globally, the field belongs to the top-ten largest gas fields. Subsidence was recognised as a risk before production and from the start, subsidence data was collected regularly through levelling surveys. Since 1993 also satellite based Interferometric Synthetic Aperture Radar (InSAR) measurements are available.

Over the years the subsidence models have been revised and refined as more data became available. Compaction models have to meet two basic criteria: they have to closely match the subsidence measurements and they should be based on plausible physical mechanisms. Section 4.3 will describe the availability of data, both laboratory compaction data and geodetic data. Section 4.4 outlines the geomechanics of the Groningen field describing the compaction models and the importance of overburden behaviour. The next sections (4.5, 4.6 and 4.7) describe model calibrations and the subsidence forecasts.

4.3 Geodetic and geomechanical data

In this section two sources of data relevant for model calibration are described. First an overview will be presented of the geodetic data, followed by a description of the geomechanical data (Cm measurements). Other data such as geological data and pressure data have been described in Sections 2 and 3.

4.3.1 Survey protocol

According to regulations in the Dutch mining law (of 2002), a survey plan is required for all onshore gas/oil production activities.

The State Supervision of Mines (Staatstoezicht op de Mijnen, SodM) has to be informed every year on the status of the survey plan, whether or not changes have been made and which geodetic surveys have been planned for the coming year.

The frequency at which the surveys will be carried out is contained in the Survey plans.

For Groningen the frequency for a full levelling survey is once every 5 years.

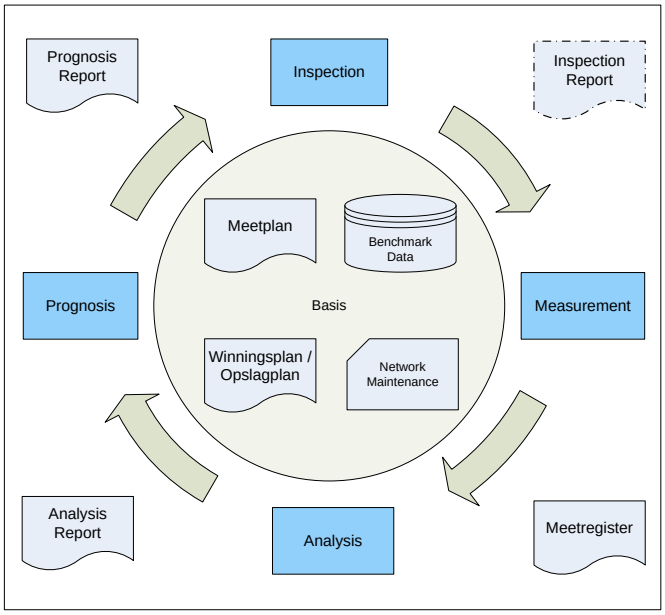

The initial survey for Groningen was carried out in 1964 but covered only the southern part of the field. The first full levelling survey for the entire area was in 1972.

Levelling surveys are executed according to the procedure as defined by SodM and Rijkswaterstaat Data-ICT Dienst (RWS-DID) per 18 August 2005.

Levelling networks are designed such, that the benchmarks at the edges of the network are just outside the subsiding area.

Results of the survey are reported in the official and publicly available Survey Register. The Survey register consists of a free network adjustment (1st phase) as a QC on the observations, a state of differences with relative heights (relative to the chosen reference benchmark) and height differences of the benchmarks between epochs and a map with the survey network and benchmarks, labelled with the height differences between the last and previous epoch. The presented height differences are not corrected for possible autonomous movement. They present the total displacement at surface. Identifying the cause (deformation due to gas extraction, autonomous movement or otherwise) can only be carried out by expert analysis and is not part of the survey register.

4.3.2 Surveying techniques

Current surveying techniques are:

- Spirit levelling
- PS-InSAR (Satellite Radar Interferometry)
- GPS (as part of GNSS: Global Navigation Satellite System)

Spirit Levelling

This technique has been used for Groningen since 1964.

Surveys are executed according to regulations defined by RWS-DID as stated in 'Productspecificaties Beheer NAP, Secundaire waterpassingen t.b.v. de bijhouding van het NAP, versie 1.1 van januari 2008'.

The equipment used includes certified, self registering, optical levelling instruments and barcode level staffs. Measurements are registered fully automatic in a registration and validation system defined by RWS-DID.

PS-InSAR

Since 2010, deformation based on PS-InSAR technique is reported, in conjunction with a number of levelling trajectories for validation.

Deformation is estimated from phase differences between the acquisitions and persistent scatterers (Hanssen, 2001). The spatial resolution depends on the presence of natural reflectors, such as buildings. To obtain a precision comparable to levelling, error sources (like atmospheric disturbance, orbital inaccuracies) need to be estimated and removed. To support this, a time series of satellite images is required (>20-25 images) and ample resolution of scatterers. The estimated deformation velocity from InSAR observations is 0.5-2 mm/year (see Ketelaar, 2009).

The big advantages of the InSAR technique are its high temporal resolution (> 10x per year) and the dense spatial resolution. No survey crew is required in the field, hence no disturbance of the area and no security risks. Moreover, the accuracy of PS-InSAR is comparable to levelling.

4.3.3 Survey design

Levelling network

The Groningen levelling network is part of the bigger Northern Netherlands network. Figure 4.1 displays the levelling network, as surveyed in 2008.

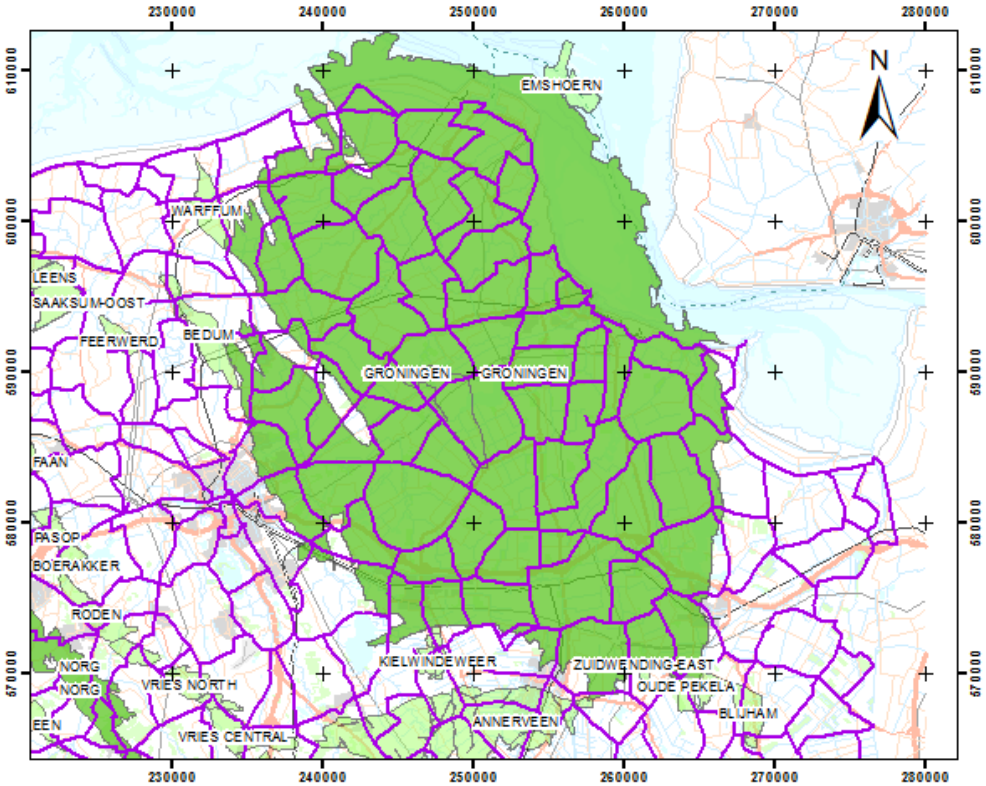

Figure 4.1 Levelling network Groningen field

PS-InSAR

The persistent scatterers (PS) have a constant reflection in time and space and correspond merely with buildings in the terrain. Below Figure 4.2 shows in green dots the persistent scatterers as detected in the descending Radarsat-2 track.

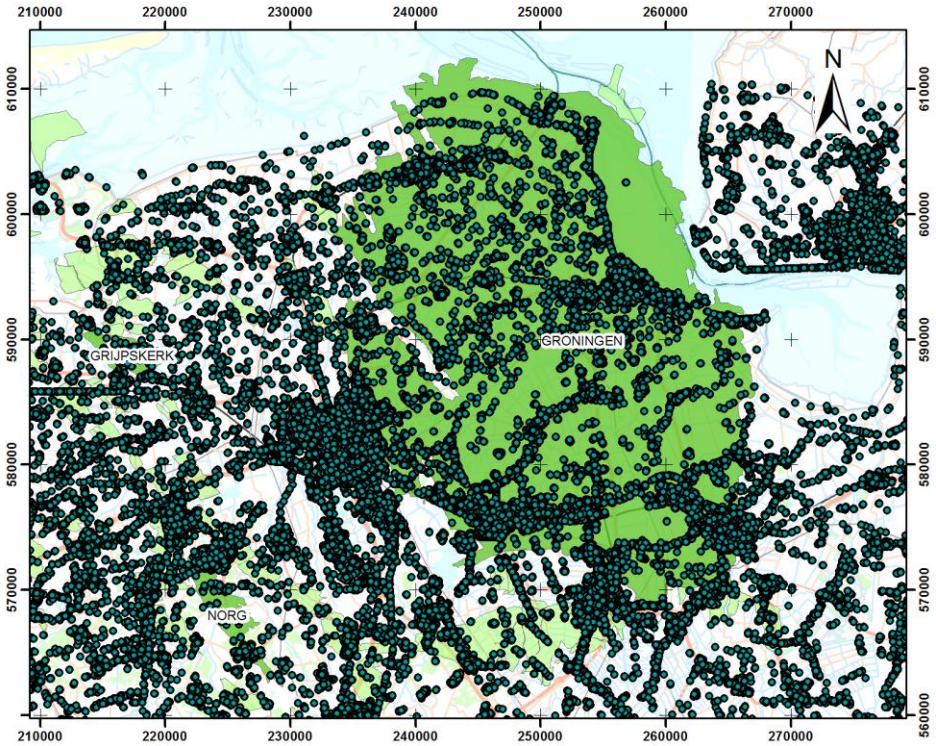

Figure 4.2 Spatial coverage with Persistent Scatterers in North-East Netherlands on the basis of images from descending Radarsat-2 track

4.3.4 Levelling and Insar data used for the calibration

The calibration is done on the "differentiestaten", a list of differential heights between the benchmarks per epoch of the levelling campaigns. The measured height differences of the levelling surveys are referenced with the geodetic program Move3 using the reference point A2080 nearby Gasselte (Drenthe). Data from the latest levelling survey in 2013 came in too late (November 2013) to be included in the calibration procedure described in this report.

The benchmarks within the area bounded by a purple square indicated in Figure 4.8 are used. RMS values were calculated for each benchmark as described in section 4.6.1. 8 out of 1000 benchmarks were excluded from the dataset as they were showing a very high RMS (higher than 7) value and showing a temporal subsidence pattern that is in disagreement with the subsidence behaviour observed in neighbouring points.

Two sets of levelling data have been used to calibrate the model. The first set only contains data that were recorded in the full levelling campaigns. These datasets are: H_04_1964, H_09_1972, H_09_1975, H_09_1985, H_08_1987, H_05_1990, H_05_1991, H_06_1993, _06_1997, H_06_1998, H_06_2003, H_08_2008.

Next to the levelling surveys also Insar surveys were used. Instead of using the Insar data as a separate dataset the Insar data was integrated with the levelling data (Figure 4.3). These combined datasets used in the calibration are: D_16_12_1993, D_16_12_1994, D_16_12_1995, D_16_12_1996, D_16_12_1997, D_16_12_1998, D_16_12_1999, D_16_12_2000, D_16_12_2001, D_16_12_2002, D_16_12_2003, D_16_12_2004, D_16_12_2005, D_16_12_2006, D_16_12_2007, D_16_12_2008, D_16_12_2009, D_16_12_2010, D_16_12_2011.

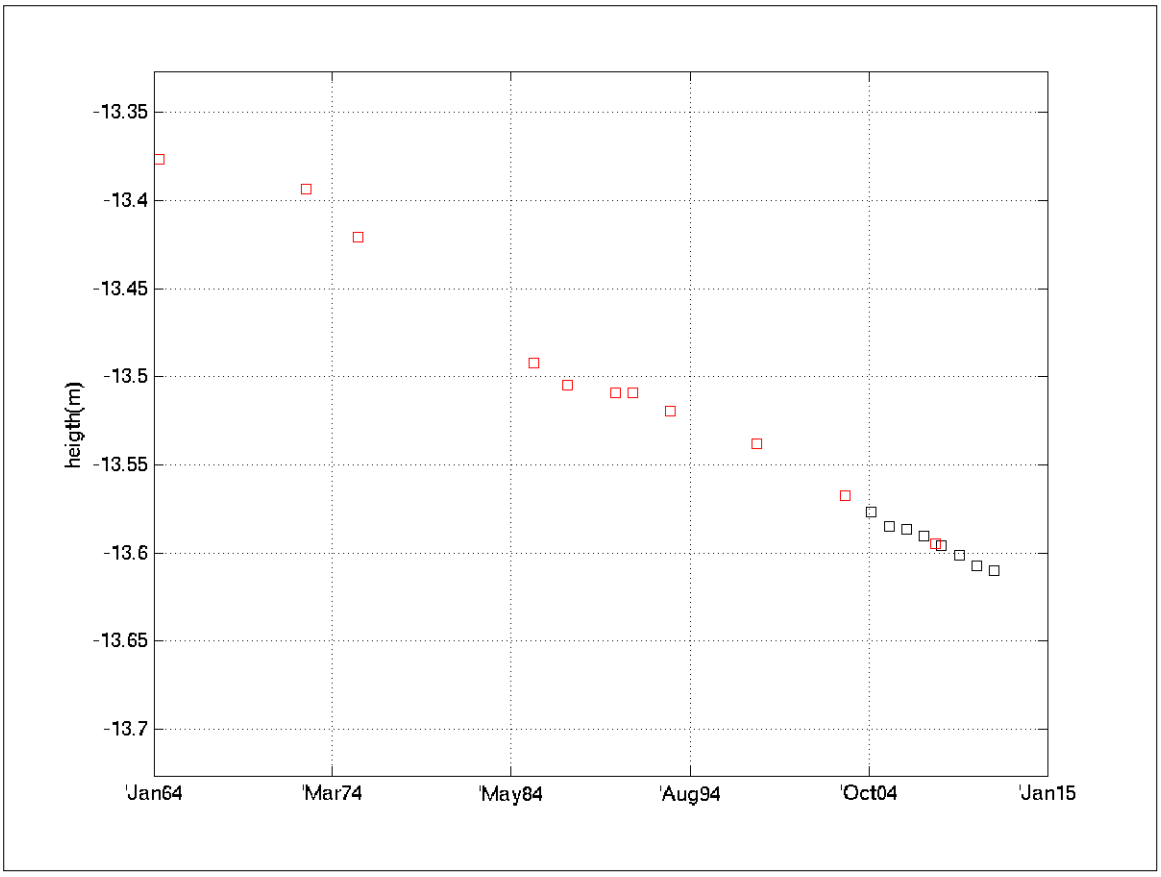

Figure 4.3 Integration of the Insar data (black squares) with the levelling data (red points)

Two datasets became available too late to be used for the calibration. These surveys are: H_07_1978, H_07_1981. They are shown for completeness in Figure 4.30 together with the 2013 survey.

4.3.5 Data from uniaxial compaction experiments

Subsidence measurements are the primary data source used in calibrating the geomechanical models. In addition, compaction experiments on plugs taken from reservoir core samples can also provide insights into the constitutive behaviour of the reservoir rock.

However, conclusions should be drawn with care. The sparse sampling density of core material cannot fully constrain the spatial variability of the reservoir compressibility. Similarly, the total compaction of the reservoir formation is a function of the reservoir thickness and the changes in pore fluid pressure, and these are not always known very accurately. In recent years much consideration has been given to the unloading of the core confining stress during exhumation, which can lead to the possible development of micro-cracks, thus making the samples more compressible. The expectation is that such 'softening' would be especially marked during the first cycle of a multi-cycle compression test. But there are many other sources of uncertainty. Therefore, the models should first match the subsidence data, while the reservoir compressibility should fall within the range of measured plug data.

ROSL samples

The Groningen Cm-values [$*10^{-5}$bar^{-1}] compare well with all other available data on ROSL plugs. Figure 4.4 plots these values as a function of porosity.. A best-fit cubic polynomial trend line with porosity fraction [-], using a least-squared regression based on all data (L2 norm), is also plotted in the graph. Based on the good agreement between Groningen data and the overall ROSL data, it was decided to use this regression fit as a starting point for the calibration of the geomechanical model to the subsidence measurements:

$$C_m = 267.3\phi^3 - 68.72\phi^2 + 9.85\phi + 0.21$$

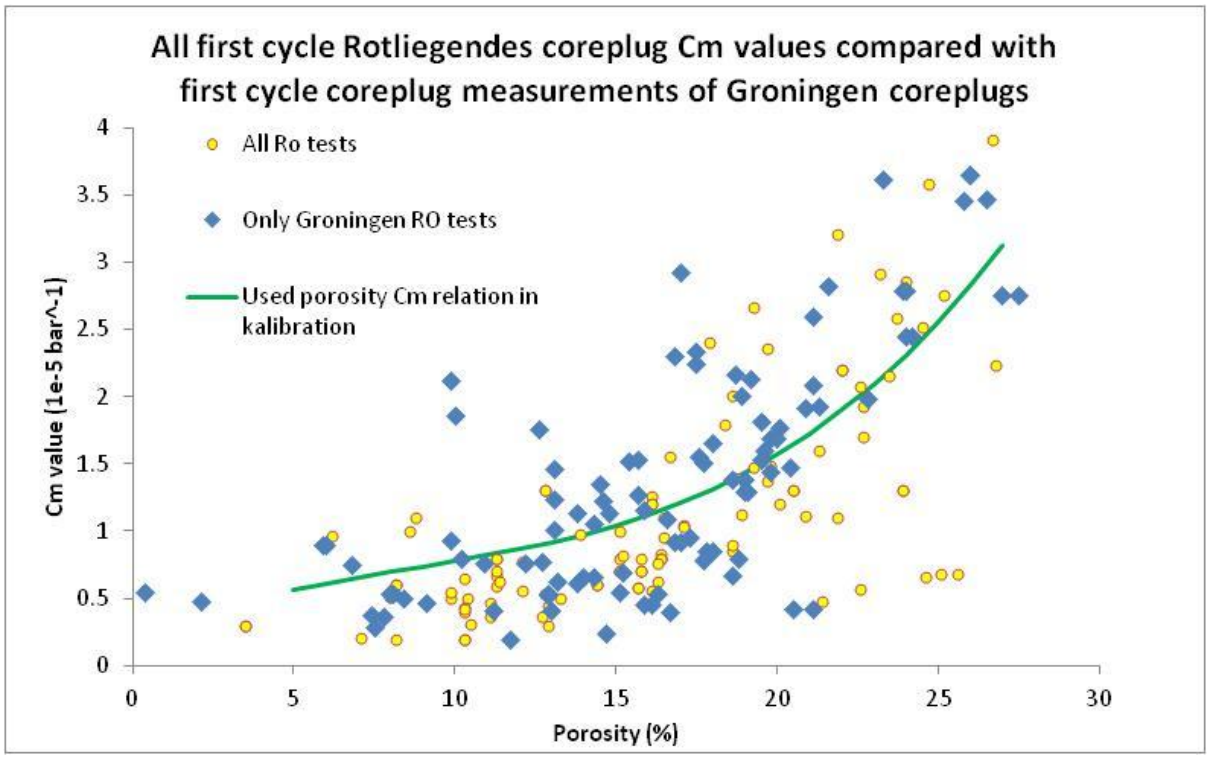

Figure 4.4 Comparison of the Groningen data to all available ROSL Cm values as a function of atmospheric porosity

Also, raw stress-strain curves are available for some of the Groningen plug tests. These measurements were used to determine values for the elastic parameters where a linear relation was observed during the test. In the case of linear elasticity, the M modulus is the inverse of the Cm. In the dynamic domain the M modulus (also called P-wave modulus) is determined by:

$$M = \rho \cdot V_p^2$$

with ρ the bulk density and V_p the P-wave velocity. As the log porosity is also closely related to the sonic velocity it is physically sound to investigate the relationship between the M-modulus determined from lab Cm measurements and the measured atmospheric porosity and use a possible trend line from this domain to compare it with other trend lines. The Young's modulus was calculated for the selected tests where the raw stress-strain curves were still available and where a linear relation was observed during the test. A numeric inversion module in the finite element simulator Geomec was used to invert for the Young's modulus and Poisson's ratio.

Figure 4.5 shows the Young's modulus and M modulus as a function of porosity with a linear trend line based on an L2 norm.

Figure 4.6 shows in blue the curve for the Cm-porosity relation based on the linear M-por trend line in Figure 4.5. This curve is close to the Cm-porosity calibrated curve based on the subsidence data. These different trend lines actually indicate the scatter of the data and the difficulty in concluding whether or not a model fits to the Cm dataset.

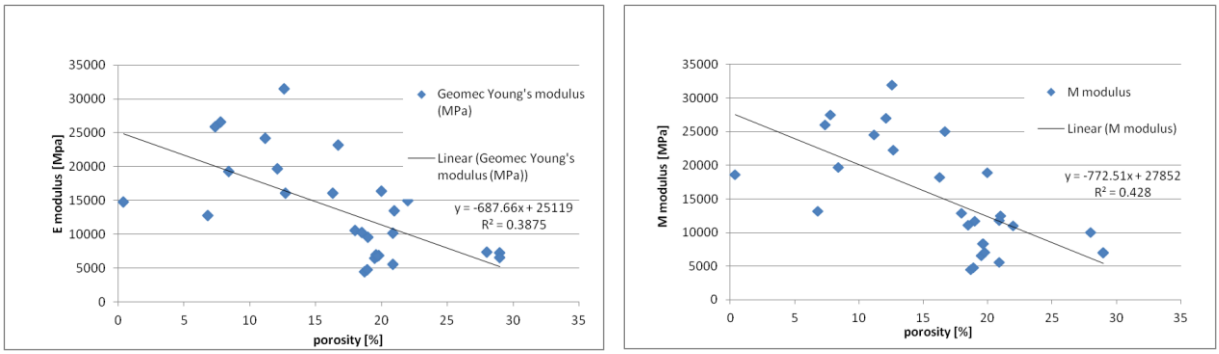

Figure 4.5 Elasticity and M modulus as function of porosity

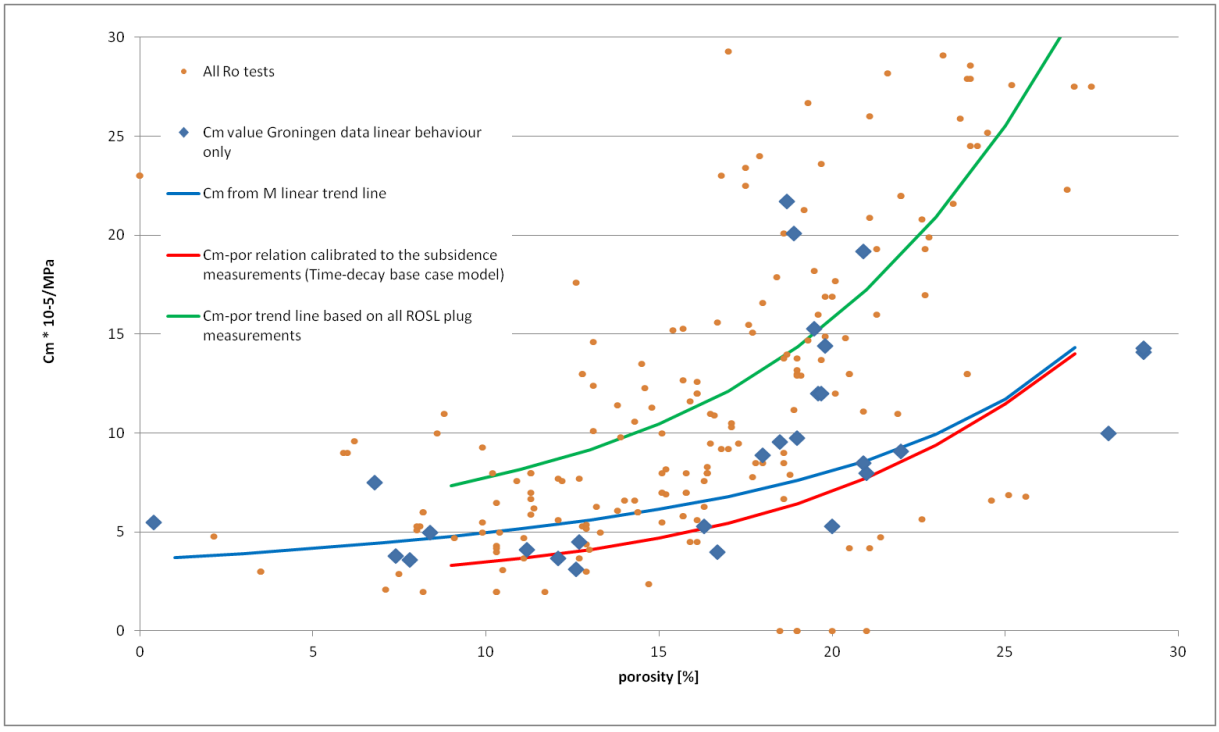

Figure 4.6 Comparison of Cm derived from M linear trend line compared to data and other trend lines

4.4 The Groningen Geomechanical model

The Groningen geomechanical model calculates the compaction at reservoir level and transfers the derived strains to surface subsidence by using a semi-analytic approach (Geertsma 1973 and Geertsma and van Opstal, 1973), incorporated in Shell's 'SubCal' software.

The compaction model has the same dimensions as the MoReS reservoir simulation model. The extent of this compaction model is shown in Figure 4.7. The areas in blue indicate the location of the aquifers which were explicitly modelled in Mores.

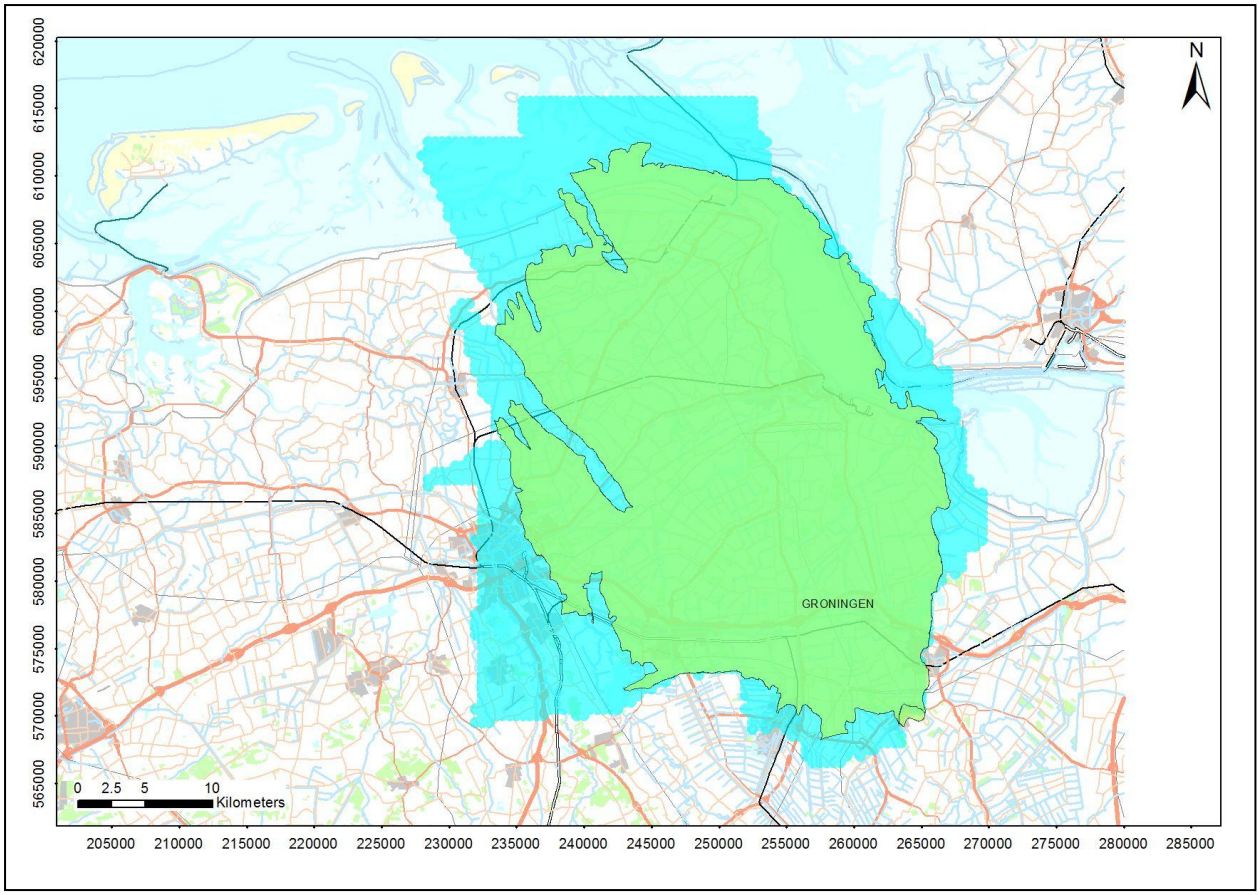

Figure 4.7 Outline of the geomechanical model; green indicates the gas-bearing part, and blue the water-bearing part included in the Mores model.

The geomechanical model uses the top reservoir map, the reservoir thickness, the reservoir pressure and the porosity as an input for the calculations. The model consists of one single reservoir layer instead of the 40 Mores layers and therefore an upscaling method is applied that is documented in section 4.4.4.

In the calibration to the measured subsidence, the effect of subsidence caused by neighbouring fields is accounted for by modelling these fields with a separate subsidence model. Only the subsidence measurements above the Groningen field (Figure 4.8) are used to compare with the calculated results.

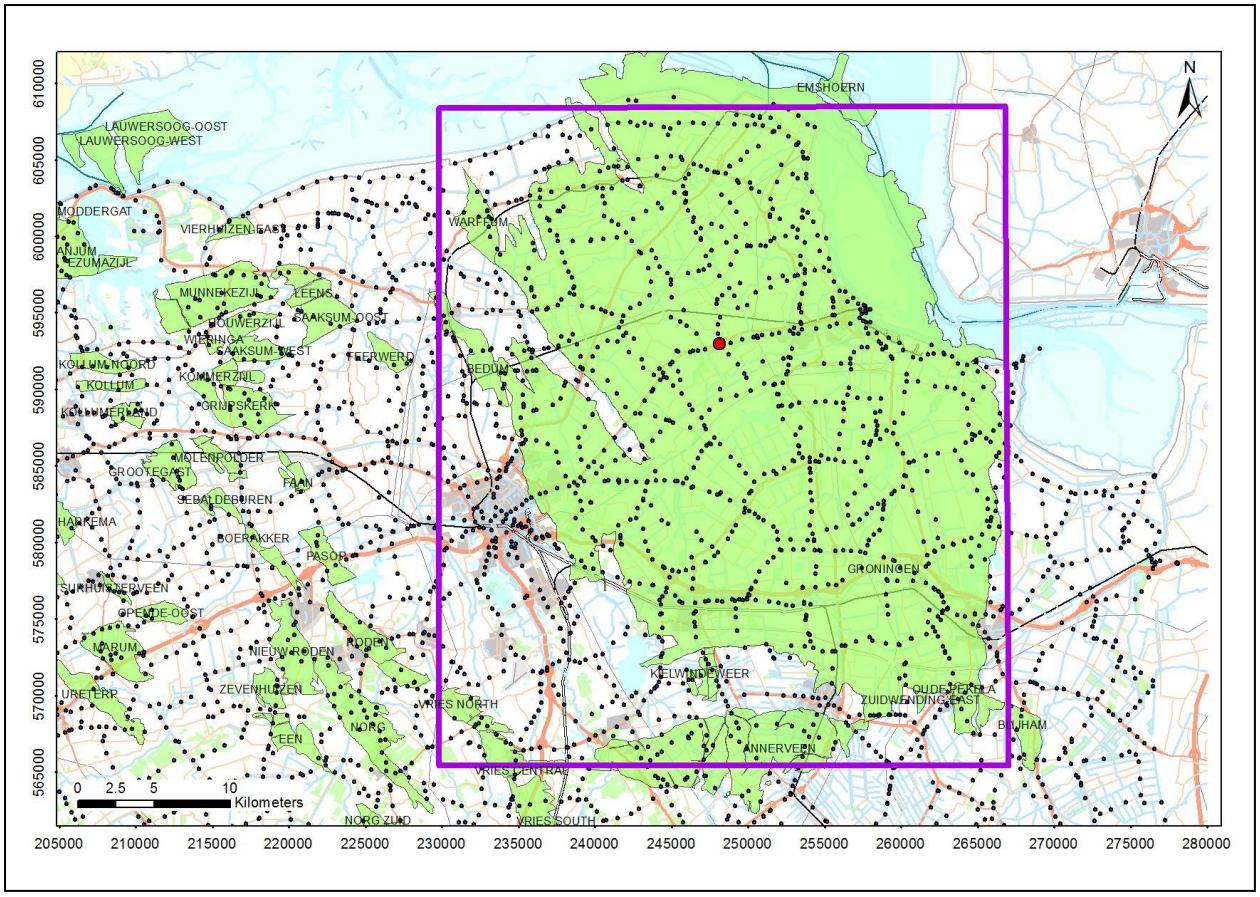

Figure 4.8 Area definition used for benchmarks used in the calibration (within the purple square). The red benchmark indicates benchmark 007E033 which is referred to in section 4.4.1.

The compaction at reservoir level is calculated with three different compaction models, the bi-linear, time-decay and isotach model, which are outlined in the next paragraphs. Calibration of the models to the subsidence data is described in sections 4.5 and 4.6

4.4.1 Linear and Bi-linear Compaction Models

The laboratory compaction measurements of Rotliegend rock consistently show a linear pore pressure - strain relationship, for conditions appropriate to gas fields in the Netherlands. This in turn, should lead to a linear relationship between pressure depletion and subsidence, assuming that the surrounding formations behave in a predominantly linear elastic manner. However, when plotting the subsidence of a benchmark near the centre of the field versus the reservoir pressure (Figure 4.9) two straights lines can be distinguished, suggesting a bi-linear shape compaction curve. This bi-linearity has also been observed in other fields, like Ameland and Roswinkel. These observations are the basis of the bi-linear compaction model.

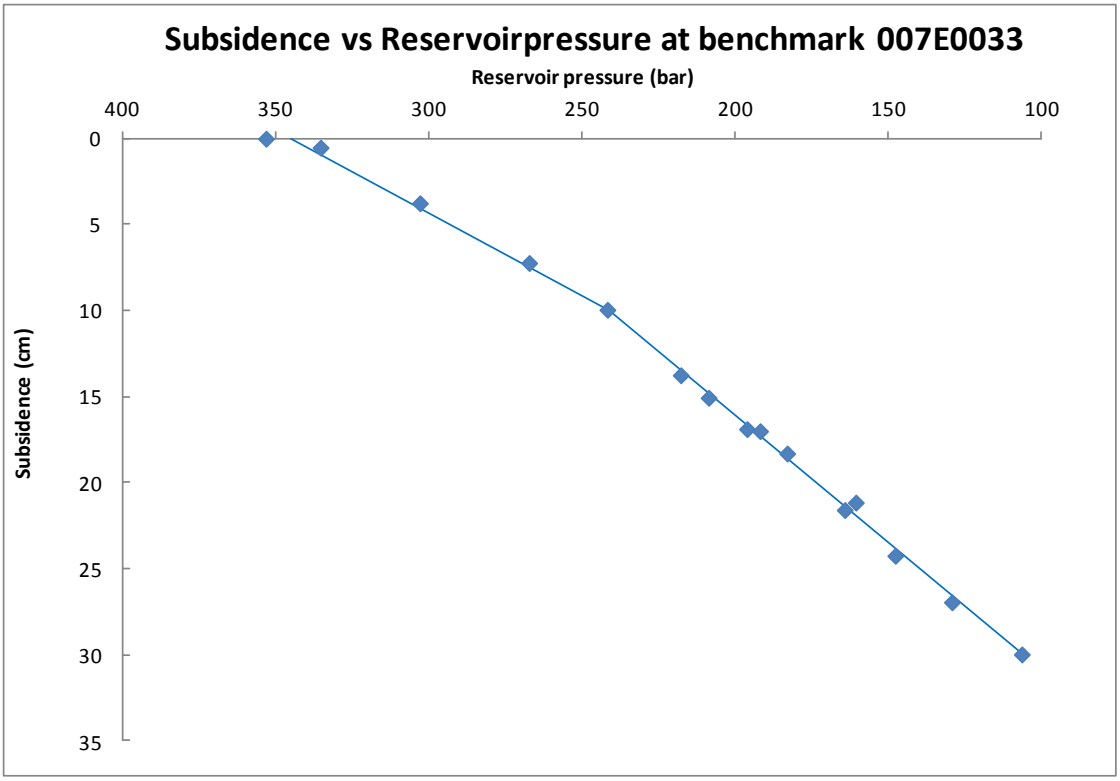

Figure 4.9 Comparison of subsidence measurements (blue dots) with reservoir pressure for Benchmark 007E0033 . The lines show a bi-linear compaction when starting linear compaction for start and one from the end.

In Figure 4.9 the pressure at which the two compaction lines meet is called the Transition pressure (P_{trans}). The C_m value used for pressures between the initial and transition pressure is called C_{mpre} and the Cm value used for reservoir pressures smaller than the transition pressure is C_{mpost}.

In general the C_m [$*10^{-5}$ bar^{-1}] value is a function of porosity [-]. In the bi-linear model the following porosity C_m relations are used:

$$C_{mpre} = m_{pre}\emptyset + c$$

$$C_{mpost} = m_{post}\emptyset + c$$

The C_{mpre} and C_{mpost} values found by calibration of the subsidence model to the measured subsidence are not related directly to the core measurements, but their values are in the range of the laboratory measurements of the 2nd and 1st cycle compaction experiments. The bi-linear compaction model was used for subsidence forecasts in the Statusreport 2010 (NAM, 2010) and in the winningsplannen of the North Netherlands fields.

A supporting hypothesis was developed in which the bilinear behaviour was explained by geological burial and subsequent partial exhumation. Formation damage of the core during drilling and extraction was invoked as an explanation of why the laboratory samples failed to display the bilinear behaviour and as a justification for using second cycle compressibility measurements for the initial reservoir stiffness (it should be realised that the 'initially stiff' reservoir compressibility was only very poorly constrained by subsidence data). However, further research studies, designed to test and characterise this bilinear law have been unconvincing.

Later in 2011 it appeared that calibration of Ameland subsidence measurements to the bi-linear model parameters returned in very high post transition pressure C_m values, higher than the laboratory ones. Close examinations of the measurements made apparent that this misfit was caused by ongoing subsidence whilst

the depletion had almost ceased. To solve this, a more physics based explanation was sought and found in the Time decay model.

4.4.2 Time Decay Compaction Model

The observation of a delayed, slowly accelerating subsidence, at the onset of pressure depletion, in combination with continuing subsidence after depletion has ceased, is consistent with a time lag (time decay) process; where the subsidence response to reservoir compaction is asymptotic, with a characteristic time decay constant. Processes of this type are fundamental and commonplace throughout the natural world; they are the signature of non-equilibrium dynamical systems. The archetype of processes in this class is the familiar diffusion or heat equation.

The fundamental nature of time decay processes makes it highly likely that this is the underlying physical mechanism. Indeed, one is already integrated into the subsidence modeling workflow; the main task of the reservoir simulation and history match is to solve a pressure diffusion problem, a fact that makes deficiencies in the reservoir modeling stage a very tenable explanation.

Time decay type models have been proposed as explanations for subsidence delay in the past.
Houtenbos [pers. comm., 2006] proposed a simple empirical time decay relationship between 'subsidence volume' and the mass of gas produced. A number of errors in the physical reasoning led to a rejection of this proposal by NAM and SodM. It was observed at the time though, that transfer functions of this type did appear to provide a satisfactory temporal match to subsidence data and that they are characteristic of a diffusive, and therefore physically reasonable, process. A distantly related time dependent process was contained within the Rate Type Compaction Model [RTCM] [de Waal, 1986], which also sought to explain observed subsidence delay above a number of reservoirs. This was adopted for a number of years by NAM, although subsequently rejected on the basis of divergence from observed data and subsequent critical internal review.

The resultant of a combination of independent time decay processes is itself a time decay process. This fact and the very universality of non-equilibrium dynamics makes it difficult to precisely identify the part or parts of the system that govern the decay time scale. The most obvious and likely is that pressure diffusion effects are not properly captured in the reservoir and aquifer modelling step. Salt creep is also a time dependent non-equilibrium process that has long been considered potentially significant in subsidence modelling and could also provide a possible explanation, given the sparseness of subsidence data coverage. There is also evidence of time dependent compaction processes in consolidated rock, these seem too small to be significant, but they are poorly understood and might scale with size in some non-linear manner. A rather more esoteric mechanism based on the more highly structured pressure depletion patterns that would result from more realistic conductivity distributions and a reinterpretation of poroelastic volume strain is promising. There are doubtless others not yet considered.

However, it is perfectly possible to accurately characterise the governing parameters of a time decay process and make reliable predictions, without having to know the exact causative origins. Based on this reasoning, the difficulty of identifying the exact contributory mechanism or mechanisms, and the paucity of in-situ data, NAM proposed to use a simple first order diffusive time decay function, and apply inversion to find the single time constant this required.

Volumetric Time Decay

While it cannot be claimed that the precise cause of the volumetric time decay process has been identified, it seems highly likely that it is associated with volume strain in the reservoir rather than elsewhere in the subsurface. The constrained volume strain, e_{ii}, at a point, $\mathbf{x}$, in the reservoir is then the usual instantaneous product of pressure change, Δp, and constrained uniaxial compressibility, c_m, but now convolved with a time decay function.

$$e_{ii}(\mathbf{x},t) = \Delta p(\mathbf{x},t)\; c_m(\mathbf{x}) \;*_t\; \frac{1}{\tau}\exp\left[\frac{-t}{\tau}\right]$$

Here, t, is time, $*_t$, is the convolution operator with respect to time and, τ, is a time decay constant. The best fitting time decay constants for the Groningen field were found by inversion using a semi-analytic

geomechanical model and have values of some 3 to 8 years. More sophisticated modelling would not have any significant impact on this result.

It should be realised that it is quite possible that the observed time decay is not a material property of the reservoir rock, but could be due to particularities of the reservoir geometry, pore fluids or some other factor. Therefore it cannot be assumed that the time decay constant appropriate for one reservoir can be applied to another based simply on rock type.

As has already been emphasised, the observation of a time decay effect and the ability to characterise and build predictions using it, are not dependent on precisely identifying the causative mechanism. However, for the sake of the record, a brief description will be made of one of the proposed mechanisms.

4.4.3 Linear Isotach Compaction model

In the Netherlands, this model is the most accepted model for settlement calculations in soft soil. The model is also known as the a,b,c isotachen model (den Haan, 2003). TNO (Pruiksma et al., 2013) studied the application of this model on cemented rock using the laboratory experiments from de Waal as a starting point (De Waal, 1986). Adjustments of this a, b, c istoachen model led to the definition of the linear isotach model which was also implemented by NAM and used to calibrate the compaction model and estimate future subsidence.
Figure 4.10 shows the isotach model as a spring-dashpot system (Pruiksma et al., 2013)

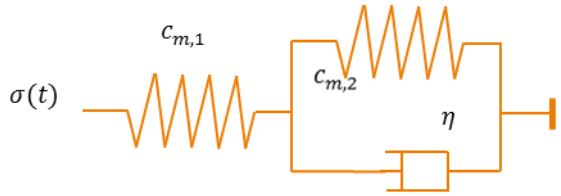

Figure 4.10 Representation of the isotach model

The total strain in the isotach model is calculated by the sum of the direct and elastic strain (ε_d) and the secular strain (ε_s) with σ' the effective stress:

$$\varepsilon = \varepsilon_d + \varepsilon_s$$

Where:

$$\varepsilon_d = f(\sigma') \text{ and } \dot{\varepsilon}_s = g'(\sigma', \varepsilon_s)$$

Pruiksma et al. 2013 proposed to linearize this model as it was demonstrated that this provided a better fit to the laboratory experiments:

This implies that:

$$\varepsilon_d = C_{m,1}(\sigma' - \sigma'_{ref})$$

and

$$\varepsilon_s = C_{m,2}(\sigma' - \sigma'_{ref}) + c\ ln\left(\frac{\dot{\varepsilon}_{s,ref}}{\dot{\varepsilon}_s}\right)$$

The term $(\sigma' - \sigma'_{ref})$ can be derived from the depletion, leaving four other parameters that need to be solved for:

$C_{m,1}$, $C_{m,2}$, c and $\dot{\varepsilon}_{s,ref}$

c is coupled to the viscosity η:

$$\frac{c}{\dot{\varepsilon}_{s,ref}} = \eta\ C_{m,2}$$

4.4.4 Upscaling of input data

The reservoir modelling has been performed using Shell's reservoir simulator MoReS. It uses a 3-dimensional gridded reservoir structure, which includes porosity and permeability information and attempts to solve for the fluid flow and pressure changes as constrained by historic production and pressure data taken from wells. The reservoir model therefore contains self consistent porosity and pressure change information that should be used in the geomechanical modeling. However, the reservoir model tends to use a finer grid size than is needed for the geomechanical model so 'upscaling' is required.

For the Groningen field, a MoReS reservoir model was built consisting of 40 vertically stacked layers and with grid dimensions of 250 m by 250 m, or less. The reservoir formation in the Geomechanical model is made up of one single layer with a lateral element size of around 500 m by 500 m. It is therefore necessary to up-scale the MoRes parameters for the geomechanical model. This is achieved by post-processing of the MoRes output file using routines coded in the general purpose mathematics package, Scilab. Figure 4.11 shows an example of a MoReS output file. The files contain the grid pressures for a single time step and a separate file is generated for each time step.

Table 'Grdcentr' contents; generated on Thu 04/03/2010 16:21 from run '001_BMBoxBehnken_lwo_200x200_001p

	date	xcentr	ycentr	zcentr	dikte	la	Pgrid	net_gross	porosity
	YEAR	M	M	M	M	INTUNIT	BAR	REALUNIT	REALUNIT
1	2036.997	206460	601770	-4249.4	1.0245	1	502.6	0.95535	0.09637
2	2036.997	206650	601770	-4221.5	1.0273	1	499.99	0.96162	0.093082
3	2036.997	206850	601800	-4195.3	1.0332	1	496.85	0.9582	0.14334
4	2036.997	207040	601850	-4174.8	1.0419	1	494.81	0.96528	0.12991
5	2036.997	207230	601900	-4160.2	1.051	1	493.52	0.94872	0.11788
6	2036.997	207410	601940	-4148.3	1.0601	1	492.16	0.94102	0.1321

Figure 4.11 Example of a Mores output file, la indicates the layer number.

Upscaling of the reservoir pressure has to take into account the the variability in the porosity and pressure depletion between the vertically stacked reservoir layers, and weigh them accordingly. This is achieved by summation of the reservoir layer compaction as a function of the layer pressure depletion and compressibility, the latter being a function of porosity. This upscaled compaction has to be equal to the compaction derived for the upscaled layer. The porosity of this upscaled layer is:

$$\emptyset_{\mathrm{av}} = \frac{\sum_{\mathrm{i}}(\mathrm{h_i}\emptyset_i)}{\sum_{\mathrm{i}} h_i}$$

Where $\emptyset_i$ and h_i are the porosity and thickness for each reservoir model layer, respectively. Summation is over the appropriate number of grid layers.

Upscaling the pressure change is less straightforward. The objective is that the up-scaled compaction using a Δp_{avg} is the same as the compaction from the non up-scaled model. The effect of compaction in the individual layers should therefore be included in the upscaling procedure.

The change in thickness of each reservoir model layer is given by:

$$\Delta h_i = c_m(\emptyset_i)\Delta p_i h_i$$

Where $c_m(\emptyset_i)$ is the compaction coefficient as a function of the layer porosity and Δp_i is the pressure change in layer, *i*. The aggregate change in reservoir thickness across the vertically stacked layers is given by:

$$\Delta H = \sum_i c_{mi}(\emptyset_i)\Delta p_i h_i$$

where H indicates the stacked layer thickness. The upscaled pressure across the stacked thickness, $\overline{\Delta p}$, is then given by:

$$\overline{\Delta p} = \frac{\Delta H}{c_m(\emptyset_{\mathrm{av}}) * H}$$

This upscaled pressure was found to be insensitive to the detailed functional form of the compressibility-porosity relationship.

4.5 Comparing the finite element model with Geertsma and van Opstal, the possible influence of rock salt creep

In this section, the subsidence calculation results from two different models are compared: a finite element model (FEM) and the analytical Geertsma and van Opstal model. The objective of this comparison is to illustrate the impact of viscous salt deformation on the subsidence. If the effect on the subsidence is small, the analytical model can be used for further predictions.

4.5.1 Zechstein salt creep

Rock salt behaves like a highly viscous non-Newtonian fluid. Many investigators have proposed constitutive models where strain rate is a function of differential stress (usually a power law) and absolute temperature (usually exponential). Power law equations of the type presented below are widely accepted and used to calculate deformation for a wide range of geotechnical problems such as cavern closure [e.g. Weertman, 1955; Heard, 1972; Munson and Dawson, 1979].

$$\dot{\varepsilon} = \sum_{\mathrm{i}} A_{\mathrm{i}} \left(\frac{\sigma}{\sigma_0}\right)^{n_i} \exp\left(\frac{-Q_{\mathrm{i}}}{R \cdot T}\right)$$

Here the shear strain rate, $\dot{\varepsilon}$, is a function of: absolute temperature, T, shear stress, σ, a shear stress normalisation term, σ_0, and the gas constant, R. Values for the scaling parameters, A_{i}, the activation energies, Q_{i}, and the power law terms, n_{i}, are then determined from fits to experimental data.

These constitutive equations can be simplified by realising that different creep mechanisms are dominant for different stress and temperature domains [Munson, 1979]. Of particular importance for this study is the observation that a pressure solution creep mechanism becomes the dominant flow law at low values of differential stress and moderate temperatures [Spiers et al., 1986; Spiers and Carter, 1998]. This obeys a simple unitary (i.e. linear) power law dependence on shear stress, i.e. it is a Newtonian fluid.

$$\dot{\varepsilon} \rightarrow A \left(\frac{\sigma}{\sigma_0}\right) \exp\left(\frac{-Q}{R \cdot T}\right)$$

where $A = B/Td^{\beta}$ (with d is the effective grain size length scale, and B a material constant). Hence the creep constant (A) is highly dependent on the grain size of the salt.

There is precedent in the application of linear salt creep to geomechanical models in this region. Breunese et al. [2003] observed that such linear pressure solution creep could explain the temporal and spatial pattern of the subsidence above two deep salt caverns in the northern part of the Netherlands. Representative grain sizes, found in cores from the Zechstein, range from 3 mm to 20 mm length scale. The stress normalization term, σ_0, is set to 1 MPa while Q/R corresponds to 3007 K. The temperature gradient is 0.03 K m^{-1} with a reference temperature of 373.15 K (100ºC) at 3000 m TVDSS. However, the relative insensitivity of the scaling parameter, A, compared to the exponential term, permits the use of a constant mean temperature (378.15 K, 105ºC) in its determination, see Table 4.1. This range was then applied to the Zechstein layer elements in a numerical geomechanical model to compare with the analytical solution that doesn't account for salt behaviour (section 4.5).

Grain size salt [mm]	A [s^{-1}]
3	3.94E-08
20	1.39E-10

Table 4.1 Grain size and associated scaling parameter, A, range used in models.

The FEM contains, besides the reservoir layer itself, a description of the layers of the over- and underburden. Rather than assuming a rigid basement in the analytical approach we explicitly model as accurate as possible the stiffness contrasts between reservoir and burden. The finite element model was tested for salt creep applying two sets of salt flow parameters. Another run was made using linear-elastic behaviour of the salt. Finally, the possible effect of element type (linear hexahedron versus linear tetrahedron) was tested for the "medium salt" case. The bottom depth of the finite element model was set to 7000m. Mechanical parameters for the different layers used in the finite element model are tabulated in Table 4.2.

Unit	Young's Modulus [GPa]	Poisson's ratio	Density [kg m^{-3}]	Remarks / non-linear parameters
North Sea	2	0.3	2150	
Chalk	10	0.25	2350	
Lower Cretaceous / Triassic	16	0.25	2300	
Zechstein	30	0.35	2200	Q/R 3007 K A 1,69E-09 s^{-1} (medium salt) A 1.39E-10s^{-1} (slow salt) Or linear model
Ten Boer Claystone	40	0.2	2300	
Rotliegendes ROSLU ROCLA ROSLL	1.-40 (base case)	0.2	2300	In drained area depending on the porosity (fraction): $C_m = 267.3 * \varphi^3 - 68.72 * \varphi^2 + 9.85 * \varphi + 0.2107$ E derived from Cm* In undrained area: E = 44 GPa
Carboniferous	40	0.2	2300	

* C_m is uniaxial compaction coefficient [10^{-5} bar^{-1}] $Cm = \frac{1}{E}\frac{(1+\nu)(1-2\nu)}{1-\nu}$

Table 4.2 Used parameters in finite element model for over- and underburden layers.

The Cm for the analytical model is based on the same relation with porosity as listed in Table 4.2. Both models used a time-decay corrected pressure input with an arbitrary time-decay of five years.

The lateral boundary of the finite element model is set at about one reservoir size (40 km) of the reservoir (Figure 4.12) to minimize boundary effects on the displacement.

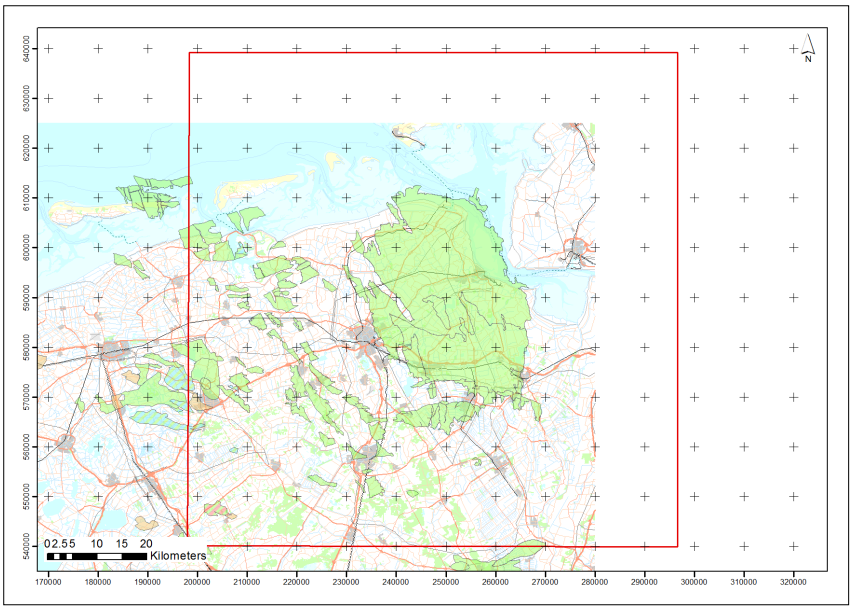

Figure 4.12 Extend of finite element model indicated by the red box.

The difference between these models is shown in Figure 4.13 to Figure 4.15. Figure 4.13 shows the subsidence contours for the analytical and Geomec model for 2008 compared with the subsidence results from the FEM using a medium fast salt. The figure shows that the contours are quite close to each other meaning that the impact of the salt on the subsidence bowl is very limited.

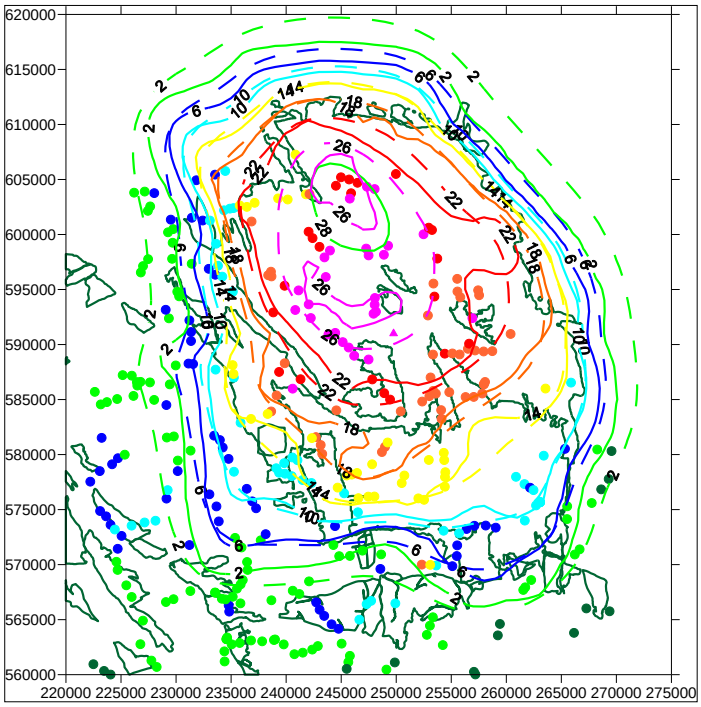

Figure 4.13 Comparison of the subsidence contours from the analytical model (dashed) and Geomec model(line) for the year 2008.

Figure 4.14 and Figure 4.15 show the subsidence of the analytical model (line) and the finite element models using three salt flow models (dots) near the deepest point of the subsidence bowl and in the North-West Aquifer respectively. The finite element models are calculated for a limited number of years (dots).

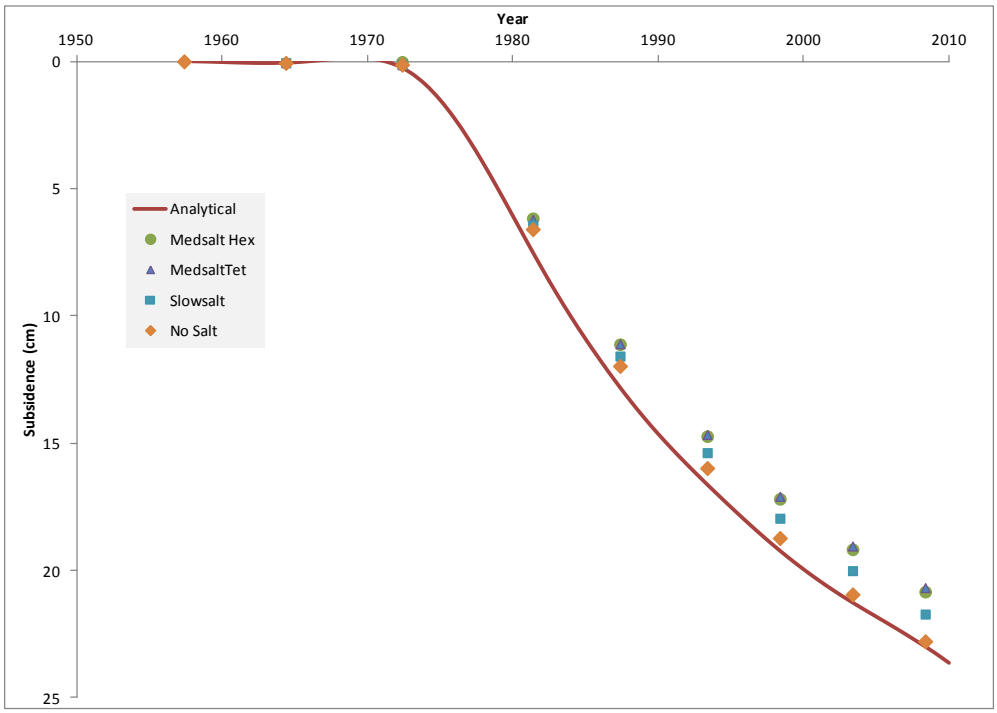

Figure 4.14 Subsidence versus time near the deepest point (x=240000 y=591000) for Geomec models and analytical model

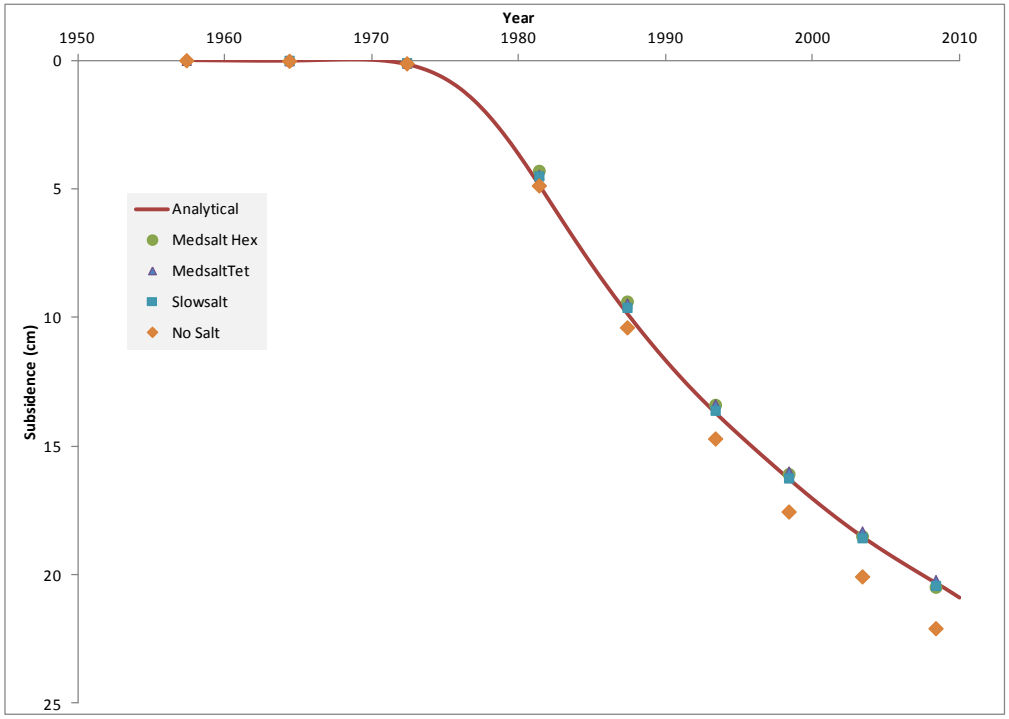

Figure 4.15 Subsidence versus time in the NW aquifer (x=237000 y=603000) for Geomec models and analytical model (Geertsma and van Opstal)

Finally, Figure 4.16 shows a comparison between the modelled subsidence for the year 2008 of the analytical model (Geertsma and van Opstal) and the finite element model (Geomec) using different salt parameters.

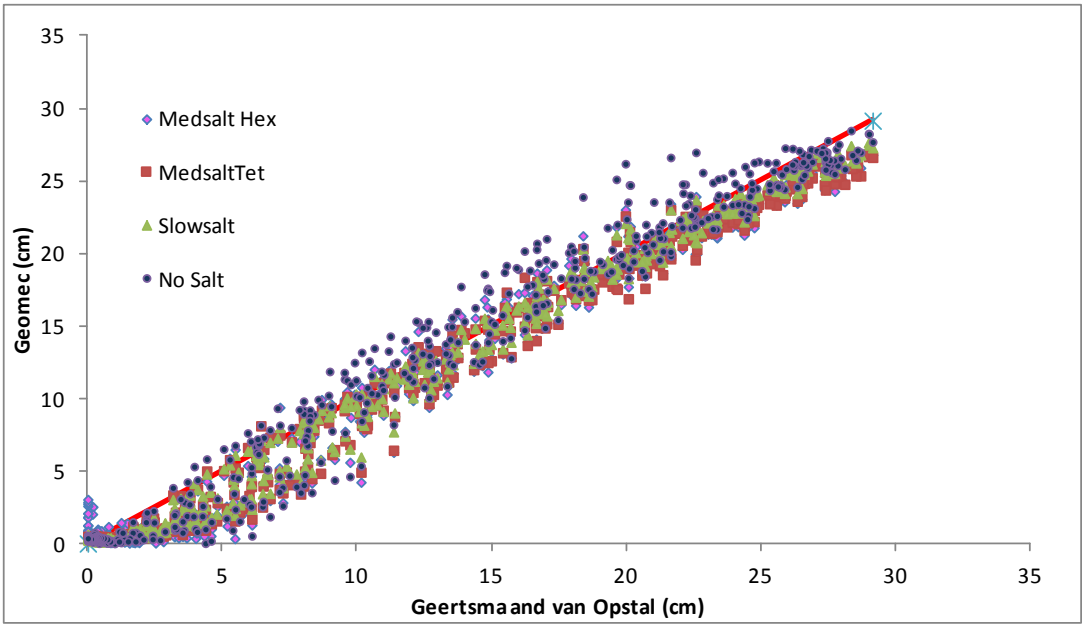

Figure 4.16 Comparison subsidence calculation between Analytical(Geertsma and van Opstal) vs Finite element models(Geomec) for 2008

Conclusion

As the shape of the subsidence bowl between the analytical and finite element model is very similar and the difference in calculated subsidence, also between the different salt realisations, is small, we conclude that the subsidence calculation with the analytical model will give sufficiently accurate results.

4.6 Calibration of the model

For the purposes of subsidence prediction and preparation of the Winningsplan a representative, or 'base case', model must be selected. Throughout this document there are references to improved model fits and matches to subsidence data. This section describes the method used to make these judgements and the results for the different compaction models.

4.6.1 RMS of all benchmarks using epoch combinations

A relatively simple comparative measure of model fit was created by determining the residuals between the surveyed and modelled subsidence at all benchmarks for a number of different time spans, termed epochs, and calculating the total variance weighted root-mean-squared (RMS) value. A trivial sequential set of epochs can be envisaged, shown schematically in Figure 4.17(a), where the last survey of a previous epoch becomes the first survey of the next epoch. However, the comparatively small subsidence signal between subsequent levelling campaigns means that this approach would suffer from low signal-to-noise ratio. A comprehensive scheme including all possible epoch combinations could also be considered. Figure 4.17(b) schematically represents all the epoch combinations that include the first levelling campaign and similar epoch sets can be generated for each campaign, while excluding duplicates. This again though includes a large number of epochs with low signal-to-noise ratio while being considerably more computationally expensive. Instead a robust metric was created using a standardised subset of epochs that were of sufficient duration to provide good signal-to-noise ratio while keeping computation to a moderate level. These are shown schematically in Figure 4.17(c).

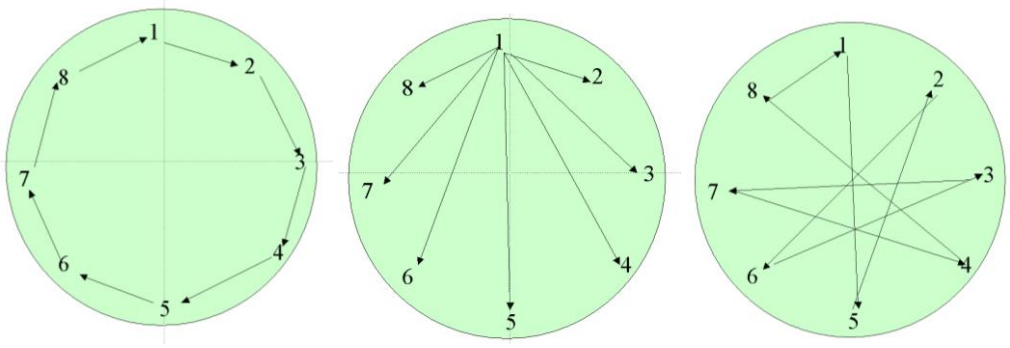

Figure 4.17 Schematic showing epoch combinations used in the calibration process: a) sequential, b) all possible combinations (example shows combinations with survey 1 only) c) efficient method used in current analysis.

Figure 4.18 shows an example plot where measured and modelled subsidence are plotted against each other for a variety of epochs and the calculated RMS value given.

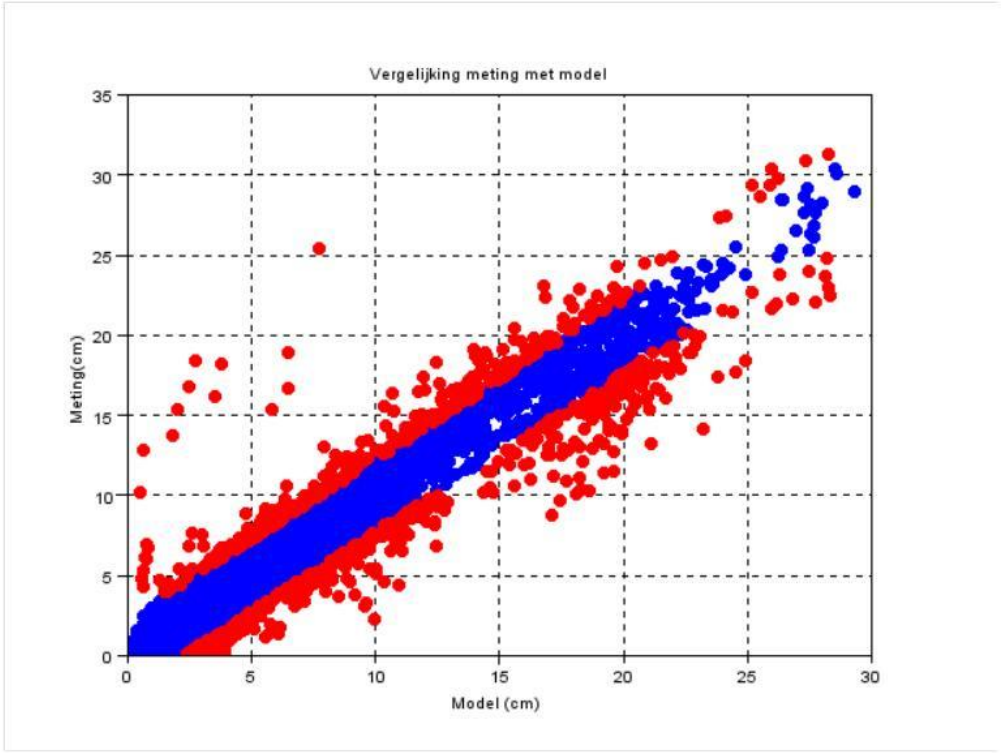

Figure 4.18 Example of 'RMS' graph showing the modeled subsidence against the measured subsidence, in cm.

4.6.2 Basecase model

For the three compaction models a calibration was made with the levelling data. Starting from the best fit (lowest RMS), a Monte Carlo simulation was done to illustrate the sensitivity of the different compaction parameters. This simulation showed that for the bilinear and time decay model the Cm value is well constrained. The range of Cm values which give acceptable RMS results for the isotach model is large.

As basis a first cycle Cm [10^{-5} bar^{-1}]-porosity [-] relation is used,

$C_m = 267.3\phi^3 - 68.72\phi^2 + 9.85\phi + 0.21$ [10^{-5} bar^{-1}]

For the purpose of calibrating the model to the subsidence, a $C_{mfactor}$ is introduced that is basically a multiplication factor:

$C_m = C_{mfactor} * (267.3\phi^3 - 68.72\phi^2 + 9.85\phi + 0.21\ )$ [10^{-5} bar^{-1}]

In the next paragraphs the results are discussed in more detail for the various compaction models.

4.6.3 Results for the Bi-linear model

The calibration of the bi-linear model resulted in the following parameters for the compaction model showing the lowest RMS value according the method explained in section 4.6.1.

$C_{mpre} = 1.31 \cdot \emptyset + 0.11$

$C_{mpost} = 3.14 \cdot \emptyset + 0.11$

$P_{trans} = 234$ bar

A comparison of the measured versus modelled subsidence for the full levelling surveys is shown in Figure 4.19, using these values for m_{pre}, m_{post} and c.

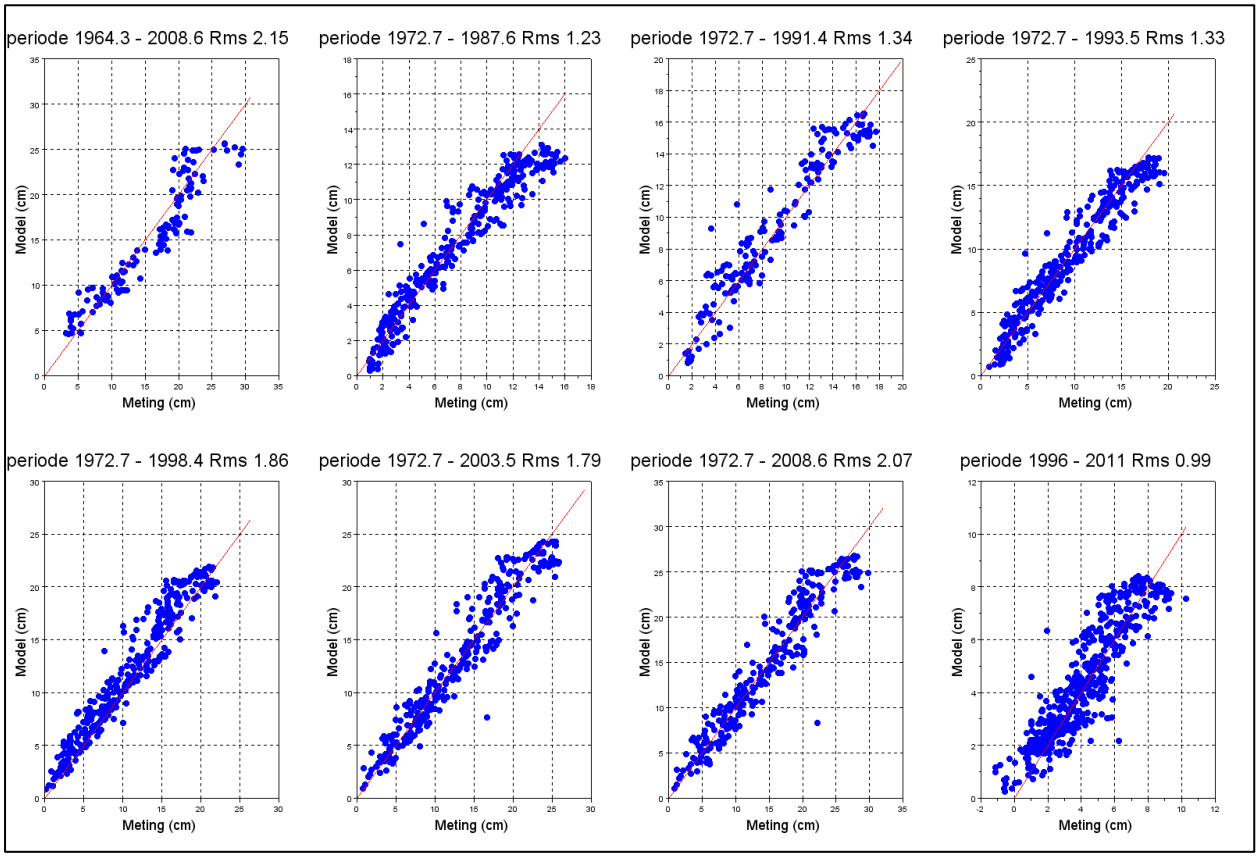

Figure 4.19 Measured vs. modeled subsidence for the full levelling and insar surveys (1996-2011) for the bi-linear model

To investigate the uniqueness of this solution a Monte Carlo simulation to the bi-linear compaction parameters was done. The parameters investigated were m_{pre}, m_{post} and P_{trans}, whilst c was kept constant at 0.11x10^{-5} bar^{-1}.

The results are shown in Figure 4.20. The colours in this figure represent a certain RMS range with in green the range for RMS values < 1.4. In the left graph the best m_{pre} and m_{post} values are around 1.5 and 3, respectively. In the right graph only the best m_{pre} and m_{post} (RMS < 2) values are plotted. The colours in this plot now represent the Transition pressure. In the area where RMS for m_{pre} and $m_{post}$are lowest the colours for the transition pressure are dominated by red and blue colours indicating an optimal P_{trans} value between the 225 and 250 bar.

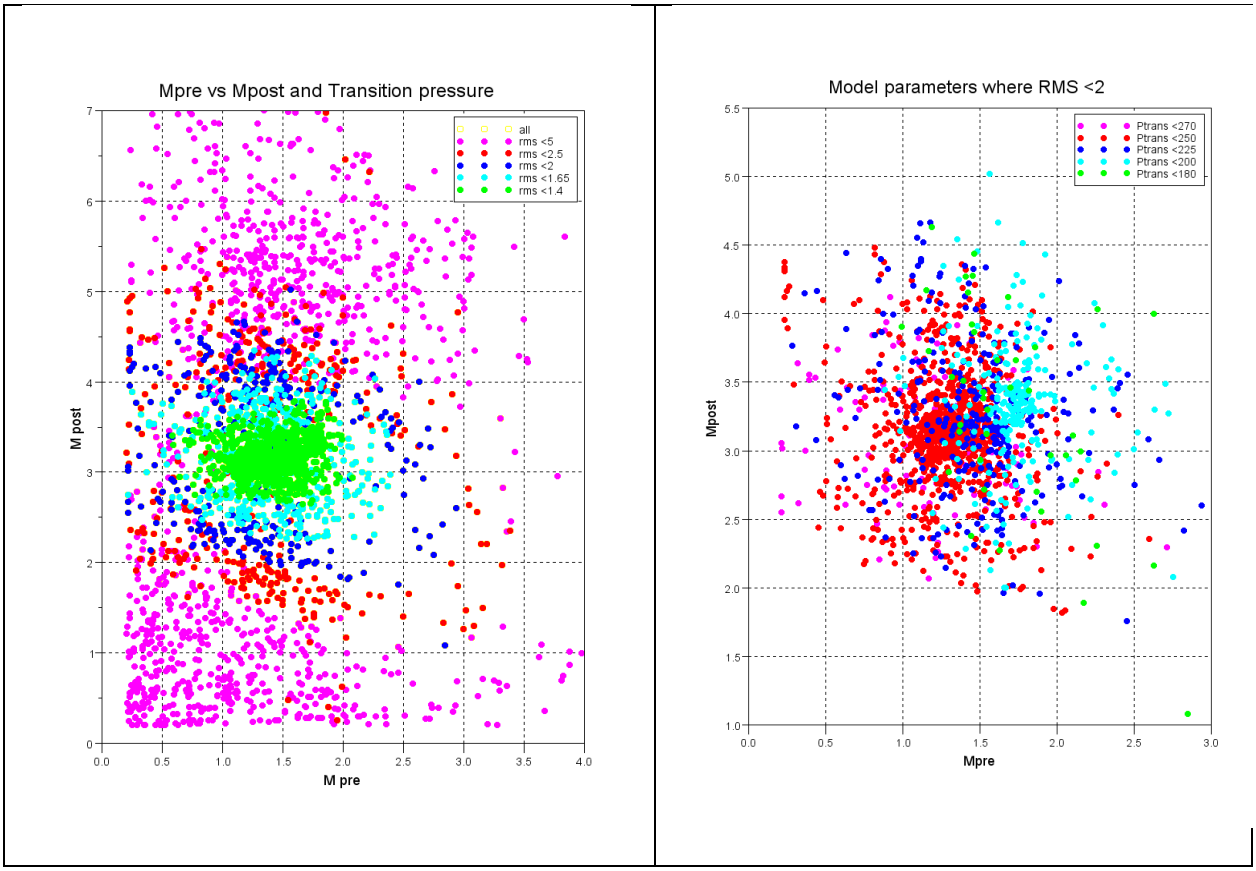

Figure 4.20 Monte Carlo analysis for the bi-linear compaction model. The left graph shows the m_{pre} versus m_{post}, the color indicates the Rms value of the combination. The right graph plots the m_{pre} versus m_{post} but now the color indicates the transition pressure.

To show the distribution of possible average Cm values for 20% porosity which resulted in a RMS < 2 in the Monte Carlo simulation a histogram was made (Figure 4.21). The Cm values are calculated for the full production period (till the end pressure of 10 bar)

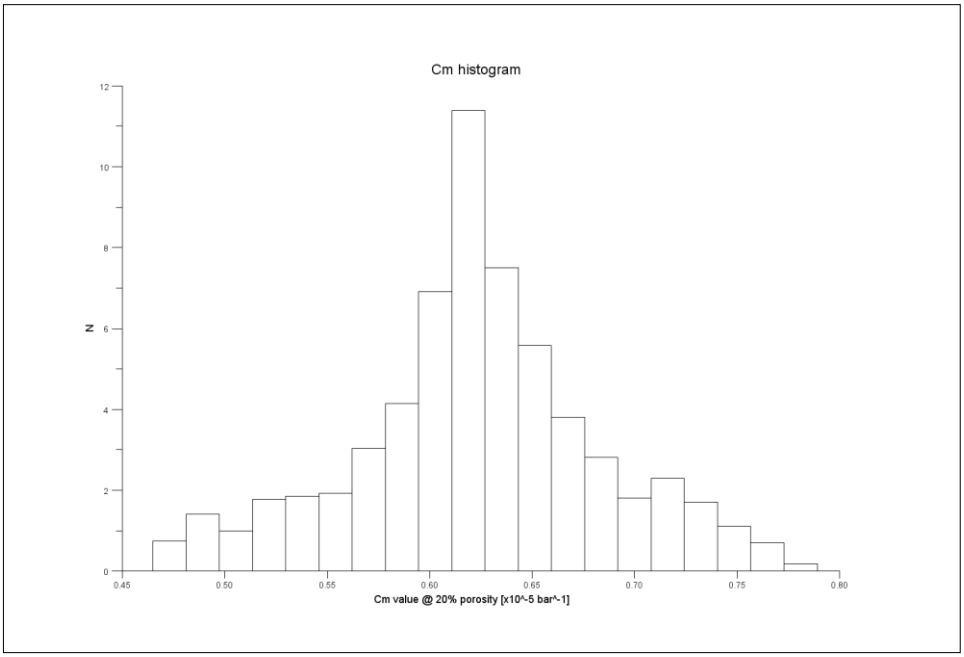

Figure 4.21 Histogram of Cm values calculated at 20% porosity for bi-linear models with an RMS < 2

4.6.4 Time decay

The calibration of the time decay model resulted in the following parameters for the compaction model showing the lowest RMS value according to the method explained in section 4.6.1.

$Cmfactor$: 0.45

decay time τ: 7.3 year

A comparison of the measured versus modelled subsidence for the full levelling surveys is shown in Figure 4.22.

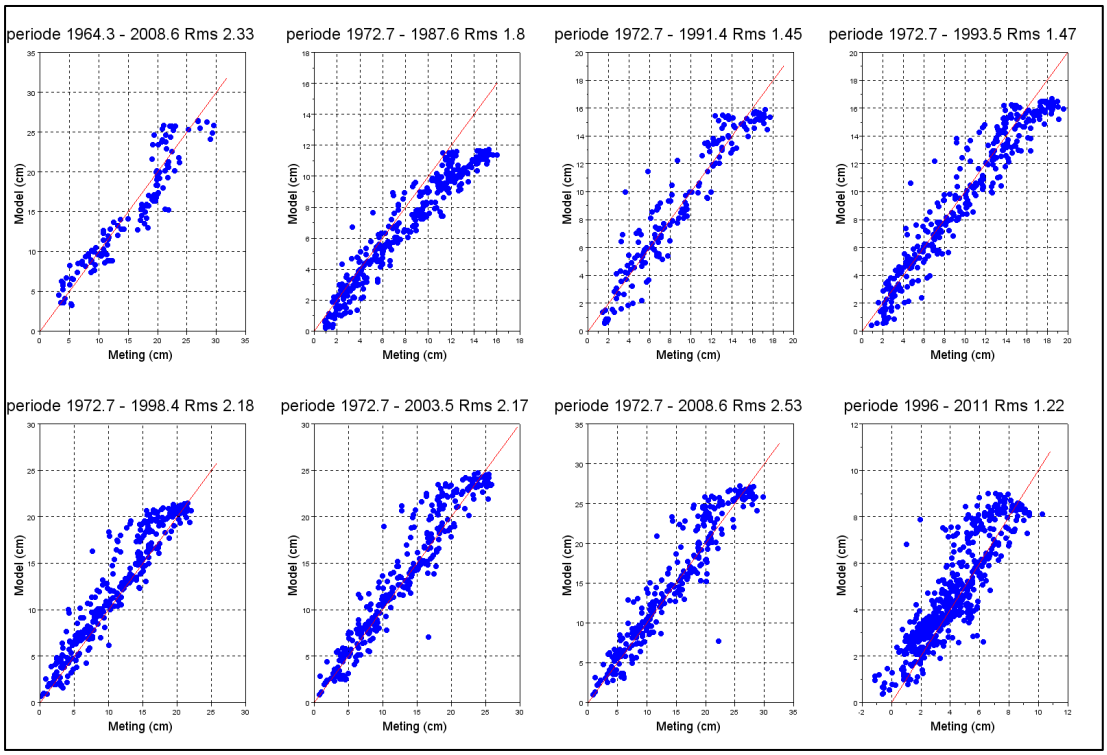

Figure 4.22 Measured vs modelled subsidence for the full levelling and a insar surveys (1996-2011) for the time decay model

To investigate the uniqueness of these parameters, a Monte Carlo simulation was carried out. The results of this analysis are shown in Figure 4.23. In this figure, the Cm factors are plotted against the resulting time decay values (in years) where the colours indicate the RMS value. An in Figure 4.24 the resulting Cm values at a porosity of 20% from the Monte Carlo combinations of a RMS < 2 are shown. These figures show a narrow bandwidth for the Cm but a wider bandwidth for the τ. The red dot indicates the parameters used for the winningsplan model. The wide bandwidth for the τ could be further constrained by making a comparison between the measured data in benchmark 7E33 with several time decay models with a variable τ (Figure 4.25). For this case, the $Cm\ factor$ was adjusted to match the modelled subsidence in 2013 to the measured subsidence. A τ of around 7 years shows the best fit with the measured data.

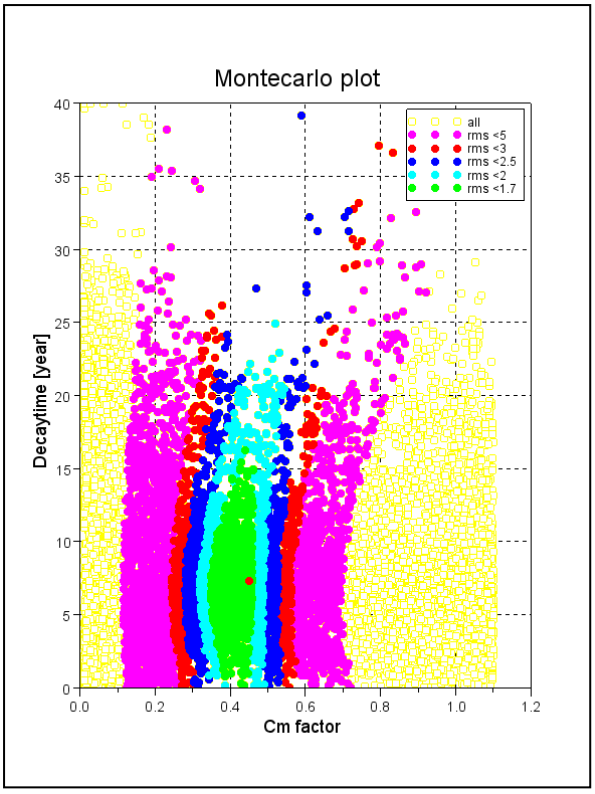

Figure 4.23 Monte Carlo analysis for the Time Decay compaction model. The dot shows the Cm and Time decay parameters used in the winningsplan model.

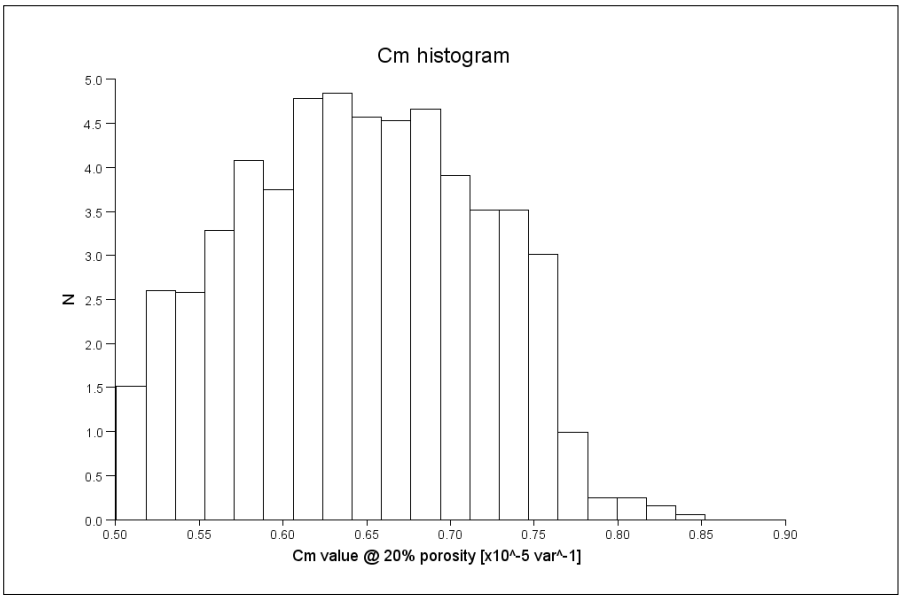

Figure 4.24 Histogram for the Cm values at 20% porosity from the Monte Carlo combinations with a RMS < 2

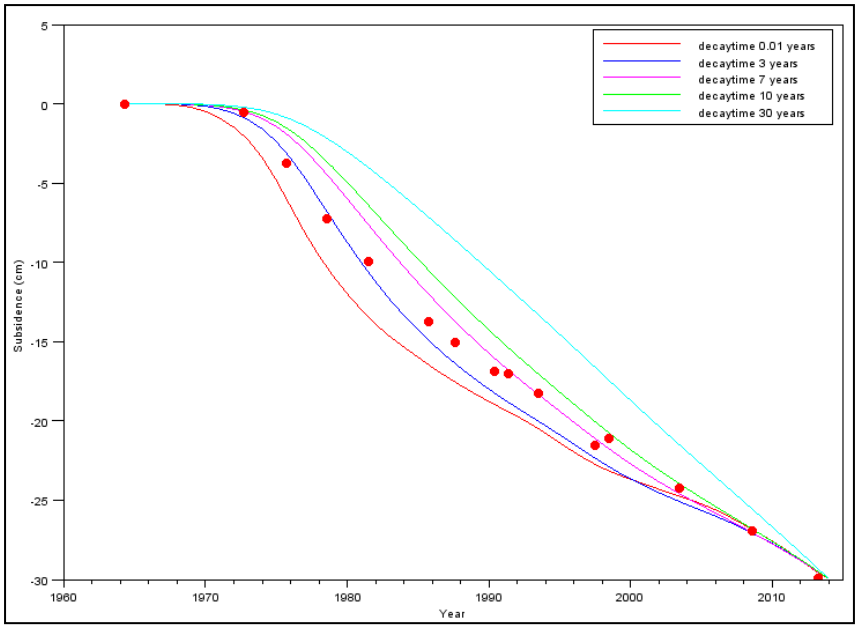

Figure 4.25 Effect of time decay on the subsidence at point 7E33 (the location of this point is indicated as a red dot in Figure 4.8)

Conclusion

With a limited set of parameters that could be reasonably well constrained by the result, the time decay model is able to produce a reasonable fit with the observed data. Therefore we treat this model as the base case model.

4.6.5 Isotach model

The Isotach model, as described in section 4.4.3, has four parameters. To investigate the uniqueness of possible parameter combinations a Monte Carlo simulation was done. The results are shown in Figure 4.26. In these figure the RMS value is plotted on the y-axis, the split between a low (blue) and a higher RMS value (yellow) was arbitrarily set at a RMS of 2. The figure shows that, out of the four available parameters, only the $C_{m,1}\text{factor}$ is reasonably constrained by the results (top left figure). The other parameters can be regarded as unconstrained. This means that a very broad range of parameter combinations is possible that all will give a good fit with the measured subsidence data. This implies that the future subsidence forecast will have a wide range as well. Note that for the η and the $\dot{\varepsilon}_{s,ref}$ the logarithm of these values is used, meaning that the distribution of these parameters is even larger.

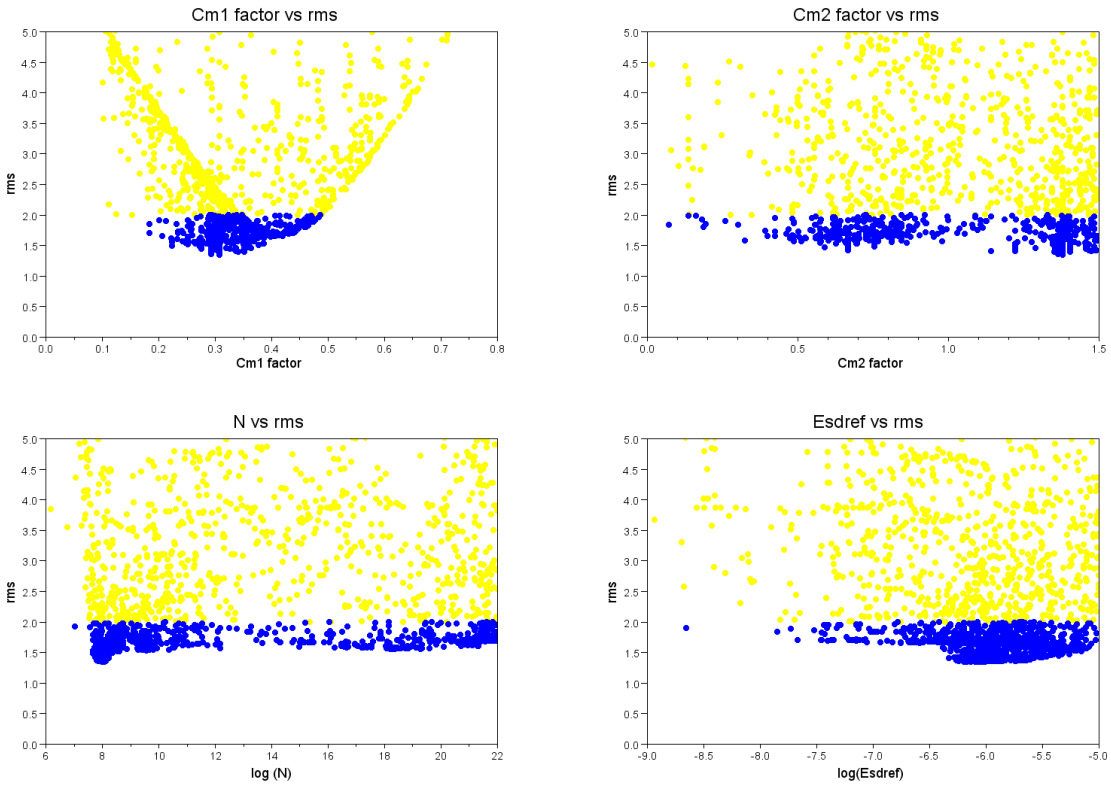

Figure 4.26 Monte Carlo analysis for the Isotach compaction model.

The resulting Cm factor is the addition of both the Cm1 and Cm2 factors. The large range of possible Cm values, at 20% porosity, is shown in Figure 4.27. For comparison the laboratory derived Cm value is 1.5 *10^{-5} bar^{-1} and the calibrated value found with the time decay model is 0.7 *10^{-5} bar^{-1}.

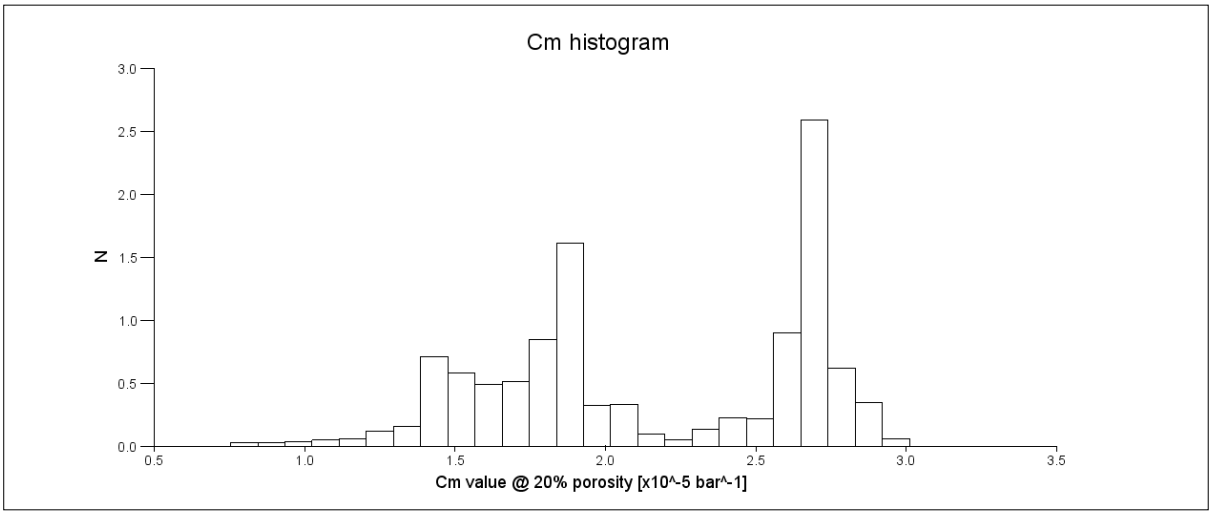

Figure 4.27 Histogram for Cm values at 20% for RMS < 2

Two cases were selected out of the wide distribution of possible realizations:

1. A realization where $C_{m,1}$factor + $C_{m,2}$factor =1, meaning that the total Cm is based on the Cm-porosity trend line of the laboratory data. We regard this case to be a "worst case"
2. A realization where $C_{m,1}$factor + $C_{m,2}$factor equals the Cm factor of the time decay model

The realization of the isotach compaction model where the Cm value is fixed to the lab Cm value ($C_{m,1}$factor + $C_{m,2}$factor =1) has resulted in the following model parameters:

$C_{m,1}$factor = 0.32

$C_{m,2}$factor = 0.68

η =1.09 10^{8} [bar.yr]

$\dot{\varepsilon}_{s,ref}$ = 0.7 10^{-6} [year^{-1}]

A comparison of the measured versus modelled subsidence for the full levelling surveys is shown in Figure 4.28. The calibration with the laboratory Cm returns in a good fit (Figure 4.28) with the measured data. Next paragraph shows that also a good fit can be obtained when a Cm value that equals the time decay Cm is being used.

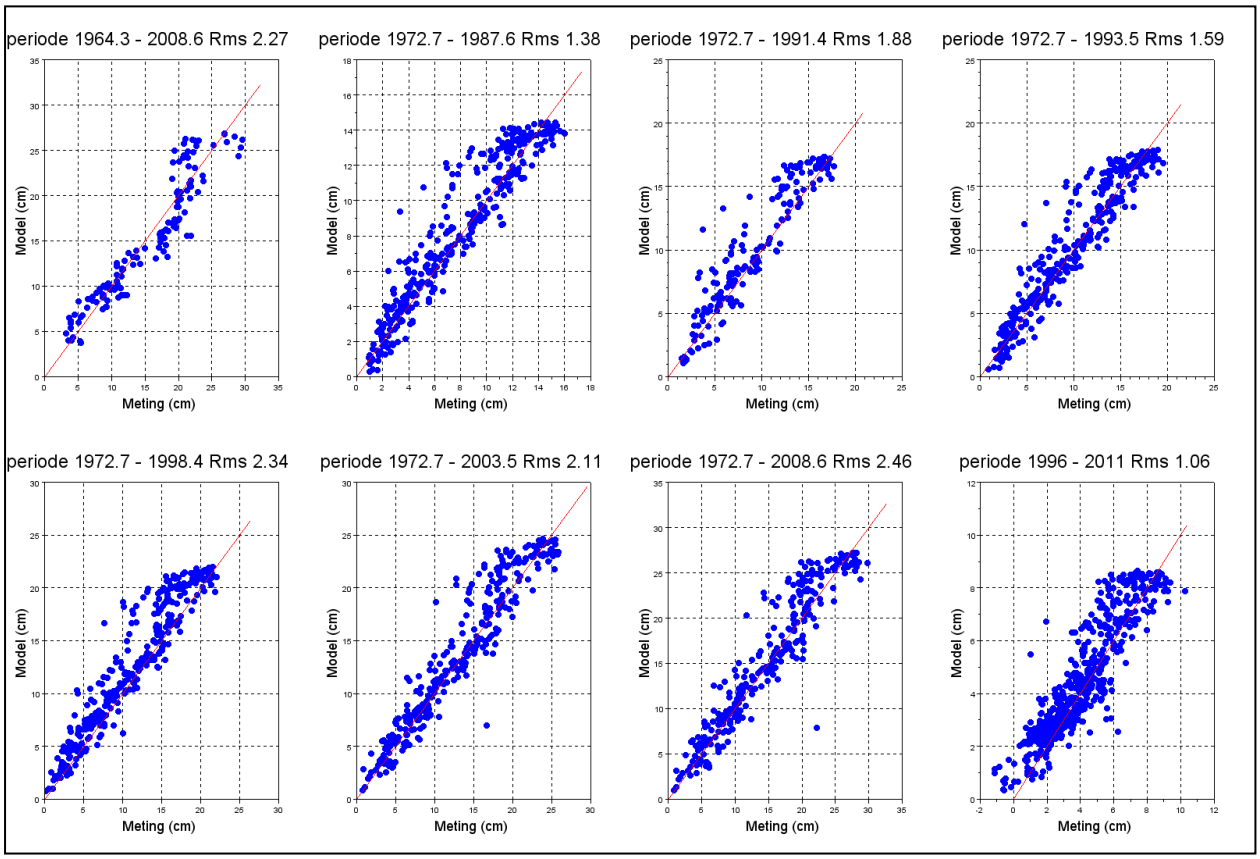

Figure 4.28 Measured vs. modeled subsidence for the full levelling and insar surveys(1996-2011) for the isotach model

2. A realization where $C_{m,1}$factor + $C_{m,2}$factor equals the Cm factor of the time decay model ($C_{m,1}$factor + $C_{m,2}$factor = 0.449) has resulted in the following model parameters.

$C_{m,1}$ factor = 0.23

$C_{m,2}$ factor = 0.22

η = 0.34 10^{8} [bar.yr]

$\dot{\varepsilon}_{s,ref}$ = 0.9 10^{-6} [year^{-1}]

The calibration plot is of this realisation shown in Figure 4.29 and is slightly better than the results of the isotach realization using the laboratory Cm value.

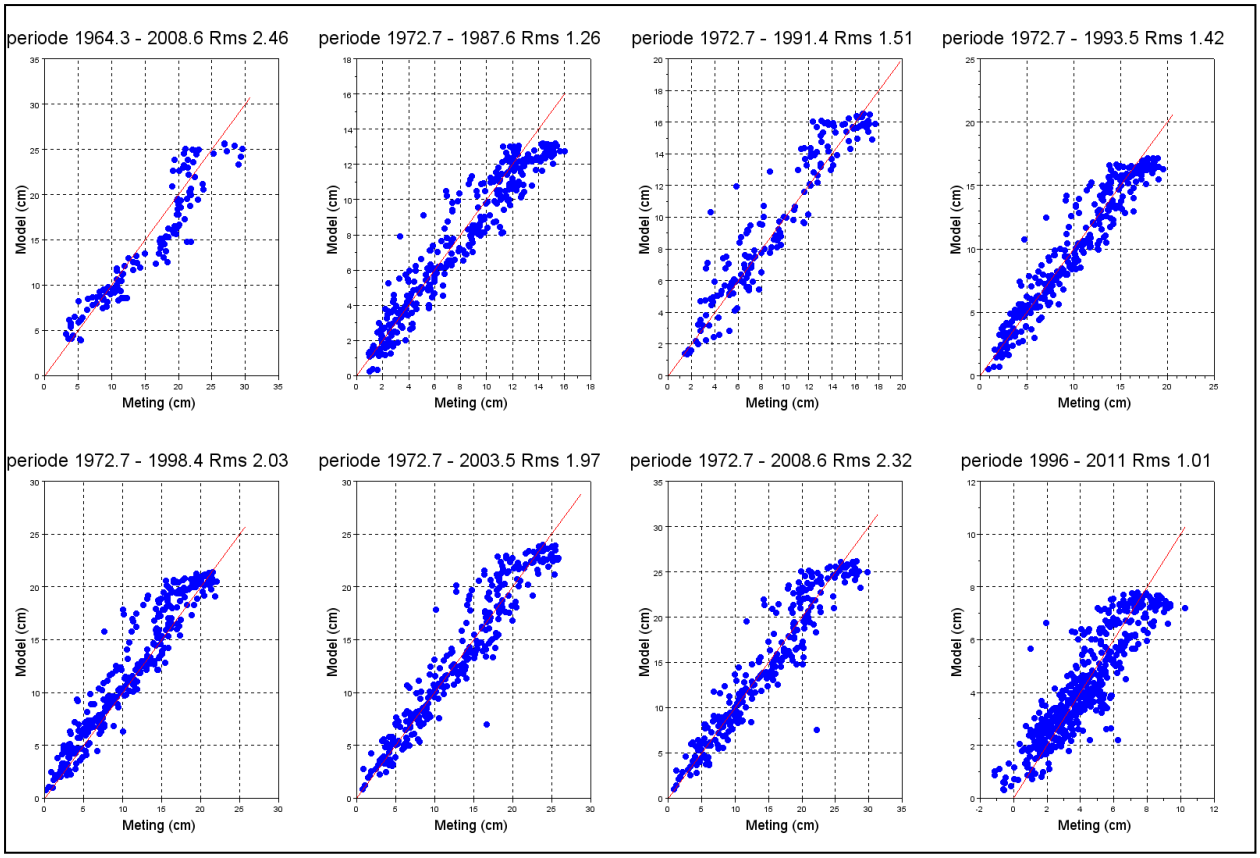

Figure 4.29 Calibration plot for the isotach model calibrated to the timedecay Cm value

4.6.6 Comparison

As shown in previous paragraphs the three compaction models show a good agreement with the measured subsidence after a calibration. The time decay model is our base case model because of the limited number of input parameters. Using the same Cm value in the various models results in more or less similar values for the forecasted subsidence as shown in Figure 4.30. The isotach model with a fit of the Cm to the laboratory measurements predicts significantly more subsidence.

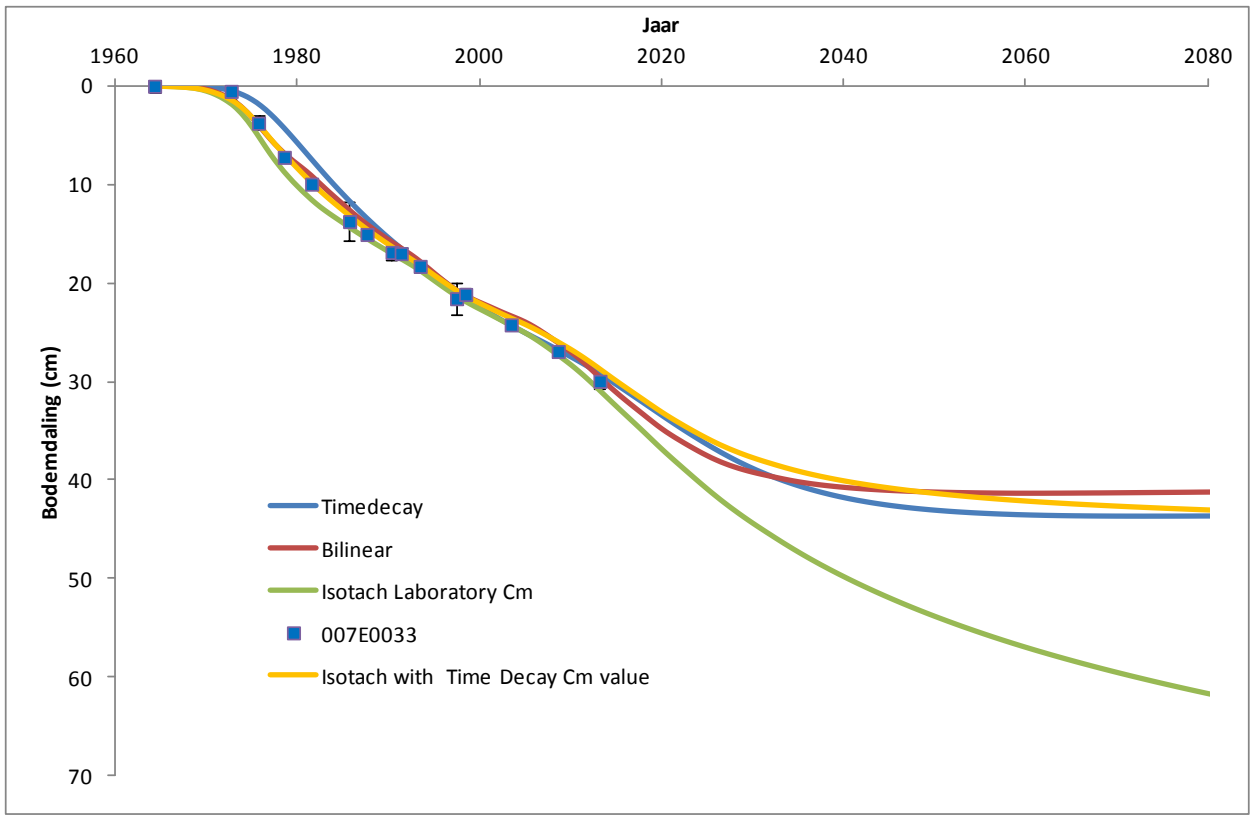

Figure 4.30 Modeled vs. measured subsidence for the different compaction models in a point near the centre of the subsidence bowl (red dot in Figure 4.8). The Isotach model has two realisations, one with the laboratory Cm value and the other with the Cm value used in the Time Decay model.

4.6.7 Conclusion

The time decay compaction model is chosen as the base case model because of the limited amount of reasonably well constrained parameters involved, and because of the good fit with the levelling data. Furthermore, the model also gives a good fit to the subsidence observed above the Ameland and Anjum Fields (NAM 2011a and NAM 2011b). Especially the better match with the continuing subsidence above the Ameland field under decreasing rate of depletion makes this model superior to the bi-linear compaction model which cannot reproduce this delayed compaction behavior.

The isotach model is the most flexible model giving a slightly lower RMS value than the other models. The drawback of this model at present is that the four parameters in the model are poorly constrained resulting in a wide range of possible subsidence forecasts.

4.7 Subsidence forecasts

As discussed in section 4.6, three different compaction models were used for history matching and for forecasting the subsidence with ongoing production. The time decay model provides the base case model while two alternative realisations are made using the isotach model: one that includes the Cm-porosity relation representing the average laboratory observations and another applying the Cm-porosity relation adopted from the calibrated time decay model. Section 4.6 and Figure 4.30 have shown that the three compaction models result in a similar value for the subsidence at a point near the centre of the subsidence bowl.

The modelled base case subsidence and the measured subsidence for the year 2008 are compared in Figure 4.31. Overall, the match with the observed measurements is reasonable to good. Figure 4.32 shows the forecast of the subsidence at the end of the field life using the same base case model. A maximum subsidence of some 46 cm is forecasted with this model.

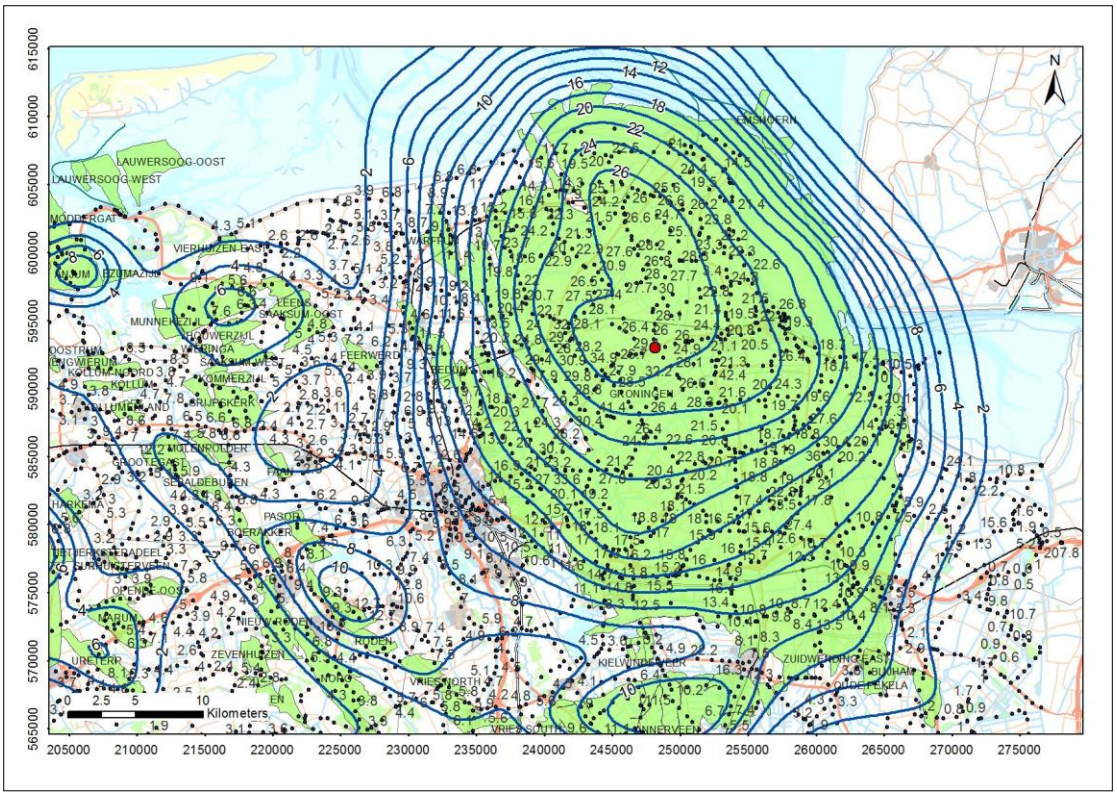

Figure 4.31 Measured subsidence (1972 - 2008) at benchmarks versu modelled subsidence since 1964 (contours) for 2008. The red dot indicates the benchmark 07E0033 which is the position for the comparison in Figure 4.8.

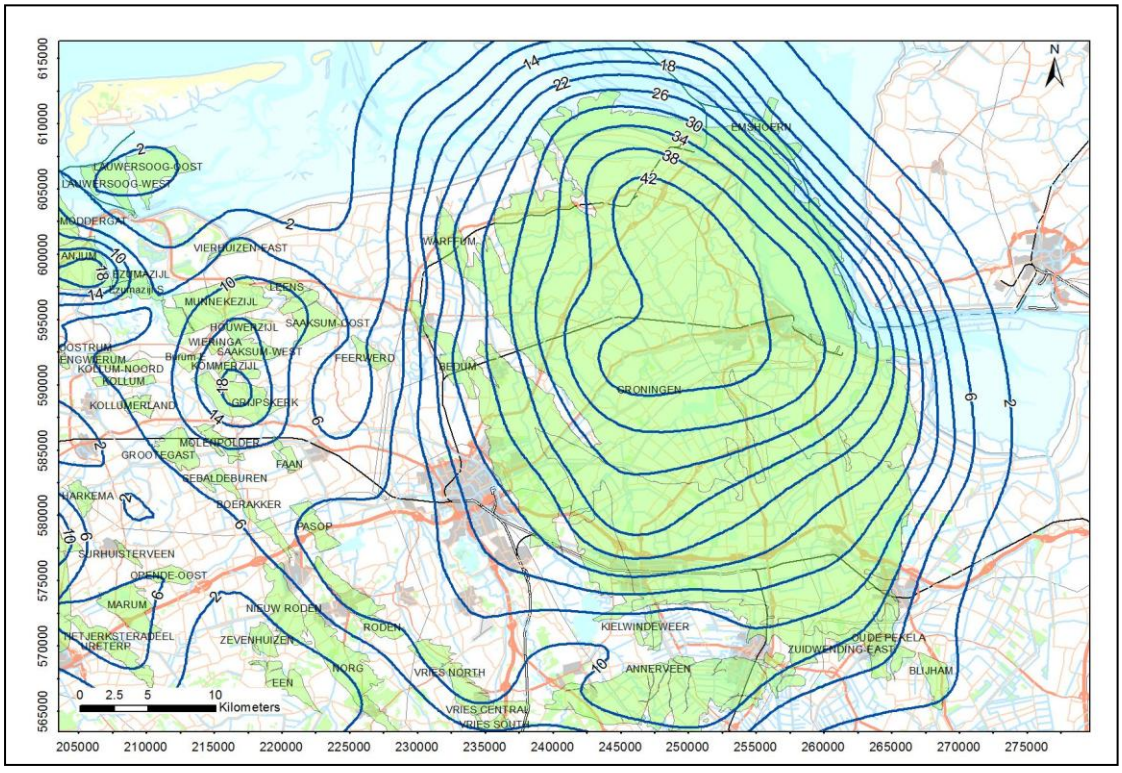

Figure 4.32 Subsidence prognosis based on the time decay model at the end of field life. This figure shows the subsidence due to gas production for the Groningen field in combination with the subsidence predicted for neighboring fields (cm).

The development of the future subsidence through time for the different compaction models is shown in Figure 4.33 to Figure 4.36. As shown in section 4.6 the bi-linear and time decay compaction models lead to comparable Cm values, which in turn leads to a comparable subsidence development (Figure 4.33 and Figure 4.34). Two variations are run for the isotach model. Figure 4.35 shows the result of the model with average laboratory data values for the Cm and Figure 4.36 shows the results with Cm relation adopted from the time decay model.

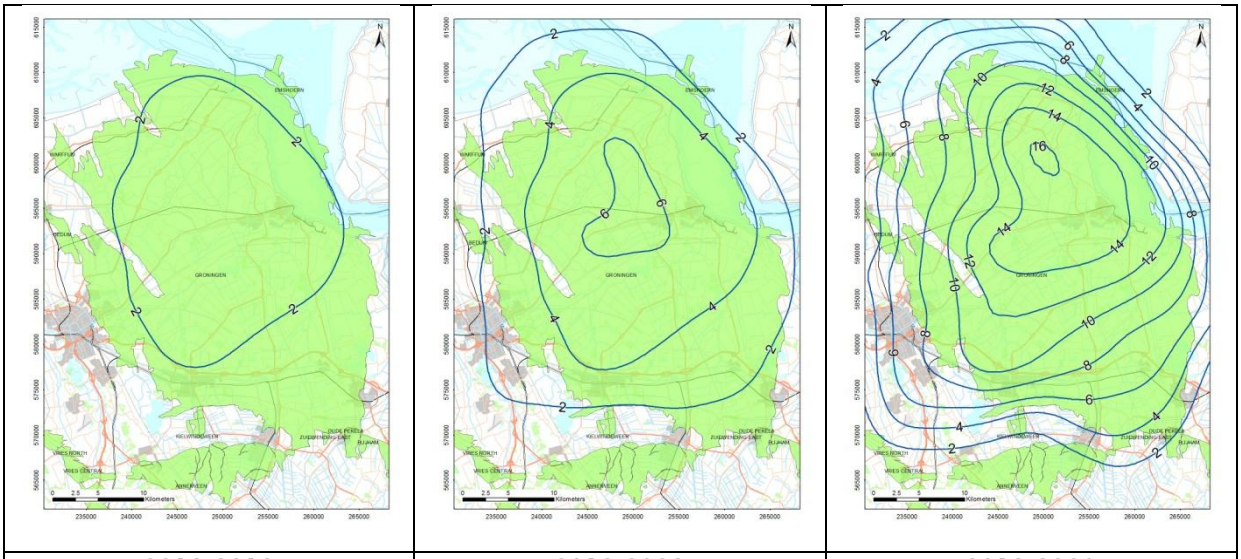

Figure 4.33 Development of the to be expected subsidence according to the time decay compaction model

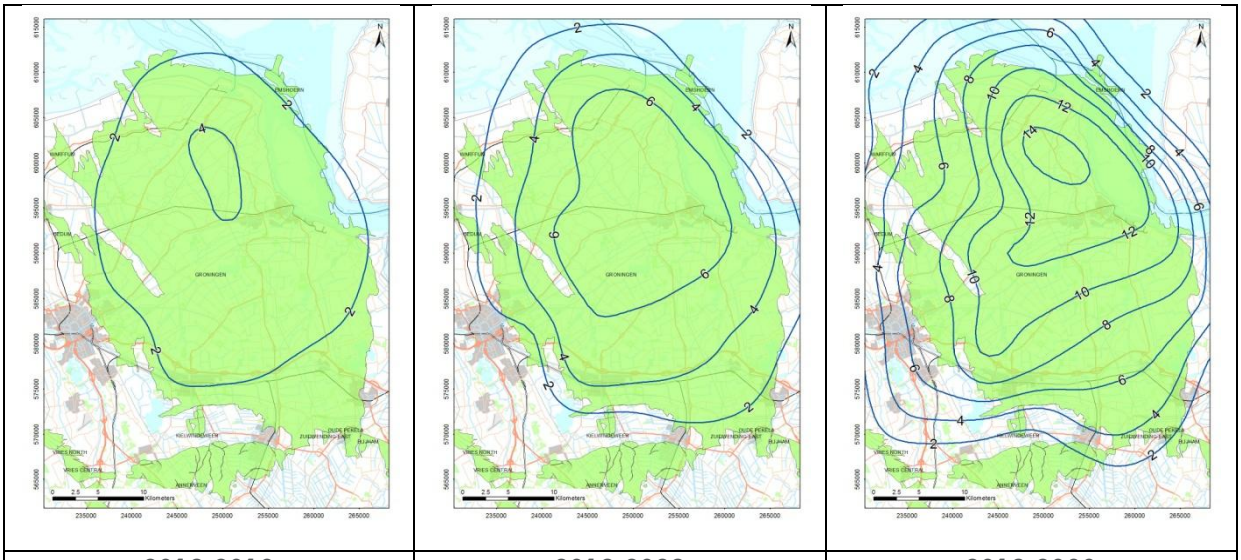

Figure 4.34 Development of the to be expected subsidence according to the bi-linear compaction model

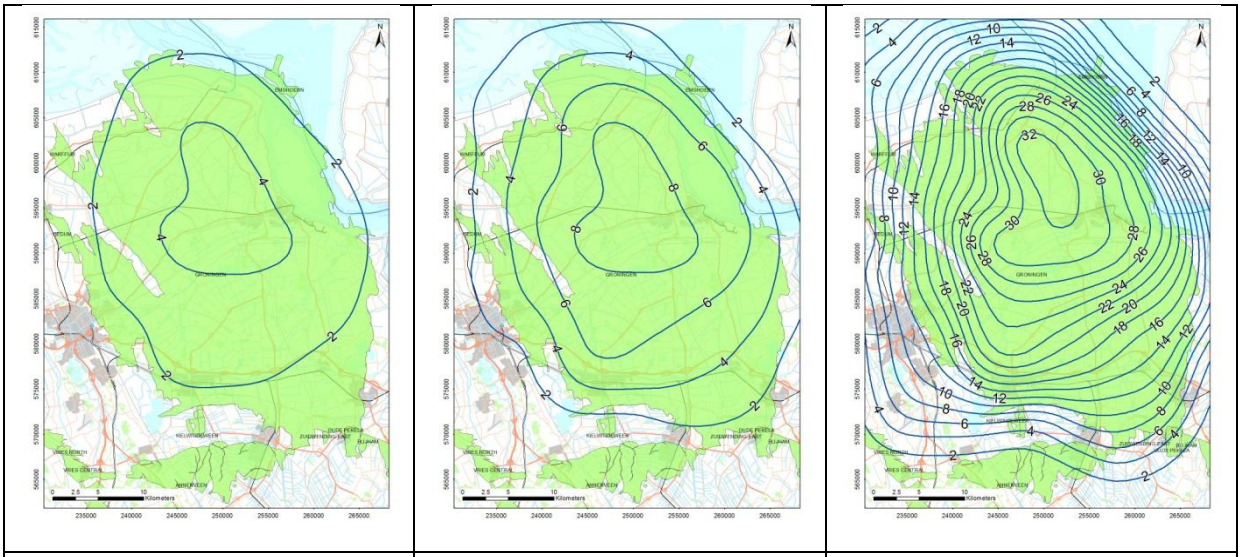

2013-2018	2013-2023	2013-2080

Figure 4.35 Development through time of the prognosed subsidence based on the isotach compaction model, and using the laboratory measured Cm value.

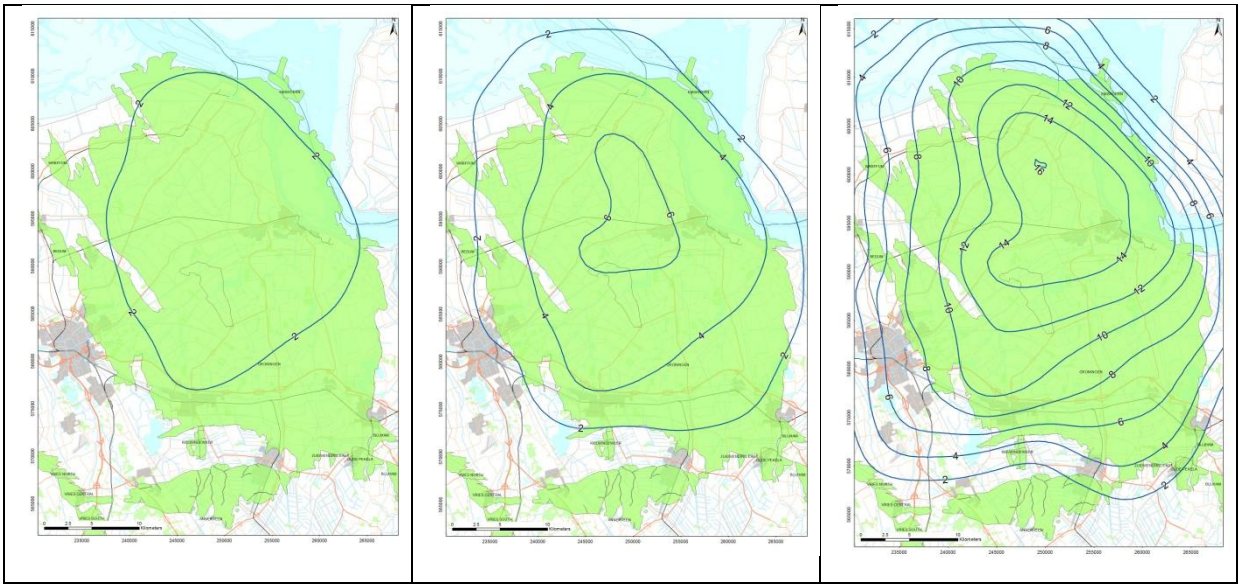

2013-2018	2013-2023	2013-2080

Figure 4.36 Development through time of the prognosed subsidence based on the isotach compaction model, and using the Cm values determined by calibration with the time decay model.

The future prognosis of the various compaction models leads to similar results when using the same Cm-porosity relationship. Only the Isotach model using the higher laboratory Cm value results in a much higher subsidence. This case his considered to represent a "worst case" prognosis.

4.8 References

Breunese, J.N, van Eijs R.M.H.E., de Meer, Kroon I.C. (2003). Observation and prediction of the relation between salt creep and land subsidence in solution mining – The Barradeel case. Proc. SMRI Conf., Chester, UK.

de Waal, J.A. (1986). On the rate type compaction behaviour of sandstone reservoir rock. PhD thesis, Technische Hogeschool, Delft.

E.J. den Haan, Het a,b,c –Isotachenmodel: hoeksteen van een nieuwe aanpak van zettingsberekeningen, Geotechniek, oktober 2003

Geertsma, J. (1973) , Land Subsidence Above Compacting Oil and Gas Reservoirs, J. Petr. Tech., pp.734-744.

Geertsma, J. and van Opstal, G. (1973). A Numerical Technique for Predicting Subsidence Above Compacting Reservoirs, Based on the Nucleus of Strain Concept. *Verh. Kon. Ned. Geol. Mijnbouwk. Gen.*, 28, pp. 63-78.

Hanssen, R. F. (2001), Radar Interferometry: Data Interpretation and Error Analysis, Kluwer Academic Publishers, Dordrecht.

Heard, H.C. (1972). Steady-state flow in polycrystalline halite at pressure of 2 kilobars. AGU Geophysical Monograph Series, 16: pp. 191-210.

J.P. Pruiksma, J.N. Breunese, K. van Thienen-Visser (2013) A general framework for rate dependent compaction models for reservoir rock. TNO 2013 R11405

Ketelaar, V. (2009), Satellite radar interferometry – subsidence monitoring techniques, Springer, Dordrecht, ISBN 978-1-402-09427-9

Munson, D.E. (1979). Preliminary Deformation-Mechanism Map for Salt (with Application to WIPP). SAND79-O076, Sandia National Laboratories.

Munson, D.E., and P.R. Dawson. (1979). Constitutive Model for the Low Temperature Creep of Salt (with Application to WIPP). SAND79-1853, Sandia National Laboratories.

NAM (2010) *"Bodemdaling door Aardgaswinning –NAM-velden in Groningen, Friesland en het Noorden van Drenthe– Status Rapport 2010 en Prognose tot het jaar 2070"* (EP201006302236)

NAM (2011a). Subsurface Technical Report Subsidence Modelling of Ameland Fields. UIE Report No: EP201105208617

NAM (2011b). Subsurface Technical Report Subsidence Modelling of Anjum and Waddenzee Fields. UIE Report No: EP201105208677

Spiers, C.J. & Carter, N.L.(1998) Microphysics of rocksalt flow in nature. In: M. Aubertin & H.R.Hardy (eds.) The Mechanical Behaviour of Salt: Proceedings of the Fourth Conference Serieson Rock and Soil Mechanics, 22, TTP Trans Tech Publications, Clausthal-Zellerfeld, pp.115-128.

Spiers, C. J., J. L. Urai, G. S. Lister, J. N. Boland, and H. J.Zwart. (1986). The influence of fluid-rock interaction on the rheology of salt rock: Nuclear Science and Technology,EUR 10399 EN, 131 p.

Weertman, J. (1955). Theory of steady-state creep based on dislocation climb. J. Appl. Phys. 26 (10), 1213–1217.

5 Illustrative examples of induced seismicity from other locations

5.1 Introduction

The largest earthquakes are associated with tectonic movements but earthquakes of small and intermediate magnitude can, in some cases, be induced by human activities. Induced seismicity has been linked to mining, the filling of (surface) reservoirs and engineering operations for oil and gas extraction, geothermal energy production and waste fluid disposal. Current seismicity observed in the North of the Netherlands is generally accepted as being induced by gas production from the Northern gas fields – Groningen and others.

In section 6.2 the geomechanics underlying production induced seismicity is discussed. The magnitude of the resulting earthquakes will be determined by the size of the slip plane, the amount of slip occurring and the rock properties. The amount of seismic energy radiated will also be dependent on the change in stress which occurs or, equivalently, the speed of propagation of the earthquake rupture across the fault plane. Modern theories of friction (Scholz 1998) explain and distinguish between the unstable so-called stick-slip motion on faults characterizing earthquakes and stable sliding or creep motion by which stresses can be released without seismicity.

In some cases it is possible that pore pressure changes and compaction or inflation could trigger the release of pre-existing stress in the subsurface – this scenario is sometimes referred to as triggered seismicity in recognition of the fact that the stresses being released are not solely due to the triggering process itself. Triggered seismicity might be expected in tectonically active areas of the world.

Reviews of induced seismicity have been presented in the open literature by (among others) Guha (2000), Suckale (2010), Klose (2013) and the Committee on Induced Seismicity Potential in Energy Technologies (2013). These reviews present lists of known cases coming from the oil and gas industry and other energy industry sectors such as geothermal and hydroelectric power production. It is clear from these lists that although Groningen is one of the better known cases of a gas field exhibiting induced seismicity it is by no means the only such field. In the majority of cases however, oil and gas production appears to proceed without any observed induced seismicity.

The following paragraphs give a brief summary of some of the more relevant cases of induced seismicity documented in the open literature. A similar summary can be found in Dost and Kraaijpoel (2013). The cases chosen below are discussed as being illustrative of certain relevant aspects of inducd seismicity. It should however be emphasized that none of the known cases is analogous to the Groningen field in every respect (geological setting, lithology, size, etc.) and as such there is a limit to the applicable lessons which can be learned from the study of analogues. The purpose of this summary of other cases is to place the Groningen field example in a broader seismological context and so show that Groningen's induced seismicity is not without precedent.

5.1.1 Gazli

The most extreme case known of seismicity associated with gas production is from the Gazli field in Uzbekistan: between 1962 and 1984 a number of earthquakes with magnitudes of up to about 7 occurred on a large thrust fault complex, to the NE of the field (Simpson and Leith 1985, Grasso 1992 and Amorèse et al 1995). Details given in the literature are limited but it is generally quoted as an example of induced seismicity. It could however be argued that the earthquakes may have been tectonic in origin, possibly triggered by production of the gas field. While the true nature of the Gazli events will probably remain open for debate it should be seen as an illustration of the possible scale of induced or triggered seismic events.

5.1.2 Lorca

In 2011 a shallow (about 3km) magnitude 5.1 earthquake occurred close to the Spanish town of Lorca, apparently triggered by prolonged ground water extraction (Avouac 2012). Much damage was done to buildings and there were 9 deaths. Although not an example associated with extraction of hydrocarbons, this case does show that moderate magnitude induced or triggered earthquakes can cause significant damage at surface if sufficiently shallow.

5.1.3 Rotenburg

In 2004 a magnitude 4.4 event occurred at a depth between 5 and 7 km, probably induced by gas production from the nearby Söhlingen or Rotenburg gas fields in Germany where the depth of the Rotliegend reservoir is 4.5 – 5 km (Dahm et al. 2007). Also being Rotliegend gas fields, Rotenburg and Söhlingen are particularly relevant examples, but their sizes are not comparable to the Groningen field.

5.1.4 Lacq

At the Lacq gas field in Southern France more than 2000 local events with magnitudes of up to 4.2 were detected using two permanent local seismic networks between 1974 and 1997 (Bardainne et al 2008). Larger events with magnitude up to 5.7 sometimes attributed to the field (Klose 2013) are more likely natural seismicity associated with the tectonics of the Pyrenees, some 20 – 30km farther to the South (Dost and Kraaijpoel 2013, Segall et al 1994 and Bardainne et al 2008 but see also Grasso 1992; Klose 2013 does not distinguish between induced and triggered events). Although Lacq is another gas field exhibiting significant levels of induced seismicity it is not a good analogue for Groningen given the differences in tectonic setting (close to a mountain range) and lithology (the reservoir is a carbonate).

5.1.5 Yibal

This field in Oman comprises a producing gas reservoir undergoing significant pressure depletion and compaction (surface subsidence rates up to 50 mm per year are observed), and a deeper producing oil reservoir under water flood. Integrated interpretation of geodetic data (InSAR and GPS) and passive seismic data (from both deep down-hole and shallow buried arrays) has lead to the recognition that major fault systems crossing the field are being reactivated by depletion of the gas reservoir leading to differential compaction across faults (Bourne et al 2006). Large numbers of induced microseismic events have been detected with relatively high magnitudes (two-thirds of all located microseismic events are larger than magnitude -1.5) and some of the largest events have been felt at surface. The data shows that fault slip is not limited to the depleting gas reservoir interval but extends significantly above and below below this.

5.1.6 Ekofisk

Ekofisk is a Norwegian North Sea oil field which has experienced significant sea bed subsidence (more than 8m at the crest of the structure – see Ottemöller et al 2005) due to production from the initially over-pressured chalk reservoir. A magnitude 4.4 earthquake occurred on 7th May 2001 and was strongly felt on platforms in the area but did not cause damage to facilities or wells. Detailed analysis revealed (Ottemöller et al 2005) that the event appears to have been induced by accidental fluid injection into the overburden, rather than directly by the reservoir compaction itself.

5.1.7 Fashing

Observed events in the Fashing field in Texas of up to magnitude 4.3 are considered to be induced by oil and gas production from the Edwards Limestone formation (Keahey 1968) reservoir at a depth of about 3400m (Klose 2013, Davis et al 1995 and Frohlich 2012). On 20th October 2011 a larger, magnitude 4.8 earthquake occurred near Fashing. This event's possible origins are complicated by the fact that there are fluid disposal wells within a few km of the reported event location.

5.1.8 Other hydrocarbon fields in the Netherlands

Of the approximately125 producing hydrocarbon fields in the Netherlands only 23 are known to be seismically active (van Thienen-Visser et al., 2012). Besides Groningen, only in two other fields, i.e.

Bergermeer and Roswinkel, events with magnitude of 3.0 and above (up to M=3.5) have ocurred. Van Eijs et al (2006) argue that fault density, pressure depletion and stiffness contrast between the reservoir and seal rocks are the key parameters which correlate with the occurrence of observed seismicity in the hydrocarbon fields in the Netherlands.

5.2 Concluding remarks

Referring to tables 5.1 and 5.2 in section 5.4 which summarize the known cases of induced seismicity in the Shell Group, it can be seen that felt seismicity induced by oil or gas extraction is rare, at least in the Shell Group's portfolio. Detailed analysis of the many apparently aseismic cases would be required to understand this in terms of the rock and fault properties and production histories. The potential for induced seismicity, particularly in and around the gas fields in the North of the Netherlands, is however properly recognized.

5.3 References

Amorèse, D., Grasso, J.-R., Plotnikova, L.M., Nurtaev, B.S. and Bossu, R. Rupture Kinematics of the Three Gazli Major Earthquakes from Vertical and Horizontal Displacements Data. Bulletin of the Seismological Society of America (1995), Vol. 85, No. 2, pp. 552-559.

Avouac, Jean-Philippe. Earthquakes: Human-induced shaking. Nature Geoscience (2012) 5: 763–764.

Bardainne, T., Dubos-Sallée, N., Sénéchal, G., Gaillot, P. and Perroud, H. Analysis of the induced seismicity of the Lacq gas field (Southwestern France) and model of deformation. Geophys. J. Int. (2008) 172, 1151–1162.

Bourne, S.J., Maron, K., Oates, S.J. and Mueller, G. Monitoring Reservoir Deformation on Land - Evidence for Fault Re-Activation from Microseismic, InSAR, and GPS Data. 68th EAGE Conference & Exhibition (2006).

Committee on Induced Seismicity Potential in Energy Technologies. Induced Seismicity Potential in Energy Technologies. The National Academies Press (2013).

Davis, S. D., Nyffenegger, P. and Frohlich, C. The 9 April 1993 earthquake in south-central Texas: Was it induced by fluid withdrawal? Bulletin of the Seismological Society of America (1995), 85 1888-1895.

Dahm, T., Krüger, F., Stammler, K., Klinge, K., Kind, R., Wylegalla, K. and Grasso, J.-R. The 2004 Mw 4.4 Rotenburg, Northern Germany, Earthquake and Its Possible Relationship with Gas Recovery. Bulletin of the Seismological Society of America (2007), Vol. 97, No. 3, pp. 691–704.

Dost, B. and Kraaijpoel, D. The August 16, 2012 earthquake near Huizinge (Groningen). KNMI report, KNMI De Bilt, January 2013.

Frohlich. C. Induced or triggered earthquakes in Texas: assessment of current knowledge and suggestions for future research. University of Texas at Austin Technical Report G12AP20001 (2012).

Grasso, J.R. *Mechanics of Seismic Instabilities Induced by the Recovery of Hydrocarbons*. Pure and Applied Geophysics, Vol. 139, No. 3/4 (1992)

Guha, S. K. Induced earthquakes. Kluwer (2000).

Keahey, R.A. Fashing Field, Atascosa-Karnes Counties, Texas. In Natural Gases of North America, Volume One, AAPG Special Volumes (1968).

Klose, Christian D. Mechanical and statistical evidence of the causality of human-made mass shifts on the Earth's upper crust and the occurrence of earthquakes. Journal of Seismology (2013) 17: 109–135.

Ottemöller, L., Nielsen, H. H., Atakan, K., Braunmiller, J. and Havskov, J. The 7 May 2001 induced seismic event in the Ekofisk oil field, North Sea. Journal of Geophysical Research (2005), Vol. 110, B10301.

Scholz, Christopher H. Earthquakes and friction laws. Nature (1998) 391(1st January 1998): 37-42.

Segall, P., Grasso, J.-P. and Mossop, A. Poroelastic stressing and induced seismicity near the Lacq gas field, southwestern France. Journal of Geophysical Research (1994), Vol. 99, B8, pp. 15,423 – 15,438.

Simpson, D.W. and Leith, W. The 1976 and 1984 Gazli, USSR, earthquakes – were they induced?

Bulletin of the Seismological Society of America (1985), Vol. 75, No. 5, pp. 1465-1468.

Suckale, Jenny. Moderate-to-large seismicity induced by hydrocarbon production. The Leading Edge March (2010): 310 – 319.

Thienen-Visser, K. van, et al. (2012). *Deterministische hazard analyse voor geïnduceerde seismiciteit in Nederland.* TNO-rapport 2012 R10198.

Van Eijs, R.M.H.E., Mulders, F.M.M., Nepveu, M., Kenter, C.J. and Scheffers, B.C. Correlation between hydrocarbon reservoir properties and induced seismicity in the Netherlands. Engineering Geology (2006) 84: 99-111.

5.4 Tables

The following tables summarize the known cases of induced seismicity in the Shell Group. Table 5.1 lists the cases in which ***felt*** seismicity is known (or, in the case of Belridge, considered likely) to be induced by oil or gas extraction from fields in the Shell portfolio.

Table 5.1 Cases of felt induced seismicity in the Shell portfolio

Region/location/OU	Field	Largest recorded event (M)	Type	Comments (Mitigation etc.)
Netherlands (NAM)	Groningen	3.6 (Huizinge)	Induced by gas production	Seismic monitoring
	Other gas fields (20% of all Dutch gas fields, particularly Annerveen, Eleveld & Roswinkel)	3.4 (Roswinkel)	Induced by gas production	Roswinkel Field abandoned
Gas production leads to compaction inducing earthquakes with normal fault mechanisms				
Oman (PDO)	Yibal	≥2.24	Induced by oil & gas production	Seismic monitoring
Gas & oil production cause differential compaction reactivating Graben faults crossing field				
Germany	Rotenburg (partners via BEB)	4.4	Induced by gas production	Seismic monitoring
Normal faulting events at or below reservoir level, considered to be induced by gas production				
California	Belridge (AERA)	No seismic/earthquake data available	Water flooding & cyclic steaming for production from diatomite	InSAR & microseismic monitoring
Production from diatomite results in significant subsidence – (felt) induced seismicity is to be expected				

Table 5.2 lists the geothermal cases in which Shell was involved and in which ***felt*** induced seismicity occurred – these were JVs of which we are no longer a part but which have been well-documented in the literature.

Table 5.2 Historic Shell involvement in geothermal joint ventures with well documented felt induced seismicity

Region/location/OU	Field(s)	Largest recorded event (M)	Type	Mitigation
El Salvador	Berlín	>3	Fluid injection/fraccing	Seismic monitoring and traffic light system
France (Alsace)	Soultz-sous-Forêts	>3	Fluid injection/fraccing	Seismic monitoring

6 Release of energy by Earthquakes

6.1 Analysis of the induced earthquake record

6.1.1 Frequency-magnitude distribution

Since the first earthquake recorded in the north of the Netherlands in December 1986, KNMI has compiled a steadily growing catalogue of earthquakes. At the time of writing their report, Dost et al. (2012) commented that the catalogue for the north of the Netherlands contained 640 events. The following analysis is restricted to the 187 events with a magnitude of at least 1.5 recorded between 1st April 1995 and 30th October 2012. This start date corresponds to the earliest date for which the monitoring network was capable of locating all earthquakes of at least magnitude 1.5. This end date reflects the data available when technical studies commenced following the magnitude 3.6 Huizinge earthquake in August 2012.

Throughout this report we will refer to moment magnitude and local magnitude interchangeably because KNMI asserts the local magnitude scale is essentially indistinguishable from the moment magnitude over the observed magnitude range within a 95% confidence interval of ±0.2. However, this correspondence is subject to an ongoing further investigation by KNMI (Dost & Kraaijpoel 2013) and may be revised in the near future.

The number of observed earthquakes, N of at least magnitude, M, within a given region and period of time follows the log-linear frequency-magnitude relationship known as the Gutenberg-Richter law (Gutenberg & Richter 1954):

$$\log_{10} N(M) = a - bM \tag{6.1}$$

The b parameter, known as the b-value, describes the relative decline in abundance of larger magnitude earthquakes relative to smaller ones and is therefore central to estimating the probability of larger earthquakes occurring from an observed population of smaller earthquakes. Consider a monitoring system that reliably observes all earthquakes within a given region of at least magnitude M_c (known as the magnitude of completeness). If the b-value and M_{min} remain unchanged, the probability, p_1, that the next independent observable earthquake exceeds magnitude M is:

$$p_1 = 10^{-b(M-M_c)} \tag{6.2}$$

For a future sequence of n independent observable earthquakes, it follows that the probability, p_n, of at least one exceeding magnitude M is:

$$p_n = 1 - (1 - p_1)^n \tag{6.3}$$

This probability depends on the b-value. Various different methods for estimating the b-value from the 187 earthquakes within the Groningen Field all agree that b = 1.0 (Bourne & Oates 2012). Figure 6.1 compares this frequency-magnitude model with its 95% confidence interval to the observed frequency-magnitude distribution. Notice how the confidence interval is disproportionately larger for the rarer and larger magnitude events that are the least well sampled within the catalogue. Consequently, although the differences between this model and the observations are greatest for the larger magnitude events, none of these differences is statistically significant given the small number of such events within the catalogue.

Monte Carlo analysis to investigate the range of different b-values consistent with these data indicate a 68% chance of $0.85 < b < 1.26$ and a 95% chance of $0.68 < b < 1.5$. Dividing these earthquakes into subsets corresponding to different time intervals shows there was no statistically significant variations in b-value with time.

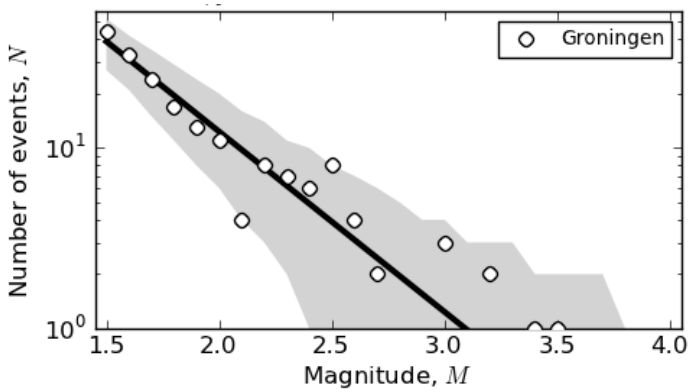

Figure 6.1 *The frequency-magnitude distribution of earthquakes observed in the Groningen Field. Circles denote the number of earthquakes within the magnitude interval M-0.05 to M+0.05. The thick black line denotes the frequency-magnitude model of b=1.0. Grey shading denotes the 95% confidence region associated with this model.*

Earthquake populations are generally observed to follow the Gutenberg-Richter frequency-magnitude distribution between lower and upper magnitude limits. The lower magnitude limit is typically the magnitude of completeness, M_c. An upper bound, M_{max}, on the frequency-magnitude distribution must also occur since arbitrarily large events are physically impossible. Determination of such an upper bound from an earthquake catalogue is however challenging because of the invariably poor statistics at the high magnitude end of the distribution. Figure 6.2 shows an example of a truncated frequency-magnitude model estimated from the observed frequency-magnitude distribution. This model is consistent with the data but so are all other truncated models for M_{max} > 3.9 including the initial model without any truncation. Consequently, given the available data, frequency-magnitude analysis cannot establish a reliable upper magnitude limit. This remains true even for all earthquakes within all gas fields in the north of the Netherlands (Bourne & Oates 2012).

The maximum magnitude estimates of 3.2 to 3.9 from de Crook et al. (1995) and the subsequent KNMI reports (de Crook et al., 1998; van Eck et al., 2006; Dost et al., 2012) obtained by fitting a truncated frequency-magnitude model to the observed frequency-magnitude distribution all appear to share a similar statistical error of over-fitting the model to the observed number of larger magnitude events by ignoring the wider confidence interval of the models, as illustrated in Figure 6.2.

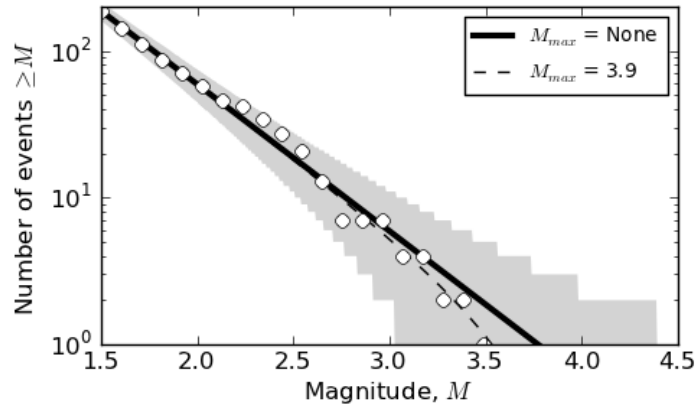

Figure 6.2 *The cumulative frequency-magnitude distribution of earthquakes observed in the Groningen Field. Circles denote the number of earthquakes of at least magnitude M. The thick black line denotes the frequency-magnitude model of b=1.0. Grey shading denotes the 95% confidence region associated with this model. The dashed line denotes an alternative frequency-magnitude model with b=1.0 and zero probability of earthquakes above magnitude 3.9.*

Table 6.1 and Figure 6.3 show that the probability of at least one earthquake exceeding magnitude 4 or 5 increases as the number of independent events of at least magnitude 1.5 increases in the future. These estimates are subject to three conditions. First, the *b*-value remaining invariant with time so that the present

range estimated from the historic data remains valid for future earthquakes. Second, minimum magnitude of reliable earthquake monitoring does not exceed magnitude 1.5 for any reason over time. Third, the probabilities only apply to the number of independent future earthquakes and these should not include any dependent earthquakes such as aftershocks. Under these assumptions, the probability of at least one earthquake exceeding local magnitude 4 during the next 30 locatable earthquakes within the Groningen Field is 0.09 with a 68% confidence limit of 0.02 to 0.20.

There is no reliable empirical evidence to support a maximum magnitude as low as 3.9 from the earthquake catalogue for the Groningen Field. Consequently, larger earthquakes are possible rather than impossible as recognized by earlier studies (de Crook et al., 1998; Wassing et al., 2004; van Eck et al., 2004; van Eck et al., 2006; Dost et al., 2012). This does not mean that there is no physical limit to the maximum possible magnitude (see section 6.1.2), but rather the seismological data under consideration here fail to provide any such constraint.

Magnitude	Confidence	$n = 30$	$n = 200$	$n = 400$	$n = 800$
$M \geq 4$	$p =$	0.09	0.47	0.72	0.92
	68%	0.02-0.20	0.13-0.78	0.25-0.95	0.43-1.00
	95%	0.01-0.45	0.03-0.98	0.07-1.00	0.13-1.00
$M \geq 5$	$p =$	0.01	0.06	0.12	0.22
	68%	0.00-0.03	0.01-0.19	0.02-0.35	0.03-0.57
	95%	0.00-0.12	0.00-0.57	0.00-0.81	0.00-0.96

Table 6.1 *Probability estimates for the occurrence of at least one earthquake of at least magnitude M within the next n events of at least magnitude 1.5. The probability, p, is based on a b-value of 1.0. The 68% and 95% confidence intervals for these probabilities reflect the corresponding confidence intervals in the b-value estimate of 0.85 to 1.26 and 0.68 to 1.50 respectively.*

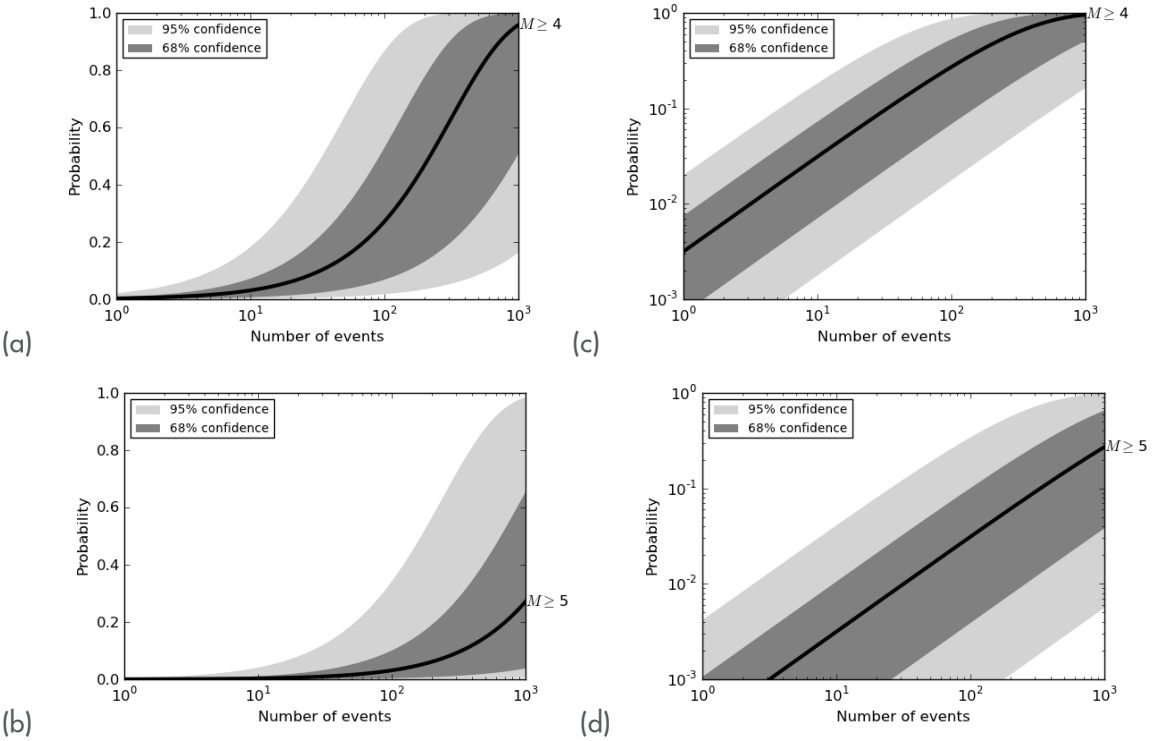

Figure 6.3 *(a, b) Estimates for the probability of the occurrence of at least one earthquake within the Groningen Field with a magnitude of at least 4 and 5 respectively. (c, d) The same as (a, b) except probabilities are shown on a log-scale. These are based on Table 6.1.*

6.1.2 Physical limits on the maximum magnitude

In the analysis presented herein, it is assumed that all past and future earthquakes in the Groningen Field are induced, by which it is understood that they are caused directly and entirely by anthropogenic activity (i.e., gas extraction). The possibility of triggered earthquakes is not currently envisaged in the model. Triggered earthquakes require that there are faults close to being critically stressed on which seismic slip is imminent. For the seismicity model developed for the Groningen field, triggered seismicity is excluded on the basis of the apparently very low natural seismicity, as revealed by both the instrumental and historical records for the region. Houtgast's (1992) catalogue of historical earthquakes in the Netherlands lists only one event – on 28th January 1262 – in the north of the Netherlands. The historical record is however unclear about the true nature of this event which may in fact have been a meteorological event rather than an earthquake. The currently very low levels of natural seismicity in the northern Netherlands makes it reasonable to assume that the field is free from incipient natural earthquakes caused by significant fault ruptures.

There will be an upper bound to the maximum magnitude of earthquakes that can be induced by gas production from the Groningen Field due to the finite elastic energy or strain associated with reservoir compaction or the finite size of pre-existing faults. Estimates of these limits for the Groningen Field indicate a maximum magnitude of M=6.5 if all strain accumulated over the life cycle of the field were released in a single event at the very end of field life. Although an event of this size may be physically possible, the probability of this to happen is essentially zero. Therefore, this magnitude represents an absolute physical upper limit.

6.1.3 Finite strain limit

An earthquake is an abrupt slip on a fault surface as one side of the fault moves relative to the other. This process releases elastic strain energy stored in the region surrounding the fault by transferring strain from that region and localizing it along the fault. The largest possible induced earthquake corresponds to releasing all the elastic strain associated with the ultimate reservoir compaction in a single event that involves simultaneous slip on many faults.

One measure of the size of an earthquake is seismic moment. This is simply the product of the average slip on the fault, the area that slipped, and the shear modulus which is a material constant describing the shear stiffness of the surrounding medium. A mathematical consequence of this definition is that the average strain due to slip on faults within a given volume is simply proportional to the total seismic moment per unit volume (Kostrov 1974). In the particular case of reservoir compaction, this means the total seismic moment is equal to the product of the bulk reservoir volume decrease and the shear modulus (McGarr 1976). Given the current linear elastic model for ultimate reservoir compaction, the expected ultimate bulk reservoir volume decrease is about 3.3 x 10^8 m^3. For a representative shear modulus of 10^{10} Nm^{-2} (10 GPa) the maximum total seismic moment that could be mobilized is 7.7 x 10^{18} Nm.

The relationship between the magnitude, M, and the seismic moment, M_o, takes the form

$$\log_{10} M_o = c + dM \qquad (6.4)$$

where typically c = 9.1 and d = 1.5 (Hanks & Kanamori 1979). So if the maximum seismic moment were released during a single earthquake, this would be equivalent to a magnitude 6.5. Alternatively, if this total seismic moment were released by a population of individual earthquakes with a b-value of 1, then the expected largest earthquake would still be about magnitude 6.3 as the largest event is expected to release about half the total seismic moment (Bourne & Oates, 2013).

6.1.4 Finite fault size limit

If future earthquakes are required to fit within the existing size of known faults then the largest of these faults would limit the maximum magnitude. This approach was previously used to yield estimates for the maximum magnitude of 3.9 for gas fields in the north of the Netherlands (Crook et al. 1998; Muntendam-

Bos et al. 2008). In reviewing this second study, Hager & Toksöz (2009) concluded the maximum magnitude estimate depended entirely on an uncertain choice for the maximum fault slip area, although the result of magnitude 3.9 was considered acceptable given its exact agreement with the maximum magnitude obtained from frequency-magnitude analysis of the historic earthquakes (van Eck et al., 2006). However, this result subsequently proved unreliable for the reasons described in section 6.1.1.

A magnitude 4 event may occur on an equi-dimensional fault surface of no more than 1.1 km by 1.1 km for a 1 MPa stress drop and a fault slip of 90 mm (Bourne & Oates 2013). The fault height is poorly constrained in the Groningen field. Nevertheless, there are numerous pre-existing faults substantially larger than this mapped within the Groningen Field that could be associated with a fault slip area larger than 1.21 km^2 (see Fig. 2.3). Consequently any argument based on the lack of sufficiently large pre-existing fault surfaces cannot reliably constrain the maximum magnitude to be as low as *M*=4.

An alternative method is to infer the maximum slip area from estimates of the maximum slip and the minimum stress drop (Bourne & Oates 2013). Although the maximum displacement is bound not to exceed the maximum reservoir compaction, the minimum stress drop assumption of 1 MPa remains somewhat uncertain. The resulting maximum magnitude estimate of 5.8 corresponds to a mean fault slip of 0.3 m on a 60 km long fault spanning the long-axis of the field with a dip extent of 3000 m. The aspect ratio of this slip surface is 20:1 which is large but not impossible given the range of aspect ratios observed for normal dip-slip earthquakes (e.g. Leonard, 2010). There is no geomechanical requirement for the slip area to remain inside the reservoir, although the Zechstein salt formation located directly above the reservoir may prevent fault slip initiating above the reservoir. Uncertainty about the minimum stress drop means this maximum magnitude estimate is less reliable than the previous estimate based on finite strain.

6.1.5 Finite mass limit

Using a world-wide catalogue, Klose (2012) obtained a statistical correlation between the observed maximum magnitude of induced earthquakes and human-made mass shifts on the Earth's upper crust. For normal faulting regimes such as within the northern Netherlands the regression between observed magnitude and mass-shift obtained by Klose indicates an expected magnitude of 4.7 to 5 for a mass shift of 2 to 2.5 Gt corresponding to an ultimate gas production of 2800 x 10^9 m^3.

However, there is still substantial variation within the catalogue about this expected value so the upper bound for this mass-shift will be somewhat larger. Although Klose did not estimate an upper bound, based on the variation within the catalogue, a reasonable upper bound for the magnitude of an earthquake induced by a 2.5 Gt mass-shift within a normal faulting regime is about M= 6. Further restricting the catalogue to just those events due to gas extraction within a normal faulting regime the largest earthquake in Klose's catalogue is the 1967 M=5.7 Arette (Lacq gas field) event in France (Segall et al. 1994). However, it remains unclear if this event was induced by gas production or is part of natural seismicity associated with the Pyrenees.

6.2 The earthquake strain model

Reservoir pressure depletion induces reservoir compaction, and together they induce poro-elastic stress changes within and around the reservoir (Segall 1989). In some places the changes in the shear stress and the effective normal stress acting on a pre-existing fault may be sufficient to equal its resistance to slip due to its internal friction, cohesion, and initial stress state. Under these conditions the fault is critically stressed and destabilized with no further resistance to slip (see section 9 for further details). These places are then vulnerable to experiencing earthquakes. Within the reservoir normal faulting may be induced e.g. the Lacq field (Segall et al. 1994) and the Ekofisk field (Zoback & Zinke 2002). Outside the reservoir reverse faulting may be induced (Segall 1989). Within and outside the reservoir induced fault slip may localize along faults subject to differential compaction, *i.e.* more compaction on one side of the fault relative to the other side of the fault, *e.g.* the Eleveld field (Roest & Kuilman, 1994) and the Yibal field (Bourne et al. 2006).

By definition, critical stress is a necessary condition for induced seismicity but it is insufficient for two reasons. First, knowledge of the internal friction, cohesion, and initial stress state of each fault is uncertain and may vary considerably among individual faults. Second, even if a critical stress state is known it does

not determine the amount and area of slip on the fault which governs the magnitude of any induced earthquake.

The amount and area of slip on a critically-stressed fault depends on the average elastic strain within the surrounding medium. Slip on a fault may be viewed as a mechanism for accommodating strain. During fault slip some elastic strain within the surrounding medium is transferred to and localized along the fault as a displacement discontinuity. Consequently, the average strain accommodated by a population of faults that slipped is simply proportional to their total seismic moment per unit volume (Kostrov 1974). Knowledge of the strain field therefore places an upper bound on the total seismic moment of earthquakes induced under that strain field.

In the case of a compacting reservoir, the maximum total seismic moment scales with the bulk reservoir volume change (McGarr 1976) under conditions where lateral gradients in the vertical strain are negligibly small. This model represents the physical limit where slip on faults accommodates all induced strain. Equivalently the gravitational potential energy released by reservoir compaction and subsidence also scales with the bulk reservoir volume change and represents the physical limit where the mechanical work done by slip on faults cannot exceed the released gravitational potential energy that was stored by elastic deformations within and around the reservoir. The fault strain and the fault work descriptions are fundamentally equivalent. For convenience, let us continue to describe the earthquake model in terms of strain.

The observed total seismic moment may be significantly less than the maximum total seismic moment because not all strain may be accommodated by fault slip and not all fault slip may be seismogenic. For instance, elastic strains may remain in places where faults are not critically-stressed, ductile strains may occur depending on the rheology and the strain rate of the medium, and faults may creep without radiating seismic energy.

In the case of a compacting reservoir, subsidence measurements are able to reliably constrain a geomechanical model for reservoir compaction with a lateral resolution comparable to the reservoir depth. This means that sufficiently dense subsidence measurements are at best able to constrain the distribution of average reservoir compaction on a length-scale of about 3 km. Knowledge of the strain field provided by this geomechanical model places an upper bound on the total seismic moment of earthquakes induced by reservoir compaction.

The fraction of strain accommodated by seismogenic fault slip cannot yet be predicted by geomechanical models – but it can be measured in the field by comparing historic seismicity and subsidence observations.

6.2.1 Stress, compaction, faults and earthquakes

The current earthquake monitoring network is able to measure the epicenter of all earthquakes of at least magnitude 1.5 with a standard error of 500 m (Kraaijpoel et al. 2008). Due to the geometry of this network earthquake depths cannot in general be determined reliably and so event depth is routinely assigned to a reservoir depth of 3 km (Kraaijpoel et al. 2008).

Earthquake epicenters during the period 1995 to 2012 (Figure 6.4) were preferentially located within the central part of the field and were rare or absent elsewhere notably including the 100 km^2 south-east corner of the field. Let us now consider how this observed distribution of earthquake epicenters relates to the distribution of critical stress, reservoir compaction, and pre-existing faults within and around the reservoir.

Critical stress

The stress state inside the reservoir is the sum of the initial stress state and the stress change induced by gas production which essentially varies linearly with local reservoir pressure depletion. Pressure depletion is essentially uniform through most of the reservoir (Figure 6.4, left panel). Despite equivalent levels of pressure depletion in the central and south-east regions of the Groningen field, only the central region experienced seismicity. Both regions experienced similar stress changes, but only one experienced observed seismicity. One possibility is that the initial shear stress was less or the faults in the south-east are stronger and therefore still able to resist slip. These are unlikely given the geological history, fault density

and fault orientations are indistinguishable from the central region. Alternatively it seems generally more plausible that some faults within the south-east were destabilized and seismogenic too. However, given the relatively low levels of reservoir compaction in this area, the amount of slip on these faults is so small that the associated earthquakes remain below the earthquake monitoring threshold of magnitude 1.5 and so remained undetected. Critically stressed faults are then a necessary but insufficient condition for observable seismicity within the Groningen Field.

Compaction and differential compaction

At any location within the reservoir, the average shear strains induced by reservoir compaction are primarily dependent on the average local reservoir volume change. Lateral gradients in vertical strain may also contribute, particularly the larger gradients that might exist due to differential compaction on either side of pre-existing faults (e.g. Rest & Kuilman 1994).

Figure 6.4 compares the reservoir volume change per unit area (*i.e.* average reservoir compaction) and lateral compaction gradients present with the current reservoir compaction model with the observed earthquakes. Earthquake epicenters preferentially occurred within the places of greater reservoir compaction (Figure 6.4, centre panel), but there is no evidence of similar clustering along the fault bound lineaments associated with the greatest compaction gradients in the model or indeed any particular mapped faults (Figure 6.4, right panel). Given the standard error of 500 m in epicenter locations (Kraaijpoel et al., 2008) it remains uncertain if all true epicenters are located on mapped faults. Equally, because the subsidence data are not sensitive to compaction gradients localized across faults, the true distribution of compaction gradients remains uncertain.

The amount and sense of induced slip depends on the detailed geometry of the intersection between the fault and the reservoir (e.g. Mulders 2003) but scales with reservoir compaction. Given the detailed geometries of reservoir-fault intersections are largely uncertain it is reasonable to assume any variability in these geometries is uniformly distributed throughout the reservoir. Under these circumstances, the faults most likely to experience greatest differential compaction are those located in the region of greatest reservoir compaction. Consequently, without additional detailed information about the distribution and geometry of reservoir-fault intersections, the differential compaction model is equivalent to the earlier strain model (Kostrov 1974; McGarr 1976). The upgraded earthquake monitoring network may yield better information about the relationship between induced seismicity, mapped faults, and differential reservoir compaction.

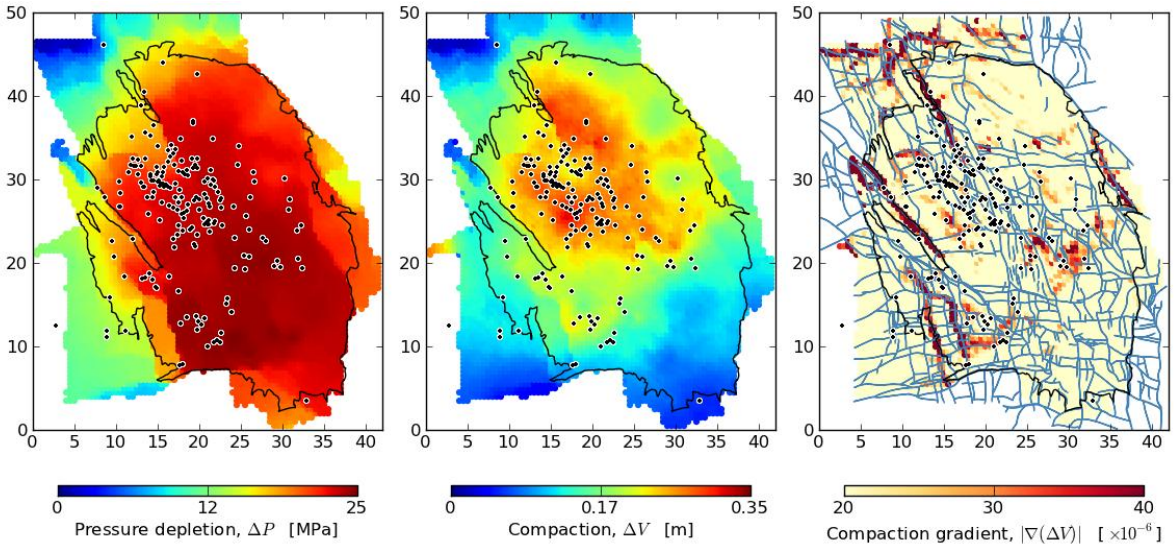

Figure 6.4 *The locations of $M \geq 1.5$ earthquakes between 1995 and 2012 in relation to reservoir pressure depletion, reservoir compaction, and compaction gradients from 1957 to 2012.*

6.2.2 Earthquakes and gas production

Total seismic moment and gas production

The fraction of induced strain accommodated by seismogenic fault slip within the Groningen Field is central to assessing future seismicity on the basis of future gas production and reservoir compaction. Let us call this the fault strain partition fraction, or α. The behavior of this partition fraction may be appreciated by comparing the total observed seismic moment with that expected from the strain model as a function of cumulative gas production since April 1995 (Figure 6.5). The observed total seismic moment at the end of this period is about 10^{15} Nm. However given the change in reservoir compaction over the same period, the total seismic moment expected if all this strain had been accommodated by seismogenic slip on faults, *i.e.* $\alpha = 1$, is about 2×10^{18} Nm. Clearly, most of the strain was not accommodated by earthquakes and the observed partition fraction is extremely small at $\alpha = 5 \times 10^{-4}$, or 1 part in 2000. However, Figure 6.5 also indicates that this partition factor may have increased with production over the period by a factor of 5 from an initial value of about $\alpha = 2 \times 10^{13}/2 \times 10^{17} = 10^{-4}$. If this trend is real and sustained then it represents an escalation in the expected total seismic moment released per unit gas production.

Due to the stochastic nature of earthquakes, the observed total seismic moment of 187 events with a *b*-value of 1 might equally have taken a different value. The probability distribution of these different values is a Pareto sum distribution (Zaliapin et al. 2005). A notable feature of this distribution is the extremely skewed distribution of confidence bounds around the median, for example the 95% confidence interval shown in Figure 6.5 extends from just below the median to a factor of 100 above. Consequently this apparent trend of increasing total seismic moment per unit gas production is not yet statistically significant as a strain model with constant partitioning ($\alpha = 5 \times 10^{-4}$) does not yet fall outside the 95% confidence interval. Nonetheless, it is appropriate to be conservative about this uncertainty and to recognize the possibility that the partitioning factor may continue increasing with production.

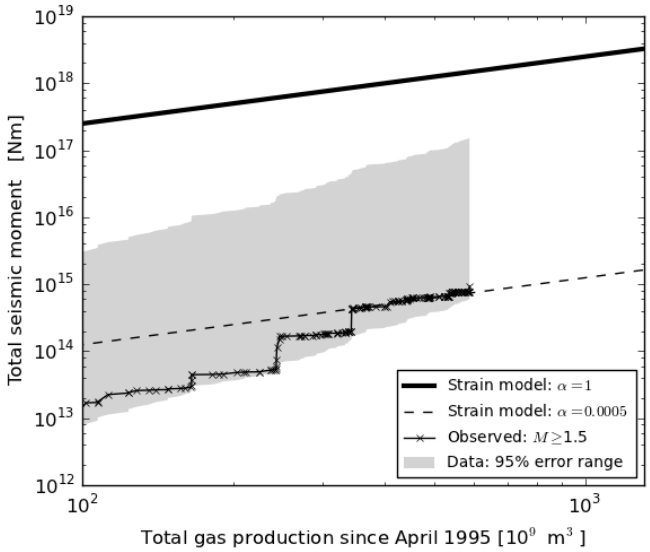

Figure 6.5 *Total observed seismic moment from M≥1.5 events since April 1995 as a function of total gas production since April 1995. The observed trend suggests the expected total seismic moment per unit production increased. However, given the limited duration of this trend relative to the uncertainty, the significance of this trend is not yet clear.*

Activity rate and cumulative production

The number of M>1.5 events within a given interval of gas production, known as the activity rate, appears to have increased with cumulative production (Figure 6.6). A constant activity rate would appear as a straight line, but the data clearly indicate an increasing slope with cumulative production suggesting an increasing activity rate with cumulative production. However, the statistical significance of this apparent trend needs careful consideration. Due to the stochastic nature of earthquakes the appropriate statistical test is the Kolmogorov-Smirnov test for a homogeneous Poisson point process. This test is represented in Figure 6.6 by the 95% and 99% confidence intervals (solid grey lines) around the constant activity rate model (dashed grey line). If the data are not contained within these confidence bound then the model may be

rejected with that same confidence level. Figure 6.6 a clearly shows the data continuously outside the 99% confidence bound over the interval of normalized production from 0.3 to 0.6.

However, this analysis is based on all the events being statistically independent of each other. One standard test for event independence is that the distribution of waiting times between events should reflect random chance. However, the observed distribution of waiting times indicates an over-abundance of waiting times of less than three days (Bourne & Oates 2013). Repeating the Kolmogorov-Smirnov test after excluding these potentially correlated events yields a marginal result (Figure 6.6 b). The possible inter-dependence between some events clearly confuses the assessment of activity rates escalating with cumulative production.

In summary, the number of M≥1.5 events per unit gas production increased with cumulative production, but the number of independent events per unit gas production may have remained constant.

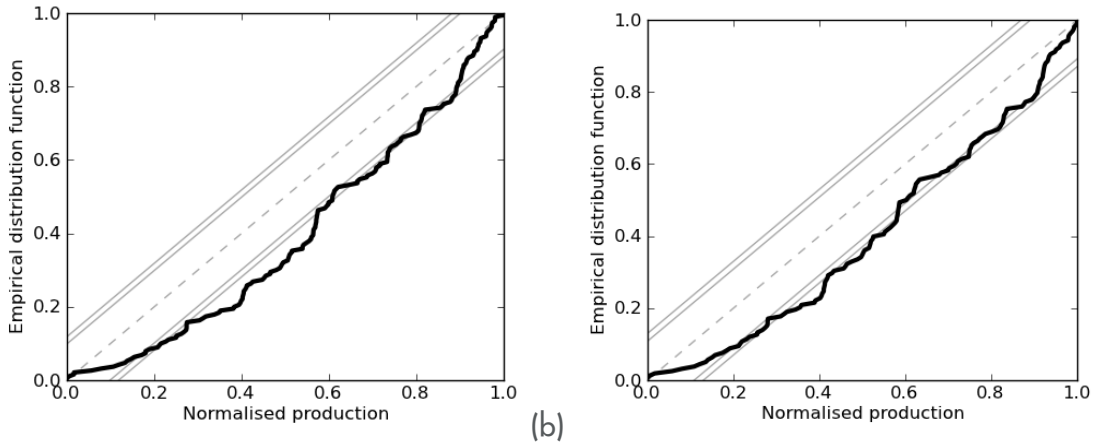

Figure 6.6 *The evidence for any increase in the number of earthquakes per unit gas production is weak due to uncertainty about event clustering. (a) The observed cumulative distribution of M≥1.5 event numbers with respect to production. The dashed grey line denotes the homogeneous Poisson process model, i.e. the expected number of events per unit production is constant. Solid grey lines denote the 95% and 99% confidence interval for this model according to the Kolmogorov-Smirnov test statistic. (b) As (a) except excluding events within 3 days of the previous event that are likely not independent.*

Activity rate and production rate

The The volume of gas produced between successive events, the inter-event gas volume, is simply the inverse of the activity rate. The inter-event gas volumes measured for the M ≥ 1.5 events from April 1995 to October 2012 when plotted against the rate at which those gas volumes were produced (Figure 6.7) do not show significant sensitivity to the historic variation in production rate, even allowing for the possibility of a 12 month delay between gas production and earthquake occurrence.

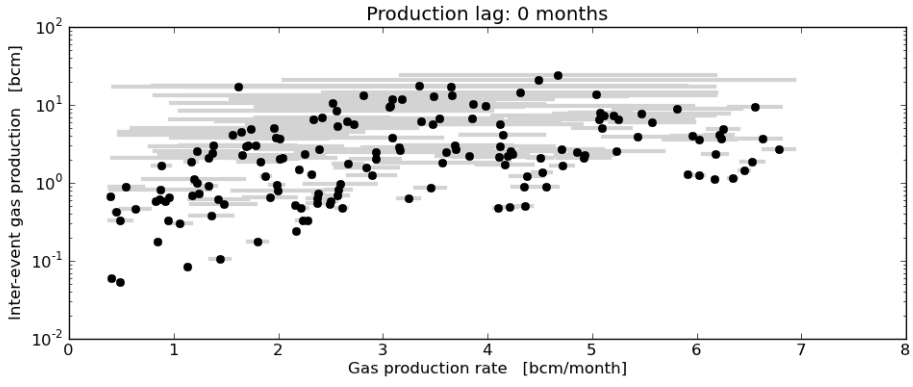

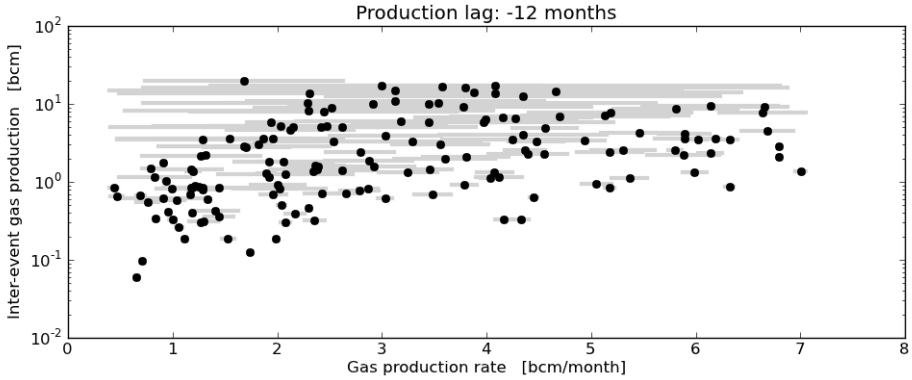

(b)

Figure 6.7 *Inter-event gas production exhibits little sensitivity to the rate of gas production. To avoid any bias of event clustering, all events within 3 days of the previous event were excluded. Dots and grey bars denote the average and the range of inter-event production rates respectively; in some instances the grey bar is so small as to be covered by the black dot; (a) and (b) represent 0- and 12-months lag times, respectively.*

Muntendam-Bos & de Waal (2013) used the same historic data to show one instance of a fit to these data with a preliminary model for the activity rate based on the cumulative gas production and the annual rate of gas production with a delay of a year. Though the authors did not assess uncertainties in the estimated model parameters, they did conclude that if production rates were lowered to12 bcm/year there would be "almost no earthquakes with magnitudes ≥1.5 would occur after a number of years". Figure 6.7 shows the actual variability in the historic data and so offers a simple means of assessing the validity of this conclusion. For historic gas production rates of about 12 bcm/year (1 bcm/month), Figure 6.7 indicates historic inter-event volumes of gas production in the range of 0.1 to 1 bcm. This is equivalent to instantaneous activity rates of 12 to 120 M≥1.5 events per year which clearly contradicts the conclusion of almost no earthquakes. This contradiction arises because Muntendam-Bos & de Waal did not assess uncertainty in their estimated model parameters despite the large observed variability between activity rates and production rates.

6.2.3 Earthquakes and compaction

Seismic moment and compaction

Let us now consider how the strain partitioning factor, α, may vary with reservoir compaction. To measure this effect, each M ≥ 1.5 event between April 1995 and October 2012 was compared to the 2012 reservoir compaction map (Figure 6.4). This compaction map was divided into discrete regions bounded by a set of compaction contours. Within each region, the total observed seismic moment may then be compared to the reservoir moment (Figure 6.8a). The reservoir moment is simply the maximum seismic moment if all strain is accommodated by slip on faults, *i.e.* $\alpha = 1$. The fraction of the total seismic moment to the reservoir moment is then a measure of the partitioning factor for each region that corresponds to a narrow range of reservoir compaction values. These results (Figure 6.8b) clearly indicate the partitioning fraction increases significantly with compaction in an approximately log-linear fashion.

Doubling the reservoir compaction from 0.15 m to 0.3 m increased the partitioning fraction by a factor of 100. An exponential functional form was therefore chosen for the strain partitioning model. The uncertainty bounds on the data follow Pareto sum distributions that were approximated by a log-normal distribution where the standard deviation was set equal to the approximation for Pareto sums, as obtained by Zaliapin et al. (2005). This reduced model parameter estimation to a standard least-squares regression. The maximum likelihood model is shown in Figure 6.8b. Uncertainties in this model were estimated using the Monte Carlo bootstrap sample-resample method to obtain the probability distribution of all models consistent with the data. The 95% confidence interval for this distribution of models is indicated in Figure 6.8(b).

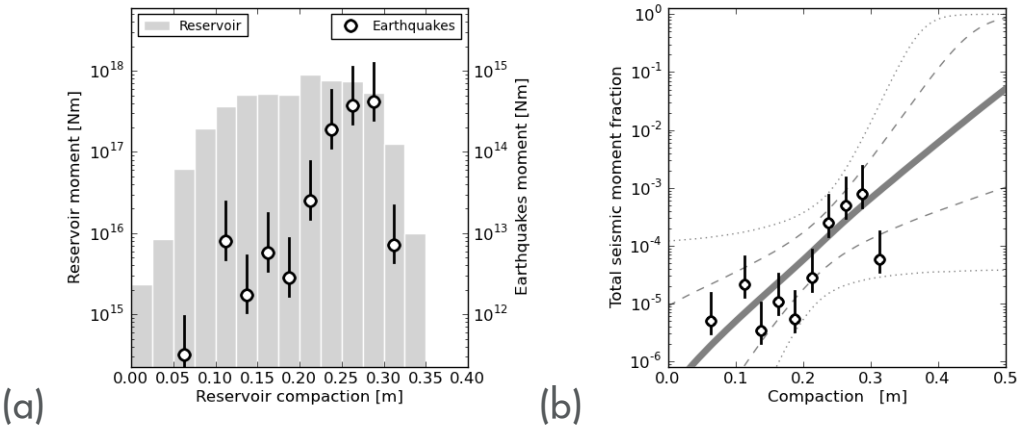

Figure 6.8 *(a) The distribution of reservoir moment and earthquake moment with reservoir compaction. (b) The ratio of earthquake moment to reservoir moment (total seismic moment fraction) significantly increases with reservoir compaction. An exponential model fit to the observed total seismic moment fractions (solid line) and the associated 68% and 95% confidence intervals found by Monte Carlo analysis.*

Activity rate and compaction

Repeating the process described in the previous section but for the number of events and the reservoir volume reduction similarly indicates a significant increase in the number of events per unit reservoir volume reduction (Figure 6.9).

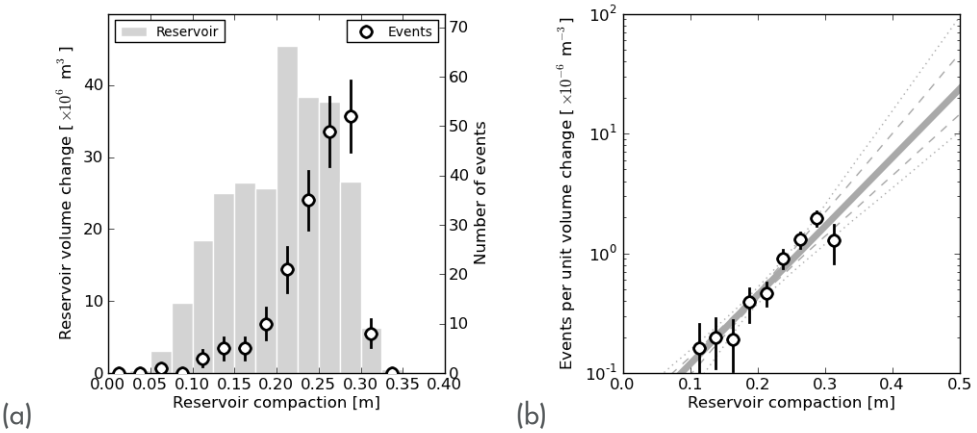

Figure 6.9 *(a) The distribution of reservoir volume change and M ≥ 1.5 event numbers with reservoir compaction. (b) The number of events per unit reservoir volume change significantly increases with reservoir compaction.*

6.2.4 Seismological model

A seismological model is required to explain the observed seismicity and provide a framework for assessing future seismicity. Such a model cannot and will not predict individual earthquakes but it should provide a reliable means of characterizing the statistical properties of future earthquakes; such as the probability of exceeding a given earthquake magnitude over some given time interval. The seismological model developed for this purpose is based on the concept of induced earthquakes accommodating induced strain. Information about the induced strain field is available within the existing linear elastic geomechanical model. This geomechanical model for reservoir compaction is based on past and planned future gas production and calibrated to match the observed subsidence measurements. Information about the fraction of this strain released as earthquakes is based on a statistical model for fault strain partitioning as a function of reservoir compaction calibrated to the observed relationship between earthquakes and reservoir compaction between 1995 and 2012.

For a given time interval the median total seismic moment is simply the product of the incremental volume change per unit area and the median strain partition factor integrated over the entire reservoir. Repeating this process over the full statistical distribution of partitioning models yields a probability distribution for total seismic moment (Figure 6.10).

Repeating this entire process for the set of multiple time intervals that all begin at the start of production and end on one of the subsequent years up until the end of production, yields a model for the expected total seismic moment as a function of past and future gas production (Figure 6.11). This seismological model was constructed based on the map distribution of earthquakes and reservoir compaction in 2012. By means of cross-validation, the model-based prediction for the cumulative total seismic moment with cumulative gas production should agree with the observed cumulative total seismic moment between 1995 and 2012. The agreement between the two shown in Figure 6.11 indicates that the seismological model provides a good description of both the areal and temporal development of seismicity in the Groningen Field. Note that the uncertainty range around the seismic moment and the magnitude is not constant but instead grows significantly in the future. Further data gathering is required to shift this growth of the uncertainty further towards the future.

Based on this seismological model, Figure 6.12 shows the probability of exceeding a given earthquake magnitude over the 10-year interval from 2013 to 2023 and over the expected remaining lifetime of production. These estimates are contingent on the validity of the compaction model, gas production continuing according to the current production plan and the historic fault strain partitioning trend being a guide to the future fault strain partitioning. In this context it is important to note that alternative geomechanical models do exist and are also calibrated to the historic subsidence but differ in their predictions of future reservoir compaction. These represent epistemic uncertainties about future reservoir compaction. Also, the seismological model represents the case of no time delay between reservoir compaction and the associated induced earthquakes. This is consistent with the limited evidence available so far for little or no time delay between changes in production rate and changes in earthquake activity rates (Bourne & Oates 2013). However given the uncertainties associated with the limited number of historic earthquakes it remains possible that new information will reveal the need revise the seismological model to include a distribution of earthquake waiting times.

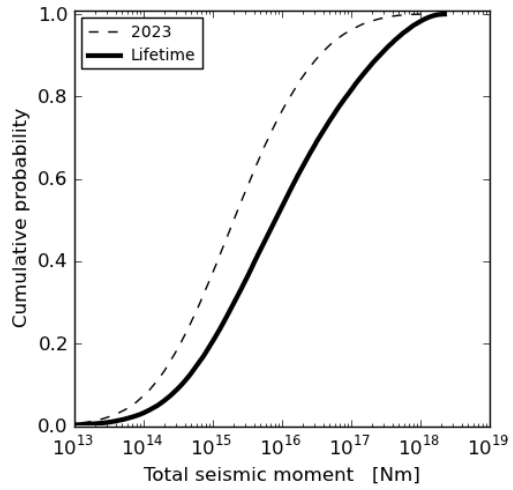

Figure 6.10 The cumulative probability distribution of total seismic moment predicted for the 10-year period from 2013 to 2023 and for the remaining lifetime of production based on the current production plan and the current reservoir compaction model.

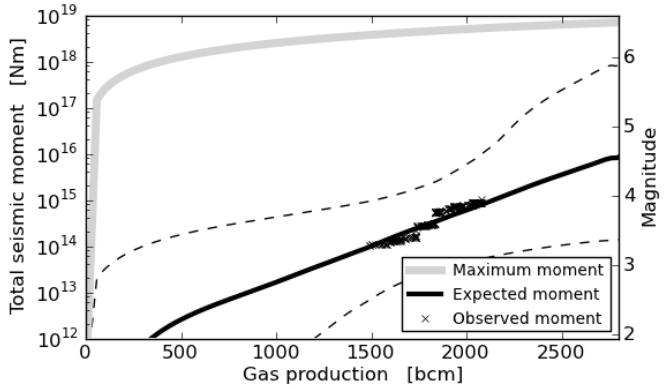

Figure 6.11 *Model for the expected total seismic moment released as a function of cumulative gas production since the start of gas production. Dashed lines denote the 95% confidence interval for this model. This model is only applicable if the past and future seismicity follow the same trend as the observed seismicity between 1995 and 2012. The grey line denotes the maximum magnitude if all the previously accumulated reservoir moment were to be released in a single event at that moment. Note that the left axis denotes the cumulative total seismic moment of all earthquakes, whereas the right axis is the magnitude of a single event that releases the same seismic moment.*

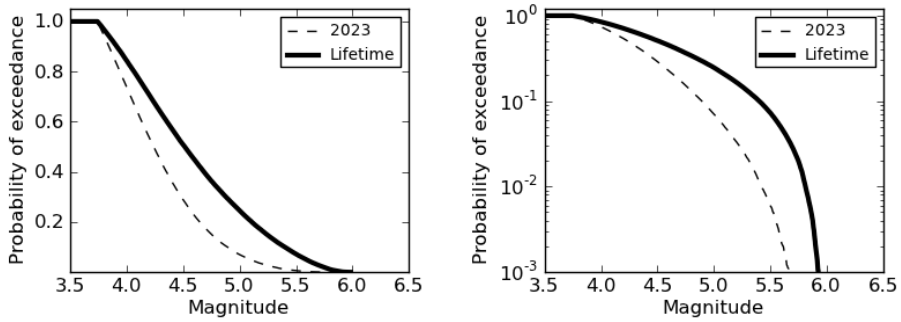

Figure 6.12 *Probability of exceeding a given magnitude over the period up to 2023 and over the remaining lifetime of gas production. These are contingent on future induced earthquakes following the same trend of increasing fault strain partitioning observed within the historic earthquake catalogue and a constant b-value of 1.*

6.3 Potential influence of Time-Dependent and Rate-dependent Effects on future Seismicity

The seismological model used to explain historic seismicity and to predict future seismic hazards depends on reservoir compaction. Gas production causes reservoir pore pressure depletion. Pressure depletion causes reservoir compaction. Reservoir compaction induces strains in and around the reservoir. Most of this strain is accommodated by elastic deformations. As gas production continues, these induced strains increase and so do the mechanical loads acting on pre-existing faults located in and around the reservoir. On occasion these loads exceed the local frictional strength of a particular fault segment. This fault segment will then slip, relaxing the mechanical load acting on the fault until frictional resistance prevents further slip. This process transfers strain from the surrounding medium and localises it along the fault.

Once initiated, fault slip may occur steadily and slowly in a stable creeping process that generates no earthquakes. Alternative, fault slip may occur abruptly with the fault then stuck until the cycle repeats. This stick-slip behaviour generates an earthquake with every cycle of fault slip. The amount and area of abrupt slip on the fault determines the magnitude of the earthquake. By slipping, a population of faults may accommodate some of the induced strains. Induced seismicity depends on the amount of induced strain, the fraction of induced strain accommodated by fault slip, and the fraction of fault slip that is seismogenic. All three factors are likely increasing with the ongoing gas production. Alternative production plans may reduce future seismicity relative to the current production plan by reducing the rate of increase in one or more of these three factors.

The influence of different future production rate scenarios on the seismic hazard over the next 3, 5 and 10 years is described in Section 8.9. Their influence depends on time-dependent and rate-dependent effects. Some of these effects are included in the seismic hazard assessment based on evidence from the observed historic behaviour of the Groningen Field. Others are currently excluded given the absence of evidence from past field behaviour, or the absence of any influence on the hazard during model sensitivity tests.

6.3.1 Time-dependent effects

Three possible time-delays exist between gas production and induced seismicity. First, there is a time-delay between gas production at the wells and pressure depletion within the area of seismicity due to the time required for pressure diffusion within the gas reservoir. This is well-measured by reservoir pressure gauges over the production history of the field and well-modelled by the current reservoir simulation model. Currently, this represents a time-delay of about 3-5 years between any reduction in production rates from the southern well clusters and a corresponding reduction in the rate of pressure depletion. This time-delay is included in the seismic hazard assessment.

Second, there is a potential time-delay between reservoir pressure depletion and reservoir compaction due to wide range of potential non-equilibrium processes such as compaction creep. This time-delay should be evident as a delay between reservoir depletion and surface subsidence. Analysis of these data indicates a characteristic time-delay between depletion and compaction of 0 to 10 years. The linear and bi-linear reservoir compaction models included in the hazard assessment represent the case of a zero time-delay. The time-decay reservoir compaction model included in the hazard assessment represents the case of a 5-year characteristic delay. Further studies are ongoing to investigate time-dependent compaction behaviour.

Third, there is a possibility of a time-delay between reservoir compaction and induced seismicity. This is currently excluded from the hazard assessment because a zero time-delay model is sufficient to explain the historic seismicity as a function of compaction. Nonetheless, there remains a possibility of some continued seismicity after reservoir compaction ends.

6.3.2 Rate-dependent effects

Lower strain rates associated with lower gas production rates might, in principle, offer opportunities to lower the seismic hazard in one of three ways. First, lower strain rates might also lower the induced strain per unit depletion. There is some experimental evidence for this effect from rate-dependent compaction tests on sandstone reservoir rocks. This possibility is represented by two different varieties of Isotach reservoir compaction models that are included in the seismic hazard assessment.

Second, lower strain rates might lower the fraction of strain accommodated by slip on faults. Lower strain rates might lower the loads acting on faults, thereby reducing the number of slipping faults. Third, lower strain rates might lower the fraction of seismogenic slip on faults. If either of these two possible effects were significant during the period of observed historic seismicity then some variation in seismicity with varying production rate might be present.

Using these data, Muntendam-Bos & Waal (2013) show one instance of a fit with a preliminary rate-dependent model for the activity rate based on the cumulative gas production and the annual rate of gas production with a delay of a year. Though the authors did not assess uncertainties in the estimated model parameters, they did conclude that if production rates were lowered to 12 bcm/year there would be "almost no earthquakes with magnitudes ≥1.5 would occur after a number of years". Figure 6.7 shows that at this production rate M≥1.5 events occurred at instantaneous activity rates of 12 to 120 per year which clearly contradicts the conclusion of almost no earthquakes. Given this absence of field evidence these mechanisms are not currently included in the hazard assessment.

Some experimental data do appear to suggest the possibility of rate-dependent effects that might limit stress development in granular materials (e.g. Hartley & Behringer 2003). However, these results are more applicable to loose sands rather than sandstones and the measured effects were for strain rates substantially greater than those within the Groningen reservoir. Lahaie & Grasso (1999) analysis seismicity induced by gas production from the Lacq reservoir in France to conclude the b-value depends on the rate of gas production. They conclude that lower production rates might be beneficial as they yield higher *b*-values meaning the relative contribution of larger magnitude earthquakes to the total seismicity is less. This

possible benefit was assessed for the Groningen field by testing the influence of *b*-value on the seismic hazard. The results indicate even substantial variability in *b*-value has almost no influence on the seismic hazard. This is due to stochastic variability in the ground motion prediction equation counter-acting the variability in seismicity due to changes in the *b*-value.

6.4 Conclusions

- According to current model-based predictions for the areal distribution of reservoir compaction at the end of field life, an induced earthquake of M>6.5 is physically impossible. This limit, however, provides no information about the likelihood of an induced $M \leq 6.5$ earthquake.
- The location, frequency and magnitude of observed earthquakes in the Groningen field are consistent with bulk reservoir volume changes (compaction), being the main source of seismicity.
- The fraction of bulk reservoir volume changes accommodated by seismogenic fault slip is about 0.1%. If this fraction were invariant with production, the maximum magnitude of a future event is expected to be *M*=4.5 with a 95% upper bound of *M*=5.5.
- There is evidence that the release of seismic moment per unit production escalated with increasing production volume. If this trend continues with future production, an increasingly large fraction of the induced strain may be accommodated by seismogenic fault slip.
- The fraction of induced strain accommodated by earthquakes is likely increasing with increasing reservoir compaction. This explains the observed temporal and areal distribution of earthquakes.
- If this escalation trend continues with future production the footprint of earthquakes is expected to continue extending from the centre towards the edges of the field, but the relative abundance of earthquakes will continue to be localized within the regions of largest reservoir compaction in the centre of the field.
- If future seismicity follows the same trend of increasing fault strain partitioning observed in the historic earthquake catalogue, then based on the current analysis there is a 1 in 2 chance of *M*>4.2, a 1 in 10 chance of *M*>4.9, and a 1 in 100 chance of *M*>5.4 before the end of 2023. These estimates include known uncertainties associated with the trend of seismogenic fault slip accommodating an increasing fraction of the induced strain but currently exclude the possible trend of the *b*-value decreasing with compaction that may increase the likelihoods stated. These estimates also exclude the possibility of triggered earthquakes that may increase these likelihoods.

6.5 Recommendations for further work

The recommendations below will address the main remaining uncertainties and aim to provide a better description of the seismicity and hazard.

- Use the improved earthquake monitoring results expected to become available from the enhanced earthquake monitoring network to characterize the depth distribution of earthquakes and their spatial relationship to mapped faults subjected to differential compaction. If appropriate, update the seismological model according to this new information.
- Assess epistemic and aleatory uncertainty associated with the reservoir compaction model and include this in the estimates for the fault strain partition and future total seismic moment release.
- Complete a full 3D poro-elastic simulation of the geomechanical response of the field calibrated by the historical subsidence, gas production, and reservoir pressure depletion data.
- Investigate different options for obtaining a robust bias-free estimate for fault strain partitioning based on historic seismicity and compaction to validate or improve the current method. Consider extending the strain partitioning analysis to explicitly allow for differential compaction inducing slip on specific known faults and also the possibility of anelastic strains within the reservoir.
- Re-assess the characterization of correlated earthquakes to ensure these do not bias the hazard assessment.
- Further investigate the possibility of any weak but statistically significant evidence for the effect of gas production rate on the lifetime earthquake hazard.

- Further investigate evidence for any statistically significant time delay between pressure depletion and reservoir compaction and between reservoir compaction and seismicity.
- Re-assess the seismological model at regular intervals in relation to future earthquakes and subsidence. Assess the continuing validity of model assumptions and the influence of uncertainties on this seismological model.

6.6 References

Bourne, S J & Oates, S., 2013. *Probability of an earthquake greater than magnitude 4 due to gas production from the Groningen Field*, Rijswijk, The Netherlands.

Bourne, S.J. et al., 2006. *Monitoring deformation of a carbonate field in Oman: Evidence for large-scale fault reactivation from microseismic, InSAR & GPS*. In 68th EAGE Conference and Exhibition, Vienna.

Bourne, S.J. & Oates, S., 2013. *Induced strain and induced earthquakes within the Groningen Gas Field: Earthquake probability estimates associated with future gas production*, Rijswijk, The Netherlands.

Crook, de T., Dost, B & Haak, H.W., 1995. *Analyse van het seismische risico in Noord-Nederland*,

Crook, de T., Haak, H.W. & Dost, B, 1998. *Seismisch risico in noord-Nederland* Technical., Koninklijk Nederlands Meteorologisch.

Dost, Bernard et al., 2012. *Monitoring induced seismicity in the North of the Netherlands: status report 2010*,

Dost, Bernard & Kraaijpoel, D., 2013. *The August 16 , 2012 earthquake near Huizinge (Groningen)*, de Bilt, The Netherlands.

Eck, van T. et al., 2004. *Seismic hazard due to small shallow induced earthquakes* WR 2004-01., Koninklijk Nederlands Meteorolgisch.

van Eck, Torild et al., 2006. Seismic hazard due to small-magnitude, shallow-source, induced earthquakes in The Netherlands. *Engineering Geology*, 87(1-2), pp.105–121. Available at: http://linkinghub.elsevier.com/retrieve/pii/S0013795206001803 [Accessed November 6, 2012].

Gutenberg, B. & Richter, C., 1954. *Seismicity of the Earth and Associated Phenomena* 2nd editio., Princeton University Press, Princeton, New Jersey.

Hager, B.H. & Toksöz, M.N., 2009. *Technical Review of the Bergermeer Seismicity Study, TNO Report 2008-U-R1071/B*, Cambridge, MA, USA.

Hanks, T.C. & Kanamori, H., 1979. Moment magnitude scale. *Journal of Geophysical Research*, 84(B5), pp.2348–2350.

Hartley, R.R. & Behringer, R.P., 2003. Logarithmic rate dependence of force networks in sheared granular materials. Nature, 421(6926), pp.928–31. Available at: http://www.ncbi.nlm.nih.gov/pubmed/12606996.

Klose, C.D., 2012. Mechanical and statistical evidence of the causality of human-made mass shifts on the Earth's upper crust and the occurrence of earthquakes. *Journal of Seismology*, 17, pp.109–135. Available at: http://www.springerlink.com/index/10.1007/s10950-012-9321-8 [Accessed November 13, 2012].

Kostrov, V.V., 1974. Seismic moment and energy of earthquakes, and seismic flow of rocks. *Izv. Acad. Sci. USSR Phys. Solid Earth, Eng. Transl.*, 1, pp.23–40.

Kraaijpoel, D. et al., 2008. Location of induced earthquakes in the Netherlands gas fields. In *ESC General Assembly 2008, September 7-12, 2008, Hersonissos*.

Lahaie, F. & Grasso, J.R., 1999. Loading rate impact on fracturing pattern: Lessons from hydrocarbon recovery, Lacq Gas Field, France. Journal of Geophysical Research, 104(B8), p.17941. Available at: http://doi.wiley.com/10.1029/1999JB900139.

Leonard, M. (2010). Earthquake Fault Scaling: Self-Consistent Relating of Rupture Length, Width, Average Displacement, and Moment Release. *Bulletin of the Seismological Society of America*, *100*(5A), 1971–1988. doi:10.1785/0120090189

Maury, V.M.R., Grassob, J.-R. & Wittlinger, G., 1992. Monitoring of subsidence and induced seismicity in the Lacq Gas Field (France): the consequences on gas production and field operation. *Engineering Geology*, 32(3), pp.123–135. Available at: http://linkinghub.elsevier.com/retrieve/pii/001379529290041V.

McGarr, A., 1976. Seismic Moments and Volume Changes. *Journal of Geophysical Research*, 81(8), pp.1487–1494.

Muntendam-Bos, A.G. et al., 2008. *Bergermeer Seismicity Study*, TNO report 2008-U-R1071/B.

Muntendam-Bos, A. G., & Waal, J. A. de. (2013). *Reassessment of the probability of higher magnitude earthquakes in the Groningen gas field: Including a position statement by KNMI*. Retrieved from http://www.sodm.nl/sites/default/files/redactie/20130116 groningen seismicity report final.pdf

Segall, P., 1989. Earthquakes triggered by fluid extraction. *Geology*, 17(October), pp.942–946.

Segall, Paul, Grasso, J.-R. & Mossop, A., 1994. Poroelastic stressing and induced seismicity near the Lacq gas field, southwestern France. *Journal of Geophysical Research*, 99(B8), pp.15,423–15,438.

Wassing, B B T, Van Eck, T & Van Eijs, R.M.H.E., 2004. *Seismisch hazard van geïnduceerde aardbevingen Integratie van deelstudies*, Utrecht: TNO.

Zaliapin, I.V., Kagan, Y.Y. & Schoenberg, F.P., 2005. Approximating the Distribution of Pareto Sums. *Pure and Applied Geophysics*, 162(6-7), pp.1187–1228. Available at: http://www.springerlink.com/index/10.1007/s00024-004-2666-3 [Accessed November 16, 2012].

Zoback, M. & Zinke, J., 2002. Production-induced Normal Faulting in the Valhall and Ekofisk Oil Fields. *Pure and Applied Geophysics*, 159, pp.403–420.

7 Movement at surface

7.1 Ground-Motion Prediction Equations (GMPEs)

Earthquake hazard is sometimes discussed in terms of magnitude, which only defines the amount of seismic energy released at the source of an earthquake. To characterize the hazard in a manner that is relevant to the potential impact of the earthquake on the built environment (houses, infrastructure, etc.), it is necessary to quantify the hazard in terms of the nature of the ground shaking produced at any given surface location. Strong shaking produced by earthquakes is recorded on accelerographs, which register the particle acceleration experienced at the instrument location as a function of time. There are many different parameters that are used to characterize the shaking recorded in such accelerograms, each of which conveys only some features of the ground motion. The simplest and most widely-used of these parameters is the maximum amplitude on the acceleration time series, the peak ground acceleration (PGA). Integration of the accelerogram over time yields the velocity time-series, the maximum amplitude of which is another commonly used parameter, PGV (peak ground velocity). Both of these parameters are illustrated in Figure 7.1.

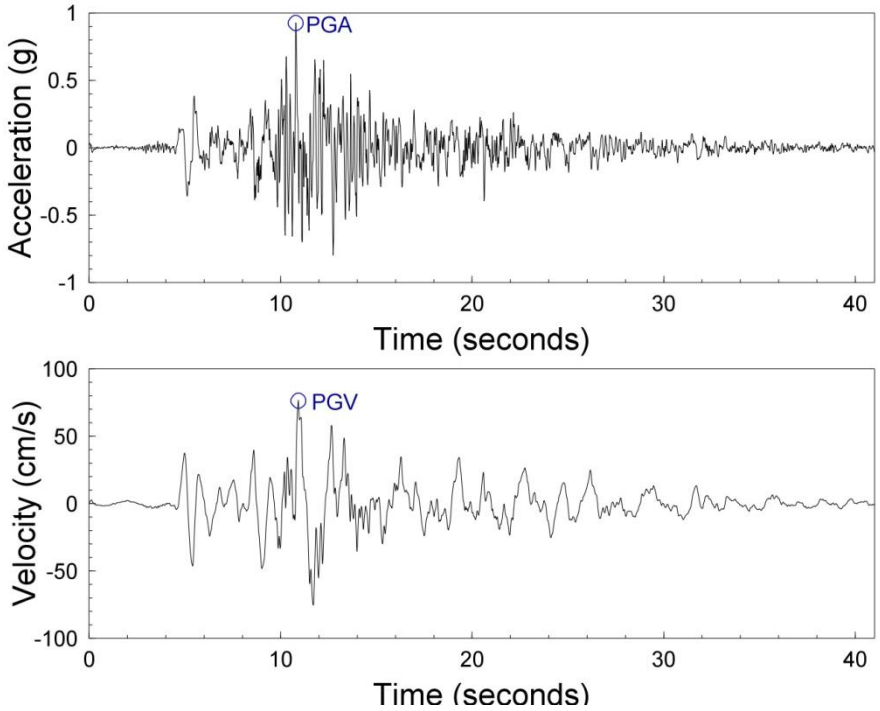

Figure 7.1 Example of acceleration and velocity time-series of strong earthquake shaking, with PGA and PGV indicated (not based on Groningen)

In order to estimate the expected values of parameters such as PGA and PGV at a given location as a result of a specific earthquake scenario, equations are required that relate the parameter of interest to variables that characterize the earthquake, its location with respect to the site of interest, and the nature of the site itself. The earthquake itself is generally characterized by its magnitude, M, and the style-of-faulting, SoF (*i.e.*, normal, reverse or strike-slip rupture); the relative locations of the earthquake and the site by the distance, R, that separates them; and the site itself by a classification of its stiffness, most commonly now using the average shear-wave velocity over the uppermost 30 meters, V_{s30}. Using larger collections of ground-motion recordings, empirical equations are obtained fitting a suitable functional form, relating PGA or PGV to the variables listed above. Such equations have often been referred to as 'attenuation relationships' but this is now considered a misnomer since they describe both how the peak motions decay with distance and how they scale with magnitude and other parameters. For this reason, these relationships are now generally called ground-motion prediction equations, or GMPEs.

A very important feature to note with such equations is that the data always show a large scatter around the best fit obtained through regression analyses. Residuals are calculated as the difference between

recorded and predicted values of PGA or PGV, and the distribution of these residuals represents the scatter in the predictions. This scatter exists for several reasons, including the influence of variables that are not included in the equations (*e.g.*, stress drop, fault rupture directivity effects, azimuthal variations in energy propagation from the source, differences in the deeper geological structure) and the fact that the explanatory variables employed, such as V_{s30}, can yield identical values for very different sites with markedly distinct dynamic response characteristics (*e.g.*, Papaspiliou *et al.*, 2012). Several studies have shown that when the equations are derived in terms of the logarithmic value of PGA or PGV, the residuals conform to a standard normal (Gaussian) distribution, which is fully characterized by the standard deviation, σ (sigma).

The consequence of the scatter in the residuals is that GMPEs cannot be considered to predict unique values of PGA or PGV for a given combination of magnitude, style-of-faulting, distance and site classification, but rather a probabilistic distribution of values of peak acceleration or velocity. The general form of a GMPE is therefore expressed as:

$$\log(PGA) = f(M, SoF, R, V_{s30}) + \varepsilon\sigma \qquad (7.1)$$

In this expression, the term ε is simply the normalized residual, or in other words the number of logarithmic standard deviations above or below the median (or logarithmic mean) value of the predicted peak motion. Figure 7.2 illustrates these concepts with examples of a GMPE from California and recorded PGA values from a single earthquake in that region.

If the scatter in the distribution of residuals is used when GMPEs are deployed to estimate PGA and PGV values, the median values of the peak motion that will be obtained will have a 50% chance of being exceeded at each location in the event of the earthquake scenario taking place. If calculations of the impact of a hypothetical earthquake scenario (in terms of damage to buildings, for example, through the use of fragility functions relating expected levels of damage in different building types to PGA or PGV) are made using only predicted median levels of motion, the result will be severe underestimation. The reason for this is that the lognormal distribution is strongly asymmetrical hence correct sampling of the full distribution would produce several very high values of PGA or PGV, leading to greater damage.

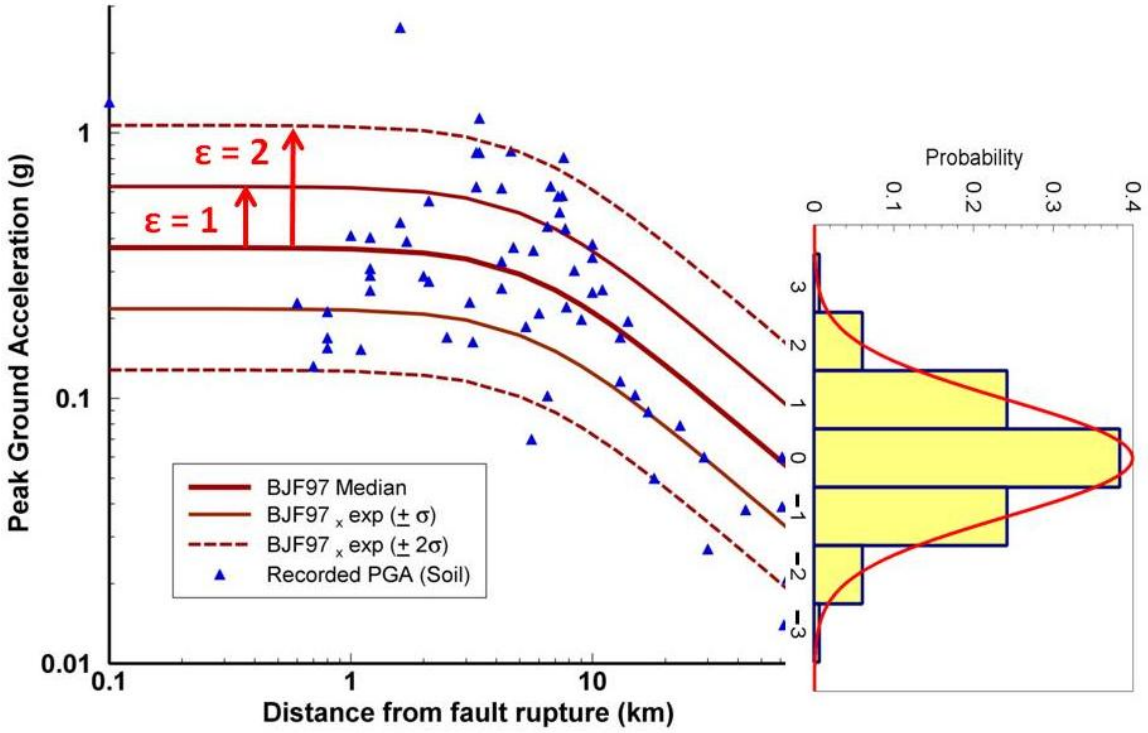

Figure 7.2 *PGA values (blue triangles) recorded on soil sites during the magnitude 6.0 earthquake that occurred in Parkfield, California, in September 2004, plotted as a function of distance, and compared with predictions from the Californian GMPE of Boore et al. (1997). The predicted PGA values are shown for*

the median values and for one and two standard deviation above and below the logarithmic mean. Figure adapted from Bommer & Abrahamson (2006).

In passing, it is worth noting that in regions of less frequent seismic activity, where there are generally very few, if any, recordings of stronger shaking from moderate-to-large earthquakes, it is common practice to analyse recordings of smaller earthquakes to infer stochastic source, path and site parameters that can be related to the Fourier spectra of the motions. These parameter suites can then be used to simulate ground motions from larger earthquakes (*e.g.*, Boore, 2003). Such simulations can then be used to either directly derive so-called stochastic GMPEs (*e.g.*, Rietbrock et al., 2013) or to apply adjustments to empirical GMPEs from other regions to render them more appropriate to the target region for their application (*e.g.*, Campbell, 2003). Although such approaches provide a convenient option for developing GMPEs in the absence of extensive strong-motion databases, their use is not straightforward.

The most fundamental challenge in using the stochastic approach is that there are significant trade-offs between the different source, path and site parameters obtained through the inversions, with the result that there are many combinations of these parameters that are consistent with the Fourier amplitude spectra of the recordings from small-magnitude earthquakes. The problem then arises when these suites of parameters are used to estimate PGA and PGV from larger earthquakes since the different parameter values can lead to widely divergent results. Additionally, for certain parameters, such as the stress drop associated with the fault rupture, assumptions need to be made regarding whether or not the value should remain constant over all magnitude, an issue on which there are divergent views within the seismological community. Moreover, without running very large numbers of simulations that sample the full ranges of all the stochastic source, path and site parameters (considering their correlations), it is difficult to obtain meaningful estimates of the aleatory variability associated with stochastic GMPEs. In view of these challenges, and the absence of an available study performing stochastic inversions for weak motions in the Netherlands, the focus in this application is entirely on the use of empirical GMPEs.

7.2 Development of GMPEs for Groningen

This section describes the development of appropriate GMPEs for use in the seismic hazard and risk assessments for the Groningen gas field. The uncertainty associated with the proposed models, as well as some important aspects of characterizing the ground shaking hazard that are not covered by these equations but which need careful consideration, are also briefly discussed.

7.2.1 Criteria for Groningen GMPEs

The first step was to establish the requirements for the ground-motion prediction equations for application to the assessment of seismic hazard (probability of different levels of ground shaking) and seismic risk (probability of different degrees of consequences in terms of damage to buildings) due to induced earthquakes in the Groningen gas field. These requirements are as follows:

1. Compatible equations to predict both PGA and PGV. This is required because many of the available fragility functions that could be adopted or adapted for the risk analysis are characterized in terms of PGA (*e.g.*, Bothara *et al.*, 2010), whilst PGV is widely recognized to be a more robust indicator of the damage potential of ground shaking by virtue of its relation to the energy content of the motion (*e.g.*, Bommer & Alarcón, 2006). PGV has also been found to perform better than PGA as a basis for estimating Modified Mercalli intensities from ground-motion parameters (Wald *et al.*, 1999; Dangkua & Cramer, 2011; Worden *et al.*, 2012).
2. The equations need to be applied to earthquakes from magnitude M_w 1.5 to M_w 6.5, which is the range considered in the probabilistic seismic hazard analysis (PSHA). This is an important consideration since most current GMPEs are derived for application to earthquakes of M_w 5 and greater. Several recent studies have shown that when such equations are extrapolated for application to smaller earthquakes, they lead to gross overestimation of the ground motions (Bommer *et al.*, 2007; Atkinson & Morrison, 2009; Chiou *et al.*, 2010).
3. Since the individual earthquake events in the seismicity model are represented as points (hypocenters, which are defined by an epicentral location and a constant focal depth of 3 km), it is important to use a GMPE that is also based either on hypocentral distance, R_{hyp}, or else on epicentral distance, R_{epi}, but derived from data with a similarly shallow depth distribution. This criterion is important because most

modern GMPEs use distances measured relative to the finite fault rupture, but employing such equations in PSHA in which earthquakes are represented as hypocenters will lead to underestimation of the hazard contributions from larger magnitude earthquakes (Bommer & Akkar, 2012).

4. The ground surface conditions in much of the Groningen field have been classified as being soft soils, typically with a time-average shear-wave velocity over the top 30 meters, V_{s30}, on the order of 200 m/s. The GMPE therefore needs to be calibrated to such soft soil sites or include V_{s30} as an explicit predictor variable that can take such a small value.
5. As well as reporting the standard deviation (sigma) to characterize the distribution of logarithmic residuals, the decomposition of sigma into between-earthquake and between-station components is required. The first component represents how different is the average level of shaking from average earthquakes of the same magnitude and style-of-faulting (which may reflect, for example, the stress drop), whereas the second represents how the motion at individual locations during one earthquake differ from average predictions for sites on similar geology at the same distances (which is effectively the spatial variability of the motion). When calculations are performed using Monte Carlo simulations to estimate ground shaking at many locations and the consequent impact on the built environment, it is necessary to correctly sample these two components of variability for each earthquake and then for all the sites at which the shaking is calculated (see Crowley & Bommer, 2006).

Ideally, the equation would also be applicable to the region under study, which would arise from being derived from local recordings or else using data from a clearly analogous region.

The first criterion alone greatly reduced the number of published equations under consideration since although there are many GMPEs available for PGA (Douglas, 2011), the number that also provide PGV predictions is considerably smaller (Douglas, 2012). None of the equations in contention automatically satisfy all of the other requirements, so the search focused instead of identifying GMPEs which satisfied some of these criteria and for which it would be relatively straightforward to make adjustments for the non-compliance with other criteria. This excludes, for example, the equations of Douglas *et al.* (2013) derived from recordings of induced earthquakes from geothermal fields and other areas worldwide, since although they satisfy several of the requirements, they are calibrated to a unique value of V_{s30} (1,100 m/s). The application of these equations to the Groningen field would therefore require site response analyses to transform the predicted motions at a horizon within the underlying bedrock to the ground surface, which would impose a significant computational penalty on the hazard calculations. Moreover, without extensive and detailed field and laboratory tests to determine the dynamic characteristics of the overlying soils, such a step could introduce considerable additional uncertainty into the estimates of surface motions.

After consideration of some 17 equations derived using data down to smaller magnitude ($M_w < 3.5$), the choice was made to select the equations of Dost *et al.* (2004) as these were derived for shallow earthquakes in the Netherlands (section 7.2.2). Although derived in terms of local magnitude, M_L, rather than moment magnitude, M_w, in the range of application it may be assumed that the two scales are equivalent (*e.g.*, Deichmann, 2006). The equations are derived in terms of R_{hyp} from recordings of shallow, mostly induced (from the Roswinkel field), earthquakes in the Netherlands, with most of the recordings coming from relatively soft soil sites. The two criteria that the Dost *et al.* (2004) equations do not fully satisfy relate to the magnitude range and to the decomposition of sigma. The problem with the former is that the equations only model linear scaling of PGA and PGV with magnitude, which leads to unrealistically high motions from larger earthquakes. However, a non-linear modification to the magnitude scaling at higher values was made using the scaling from the R_{hyp}-based model of Akkar *et al.* (2013). Similarly, a separation of the total standard deviation into between-event and within-event sigmas was made on the basis of ratios inferred from other GMPEs.

7.2.2 The Groningen Ground-Motion Database

In essence the Dost *et al.* (2004) equations for PGA and PGV were chosen on the basis of having been derived from recordings of small-magnitude, shallow earthquakes in the Netherlands, which at face value would make them obvious candidates that are likely to be applicable to the Groningen hazard and risk studies. Shortly after these equations were chosen, the opportunity to test this assumption arose when 40 pairs of PGA and PGV values from recordings of 8 earthquakes with magnitude in the range 2.7 to 3.6 in the Groningen field were made available by Bernard Dost of KNMI. Figure 7.3 shows the peak motions

plotted against hypocentral distance to the recording station, after adjustment to a common magnitude of M_w 3.6 using the scaling terms in Dost *et al.* (2004). Shown on the same plot are the median predicted values of PGA and PGV from the Dost *et al.* (2004) equations for an earthquake of this size, together with the predictions at the plus-and-minus-one-standard deviation levels.

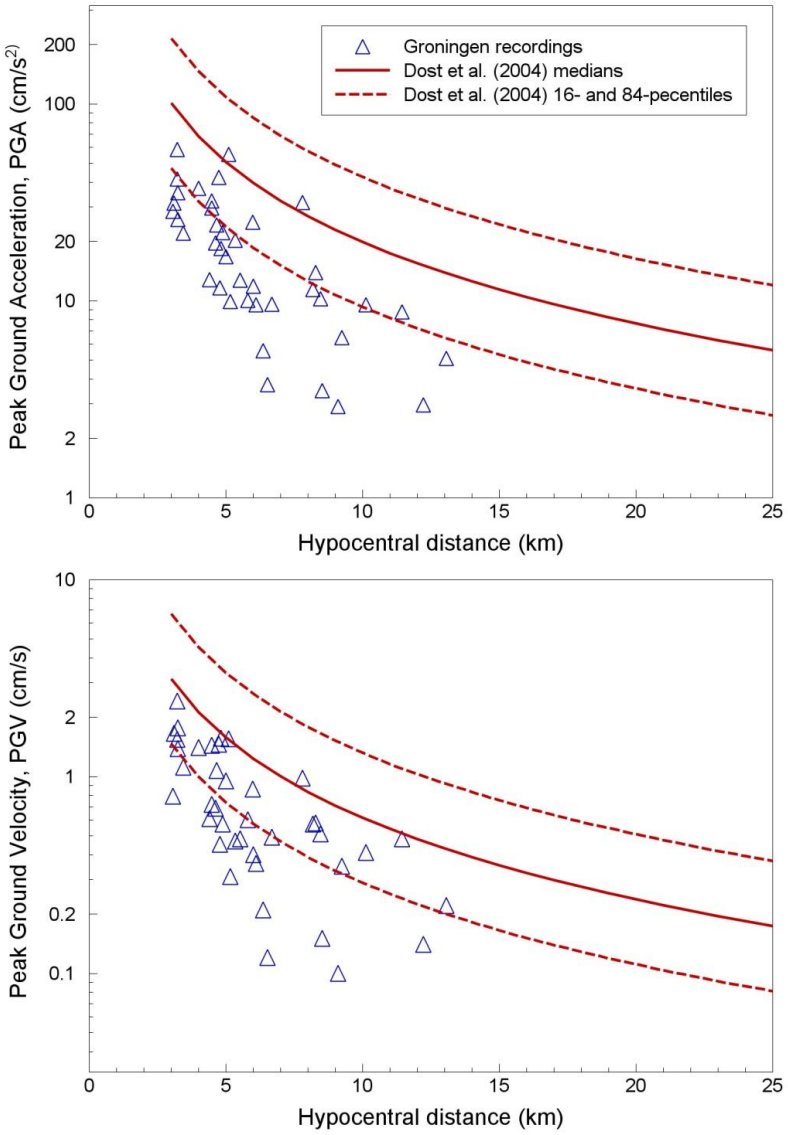

Figure 7.3 PGA and PGV values from induced earthquakes in the Groningen field (normalized to M_w 3.6) plotted against distance and compared to the predicted values from the Dost et al. (2004) equations.

It is immediately apparent from the plots in Figure 7.3 that the Dost *et al.* (2004) equations over-predict the recorded peaks, on average by a factor of about 3 (the standard deviation on the $\log_{10}$ peaks in. Given that the equation is derived from recordings of small-magnitude shallow earthquakes, this raises questions as to what causes the surface motions in the Groningen field to be of such low amplitude. The issue of over-estimation by GMPEs derived from recordings of larger magnitude earthquakes is not relevant since the Dost *et al.* (2004) model is based on recordings from earthquakes of comparable magnitudes.

Another possibility that might be considered is that the Groningen earthquakes are associated with exceptionally low stress drops, which could be supported by the observation of positive correlation between focal depth and stress drop (*e.g.*, EPRI, 2006). If this were the explanation invoked for the low amplitudes of the Groningen recordings, it would be difficult to explain why a similar effect was not observed in the Roswinkel recordings that dominate the Dost *et al.* (2004) database. Moreover, unpublished studies of the Groningen earthquakes at KNMI do not indicate that the earthquakes were of particularly low stress drop (Dr Bernard Dost, *personal communication*, 2013).

Before considering other potential mechanisms that could lead to the low amplitudes of acceleration and velocity observed in the Groningen field recordings, it may be useful to look at another characteristic of the recordings, namely the ratios of peak velocity to peak acceleration (PGV/PGA). This ratio is considered to be an indication of the frequency content of the ground motion (*e.g.*, Pavel & Lungu, 2013), with higher values of the ratio corresponding to motions dominated by lower frequencies of motion. Figure 7.4 shows the ratios from the Groningen recordings, compared with the ratios inferred from median predicted values of PGV and PGA from the GMPEs of Dost *et al.* (2004) and Akkar *et al.* (2013). The strong dependence of the ratio on earthquake magnitude is immediately apparent, and is entirely consistent with the expectation from both seismological theory and empirical data that larger earthquakes produce ground motions with relatively lower frequency contents. The surprising feature of the plot, however, is that the ratios calculated from the Groningen recordings are very large compared to what would be expected from earthquakes in this magnitude range. The implication would be that the mechanism leading to diminished amplitudes of the motion preferentially suppresses high-frequency motions. This might suggest the influence of the soft soils at the ground surface, which include peat layers in some locations, since such deposits can effectively filter out the higher frequency motion. However, soft soil layers that would tend to significantly reduce PGA in this way would be expected to have a much lesser effect on PGV and more likely to result in some amplification of the peak velocity. Pronounced diminution of both PGA and PGV might result from extremely non-linear response of the soil layers, but this would require much more energetic motions than those that could be generated by such small-magnitude earthquakes. Therefore, near-surface attenuation by soft soil layers is an unlikely reason for the low amplitudes of both PGV and PGA.

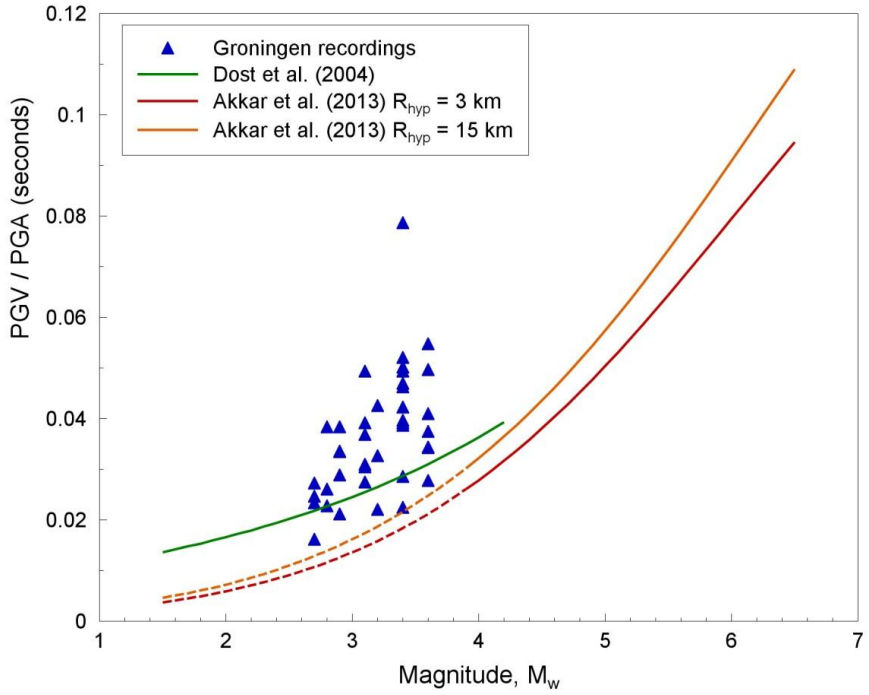

Figure 7.4 *PGV/PGV ratios from the Groningen field data plotted against earthquake magnitude. The curves are ratios calculated from the GMPEs of Dost et al. (2004) and Akkar et al. (2013), the latter plotted for V_{s30} = 200 m/s.*

The cause for the low amplitudes of the recorded motions in the Groningen field is most probably related to the presence of a high-velocity layer directly above the gas reservoir (Figure 7.5). This high-velocity layer is the so-called basal anhydrite encountered in the lowest part of the Zechstein salt formation that overlies the gas reservoir (section 2.1.2). The influence of this layer in terms of reflecting and refracting upward propagating seismic waves is discussed by Kraaijpoel & Dost (2013). The presence of such a strong velocity inversion is very likely to inhibit the strength of direct wave arrivals to the ground surface and this is therefore the most likely explanation for the low levels of recorded motion in the Groningen gas field. That this is the most likely explanation for the over-estimation of the recorded peaks illustrated in Figure 7.3 is supported by the fact the Roswinkel gas reservoir is located above the Zechstein formation (*e.g.*, Duin *et al.*, 2006).

The apparently larger impact of the basal anhydrite on high-frequency motions (and hence on PGA) than on PGV would be explained by the very limited thickness of the high-velocity layer, which results in its presence only having a notable effect on seismic energy with short wavelengths (*i.e.*, high-frequency motions). If this is the case, then the beneficial effect would diminish to some extent with increasing earthquake magnitude and radiated wave fields with relatively more low-frequency content. Similarly, if the fault ruptures for larger earthquakes initiating in the reservoir were to rupture upwards, the radiation from the portion of the fault rupture above the basal anhydrite would clearly not be affected by the velocity contrast resulting from this stratigraphic feature.

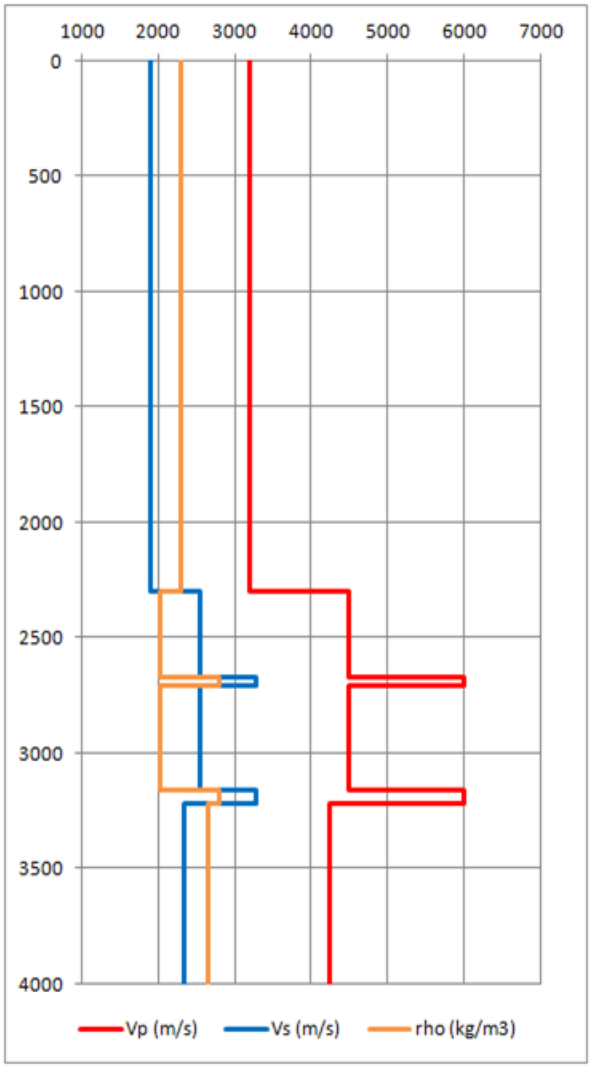

Figure 7.5 *Profiles of S-wave and P-wave velocities and mass density at a location in the southern part of the Groningen field. The gas reservoir is a little of 3 km below the ground surface, directly below the lower high-velocity layer (Oates & Noble, 2011).*

7.2.3 Selection and Modification of the Akkar et al. (2013) GMPE

The Dost *et al.* (2004) GMPE was originally chosen on the basis of having been derived from recordings of small-magnitude, shallow-focus earthquakes in the Netherlands. In view of some of the shortcomings of the model with regards to other selection criteria listed in Section 7.2.1, and the marked overestimation of the peaks from the Groningen field recordings (none of which were used in the derivation of the equations), it was decided to select another equation as an alternative.

The models of Akkar *et al.* (2013) were identified as satisfying nearly all of the selection criteria established to fulfill the project requirements. The study presents completely consistent equations for both PGA and PGV, and includes equations in which the hypocentral distance metric is used. These equations include V_{s30} as an explanatory variable and are applicable for a range of values that extends to below 200 m/s (and

moreover they model the non-linearity in the site response for soft sites and stronger bedrock motions). The equations also provide the standard deviation of the aleatory variability decomposed into between-event and within-event components. The one criterion that the equations do not satisfy (apart from the obvious shortcoming of not being based on data from Groningen or from the Netherlands) is that the range of earthquake magnitudes for which they are derived (M_w 4 to 7.6) does not extend as low as required. The lower magnitude limit was set at M_w 4 rather than the more common threshold of M_w 5 precisely to avoid overestimations at lower magnitudes, but extrapolating the equations to M_w 1.5 would carry very considerable uncertainty. Moreover, the extrapolated predictions for the magnitude-distance combinations of the Groningen earthquake recordings (and for normal-faulting earthquakes and V_{s30}=200 m/s) overestimate the recorded PGV values as much as the Dost *et al.* (2004) equation and the recorded PGA values by an even greater margin.

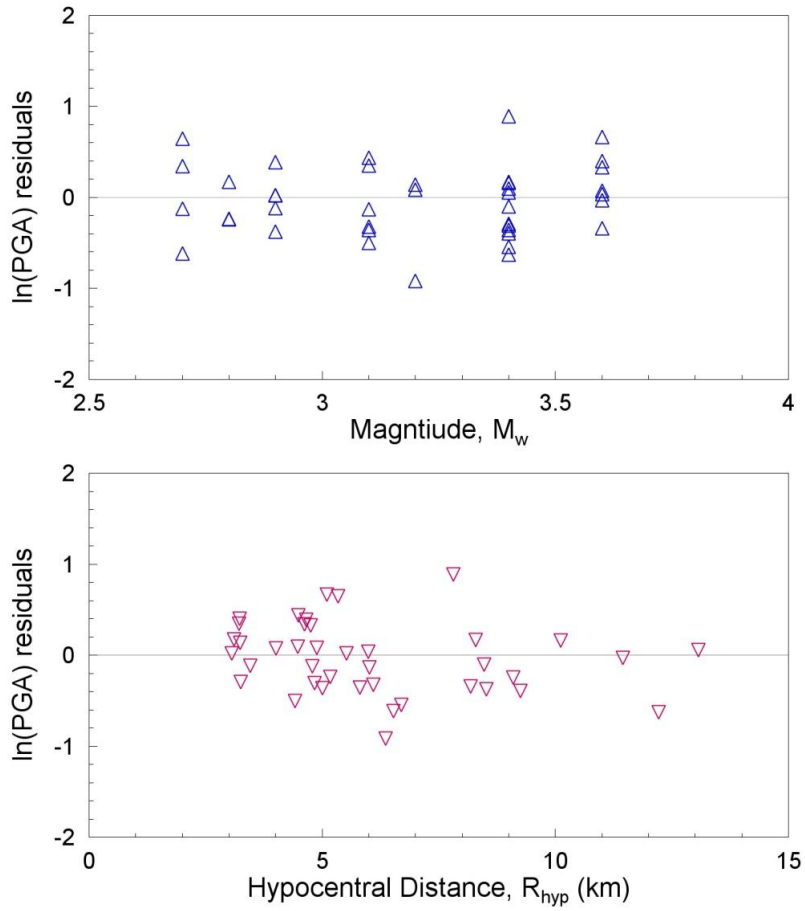

Figure 7.6 *Residuals of PGA calculated from the Groningen field motions with respect to predictions from the adjusted Akkar et al. (2013) equation. The residuals are calculated from the natural logarithm of the observed value minus the natural logarithm of the predicted median value.*

In order to develop a model that is simultaneously well-constrained for larger magnitudes and consistent with the Groningen field recordings at smaller magnitudes, adjustments were made to the magnitude scaling and magnitude-dependent attenuation terms in the Akkar *et al.* (2013) model such that the equation could be fitted to the Groningen data and remain unchanged above a certain magnitude threshold, without introducing a discontinuity between the equations for small and large magnitudes. The coefficients for these adjustments were found by inspection rather than rigorous statistical fitting, which means that there may be other suites of values that produce slightly better fits to the data; however, since the adjusted equations are not being extrapolated far beyond the range of the data to which they are adjusted, such minor differences are of no importance. The adjusted equations provide a very good fit to the Groningen data, as the residual plots for PGA in Figure 7.6 illustrate clearly (the plots for PGV residuals look very similar).

The final question to be addressed in developing the modified Akkar *et al.* (2013) equations for hazard and risk analyses in the Groningen field is whether it was necessary to make any modifications for the standard deviation for the smaller-magnitude portion of the adjusted equations. A number of GMPEs have sigma values that increase with decreasing magnitude, although it is still debated whether this is an artefact of poorly-determined magnitude and distance values for smaller events (*e.g.*, Strasser *et al.*, 2009). The decision was taken to maintain the standard deviations for PGA and PGV—and their decomposition into between-event and within-event parts—across the full range of magnitudes, for two reasons. The first of these is that the sigma values are already large (and possibly inflated by 'noisy' metadata associated with the small-magnitude recordings in the original database). The second is that the standard deviations of the residuals shown in Figure 7.6 are relatively small, which notwithstanding the small sample size from which they are calculated suggests that the variability in the small-magnitude predictions is not particularly large.

7.2.4 Epistemic Uncertainty in Ground-Motion Predictions

The modified Akkar *et al.* (2013) equations for PGA and PGV were developed as a starting model for the estimate of peak ground motions from potential induced-earthquakes in the Groningen field, but it is important to acknowledge that there is considerable epistemic uncertainty associated with the application of these equations. Epistemic uncertainty refers to the uncertainty arising from incomplete knowledge, which is distinct from the aleatory variability associated with the ground-motion predictions. Since the database of Groningen ground-motion recordings is relatively sparse, and may therefore represent a biased sample, there is some degree of epistemic uncertainty even in the range of small-magnitude predictions. Even in regions with abundant databases of ground-motion recordings, such as California, it is common practice in seismic hazard assessment to combine several locally-derived GMPEs in a logic-tree formulation (*e.g.*, Bommer *et al.*, 2005), and moreover to impose additional increments of uncertainty in the median predictions to reflect the epistemic uncertainty that may arise from biases in the data and lack of data in certain ranges of magnitude and distance (Petersen *et al.*, 2008). For the prediction of ground-motion amplitudes from earthquakes of M_w 4 and larger in the Groningen field, for which there are no data whatsoever, the epistemic uncertainty must, by definition, be even larger.

For the current hazard model, time constraints have prevented the development of suitable model for the range of epistemic uncertainty in the ground-motion predictions, which is a non-trivial undertaking if it is to be done properly (Bommer, 2012). However, it should be borne in mind that there is likely to be an appreciable level of epistemic uncertainty associated with the application of the proposed preliminary equations, and the precision with which the resulting ground motions and hazard levels can be calculated should not be interpreted as representing accuracy.

7.2.5 Spatial Correlations in Ground Motions

The GMPEs developed for and applied in this hazard study effectively assume complete independence between the motions at different locations as a result of a particular earthquake. In practice, analyses of recordings from dense strong-motion recording networks have shown that the peak motions at closely-spaced instruments tend to be correlated (*e.g.*, Boore *et al.*, 2003). The correlation decays rapidly with increasing separation of the stations, but can be quite high for distances of less than about 3 km.

Considering spatial correlation of ground motions in probabilistic seismic risk calculations (using, as in this project, Monte Carlo sampling), will tend to lead to higher levels of estimated damage and loss. The reason is that the spatial correlation will produce large pockets of elevated levels of motion, and for those simulations where these coincide with densely-populated areas of vulnerable building stock, it can be expected that particularly high damage levels will result (*e.g.*, Crowley *et al.*, 2008). In the exploratory risk calculations run so far, spatial correlation of the ground motions has not been explicitly included, which might ordinarily lead to some underestimation of the impact on the building stock. However, the calculations have been performed on spatially-aggregated building stock, in which PGA values are calculated at the centre points of a 3x3 km grid, and the same level of shaking applied to all building locations within that square. This discretization of the exposure (building stock), which is adopted for computational efficiency, produces a very similar effect to that which would result from explicit inclusion of spatial correlation of ground motions.

7.2.6 Duration of Ground Shaking

Another important feature of the ground motion is the duration of the strong shaking interval, which can also be characterized by the effective number of cycles of motion. For structures such as unreinforced masonry, which degrade in both strength and stiffness under repeated cycles of loading, the duration of the shaking has an important influence on the degree of damage experienced under a given amplitude of ground motion (*e.g.*, Bommer *et al.*, 2004). One approach that could be used to incorporate this feature of the ground shaking into the seismic hazard analysis would be a vector analysis that simultaneously estimating both PGA and duration by using a suitable expression for the correlation between the residuals in the prediction of the two parameters. Such functions have been derived by Bradley (2011) who found a negative correlation between peak amplitudes and duration, such that when the hazard analysis produces relatively high values of PGA, for example, these would correspond to motions with very short durations.

Since the hazard is currently being characterized only in terms of PGA and PGV, the influence of duration must be accounted for in any fragility functions used to estimate damage. This is especially the case if the fragility functions adopted are based on field observations following earthquakes of larger magnitude, or else from experiments or analyses using recordings of larger magnitude earthquakes, since the Groningen hazard study is considering a range of magnitudes that are centered on much smaller values than those generally involved in earthquake damage and loss estimations. The duration of ground shaking scales strongly with magnitude and small-magnitude earthquakes will generally be expected to produce ground motions of very short duration (*e.g.*, Bommer *et al.*, 2009).

7.3 Conclusions

This chapter has described how the energy by an earthquake moves to the surface and causes movement of the ground. In the next chapter, this is combined with the insights into the induction of earthquakes (Chapter 6) motions to provide hazard maps. The following conclusions have been drawn:

- Recorded peak ground accelerations (PGA) and velocities (PGV) from induced earthquakes in the Groningen field show remarkably low amplitudes, even compared to recordings from earthquakes of similar magnitude in the Roswinkel field.
- The most likely explanation for these low amplitudes is the effect of the high-velocity, high-density basal anhydrite layer in the Zechstein formation immediately above the Groningen gas reservoir, since this creates a strong negative impedance contrast.
- The beneficial effect of the basal anhydrite is not assumed to hold for motions from larger earthquakes (M>4) until verified by other investigations, and for the initial hazard analysis it is assumed that ground-motion amplitudes will be comparable to those recorded in tectonic earthquakes.
- On this basis, ground-motion prediction equations (GMPEs) derived from recordings of tectonic earthquakes in Europe and the Middle East have been adopted for the prediction of PGA and PGV. The equations were selected on the basis of using hypocentral distance, which is consistent with the way earthquakes are modelled in the hazard analysis, and including a term for site amplification effects that is able to model the influence of the soft near-surface conditions encountered in much of the Groningen field.
- The equations have been adopted in their original form for larger earthquakes, but adjusted below a threshold magnitude (4.2 for PGA, 3.8 for PGV) in order to provide a good fit to the Groningen data at smaller magnitude levels.
- Additional work is required to refine the local applicability of the selected GMPEs to the Groningen field and also to estimate the associated levels of epistemic uncertainty.
- Since currently only PGA and PGV are being predicted in the hazard analysis, it is important to take account of the fact that for most of the earthquakes considered in the hazard analysis, the duration of shaking will be short as a result of the small magnitude of these earthquakes.

7.4 References

Akkar, S., M.A. Sandıkkaya & J.J. Bommer (2013). Empirical ground-motion models for point- and extended-source crustal earthquake scenarios in Europe and the Middle East. Bulletin of Earthquake Engineering, in press, DOI 10.1007/s10518-013-9461-4.

Atkinson, G.M. & M. Morrison (2009). Observations on regional variability in ground-motion amplitude for small-to-moderate magnitude earthquakes in North America. Bulletin of the Seismological Society of America 99(4), 2393-2409.

Bommer, J.J. (2012). Challenges of building logic-trees for probabilistic seismic hazard analysis. Earthquake Spectra 28(4), 1723-1735.

Bommer, J.J. & N.A. Abrahamson (2006). Why do modern probabilistic seismic hazard analyses lead to increased hazard estimates? Bulletin of Seismological Society of America 96(6), 1967-1977.

Bommer, J.J. & S. Akkar (2012). Consistent source-to-site distance metrics in ground-motion prediction equations and seismic source models for PSHA. Earthquake Spectra 28(1), 1-15.

Bommer, J.J. & J.E. Alarcón (2006). The prediction and use of peak ground velocity. Journal of Earthquake Engineering 10(1), 1-31.

Bommer, J.J., G. Magenes, J. Hancock & P. Penazzo (2004). The influence of strong-motion duration on the seismic response of masonry structures. Bulletin of Earthquake Engineering 2(1), 1-26.

Bommer, J.J., F. Scherbaum, H. Bungum, F. Cotton, F. Sabetta & N.A. Abrahamson (2005). On the use of logic trees for ground-motion prediction equations in seismic hazard assessment. Bulletin of the Seismological Society of America 95(2), 377-389.

Bommer, J.J., P.J. Stafford & J.E. Alarcón (2009). Empirical equations for the prediction of the significant, bracketed and uniform duration of earthquake ground motion. Bulletin of the Seismological Society of America 99(6), 3217-3233.

Bommer, J.J., P.J. Stafford, J.E. Alarcón & S. Akkar (2007). The influence of magnitude range on empirical ground-motion prediction. Bulletin of the Seismological Society of America 97(6), 2152-2170.

Boore, D.M. (2003). Simulation of ground motion using the stochastic method. Pure and Applied Geophysics 160(3-4), 635-676.

Boore, D.M., J.F. Gibbs, W.B. Joyner, J.C. Tinsley & D.J. Ponti (2003). Estimated ground mMotion from the 1994 Northridge, California, eEarthquake at the site of the Interstate 10 and La Cienega Boulevard bridge collapse, west Los Angeles, California. Bulletin of Seismological Society of America 93(6), 2737–2751.

Boore, D.M., W.B. Joyner & T.E. Fumal (1997). Equations for estimating horizontal response spectra and peak acceleration from western North American earthquakes: A summary of recent work. Seismological Research Letters 68(1), 128–153.

Bothara, J.K., R.P. Dhakal & J.B. Mander (2010). Seismic performance of an unreinforced masonry building: An experimental investigation. Earthquake Engineering & Structural Dynamics 39(1), pp. 45-68.

Bradley, B.A. (2011). Correlation of significant duration with amplitude and cumulative intensity measures and its use in ground motion selection. Journal of Earthquake Engineering 15(6), 809-832.

Campbell, K.W. (2003). Prediction of strong ground motion using the hybrid empirical method and its use in the development of ground-motion (attenuation) relations in eastern North America. Bulletin of the Seismological Society of America 93(3), 1012-1033.

Chiou, B., R. Youngs, N. Abrahamson & K. Addo (2010). Ground-motion attenuation model for small-to-moderate shallow crustal earthquakes in California and its implications on regionalization of ground-motion prediction models. Earthquake Spectra 26(4), 907-926.

Crowley, H. & J.J. Bommer (2006). Modeling seismic hazard in earthquake loss models with spatially distributed exposure. Bulletin of Earthquake Engineering 4(3), 249-275.

Crowley, H., P.J. Stafford & J.J. Bommer (2008). Can earthquake loss models be validated using field observations? Journal of Earthquake Engineering 12(7), 1078-1104.

Dangkua, D.T. & Cramer, C.H. (2011). Felt intensity versus instrumental ground motion: A difference between California and Eastern North America? Bulletin of the Seismological Society of America 101(4), 1847-1858.

Deichmann, N. (2006). Local magnitude, a moment revisited. Bulletin of the Seismological Society of America 96(4A), 1267-1277.

Dost, B., T. van Eck & H. Haak (2004). Scaling of peak ground acceleration and peak ground velocity recorded in the Netherlands. Bolletino di Geofisica Teorica ed Applicata 45(3), 153-168.

Douglas, J. (2011). Ground-motion prediction equations 1964-2010. BRGM/RP-59356-FR, BRGM, Orléans, France, 444 pp.

Douglas, J. (2012). Consistency of ground-motion predictions from the past four decades: peak ground velocity and displacement, Arias intensity and relative significant duration. Bulletin of Earthquake Engineering 10(5), 1339-1356.

Douglas, J., B. Edwards, V. Convertito, N. Sharma, A. Tramelli, D. Kraaijpoel, B. Mena Cabrera, N. Maercklin & C. Troise (2013). Predicting ground motion from induced earthquakes in geothermal areas. Bulletin of the Seismological Society of America 103(3), in press.

Duin, E.J.T., J.C. Doorenbal, R.H.B. Rijkers, J.W. Verbeek & Th.E. Wong (2006). Subsurface structure of the Netherlands – results of recent onshore and offshore mapping. Netherlands Journal of Geosciences 85(4), 245-276.

EPRI (2006). Truncation of the lognormal distribution and value of the standard deviation for ground motion models in the Central and Eastern United States. EPRI Report No. 1013105, Electric Power Research Institute, Palo Alto, California, 100 pp.

Kraaijpoel, D. & B. Dost (2013). Implications of salt-related propagation and mode conversion effects on the analysis of induced seismicity. Journal of Seismology 17(1), 95-107.

Papaspiliou, M., S. Kontoe & J.J. Bommer (2012). An exploration of incorporating site response into PSHA – Part I: Issues related to site response analysis methods. Soil Dynamics & Earthquake Engineering 42, 302-315.

Pavel, F. & D. Lungu (2013). Correlations between frequency content indicators of strong ground motion and PGV. Journal of Earthquake Engineering 17(4), 543-559.

Petersen, M.D. A.D. Frankel, S.C. Harmsen, C.S. Mueller, K.M. Haller, R.L. Wheeler, R.L. Wesson, Y. Zeng, O.S. Boyd, D.M. Perkins, N. Luco, E.H. Field, C.J. Wills & K.S. Rukstales (2008). Documentation for the 2008 Update of the United States National Seismic Hazard Maps, USGS Open-File Report 2008-1128, US Geological Survey, Reston, VA. 61 pp.

Rietbrock, A., F. Strasser & B. Edwards (2013). A stochastic earthquake ground-motion prediction model for the United Kingdom. Bulletin of the Seismological Society of America 103(1), 57-77.

Strasser, F.O., N.A. Abrahamson & J.J. Bommer (2009). Sigma: issues, insights, and challenges. Seismological Research Letters 80(1), 40-56.

Wald, D.J., V. Quitoriano, T.H. Heaton & H. Kanamori (1999). Relationships between peak ground acceleration, peak ground velocity, and modified Mercalli intensity in California. Earthquake Spectra 15(3), 557-564.

Worden, C.B., Gerstenberger, M.C., Rhoades, D.A. & Wald, D.J. (2012). Probabilistic relationships between ground-motion parameters and Modified Mercalli Intensity in California. Bulletin of the Seismological Society of America 102(1), 204-221.

8 Probabilistic Seismic Hazard Assessment

8.1 Interpretation of Eurocode 8 for the case of production-induced seismicity

The Eurocodes are the current technical standards for structural design in Europe, and it is now compulsory for the 28 countries in the Eurocode zone to adopt these in place of existing national standards. Eurocode 8 specifically deals with earthquake-resistant design of structures (CEN, 2006). Each country adopting Eurocode 8 must develop a National Annex to indicate how the code is implemented; the National Annex for the Netherlands has not yet been produced.

Eurocode 8 is based on a limit state philosophy, specifying structural performance targets associated with different levels of seismic loading. The fundamental requirement is for No Collapse (NC), intended to ensure life safety; this is referred to as the Ultimate Limit State (ULS), and is associated with ground motions having a 10% probability of exceedance during 50 years, or a return period of 475-years. The Serviceability Limit State (SLS) targets function of structures, comfort of occupants, and appearance of buildings, and is anchored to design ground motions with 50% probability of exceedance in 50 years, or a return period of 95 years. The 475-year return period as the basis for defining the basic design motions was adopted in most seismic codes around the world after being first introduced in the United States, despite being based on a series of rather arbitrary decisions rather than any quantitative risk considerations (Bommer & Pinho, 2006).

Eurocode 8 consists of six parts, with Part 1 defining the basic seismic actions and the other parts deal with specific structural applications. Part 3 is entitled "Assessment and Retrofitting of Buildings", for which three limit states and associated return periods are specified. The narration in the code notes that the Significant Damage (SD) Limit State, tied to ground shaking with a 475-year return period, is comparable to the NC limit state for new buildings. In this regard, Eurocode 8 is unusual in requiring that retrofitted buildings should achieve the same levels of seismic performance as new buildings, whereas it is widely accepted in earthquake engineering practice around the world that lower levels of seismic capacity can be accepted for retrofitted buildings than would be required in new buildings (*e.g.*, Grant *et al.*, 2007; ATC, 1978; NZSEE, 2006; NEHRP, 2009).

Notwithstanding the very conservative approach of requiring seismic retrofit to match the earthquake-resistant capacity of new buildings, the framework of Eurocode 8 was adopted in this report for the consideration of assessing the structural capacity of buildings in the Groningen field. This requires that the PGA and PGV values corresponding to a 475-year return period, which is equivalent to an annual exceedance probability of 0.002, must be calculated. This is done by selecting a production period, starting now and continuing for a specified number of years, and then calculating the levels of PGA and PGV that would have an average 0.2% probability of being exceeded during that period. Calculating the hazard in this way, that is, for a limited time period rather than the total hazard until the end of the field life is based on the assumption of no time delay between reservoir compaction and any associated induced seismicity. This is consistent with an analysis of changes in earthquake activity rates which indicated little or no delay relative to changes in gas production rates [Bourne & Oates 2013, Appendix C].

8.2 Hazard assessment: summary of approach and method implemented

Probabilistic seismic hazard analysis (PSHA) is understood to mean the characterization and estimation of the frequency of occurrence of stated levels of earthquake ground motion at specified locations. Estimation of predicted levels of ground motion is necessarily a probabilistic calculation but it is also common to carry out deterministic calculations (DSHA) to estimate the ground motions due to specific earthquake scenarios (Dost, 2013). As Bommer and Abrahamson (2006) point out, the fundamental difference between PSHA and DSHA is simply that PSHA integrates over all earthquake scenarios, properly weighted by probability density functions, whereas DSHA considers the effects of individual scenarios. Motivated by these arguments, the approach that has been followed for the analysis of the Groningen induced seismic hazard is PSHA.

PSHA methods can be divided into two categories: the classic approach in which *expected* ground motions are estimated directly from the underlying probability distributions and Monte Carlo approaches in which

distributions of ground motions are generated for synthetic earthquake catalogues by repeated sampling of these same probability distributions. Classic PSHA has the advantage of a significant body of literature describing the formalism and possibly advantages of speed of calculation compared with the Monte Carlo approach. A major disadvantage of the classic PSHA approach is that it is based on the assumption of stationary seismicity rates, defined in terms of frequencies of events per unit time, whereas the source model that we set out to implement is derived from a time-dependent compaction process. The Monte Carlo approach, although less well documented in the literature, has the advantage of conceptual simplicity and versatility which enabled the compaction-based source model (Section 6.2.4) to be incorporated. It is also more easily integrated with building exposure and fragility data to deliver risk or loss estimates over a large urban area (see Bommer and Crowley 2006). Initial internal discussions concluded that it was unlikely that we would find a third party PSHA software package that would properly handle the compaction-driven induced seismic hazard of the Groningen Field. It was decided therefore to write our own PSHA code, tailored to the needs of Groningen and following the Monte Carlo approach for the reasons mentioned above. To be better able to identify errors in implementation of the method, it was decided to write two independent codes, one in Python (Stephen Bourne) and the other in C (Steve Oates). There was minimal sharing of details between the two implementations apart from a general consensus on the overall method. This allowed independent cross-checking of the hazard results at any stage and has proved to be key in identifying bugs and other inconsistencies.

The Monte Carlo PSHA codes have been implemented according to the following scheme. (Bourne et al 2013). Each catalogue of earthquakes is generated by first drawing a seismic moment budget from a distribution derived from the Groningen Field compaction model (as detailed in section 6.2.4). Event locations are assigned by randomly sampling the expected event density map which itself is derived from the predicted compaction map characterizing the chosen production interval. Magnitudes are assigned by random sampling of a truncated Gutenberg-Richter type distribution where the catalogue's total moment is constrained to not exceed the moment budget. In this way a specified number of catalogues is generated and, for each event, ground motions (PGA and PGV) are calculated at each of the nodes of the surface output grid. In calculating the ground motion, the distribution of variations of the chosen ground motion prediction equation (GMPE) about its mean is randomly sampled. Hazard curves are generated for each surface location by counting the exceedances of specified ground motion thresholds and averaging over the number of simulated catalogues.

8.3 Hazard maps: PGA and PGV for a 475 year return period

Guided by the interpretation of Eurocode 8 as a standard, described above, maps of ground motion equivalent to the 475 year return period are calculated from the set of hazard curves. The PGV and PGA hazard maps generated, using the modification of the Akkar et al (2013) GMPE, described in section 7.2 above, are shown in Figure 8.1.

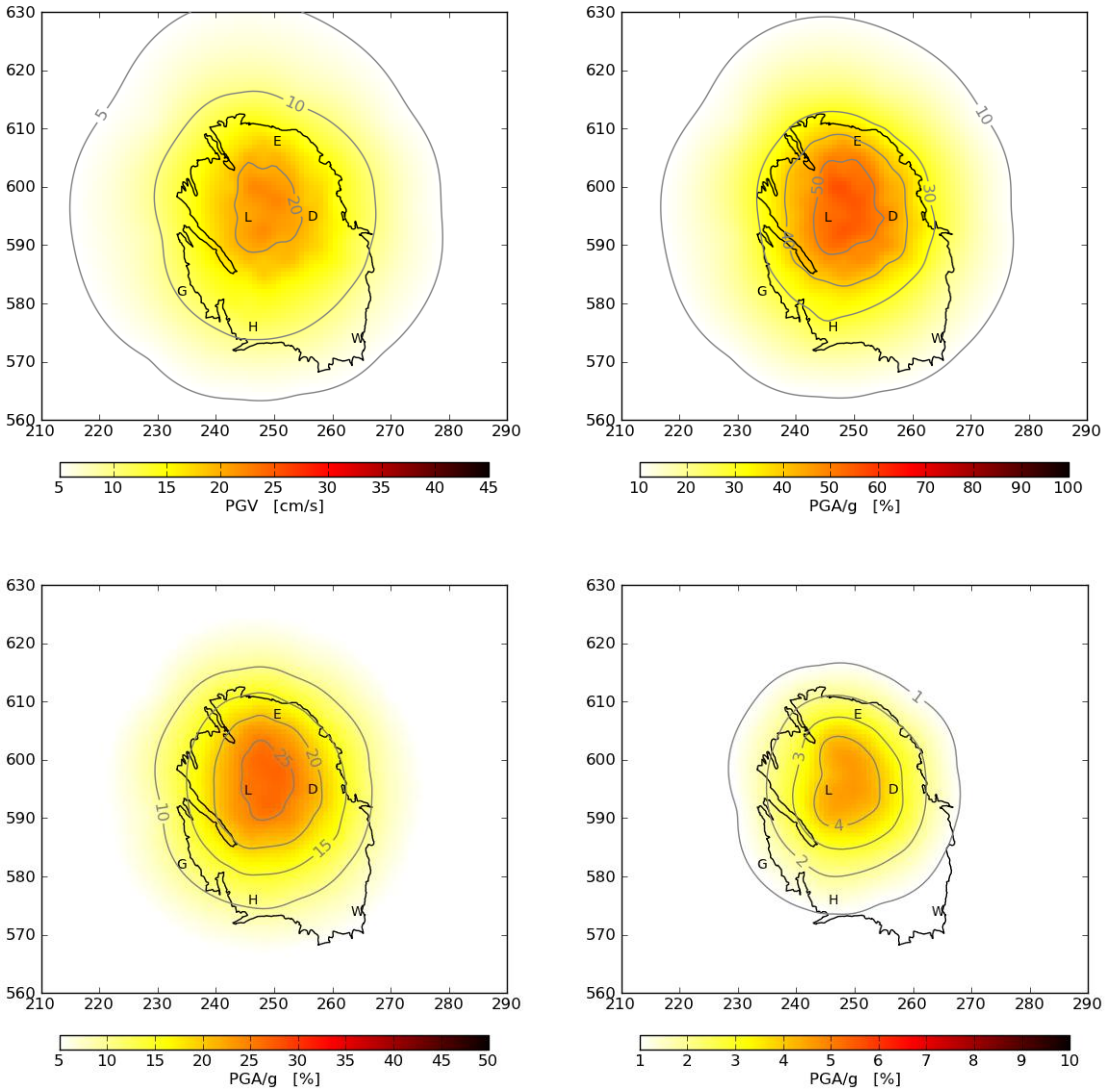

Figure 8.1 *Top Row: Predicted ground motion with an average annual 0.2% chance of exceedance, for the next 10 years from 2013 to 2023. Maximum ground motions are 22 cm/s and 57% of the acceleration due to gravity (g), located above the region of greatest reservoir compaction. The black line denotes the field outline and the letters D to W denote Delfzijl, Eemshaven, Groningen, Hoogezand, Loppersum and Winschoten respectively. Bottom Row: Predicted ground motion with an average 10% chance of exceedance and 50% chance of exceedance during the next 10 years from 2013 to 2023. In these hazard calculations the linear compaction model was used.*

The process described for generating ground motion hazard maps aggregates the numbers of exceedances at each location and so does not keep track of the combinations of event magnitude, distance and GMPE variation giving rise to the ground motion exceedance rates. Disaggregation on the other hand is the process of looking at the hazard in terms of the magnitude, hypocentral distance and GMPE variation of the events giving rise to it (Bazzurro and Cornell 1999), so that questions such as `What event magnitudes and hypocentral distances contribute most to the hazard?' can be answered in a useful way. In practice, disaggregation of the hazard requires storing additional arrays during the computation relating the magnitude, source-surface location distance and GMPE variation to the resulting surface ground motion. The disaggregated hazard is illustrated in Figure 8.2 and Figure 8.3, for PGA and PGV respectively.

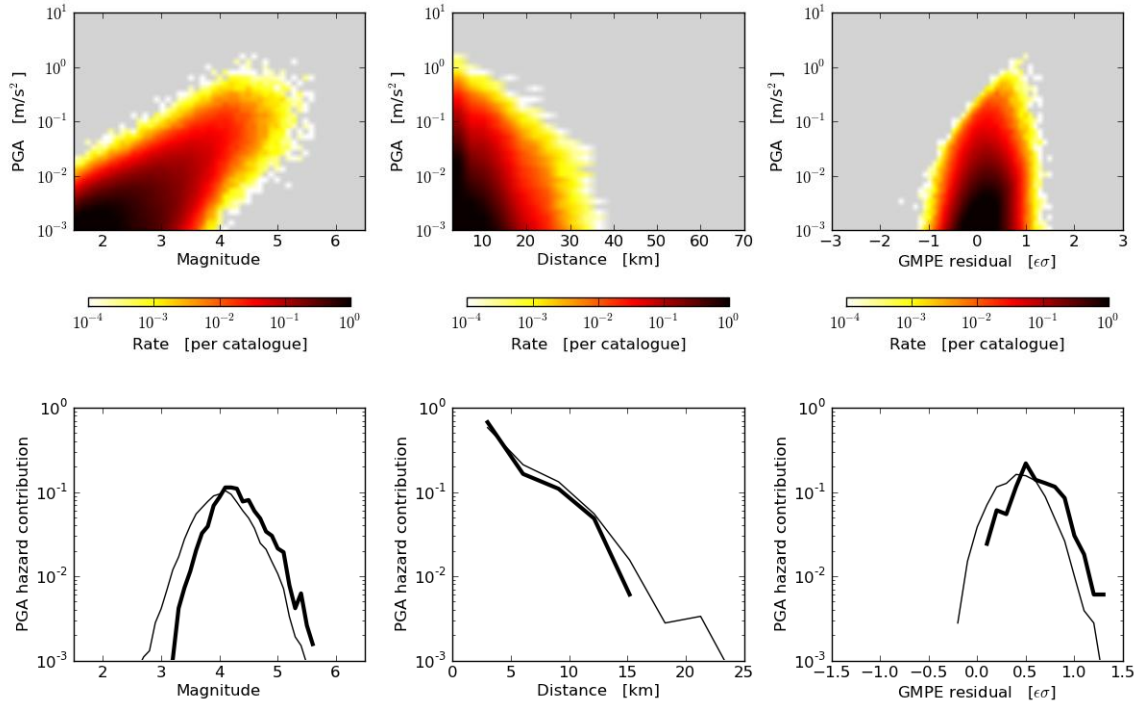

Figure 8.2 Disaggregation of the PGA hazard (see text for details).

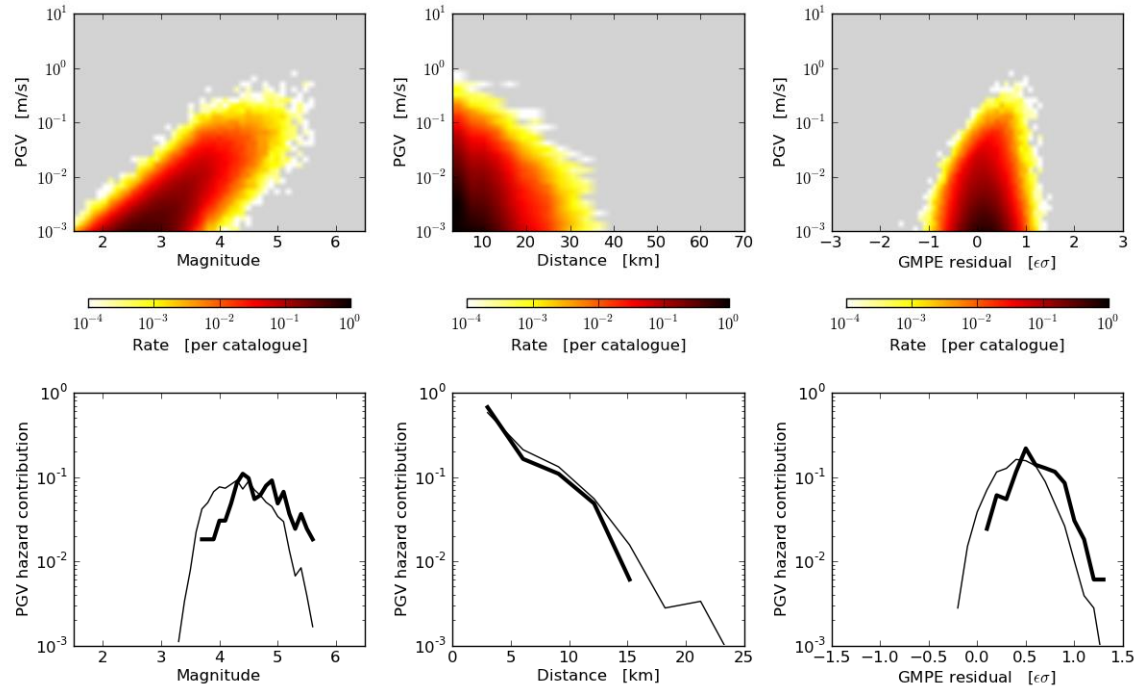

Figure 8.3 Disaggregation of the PGV hazard (see text for details).

The individual plots show: (in the first rows) the distribution of PGA occurrence rates as a function of magnitude, distance, and GMPE variation for a single surface location directly above the region of maximum reservoir compaction; (in the second rows) the fractional contribution to the total rate of peak ground velocities at this same surface location corresponding to mean annual exceedance probabilities of 0.2% (thick line) and 1% (thin line), equivalent to the Eurocode 8 performance requirements for a 10% chance over 50 and 10 years respectively.

Referring to the magnitude disaggregation plots, notice that the hazard is dominated by the intermediate magnitudes (e.g. M=4.5-5.0) typically occurring at smaller hypocentral distances. The largest magnitudes are so rare that they contribute very little to the hazard for this recurrence rate. One significant consequence of this observation is that the maximum magnitude is not an appropriate means of characterizing the seismic hazard. Note also that disaggregation of the PGV and PGA hazards leads to appreciably different dominant magnitudes reflecting the non-trivial, magnitude- and distance-dependent relationship between PGV and PGA implied by the ground motion prediction equations.

8.4 Sensitivity tests

Additional simulations were run to explore sensitivity of the calculated hazard to variations in the input. The most important of these sensitivities are summarized here.

The choice of the Ground Motion Prediction Equation (GMPE) has a major impact. Most of the simulations described in Bourne et al (2013) were run using the GMPE of Dost et al (2004), this choice having been motivated by the fact that this GMPE was the only one available which had been calibrated using data from the Netherlands (but not Groningen). Subsequent analysis of strong motion data for Groningen events, including the 2012 Huizinge event, showed however that the Dost et al (2004) and Akkar et al (2013) GMPEs significantly overestimate surface ground motions. The modification of the Akkar et al (2013) GMPE described previously (section 7.2.3) is now favored as it has been calibrated using the Groningen strong motion data and is constrained by data from elsewhere at higher magnitudes.

The production period over which average annualized ground motion exceedance rates are calculated was also shown to have a strong impact on the simulated rates. This is due to the variations in the planned production rate as the field moves from the current peak levels of off-take to lower levels of production towards the end of its intended life (see Figure 8.5). These lower future production rates correspond to lower compaction rates and so lower levels of annualized seismic hazard.

The Gutenburg-Richter *b*-value characterizing the Groningen earthquake catalogue might be expected to have a strong influence on the calculated hazard since the *b*-value, being the slope of the frequency-magnitude distribution, expresses the relative abundances of small and large events in an earthquake catalogue. Figure 8.4 (Bourne et al 2013) shows a significant variation of the *b*-value with compaction when the Groningen catalogue is divided into sub catalogues defined by compaction bins. Simulations run with a compaction-dependent *b*-value of this form give however very similar results to those obtained with a constant *b*-value of 1. As most of the expected event density corresponds to reservoir compaction in excess of 0.25m this function is approximately equivalent to decreasing the *b*-value from b=1 to b=0.8 for the entire earthquake population. The map of peak ground velocities with a mean annual exceedance chance of 0.2% shows a slight increase of up to 2cm/s within the central region of greatest reservoir compaction and a similar decrease mostly located around the southern edge of the field. It seems that the competing influences of increasing event size but reduced event number (for the large events) corresponding to the reduced *b*-value approximately balance each other out, at least in this case.

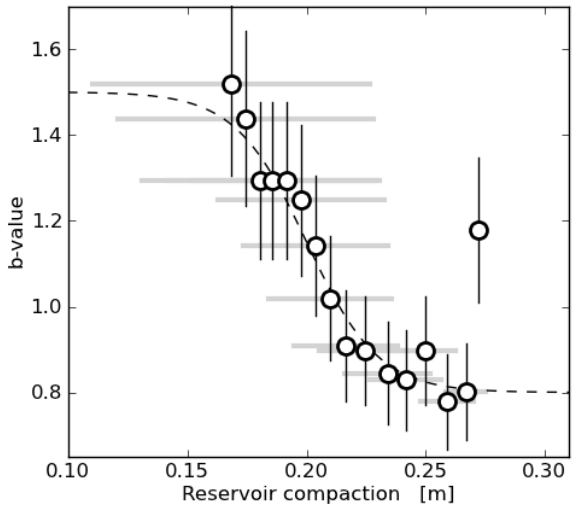

Figure 8.4 *Maximum likelihood b-value estimates for subsets of the M≥1:5 events since April 1995 binned according to reservoir compaction. Vertical error bars denote the 67% confidence interval and horizontal grey lines indicate the bin sizes.*

The main conclusion to be drawn from the results of the sensitivity tests is that better constraining the GMPE for Groningen is a top priority: this is the aim of ongoing work.

8.5 Assumptions and limitations

The most important uncertainty is the partitioning coefficient relating seismic moment budget to the volumetric strain due to compaction. The source model relies on a fit to the values of this coupling observed so far in order to estimate the impact of any future escalation. Ongoing work shows that there are also significant uncertainties in the compaction model for the field and these uncertainties translate into appreciable uncertainties in the available induced seismic moment budget.

The source model is based on the production-induced compaction with the tacit assumption that suitably located faults, pre-existing or new, will be available for the strain to be expressed as induced seismicity. A major fault mapping exercise over the field identified approximately 1700 faults from the 3D seismic data. It is assumed that many more faults than this will be undetectable on the 3D data due to having too small throws and/or extents. With thousands of faults distributed across the field the above assumption that there will be sufficient faults available on which slip can occur does not seem too restrictive. Nevertheless, an alternative approach to calculating seismic hazard would be to propose that induced earthquakes will occur only on certain major faults in the field. A model of this sort would be more akin to those used in global tectonic hazard calculations. Ongoing geomechanical work allows for evaluating the likelihood for individual faults to slip (Section 9). However, the lack of detailed information regarding fault properties (stress, friction coefficient etc.) will make it difficult to construct compelling source models of this type.

It is assumed that the seismic moment budget derives entirely from the reservoir compaction process. That is we neglect any contribution from other deformation processes such as tectonics and post-glacial rebound (see Main et al 1999) that may also contribute to the magnitude of a triggered earthquake, as discussed in section 6.1.2. See also Houtgast's (1992) catalogue of historical seismicity in the Netherlands.

Calculating the hazard for a limited time period rather than the total hazard until the end of the field life is based on the assumption of no time delay between reservoir compaction and any associated induced seismicity. This is consistent with an analysis of changes in earthquake activity rates which indicated little or no delay relative to changes in gas production rates [Bourne & Oates 2013].

The depths of the Groningen earthquakes are in almost all cases *assumed* to be 3000m, that is, the approximate reservoir depth, rather than determined from the recorded data. This is due to the fact that the monitoring array is too sparse to properly constrain event depths over most of the field. This has potential consequences for the hazard analysis in which the same assumed event depth has been used. If event

depths are significantly shallower than assumed, this will lead to higher than anticipated surface ground motions.

8.6 Time evolution of seismic hazard: projections based on planned production

The expected seismic moment release rate depends on two competing effects. First, the seismic moment released per unit of gas production increases with reservoir compaction. Second, the rate of gas production eventually decreases due to reservoir pressure depletion. Over the next 20 years or so, the first effect is expected to dominate and so the annual seismic moment is expected to tend to increase year-on-year. Thereafter, the second effect will likely dominate as the annual gas production has naturally declined to levels well- below current production rates. Figure 8.5 shows predicted initial escalation and then the long decline in annual seismic moment release according to the statistical geomechanics model. This includes a wide range of uncertainty between the expected and the upper bound of the 95% confidence interval, but the same clear temporal trend with a maximum sometime between 2025 and 2035 based on the current production plan. Such time-dependence is intrinsic to induced seismicity that necessarily has a beginning and an end. Eurocode 8 building standards were designed with time-independent natural seismicity in mind, as discussed above. Adaptation to time-variant induced seismicity needs to be addressed.

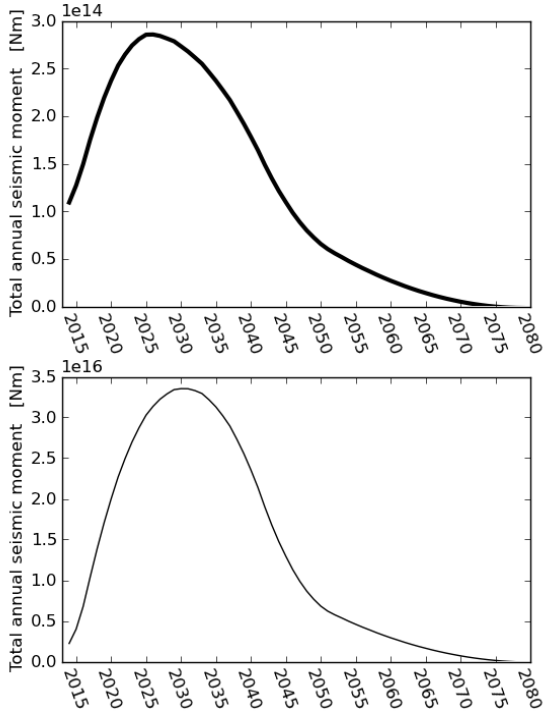

Figure 8.5 *(a) Expected annual total seismic moment release. This calculation is based on the current gas production plan and the current reservoir compaction model, the median seismic strain partitioning model, and presumes there is no delay between induced strain and induced earthquakes. (b) As (a), except for the upper bound of the 95% confidence interval of the seismic strain partitioning model.*

8.7 PGA hazard assessment

The seismological model developed recently to support Probabilistic Seismic Hazard Assessments (PSHA) for the Groningen Field (NAM, 2013) depends on future reservoir compaction. Models for reservoir compaction are well-constrained by surface subsidence measurements. However, uncertainties in these measurements and in the geomechanical relationship between subsidence and compaction means a range of different compaction models are consistent with these data. These models all exhibit similar compaction histories but predict different future compactions with differences that tend to increase with time.

Initial seismic hazard assessments were based on the linear-elastic compaction model which depends on a single parameter for reservoir compressibility as a function of porosity. An alternative time-decay compaction model has two parameters, the same reservoir compressibility parameter and a second parameter for the characteristic time-scale of exponentially-distributed delays between pressure depletion

and reservoir compaction. Monte Carlo inversion of the Groningen subsidence data indicates the characteristic time-scale is 5±5 years. This model yields a slightly better fit to these subsidence data, but this was achieved by adjusting two parameters not one, so future compactions predicted by this model may not be more reliable than those from the linear model. Nonetheless, the time-decay compaction model does offer a credible alternative compaction forecast.

The PSHA results for 2013 to 2023 based on the current production plan and the time-decay compaction model indicate a 2%, 10% and 50% chance of peak ground acceleration, PGA, exceeding 0.67*g*, 0.33*g* and 0.06*g* respectively (Figure 8.6), where *g* is the acceleration due to gravity taken to be 9.81 m/s^2. This 10-year period of assessment and the 2%, 10%, and 50% chances of exceedance are choices and the hazard results obtained depend on these choices. The choice of a 2% chance over 10 years is not equivalent to the Eurocode 8 (CEN, 2004) choice of 10% over 50 years for two reasons. First, Eurocode 8 applies to natural seismicity that does not change with time whereas Groningen experiences induced seismicity that changes with time. This means the Groningen Field will experience a different seismic hazard in each of the five 10-year intervals over the next 50 years. Second, Eurocode 8 is based on seismicity composed of independent earthquakes. This means there is a particular equivalence between probabilities of exceedance and times of exposure as described by a Poisson process. This allows the Eurocode 8 seismic performance requirement for ground motions with a 10% chance of exceedance over 50 years (often described as a 475-year return period) to be seen as equivalent to a 2% chance of exceedance over 10 years. This is not the case for the seismological model of the Groningen Field where earthquakes collectively accommodate a fraction of the strain induced by reservoir compaction. This creates a degree of inter-dependence between events so they do not exactly follow a Poisson process.

Whilst accepting there is no formal equivalence between 10% over 50 years and 2% over10 years, the results shown in Figure 8.6a are still valid on their own although there is no equivalence with Eurocode 8. Figure 8.7 shows results for a 5-year assessment period from 2013 to 2018 with a 2%, 10%, and 50% chance of PGA exceeding 0.42*g*, 0.18*g*, and 0.03*g* respectively. These PGA values are lower because there is less exposure time, less exposure to the statistical trend of increasing annual seismic moments, and less uncertainty in a shorter-term forecast. Similarly for a three year assessment period from 2013 to 2016, there is a 2%, 10% and 50% chance of PGA exceeding 0.30*g*, 0.12*g* and 0.02*g* respectively (Figure 8.8). Figure 8.9 compares the probabilities of PGA exceedance for the 10-, 5- and 3-year assessments at the location of maximum PGA.

PSHA results previously obtained for the linear-elastic compaction model (NAM, 2013) indicate a 2%, 10% and 50% from 2013 to 2023 of PGA exceeding 0.56*g*, 0.27*g*, and 0.05*g* respectively. This is an example of epistemic uncertainties due to current lack of knowledge about the mechanisms governing future reservoir compaction on the field length-scale and the production time-scale. The following section describes a systematic assessment of the key epistemic uncertainties and their influence on 2013 to 2023 PSHA for the Groningen Field.

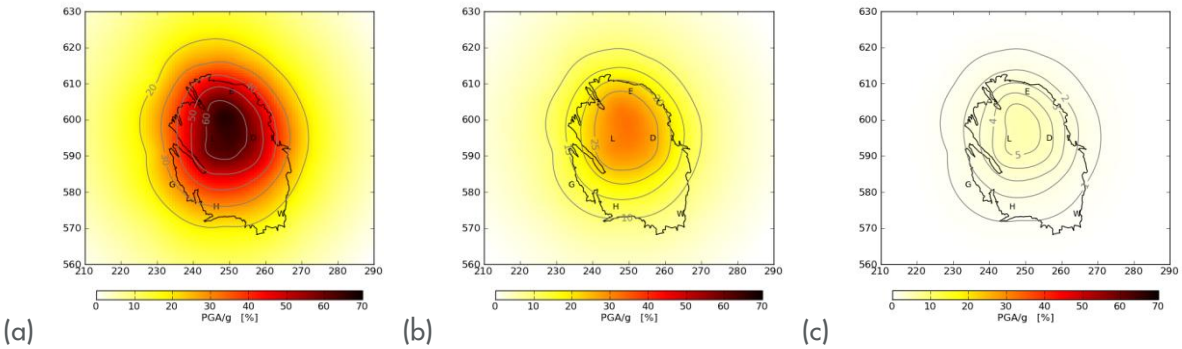

Figure 8.6 *PGA hazard maps for the 10 years from 2013 to 2023 with a (a) 2%, (b) 10% and (c) 50% chance of exceedance. This assessment is based on the current production plan, the time-decay compaction model and the Akkar et al. (2013) ground motion prediction equation modified to match accelerometer data from the Groningen Field (NAM, 2013). The maximum PGA in each case is (a) 0.67g, (b) 0.33g, and (c) 0.06g. The horizontal and vertical scales are Rijksdriehoek (RD) coordinates in km.*

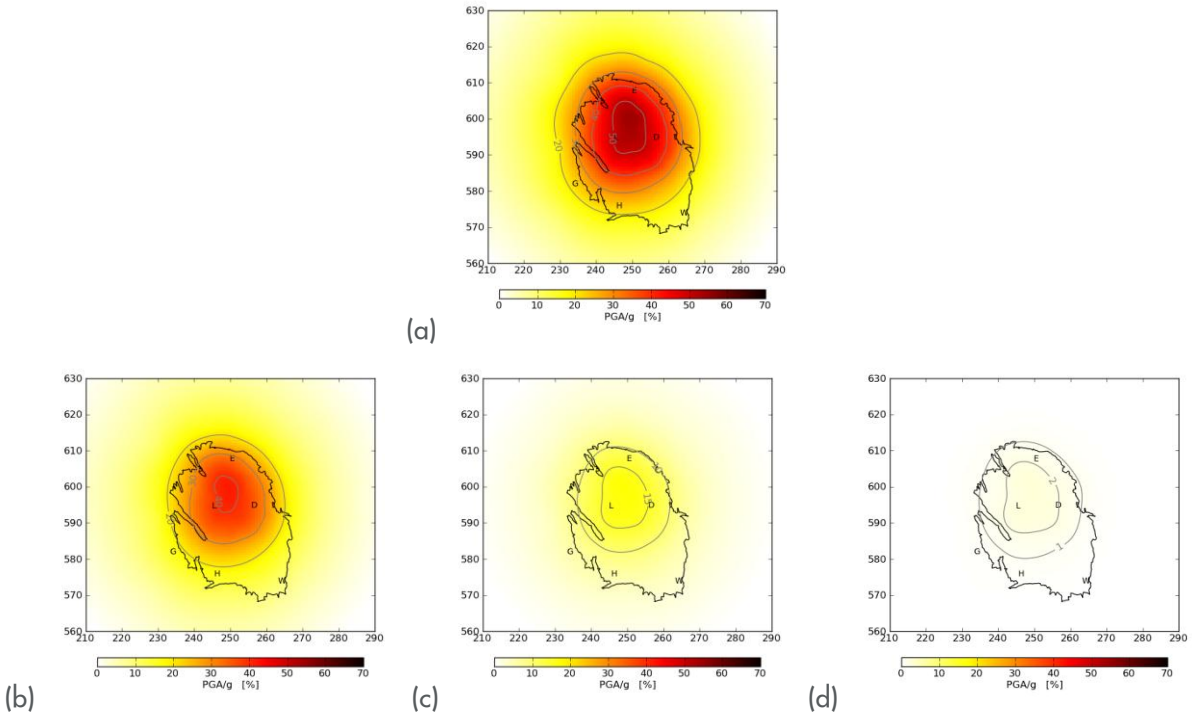

Figure 8.7 *PGA hazard maps for the 5 years from 2013 to 2018 with a (a) 1%, (b) 2%, (c) 10% and (d) 50% chance of exceedance. The maximum PGA in each case is (a) 0.54g, (b) 0.42g, (c) 0.18g, and (d) 0.03g. The horizontal and vertical scales are Rijksdriehoek (RD) coordinates in km.*

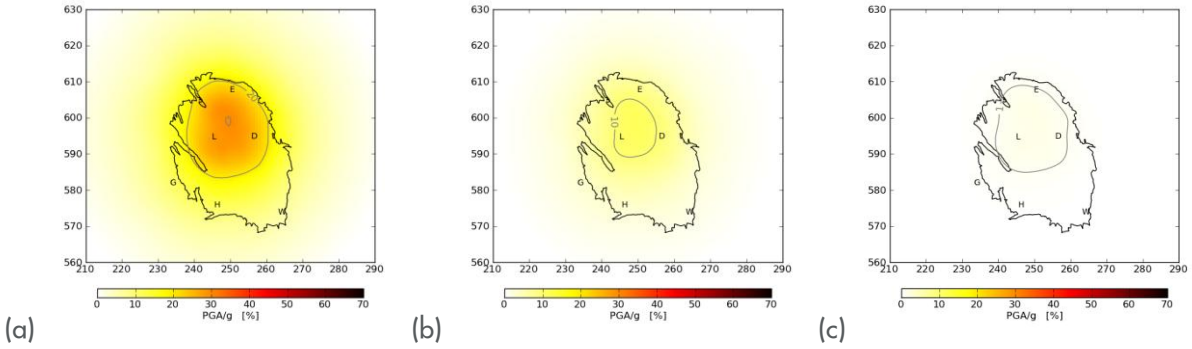

Figure 8.8 *PGA hazard maps for the 3 years from 2013 to 2016 with a (a) 2%, (b) 10% and (c) 50% chance of exceedance. The maximum PGA in each case is (a) 0.30g, (b) 0.12g, and (c) 0.02g. The horizontal and vertical scales are Rijksdriehoek (RD) coordinates in km.*

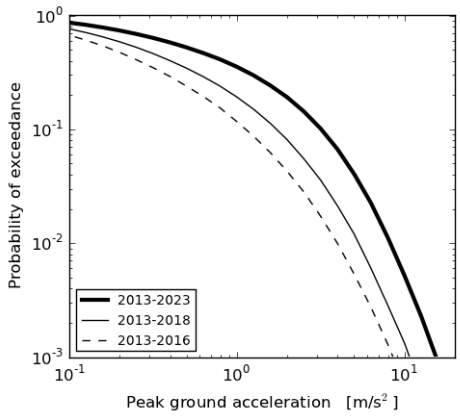

Figure 8.9 *The probability of exceedance for the maximum peak ground acceleration within the Groningen Field for three different assessment intervals: 3, 5, and 10 years. These assessments are based on the time-decay reservoir compaction model for the current production plan and the Akkar et al. (2013) GMPE modified to match accelerometer data from the Groningen Field.*

8.8 Logic-tree to assess epistemic uncertainties

True statistical variability, known as aleatory uncertainty, represents the stochastic nature of a process and is addressed in the approach to hazard assessment described here by random sampling of the appropriate distributions in the Monte Carlo simulation process. Epistemic uncertainty, on the other hand, characterises uncertainties in the values of parameters which are fixed but either unknown or known only to within a certain precision. A logic-tree approach can be used to explore the impact of key epistemic uncertainties once these have been identified and their expected ranges estimated. Each branch of the logic-tree represents a distinct scenario of a particular model and associated parameter values chosen from the spectrum of values considered to be likely. Here we describe a logic-tree approach to the characterisation of epistemic uncertainties in the PGA hazard assessment.

8.8.1 Classification of epistemic uncertainties

The experience of running the Monte Carlo hazard simulations in the current project and expert judgement, informed by previous studies, were used to identify the key epistemic uncertainties. Ranges of likely parameter values were estimated based on the recent seismological and hazard studies for the Groningen Field (Bourne & Oates 2012; Bourne & Oates 2013; Bourne et al. 2013). The logic-tree was constructed by consideration of the main components of the seismic hazard workflow: modelling of the earthquake catalogue to give moment release rate, event location and magnitude distributions and ground motion predictions for these simulated earthquakes.

Each of the uncertainties identified was characterised as likely to have appreciable or negligible impact on the hazard analysis. The uncertainties labelled as appreciable are explicitly included in the logic-tree by having branches expressing variations above and below the trunk. For those labelled as negligible no variation of the parameter value from the base case is considered. A third category was reserved for uncertainties which were excluded as being beyond the scope of the current work.

The key epistemic uncertainties – that is those labelled as appreciable – for the hazard analysis are as follows: for the source model, reservoir compaction, strain partitioning and the Gutenberg-Richter *b*-value; for the surface motion estimation, the parameterisation of the ground motion prediction equation (GMPE). These are summarised in Table 8.1. Only those sources of epistemic uncertainty classified as appreciable have been included in the logic tree. The following paragraphs give justification for the classifications chosen for the sources of epistemic uncertainty and the uncertainties included into the logic tree.

Reservoir Compaction

The reservoir compaction and the coupling constant which determines the amount of reservoir volume change expressed as seismicity, are the fundamental elements in the source model. Future compaction is predicted using a range of possible models, constrained by subsidence and compaction measurements. These measurements are, however, not sufficient to unambiguously indicate which of the compaction models should be used and so several models which lead to significantly different predictions for future compaction are carried.

Strain Partitioning Factor

Similarly, there is great uncertainty in the future evolution of the value of the factor which determines the proportion of strain expressed as earthquakes. The current value is in the range 10^{-4} – 10^{-3} but future escalation to values close to 1 would have a profound effect on the hazard and cannot be excluded at this stage.

Gutenberg-Richter *b*-value

The Gutenberg-Richter *b*-value determines the relative proportion of low- and high-magnitude earthquakes in the catalogue. It is reasonably well constrained for the catalogue as a whole to-date but there are clear indications of significant variations of the *b*-value with compaction and event location. Such variations would be expected to impact the calculated hazard and so the b-value uncertainty is also given the label

"appreciable" and varied on branches of the logic-tree. Other characteristics of the earthquake catalogue to date were considered not to merit separate branches of the logic-tree. Events are currently assumed to be in the reservoir as the sparse monitoring array currently in place does not adequately constrain event depth. Similarly earthquakes are assumed to occur by normal faulting with ruptures which do not extend appreciably above the reservoir. It is felt that these assumptions are fairly robust but will be reassessed when data from the upgraded Groningen monitoring array become available in 2014 and beyond. Release of stress from tectonic sources is recognised as a possibility but is excluded at this stage given the evidence for no historic seismicity in the north of the Netherlands.

GMPE

Seismic hazard is dependent not only on the characteristics of the earthquakes themselves but also on the propagation of the seismic waves from the source to the surface. Empirical ground motion prediction equations (GMPEs) are generally used to estimate PGV and PGA at a given surface location for a source of known magnitude and location. Because of the limited history of recorded seismicity over the Groningen field there is very little ground motion data available to constrain a Groningen-specific GMPE. This is particularly true for events of larger magnitude and so the approach used has been to adapt GMPEs from other regions by calibrating with local ground motion data where possible. The form of the GMPE is therefore considered an "appreciable" epistemic uncertainty. Scale factors relative to the base-case GMPE (the modified form of the Akkar et al 2013 GMPE) are used to represent epistemic uncertainty in the GMPE. There is also uncertainty about the extent to which the predicted ground motion varies both from location to location for a single event and from event to event, but this uncertainty was considered to be of secondary importance and was labelled as "negligible".

The set of uncertainties listed in Table 8.1 is felt to be exhaustive in that it covers all components of the hazard analysis process and considers all parameters which were identified as having appreciable associated epistemic uncertainty in previous studies (Bourne & Oates 2012; Bourne & Oates 2013; Bourne et al. 2013). Other uncertainties identified were expected to be of too limited impact to justify being explored in the logic-tree.

Source	Classification of Epistemic Uncertainties		
	Appreciable	*Negligible*	*Excluded*
Seismicity	Reservoir compaction	Focal depths	Triggered events
	Strain partitioning	Rupture extent	
	b-value	Style of faulting	
GMPE	PGA for large M	σ for large M	-None-
	PGA for small M	σ for small M	
		τ, φ for large M	
		τ, φ for large M	

Table 8.1 *Classification of epistemic uncertainties. Uncertainties labelled as Appreciable are explicitly included in the logic-tree. Uncertainties labelled as Negligible are considered to be well constrained or to cause relatively small uncertainty in the hazard. These are included in the logic-tree but without any variation. Uncertainties labelled as Excluded are not considered at this stage of the assessment. M denotes earthquake magnitude, σ denotes the total stochastic variability, τ denotes the inter-event variability and ϕ denotes the intra-event variability.*

8.8.2 Topology of the logic-tree

Each branch of the logic-tree shown in the figure below represents a scenario defined by a particular set of parameter values. The main branch or trunk of the logic-tree is the base case scenario. Each branch from the trunk represents an alternative scenario with respect to the base case. For each branch, the hazard simulation was run with the specified parameter values and the estimated hazard compared with the base case (scenario 0). Figure 8.10 shows the logic-tree representing the set of chosen scenarios for the hazard calculation, following the classification of epistemic uncertainties given above. Notice that each scenario only varies one parameter relative to the base case; covariance between parameters is not considered at this stage. The base case scenario was taken as the linear compaction model, the P_{50} strain partitioning, a *b*-value of 1, and the modified Akkar et al. (2013) GMPE. Note that the time-decay model has subsequently been adopted as the preferred compaction model.

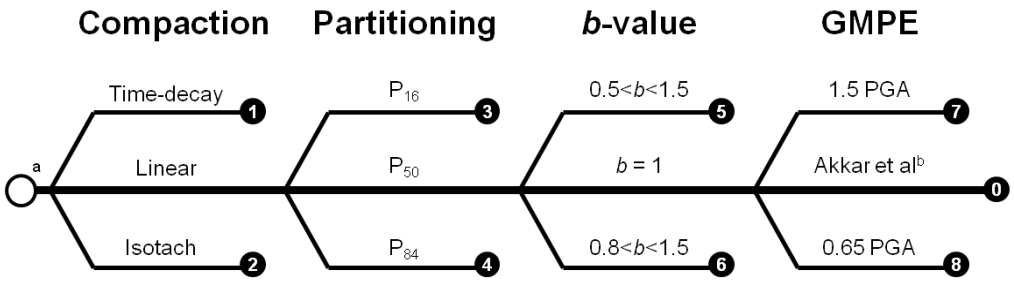

Figure 8.10 *Logic-tree to represent epistemic uncertainty in the seismic hazard assessments for the Groningen Field. [a]Based on an assessment period from 2013 to 2023. [b]Adjusted to fit magnitude 3 to 3.6 local data by (Bommer, 2013). Numbers inside black circles denote individual scenarios within the logic-tree. Each scenario takes the base case scenario values (scenario 0) for all parameters with the exception of the parameter indicated by each branch of the logic-tree.*

8.8.3 Elements of the logic-tree

Reservoir compaction

Four different compaction models are considered: the linear, bi-linear, time-decay and isotach models. The behaviour of the four compaction models is compared in Figure 8.11, which shows the cumulative and annual rates of bulk reservoir volume change and the cumulative and annual rates of the median seismic moment from 1960 to 2080. Notice that the forecasts of these models agree reasonably well for the coming 10-year period but thereafter diverge significantly from each other. In our logic-tree the linear compaction model was taken as the base case with the time-decay and isotach models as the branches. The corresponding strain partitioning, cumulative probability distributions of total seismic moment and event density maps for the interval 2013 to 2023 are given in Figure 8.12, Figure 8.13 and Figure 8.14 respectively.

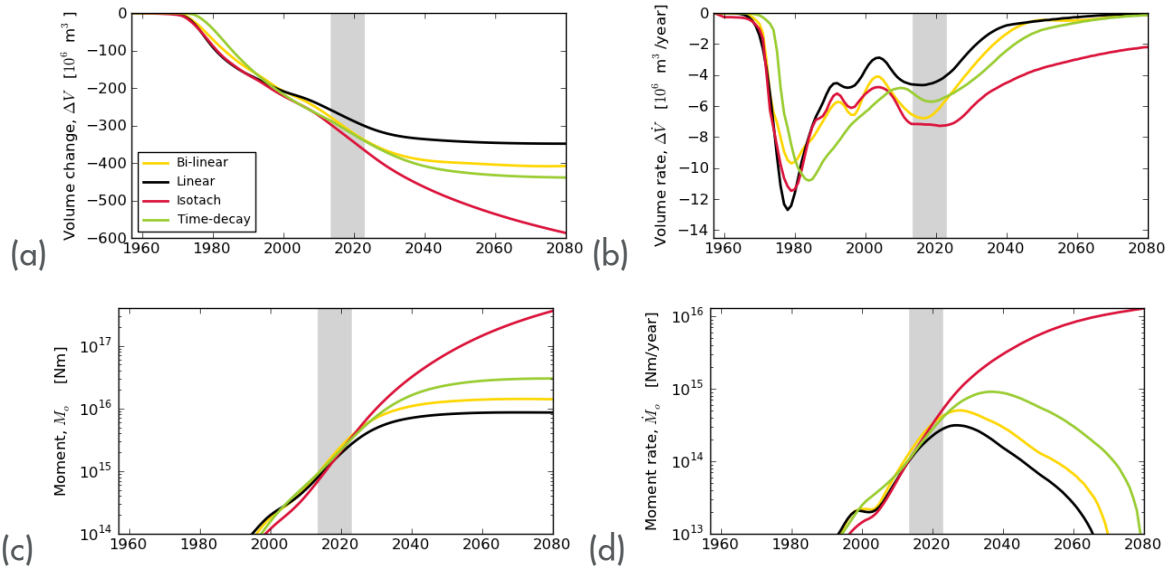

Figure 8.11 Comparison of the four different compaction models according to (a, b) the cumulative and annual rates of bulk reservoir volume change and (c, d) the cumulative and annual rates of the median seismic moment from 1960 to 2080. Grey shading denotes the 10-year hazard assessment period from 2013 to 2023.

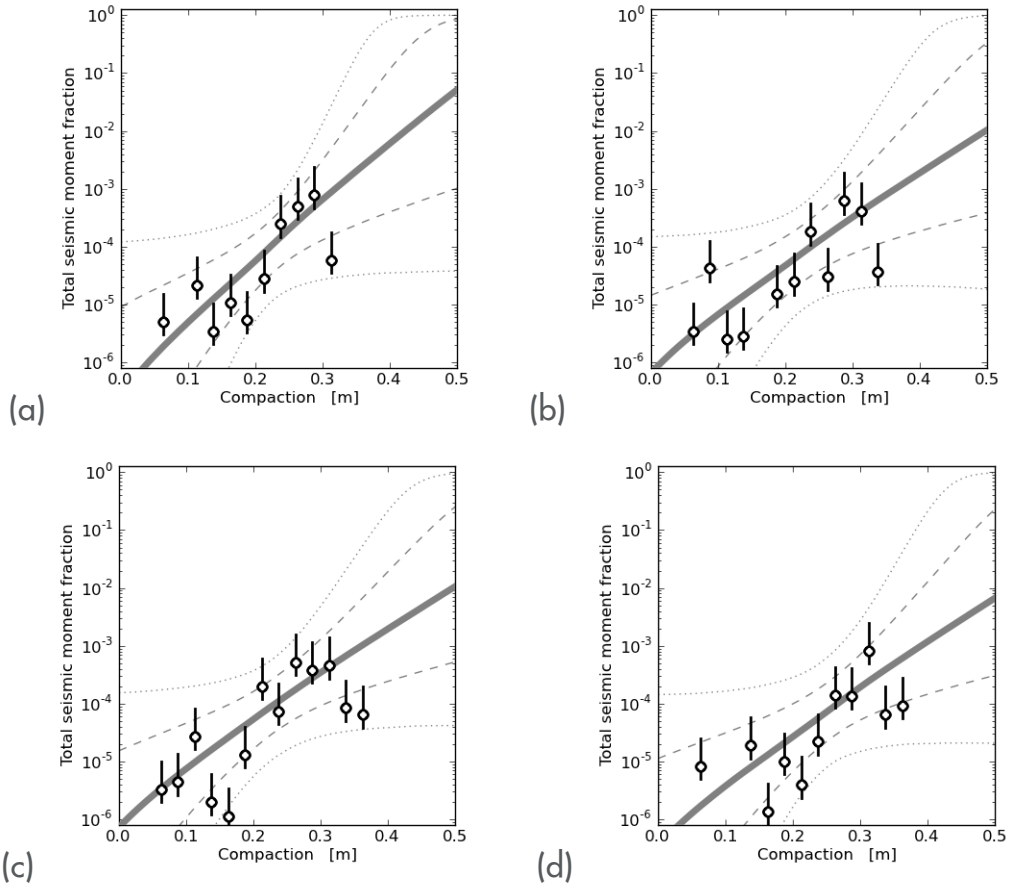

Figure 8.12 *Results of fitting the exponential strain partitioning model to the historic earthquakes for each of the compaction models: (a) linear, (b) bi-linear, (c) time-decay, and (d) Isotach and the current gas production plan (BP12).*

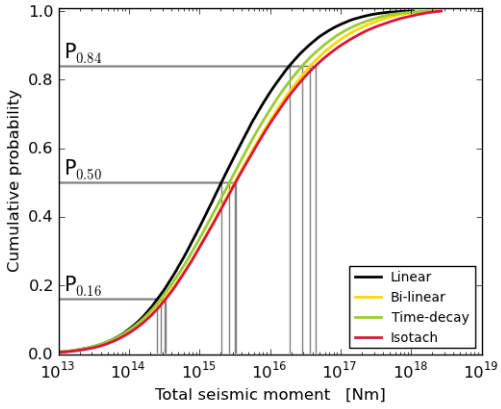

Figure 8.13 *Cumulative probability distributions of total seismic moment over the next 10 years (2013-2023) for each of the compaction models.*

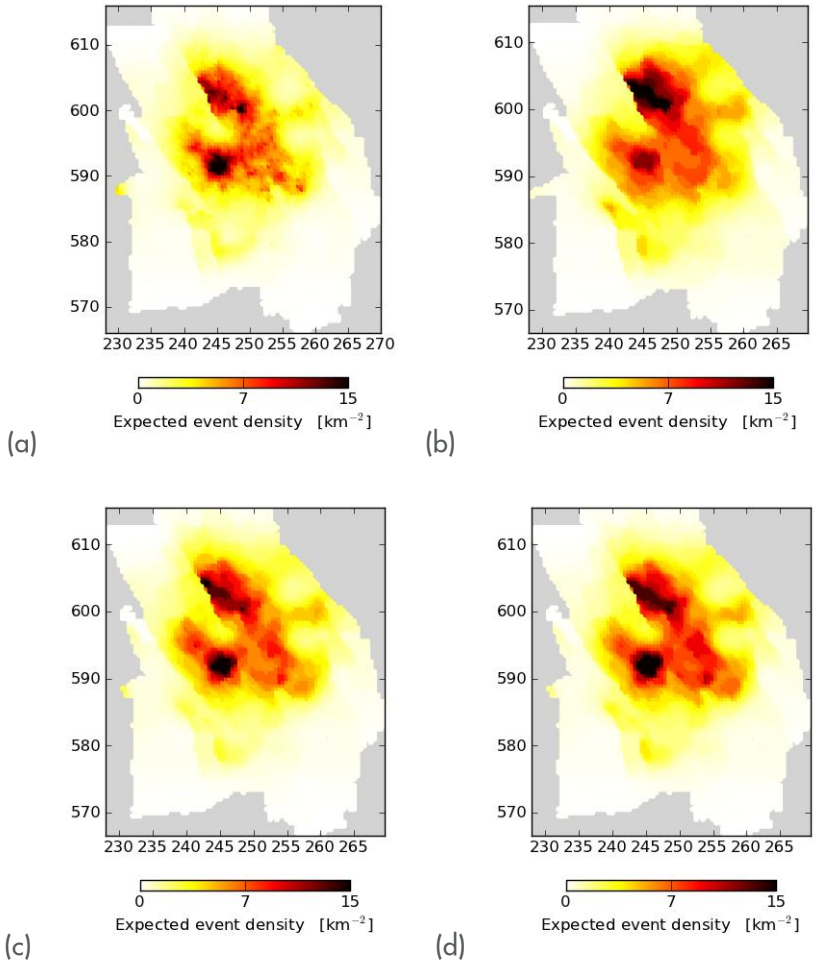

Figure 8.14 Event density maps for the interval 2013 to 2023 based on four different models of reservoir compaction: (a) linear, (b) bi-linear, (c) time-decay, and (d) Isotach. The horizontal and vertical scales are Rijksdriehoek (RD) coordinates in km.

Strain partitioning

Uncertainty in strain partitioning is significant. Moreover, there is uncertainty about this uncertainty in the sense that the relative contribution of epistemic and aleatory uncertainties is currently unknown. Within this logic-tree, we will treat the uncertainty as if it is entirely epistemic. However, in all the previous PSHA calculations it was treated as being purely aleatory by sampling the full distribution. Consequently, logic-tree hazard simulations do not sample the complete distribution of total seismic moment, but instead use a fixed value corresponding to the median or plus or minus one standard deviation from the median, that is P_{50}, P_{16} and P_{84} (see Figure 8.15). The P_{50} is the base case and P_{16} and P_{84} are the low and high case scenarios respectively.

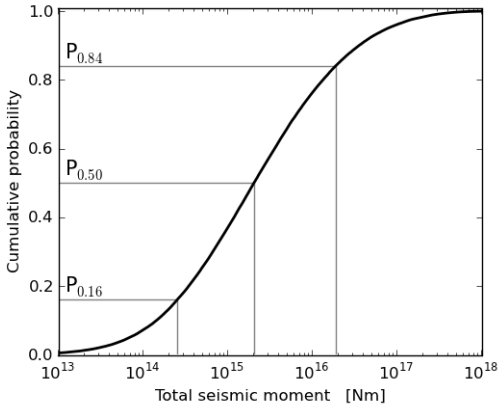

Figure 8.15 Epistemic uncertainty about strain partitioning is represented using the P_{16}, P_{50}, and P_{84} quantiles of the cumulative total seismic moment distribution.

Variation in *b*-value with compaction

The Gutenburg-Richter *b*-value characterizing the Groningen earthquake catalogue might be expected to have a strong influence on the calculated hazard since the *b*-value, being the slope of the frequency-magnitude distribution, expresses the relative abundances of small and large events in an earthquake catalogue. Figure 8.16 shows a significant variation of the *b*-value with compaction when the Groningen catalogue is divided into sub-catalogues defined by compaction bins. The logic-tree base case scenario was taken as a constant value of b=1. The alternative scenarios are defined by two compaction-dependent hyperbolic tangent functions, with $0.5 \geq b \geq 1.5$ and $0.8 \geq b \geq 1.5$ respectively, and both fit the *b*-value data (Figure 8.16). The $0.8 \geq b \geq 1.5$ scenario fits the upper envelope of the data. The other scenario fits the lower envelope of the data and has been extended to cover what is usually accepted to be the full range of physically permissible *b*-values.

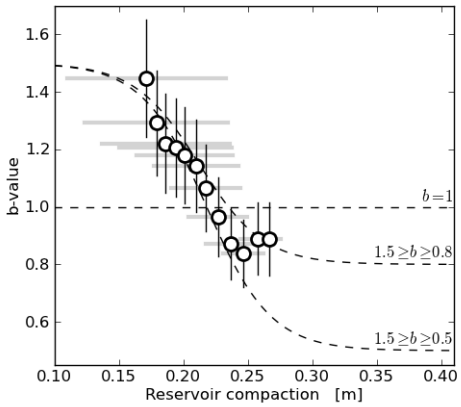

Figure 8.16 Three different models for the variation in b-value with reservoir compaction. Two of these models are parameterised as hyperbolic tangent functions to represent two possible fits to the observed b-values. The other model represents the possibility that b=1 and this apparent variation with compaction is a bias due to the small samples of earthquakes within each compaction interval. This figure is modified from Bourne & Oates (2013).

Ground motion prediction equation

The choice of the ground motion prediction equation (GMPE) has a major impact on the calculated hazard. Most of the simulations described in Bourne et al. (2013) were run using the GMPE from Dost et al. (2004); this choice was made because it was the only available GMPE calibrated to accelerometer data from the Netherlands (but not Groningen). Subsequent analysis of accelerometer data for Groningen events, including the 2012 Huizinge event, showed however that Dost et al (2004) and Akkar et al (2013) significantly overestimate surface ground motions. This motivated a modification of the Akkar et al (2013) GMPE to match the Groningen accelerometer data whilst retaining its match to larger magnitude events from elsewhere in Europe and the Middle East (NAM, 2013). This modified version of the Akkar et al (2013) GMPE is now the base case GMPE for the Groningen Field and this logic-tree. The high- and low-case scenarios were defined by scaling the PGA values by factors of 1.50 and 0.65 respectively (Figure 8.17).

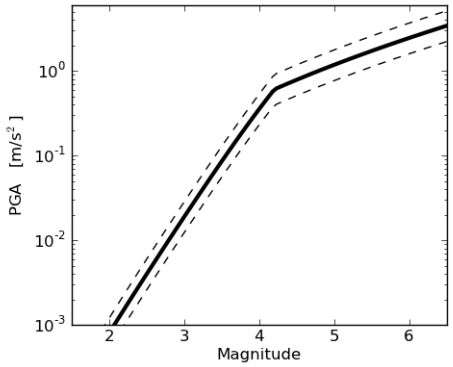

Figure 8.17 Representation of epistemic uncertainty in the GMPE for the median ground motion at a hypo-central distance of 10 km (solid line). The upper and lower alternatives to this median ground motion (dashed lines) were scaled by 1.5 and 0.65 respectively.

These scaling factors were inferred from ranges of amplification factors applied to GMPEs used in PSHA in western North America, which are based on the degree of constraint provided by the data from which they are derived – see Petersen et al., (2008) and Bommer (2013). The factors adopted take into account the fact that the Akkar et al. (2013) model is very well constrained by its database in the range of moderate magnitudes (Mw 4-5.5), which could suggest the use of smaller scaling factors than applied to the Californian equations used in the projects in western North America. However, consideration is also given to the fact that in those applications the scaling factors are applied to logic trees with multiple GMPE branches whereas for the Groningen PSHA, only a single GMPE is used. The factors are adopted for application to the unmodified Akkar et al. (2013) equations at larger magnitudes, but conservatively applied also to smaller events where the Groningen field data provide greater constraint on the modified model.

8.8.4 Results of the logic-tree

The results of the logic-tree analysis are summarised in the tornado plot, Figure 8.18. This shows the variations in the maximum PGA found within the Groningen Field area with a 2% chance of exceedance over the period 2013 to 2023. Notice that the strain partitioning uncertainty has the greatest impact of all those considered – going between the P16 and P84 seismic moment budgets for the period moves the 2% probability of exceedance maximum PGA from approximately 0.05g to about 0.6g. The GMPE scaling and compaction model choice uncertainties have significant but much smaller impacts, moving the maximum PGA by about 0.1g from its base case value. The *b*-value variations considered have negligible impact on the calculated hazard: it seems that the competing influences of increasing event size but reduced event number (for the large events) corresponding to reductions in the *b*-value approximately balance each other out, at least in this case.

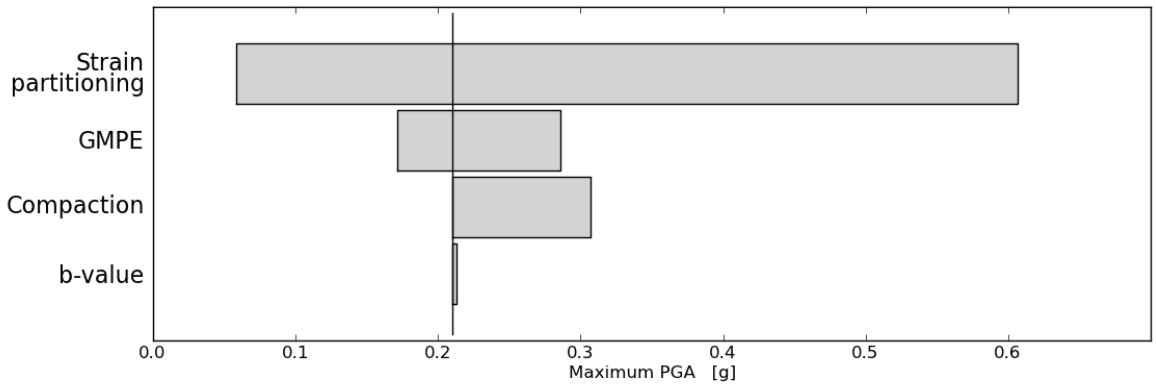

Figure 8.18 Variation in the maximum PGA found within the Groningen Field with a 2% chance of exceedance over the period 2013 to 2023 due to epistemic uncertainties represented in the logic-tree.

8.9 Seismic hazard assessments for different pressure depletion scenarios

8.9.1 Seismological assessments for each scenario

Pressure depletion scenarios comprise 5 elements: a geological realisation, a compaction model, a development scenario, a production curtailment scenario, and a production philosophy (Table 8.2). From the 288 possible permutations of these elements, a representative subset of 19 scenarios was selected for PSHA (Table 8.3). Each of these scenarios is represented by a dynamic reservoir simulation model that was adjusted to match historic gas production and reservoir pressure data and forecasts future pressure depletions and a compaction model that was adjusted to match historic subsidence data and forecasts future compactions. Based on this compaction model, the seismological model was adjusted to match the historical earthquake statistics and forecast future seismicity. Adjustment of the seismological model involves a Monte Carlo procedure to fit a strain partitioning model to match, within their uncertainties, the observed variation in seismic moment with reservoir compaction. This yields an estimate for the probability distribution of the total seismic moment released during any given time interval.

Table 8.2 Summary of the scenario elements considered for PSHA and the labels used to identify them. A complete scenario is defined by the choice of one option under each of the different headings.

Label	Scenario Elements
	A. Geological Realisations
SubCor	Model realisation with Moderate NW aquifer
NoSubCor	Model realisation with Weak NW aquifer
	B. Reservoir Compaction Models
TD	Time decay
IT	Isotach (1st cycle)
BL	Bi-linear
LN	Linear
	C. Development Scenarios
KHM1	KHM1 hook-up, 2nd, and 3rd stage compression
NWP	D1 + North Western Periphery development
NWPSWP	D2 + South Western Periphery development
	D. Production Curtailment Scenarios
SN	Market Demand
C40	40 bcm/year
C30	30 bcm/year
C20	20 bcm/year
	E. Production Philosophies
Std	Current Production Philosophy
Tremor	Alternative Production Philosophy
EStop	Emergency stop

Table 8.3 The individual scenarios selected for PSHA. The Base Case is annotated as 1.

Scenario	Scenario Elements					Id.
	A	B	C	D	E	
0	SubCor	LN	KHM1?	SN?	STD?	rm00
1	SubCor	TD	KHM1?	SN?	STD?	rm01
2	SubCor	TD	KHM1?	C30	STD?	rm05
3	SubCor	TD	KHM1	C30	Tremor	rm10
4	SubCor	TD	KHM1	C40	STD	rm12
5	SubCor	TD	KHM1	C40	Tremor	rm14
6	SubCor	TD	KHM1	SN	EStop	rm16
7	SubCor	TD	KHM1	SN	Tremor	rm18
8	SubCor	TD	NWP	SN	STD	rm20
9	SubCor	TD	NWPSWP	SN	STD	rm22
10	SubCor	IT	KHM1?	SN?	STD?	rm02
11	SubCor	IT	KHM1?	C30	STD?	rm06
12	SubCor	IT	KHM1	C30	Tremor	rm09
13	SubCor	IT	KHM1	C40	STD	rm11
14	SubCor	IT	KHM1	C40	Tremor	rm13
15	SubCor	IT	KHM1	SN	EStop	rm15
16	SubCor	IT	KHM1	SN	Tremor	rm17
17	SubCor	IT	NWP	SN	STD	rm19
18	SubCor	IT	NWPSWP	SN	STD	rm21

Figure 8.19 shows the results of this analysis for all scenarios involving the time-decay compaction model (scenarios 1 to 9). The cumulative bulk reservoir volume changes from 1960 until 2080 (Figure 8.19a) and their annual rates of change (Figure 8.19b) are the same in all scenarios from 1960 to 2013 due to matching the same historic data. After 2013, these start to differ in response to the different development and production scenarios. However, on the scale of these plots most of these differences are apparently minor with two exceptions.

- The emergency stop scenario stabilises reservoir volume decrease above 350x10^6 m^3, although volume reductions continue until 2040 as reservoir pressures equalise. Thereafter, the aquifer responds and a very small amount of the volume reduction is very slowly reversed.
- The KHM1 development under a production curtailment of 30 bcm/year and the alternative production philosophy (scenario 3) exhibits notably lower rates of reservoir volume reduction over the period 2017 to 2030; thereafter the rates are indistinguishable from the remaining scenarios.

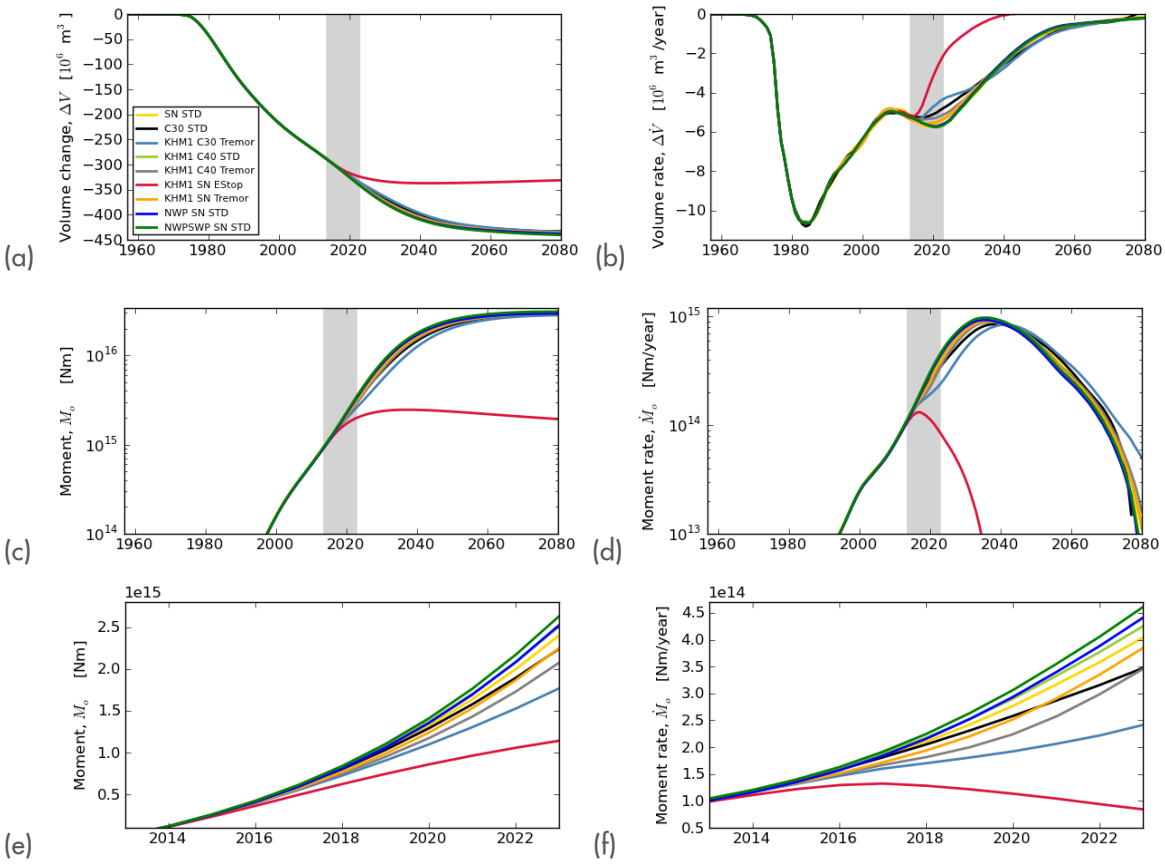

Figure 8.19 *Comparison of the different production scenarios in combination with the time-decay compaction model according to (a, b) the cumulative and annual rates of bulk reservoir volume change and (c, d) the cumulative and annual rates of the median seismic moment from 1960 to 2080. Grey shading denotes the 10-year hazard assessment period from 2013 to 2023. (e, f) Show the same curves as (c, d) except from 2013 to 2023 and on a linear scale.*

The cumulative and annual rates of the median seismic moment (Figure 8.19c-f) show similar variability with the different scenarios. The cumulative median seismic moment in 2080 is indistinguishable for all scenarios other than the emergency stop scenario. Because the seismological model was developed for reservoir compaction, the results from the emergency stop scenario are applicable until 2035 but not applicable to the subsequent slight reversal of compaction indicated after 2035. The emergency stop scenario still shows an increasing annual median seismic moment until about 2017 (Figure 8.19f). This is consistent with the current transit time for a pressure transient from the southern clusters of production wells to the centre of reservoir compaction of about 5 years. During this period the median annual seismic moment from the model increases to about 30% above the 2013 value, and does not reduce below the 2013 value until about 2021. For all other scenarios, the median annual seismic moment continues to increase until about 2035 or later. In 2023, increases above the 2013 value vary from 2.5 (scenario 3) to 4.5 (scenario 9) times larger.

There is, of course, a critical difference between the median seismic moment and the actual seismic moment which is modelled in PSHA for the Groningen Field as a random sample from the probability distribution of total seismic moment. This is a Pareto sum distribution which has strongly asymmetric confidence intervals skewed above the median. For example, there is a 10% chance of sampling a moment 10 times larger than the median. This means there is a 10% chance of the actual seismicity exceeding 10 times the median value. This stochastic variability is significantly larger than the variability between the different scenarios under consideration.

Figure 8.20 shows results for all the same scenarios, except for the isotach compaction model (scenarios 10 to 18). This isotach model is significantly different to the linear, bi-linear and time-decay models, due to the very significant effective time-delay between changes in depletion rate and corresponding changes in compaction rate. This means that even in the emergency stop scenario compaction continues with little sign of ever stopping (Figure 8.20a, b). This raises significant concerns about the physical plausibility of this particular isotach model.

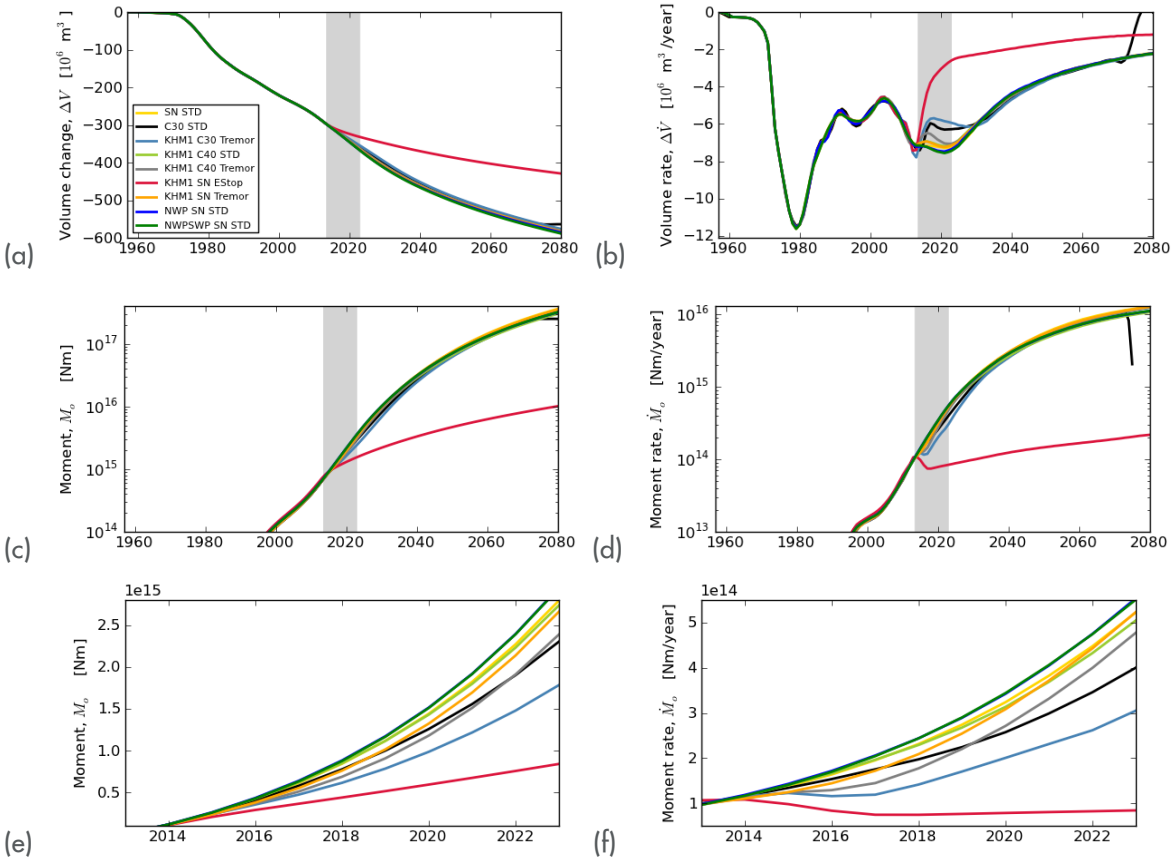

Figure 8.20 *As Figure 8.19, except for the isotach compaction model. Note that the reservoir simulation for the C30 STD scenario unexpectedly terminated in 2070, so compaction artificially constant from 2070 to 2080.*

8.9.2 Ground motion assessments for each scenario

Combining the seismological model for each scenario with a ground motion prediction equation (GMPE) in a Monte Carlo simulation yields estimates for the map distribution of peak ground velocity and acceleration with a certain chance of exceedance. These scenario assessments were based on the GMPE developed by Akkar et al. (2013) for Europe and the Middle East and its subsequent modification to match accelerometer data from the Groningen Field (NAM, 2013). At present this assessment is based on simulations of 10^4 earthquake catalogues for the period 2013 to 2023. Results are summarised as the maximum PGA and PGV values with a 50%, 10%, and 2% chance of exceedance (Table 8.4). For reference, maps of the PGA with a 2% chance of exceedance are shown for all scenarios with the time-decay compaction model (Figure 8.21) and the isotach compaction model (Figure 8.22).

Table 8.4 *Variability in the maximum PGA and PGV with different reservoir compaction models and production scenarios. P50, P10, P2 denote 50%, 10% and 2% chances of exceedance respectively over the 10-year interval from 2013 to 2023. These results are listed in descending order of the P2 maximum PGA for each compaction model. These are preliminary results – still subject to technical assurance and liable to change.*

Scenario	Maximum PGA [g]			Maximum PGV [cm/s]		
	P_{50}	P_{10}	P_2	P_{50}	P_{10}	P_2
SN STD Linear	0.05	0.27	0.56	1.8	10.2	22.4
KHM1 C40 STD Timedecay	0.06	0.34	0.69	2.3	13.1	28.4
NWPSWP SN STD Timedecay	0.06	0.34	0.68	2.4	13.2	27.9
NWP SN STD Timedecay	0.06	0.34	0.68	2.3	12.9	28.0
SN STD Timedecay	0.06	0.33	0.66	2.2	12.5	27.2
KHM1 SN Tremor Timedecay	0.05	0.31	0.64	2.1	11.9	26.2
KHM1 C40 Tremor Timedecay	0.05	0.30	0.64	2.0	11.2	25.9
C30 STD Timedecay	0.05	0.31	0.64	2.1	11.9	26.5
KHM1 C30 Tremor Timedecay	0.05	0.27	0.58	1.8	10.4	23.5
KHM1 SN Emergencystop Timedecay	0.03	0.17	0.41	0.9	6.5	15.8
NWP SN STD Isotach	0.07	0.41	0.82	2.8	16.3	36.8
KHM1 C40 STD Isotach	0.07	0.41	0.82	2.7	16.0	36.0
NWPSWP SN STD Isotach	0.07	0.40	0.81	2.8	16.1	36.5
SN STD Isotach	0.07	0.41	0.81	2.8	16.0	35.9
KHM1 SN Tremor Isotach	0.07	0.40	0.79	2.6	15.9	34.7
KHM1 C40 Tremor Isotach	0.06	0.37	0.78	2.5	14.4	33.5
C30 STD Isotach	0.06	0.37	0.76	2.4	14.6	33.8
KHM1 C30 Tremor Isotach	0.05	0.31	0.67	1.9	11.8	28.1
KHM1 SN Emergencystop Isotach	0.02	0.14	0.36	0.8	5.4	14.1

The estimated maximum PGA with a 2% chance of exceedance is between 0.69*g* and 0.64*g* for all scenarios involving the time-decay compaction model with just two exceptions: 0.41*g* for the emergency stop scenario and 0.58*g* for the KHM1 C30 Alternative (Tremor) scenario. Relative to the 0.66*g* for the base case SN STD scenario, these two exceptions represent apparent hazard reductions of 38% and 12% respectively over the period 2013 to 2023.

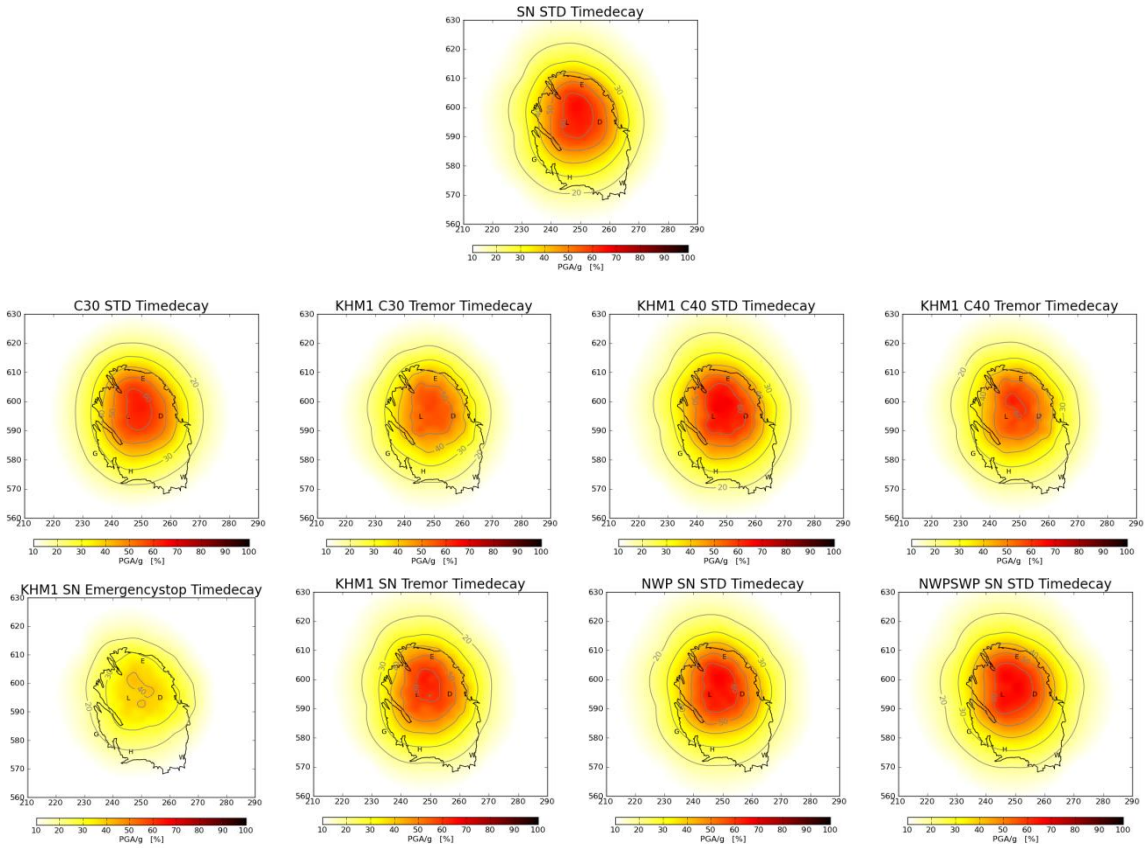

Figure 8.21 Influence of the different depletion scenarios on the PGA hazard. PGA hazard maps are shown for a 2% chance of exceedance over the period 2013 to 2023 based on the time-decay compaction model. The horizontal and vertical scales are Rijksdriehoek (RD) coordinates in km.

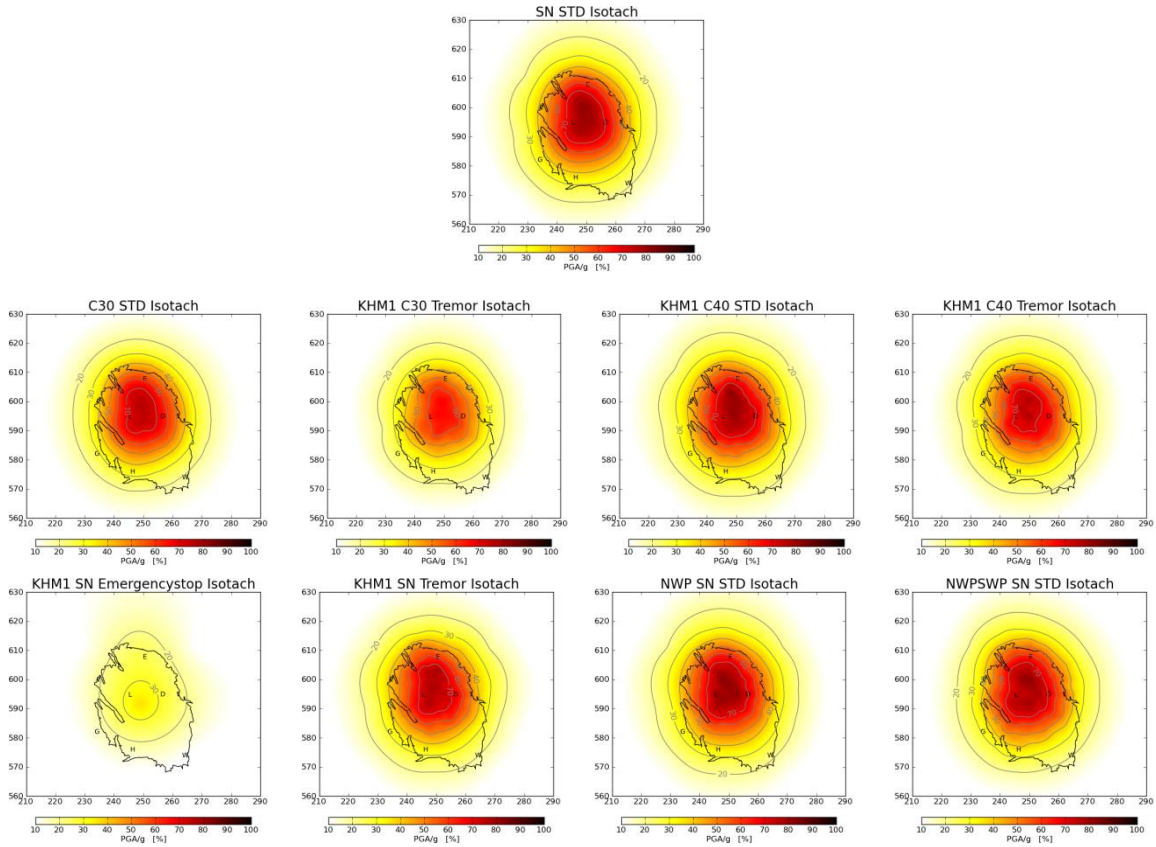

Figure 8.22 As Figure 8.21, except for the isotach compaction model. The horizontal and vertical scales are Rijksdriehoek (RD) coordinates in km.

8.10 Hazard Summary

Probabilistic seismic hazard assessment for the 10 years from 2013 to 2023 based on the time-decay reservoir compaction model indicates a 2% chance of the peak ground acceleration (PGA) exceeding 0.67*g*, where *g* is the acceleration due to gravity taken to be 9.81 m/s^2. These results were obtained using a Monte Carlo method (NAM, 2013) and the Akkar et al (2013) ground motion prediction equation modified to be consistent with ground motion data from the Groningen Field, and by including all earthquakes of at least magnitude1.5. This hazard should not be considered equivalent to the 10% chance over 50 years stipulated by Eurocode 8 because induced seismicity within the Groningen Field varies with time and is not modelled as a Poisson process. Repeating this assessment method for the 5 years from 2013 to 2018 indicates a 2% chance of PGA exceeding 0.42*g*. For the three years from 2013 to 2016, the same assessment method yields a 2% chance of exceeding 0.30*g*.

Significant epistemic uncertainties exist in the seismic hazard assessment for the Groningen Field; these are primarily associated with strain partitioning, the GMPE and reservoir compaction. This motivates further data acquisition and studies designed to reduce these uncertainties. The epistemic uncertainty attributed to strain partitioning will in some part be due to random variability (aleatory). The relative contribution of epistemic and aleatory uncertainties to the overall uncertainty in strain partitioning is unknown. Further earthquake, surface acceleration, and subsidence monitoring within the Groningen Field will provide more information that may help to better constrain these uncertainties.

Probabilistic seismic hazard assessments from 2013 to 2023 were conducted for 19 distinct scenarios that form a representative sample of the different geological, compaction, development, and production scenario elements. The results obtained indicate all these depletion scenarios yield similar seismic hazard estimates (within 5%) with two exceptions. The emergency stop scenario reduces the maximum PGA with a 2% chance of exceedance to 0.41*g*. This represents a 38% reduction compared to 0.66*g* for the current case (SN STD). Alternatively the "30 Bcm/year curtailment combined with the alternative production philosophy (KHM1 C30 Tremor) scenario reduces the hazard to 0.58*g*, 12% below the current case.

In the emergency stop scenario, the isotach model predicts significant rates of compaction will persist until long after 2080. There is no analogue field evidence to support such unexpected behaviour. Equally, laboratory measurements are unable to constrain the isotach model behaviour on the multi-decadal time-scale exhibited here. For these reasons, it is desirable to conduct an independent validation of the applicability of the isotach model to the Groningen case.

8.11 Conclusions

The main findings with respect to seismic hazard are summarized below:

- A Monte-Carlo approach to Probabilistic Seismic Hazard Assessment (PSHA) was identified as being best suited to the analysis of the Groningen field's induced seismicity.
- Independent PSHA implementations in Python and C gave the opportunity for valuable cross checking of hazard estimates.
- Summary of the maximum magnitude and maximum PGA values with 50%, 10% and 2% chances of exceedance over three different time periods of assessment according to the current production plan, the time-decay compaction model and the modified Akkar et al. (2013) GMPE is given below:

Period	Maximum Magnitude			Maximum PGA		
	P_{50}	P_{10}	P_2	P_{50}	P_{10}	P_2
2013 - 2016	3.4	4.1	4.6	0.02g	0.12g	0.30g
2013 - 2018	3.6	4.4	4.9	0.03g	0.18g	0.42g
2013 - 2023	3.9	4.8	5.3	0.06g	0.33g	0.67g

- Eurocode 8 has been adopted as a standard framework for the assessment of the seismic capacity of buildings in the Groningen field area. Consideration of PGA and PGV values corresponding to the 475-year return period specified in Eurocode 8 requires that a specific production period is chosen for calculating the annualized hazard due to the planned production and expected compaction.
- Direct comparisons with published 475-year hazard maps can be very problematic because such standard hazard maps generally impose a lower minimum magnitude limit than the M=1.5 used here, such as M=5 in California and M=4.5 in Europe.
- Disaggregation of the hazard showed that the seismic hazard is dominated by events of intermediate magnitudes (M = 4 – 5). This contrasts with the maximum possible magnitude, M≈6.5, implied by the compaction-based seismicity model, showing that the induced seismic hazard is not well characterized by M_{max}.
- The most important uncertainty affecting the calculated hazard is the very large uncertainty in the partioning coefficient relating seismic moment budget to the volumetric strain due to compaction.
- Sensitivity tests showed that the selection of a suitable ground motion prediction equation (GMPE) and the future production period chosen for calculating the annualized hazard had a strong influence on the resulting hazard estimates. Changes to the *b*-value however had limited impact on the calculated results.
- Probabilistic seismic hazard assessment for the 10 years from 2013 to 2023 based on the time-decay reservoir compaction model indicates a 2%, 10% and 50% chance of peak ground acceleration, PGA, exceeding 0.67*g*, 0.33*g* and 0.06*g* respectively, where *g* is the acceleration due to gravity taken to be 9.81 m/s2.
- For a 5-year assessment period from 2013 to 2018 the corresponding results are a 2%, 10%, and 50% chance of PGA exceeding 0.42*g*, 0.18*g*, and 0.03*g* respectively. Similarly for a three year assessment period from 2013 to 2016, there is a 2%, 10% and 50% chance of PGA exceeding 0.30*g*, 0.12*g* and 0.02*g* respectively.
- PSHA results previously obtained for the linear-elastic compaction model (NAM, 2013) indicate a 2%, 10% and 50% chance from 2013 to 2023 of PGA exceeding 0.56*g*, 0.27*g*, and 0.047*g* respectively.

- These PSHA results were obtained using a Monte Carlo method (NAM, 2013) and the Akkar et al (2013) ground motion prediction equation modified to be consistent with ground motion data from the Groningen Field, and by including all earthquakes of at least magnitude 1.5.
- It is important to point out that the 2% over 10 years hazard results listed above should not be considered equivalent to the 10% chance over 50 years stipulated by Eurocode 8 because induced seismicity within the Groningen Field varies with time and is not modelled as a Poisson process.
- Epistemic uncertainty characterises uncertainty in the values of parameters which are fixed but either unknown or known only to within a certain precision. Significant epistemic uncertainties exist in the seismic hazard assessment for the Groningen Field; these are primarily associated with strain partitioning, the GMPE and reservoir compaction. A logic-tree approach, in which each branch of the logic-tree represents a distinct scenario of a particular model and associated parameter values, was used to explore the impact of the key epistemic uncertainties on the estimated hazard. It was found that the strain partitioning uncertainty has the greatest impact of those considered. The epistemic uncertainty attributed to strain partitioning will in some part be due to random (aleatory) variability, representing the stochastic nature of the earthquake process. The relative contribution of epistemic and aleatory uncertainties to the overall uncertainty in strain partitioning is unknown. Further earthquake, surface acceleration, and subsidence monitoring within the Groningen Field will provide more information that may help to better constrain these uncertainties.
- Probabilistic seismic hazard assessments from 2013 to 2023 were conducted for 19 distinct scenarios that form a representative sample of the different geological, compaction, development, and production scenario elements. The results obtained indicate all these depletion scenarios yield similar seismic hazard estimates (within 5%) with two exceptions. The emergency stop scenario reduces the maximum PGA with a 2% chance of exceedance to 0.41*g*. This represents a 38% reduction compared to 0.66*g* for the current case (SN STD). Alternatively the KHM1 C30 Alternative (Tremor) scenario reduces the hazard to 0.58*g*, 12% below the current case.
- In the emergency stop scenario, the isotach model predicts significant rates of compaction will persist until long after 2080. There is no analogue field evidence to support such unexpected behaviour. Equally, laboratory measurements are unable to constrain the isotach model behaviour on the multi-decadal time-scale exhibited here. For these reasons, the reliability of this particular isotach model is entirely doubtful.

8.12 Recommendations for further work

The following additional work, and subsequent updating of the seismic hazard assessment, should be considered to address some of the key uncertainties discussed above.

- Identify and investigate new avenues which have the potential to better constrain the partitioning coefficient relating seismic moment budget to the volumetric strain due to compaction.
- Investigate and characterize any evidence for time delays between reservoir compaction and induced seismicity.
- Reduce uncertainty about the depth distribution of events using deep geophone arrays in wells near Zeerijp and Stedum.
- Investigate the spatial distribution and correlation length-scale of site specific (intra-event) uncertainty within the ground motion prediction equation. If necessary, include this effect in the seismic risk assessment.
- Further reduce uncertainty in the ground motion prediction equation by acquiring more surface strong motion measurements within the Groningen Field.

8.13 References

Akkar, S., Sandıkkaya, M.A. and Bommer, J.J. *Empirical ground-motion models for point- and extended-source crustal earthquake scenarios in Europe and the Middle East*. Bulletin of Earthquake Engineering (2013), in press, DOI 10.1007/s10518-013-9461-4.

ATC (1976). *Tentative provisions for the development of seismic regulations for buildings*. Report ATC 3-06, Applied Technology Council, Redwood City, California, USA.

Bazzurro, P. and Cornell, C.A. *Disaggregation of Seismic Hazard*. Bulletin of the Seismological Society of America (1999), Vol. 89, No. 2, pp. 501-520.

Bommer, J. (2013). *Proposals for New GMPEs for the Prediction of PGA and PGV in the Groningen Gas Field* (pp. 1–37). London.

Bommer, J.J. & R. Pinho (2006). *Adapting earthquake actions in Eurocode 8 for performance-based seismic design*. Earthquake Engineering & Structural Dynamics 35(1), 39-55.

Bommer, J.J. and Abrahamson, N.A. *Why Do Modern Probabilistic Seismic-Hazard Analyses Often Lead to Increased Hazard Estimates?* Bulletin of the Seismological Society of America (2006), Vol. 96, No. 6, pp. 1967–1977.

Bommer, J.J. and Crowley H. *The Influence of Ground-Motion Variability in Earthquake Loss Modeling*. Bulletin of Earthquake Engineering (2006), Vol. 4, pp. 231–248.

Bommer, J.J. and Stafford, P.J. *Seismic hazard and earthquake actions* in *Seismic Design of Buildings to Eurocode 8*, edited by Elghazouli, A.Y. Spon Press (2009) pp. 6-46.

Bommer, J. (2013). *Epistemic Uncertainty in Groningen Field GMPEs for PGA* (pp 1–8). London.

Bourne, S J, & Oates, S. (2012). *Probability of an earthquake greater than magnitude 4 due to gas production from the Groningen Field* (pp. 1–40). Rijswijk, The Netherlands.

Bourne, S., Oates, S., and Bommer, J.J. *A probabilistic seismic hazard assessment for the Groningen Field*. Technical Report. Shell Global Solutions International. Rijswijk, The Netherlands (2013).

Bourne, S.J., & Oates, S. (2013). *Induced strain and induced earthquakes within the Groningen Gas Field: Earthquake probability estimates associated with future gas production* (p. 67). Rijswijk, The Netherlands.

CEN (2004). *Eurocode 8: Design of Structures for Earthquake Resistance*. Comité Européen de Normalisation, Brussels, Belgium.

Crowley H. and Bommer, J.J. *Modeling Seismic Hazard in Earthquake Loss Models with Spatially Distributed Exposure*. Bulletin of Earthquake Engineering (2006), Vol. 4, pp. 249–273.

Dost, B., van Eck, T. and Haak, H. *Scaling of peak ground acceleration and peak ground velocity recorded in the Netherlands*. Bolletino di Geofisica Teorica ed Applicata (2004), Vol. 45, No. 3, pp. 153-168.

Grant, D.N., J.J. Bommer, R. Pinho, G.M. Calvi, A. Goretti & F. Meroni (2007). *A prioritization scheme for seismic intervention in school buildings in Italy*. Earthquake Spectra 23(2), 291-314.

Haak, H.W. and De Crook, T. *Seismische analyse van aardbevingen in Noord-Nederland*. KNMI report WR 94-1. KNMI, de Bilt (1994).

Houtgast, G. *Aardbevingen in Nederland*. KNMI report 179. KNMI, de Bilt (1992).

Main, I., Irving, D., Musson, R. and Reading, A. *Constraints on the frequency-magnitude relation and maximum magnitudes in the UK from observed seismicity and glacio-isostatic recovery rates*. Geophysical Journal International (1999), Vol. 137, pp. 535-550.

NEHRP (2009). *Recommended Seismic Provisions for New Buildings and Other Structures. Part I - Provisions*. National Earthquake Hazards Reduction Program, Federal Emergency Management Authority (FEMA), Washington D.C., USA.

NZSEE (2006). *Assessment and Improvement of the Structural Performance of Buildings in Earthquakes*. New Zealand Society for Earthquake Engineering, Wellington, New Zealand.

Petersen, M.D., A.D. Frankel, S.C. Harmsen, C.S. Mueller, K.M. Haller, R.L. Wheeler, R.L. Wesson, Y. Zeng, O.S. Boyd, D.M. Perkins, N. Luco, E.H. Field, C.J. Wills & K.S. Rukstales (2008). *Documentation for the 2008 Update of the United States National Seismic Hazard Maps,* USGS Open-File Report 2008-1128, US Geological Survey, Reston, VA. 61 pp.

9 The Role of Faults

9.1 Introduction

Reservoir compaction and subsidence is observed in all producing oil and gas fields that exhibit reservoir depletion. However, in many fields this does not lead to seismic events. Various fields in the South China Sea exhibit seabed subsidence of more than 4 meter without any reported seismic event [Davison, 2010]. Also, most depleting and compacting fields in the Netherlands have not shown seismic events to date [van Thienen, 2012]. The occurrence of reservoir depletion or reservoir compaction is therefore not necessarily leading to seismic events.

Seismic events mark the release of stored energy from the subsurface [Kanamori, 1994]. Stored energy is available in both the gas phase as well as strain energy in the solid rock structure. In general, production operations increase the level of strain energy that is available in the subsurface. The fact that seismic events are observed in the Groningen field is an indication that at least part of the strain energy is recoverable. In principle, the recoverable strain energy can either be the production-induced energy (induced seismicity) or the energy available by tectonic processes (triggered seismicity).

At least two conditions need to be satisfied to explain the occurrence of seismic events in the Groningen field:

1. The availability of recoverable strain-energy from the subsurface and
2. A failure mechanism to release (a part of) it.

Fault slip is a commonly accepted failure mechanism for the release of strain energy in seismic events [Kanamori, 1994]. However, the occurrence of fault slip cannot be considered in isolation from the behavior of surrounding formations in the subsurface, because in particular the formations in the vicinity of a slipping fault are the source of the released energy. It is imperative to understand how and where in the subsurface the depletion-induced stress change is accommodated: in reversible or irreversible formation deformation.

In this chapter the role of faults in the occurrence of seismic events is outlined in a geomechanical context. The release of energy in seismic events is related to unloading of rock mass in the vicinity of faults. Also, the development of irreversible deformations (compaction strain, salt creep or other time-dependent behavior) in and around the depleting reservoir plays an important role in the potential development of critical stress conditions on fault planes. First, the geomechanical evaluation framework is outlined to introduce the requirements for an improved understanding of the geomechanical response during seismic events in the Groningen field. Subsequently, the gaps in our knowledge and the status of ongoing modeling studies are outlined.

9.2 Seismicity in a geomechanical evaluation framework

Geomechanical evaluations take into account:

A. equilibrium of forces (stress), either statically or dynamically,
B. the (subsurface) structure that ensures that equilibrium is satisfied,
C. the material behavior of various components of the subsurface structure
D. the (depletion) loading on the subsurface structure

The displacements of and the forces acting on the subsurface structure are the independent parameters used to describe external equilibrium (Figure 9.1). The subsurface loading normally takes the form of a changing pore pressure. The subsurface structure responds with deformation (strain) in order to mobilize the required stress in any material point to ensure internal equilibrium. The stress-strain relationship that describes this response is also referred to as material behavior or the constitutive model. The subsurface structure, i.e. the layering and dipping of formations, presence of faults and formation offsets etc, is relevant in the determination of the stress re-distribution mechanism due to the imposed loading condition. In applied mechanics this is referred to as the kinematic relationship between displacements and strain.

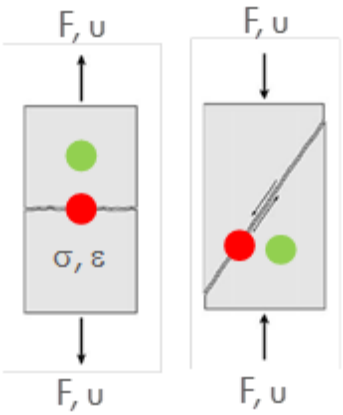

Figure 9.1 *The external force F and internal stress condition σ are in equilibrium; the constitutive model describes the relationship between stress σ and strain ε, which results in a displacement (elongation) u at location where the external force F is applied. Either the force F or the displacement u can be prescribed. The red point represents a material point that is at the onset of failure, whereas the green point is assumed in an elastic deformation state.*

9.2.1 Stored energy

Seismic events mark the release of stored energy from the subsurface [e.g. Kanamori, 1994]. From a geomechanical point of view, the subsurface moves from one state of equilibrium just before a seismic event, to another state of equilibrium with a lower level of stored energy just after the event. The stored energy in the subsurface is described by the constitutive behavior of the subsurface formation, while the energy difference between the equilibrium states can be released partly as seismic energy and also by various other energy sinks, for instance thermal energy.

The work done by an external force in Figure 9.1 (Work A = F * u) is stored in material points in the form of strain energy. This is the area under the stress-strain relationship as indicated in Figure 9.2. The total strain energy is calculated by considering the stress-stain relationship of each material point of the specimen in Figure 9.1 or a "control volume" of the subsurface. The stored energy level at the beginning of field production is determined by the "virgin" in-situ stress condition (the green point in Figure 9.2). Additional energy is stored in material points that undergo an increased effective stress level due to field production.

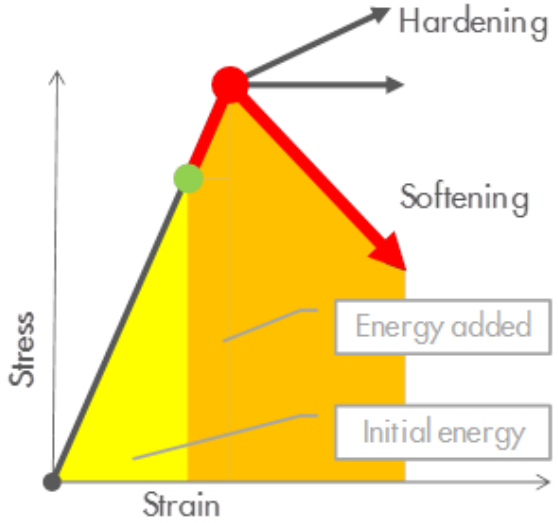

Figure 9.2 *Stress-strain relationship showing a material point in an elastic state (green) and one at the onset of failure (red). See also Figure 9.1. The strain energy stored in a material point is represented by area under the stress-strain relationship. Additional energy is stored for any material point gaining strain (red point), whereas energy is released by material points that are unloading (green and orange points).*

9.2.2 Failure

Any material has a limit to what stress level can be carried. This limit can be expressed as the tensile strength in case of tensile loading (mode 1), or the shear strength in case of shear or mode 2 loading (mode 3 failure is ignored). The stress carrying capacity of a material point can also be limited in terms of a compressive stress, which may lead to compressive failure (pore collapse) when exceeded. These failure mechanisms, which are shown conceptually in Figure 9.3, are all expressed in terms of a limit stress. Numerous models have been developed to describe the onset and post-failure behavior of all kind of materials under various loading conditions.

The post-failure behavior of a material point can be classified in so-called hardening and softening behavior (Figure 9.2). In the case of hardening behavior the stress carrying capacity still increases after the onset of failure, while it decreases in case of softening behavior. The strain energy level increases in both cases.

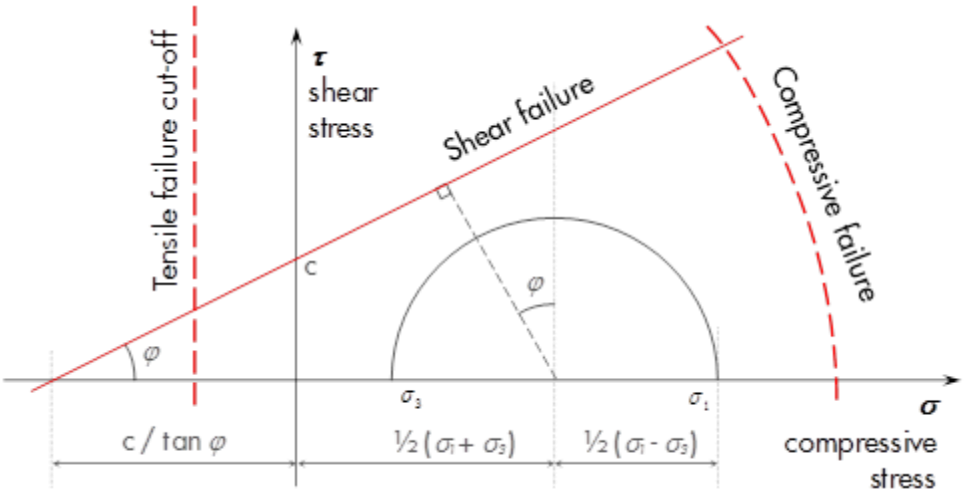

Figure 9.3 *Mohr-circle diagram relating the principal stress state to possible tensile, shear and compressive failure conditions.*

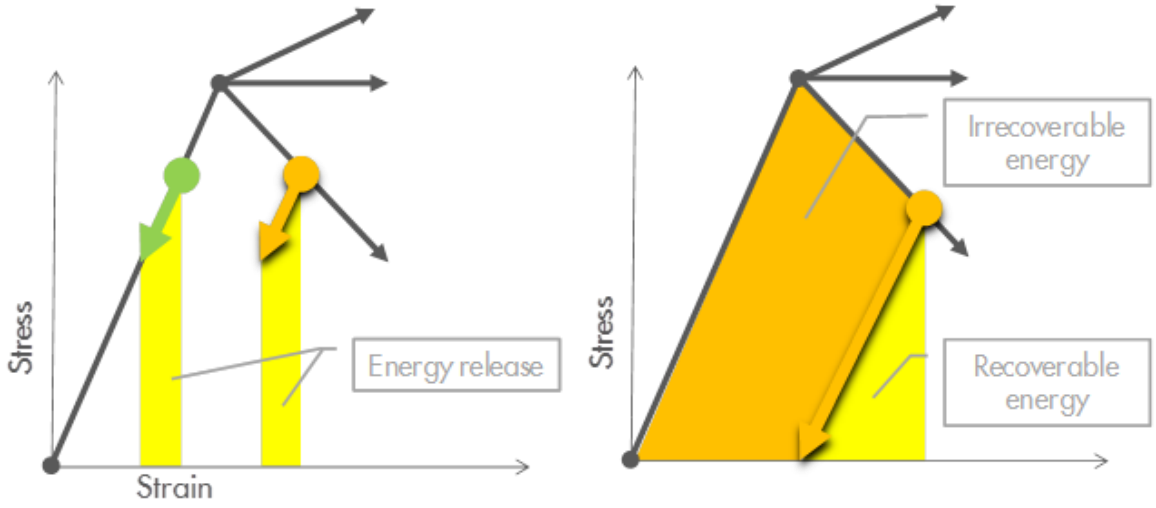

Figure 9.4 *Strain energy is released upon unloading of a material point. Part of the strain energy may be irrecoverable, which is expressed by a remaining strain after full unloading.*

9.2.3 Release of stored energy

Strain energy is released by material points that follow an unloading branch as indicated in Figure 9.4. In an idealized world, material behavior up to the onset of failure is assumed linear and elastic. This implies that no strain remains after removal of the stress (green point). Material failure is often the onset of a

nonlinear stress-strain relationship and is associated with the development of irrecoverable (in-elastic) strain. The orange point in Figure 9.4 shows the unloading behavior of a material point that has been in a post-failure state, in which not all strain energy is released.

Loading and unloading material points are both present in (subsurface) structures in which failure occurs. In case of tensile failure in the sample in Figure 9.1, the red point will show post-failure softening behavior, whereas the green material point enters an unloading branch as indicated in Figure 9.4. This is enforced by equilibrium of the sample. The green points release strain energy and the red points store strain energy. More energy is released if more material points respond like the green point. Unstable fracture propagation may occur if the energy released by the green points is larger than the energy stored in the red points.

9.2.4 The role of faults and the release of stored energy in the Groningen field

Seismic events are not possible without the occurrence of a failure mechanism. Fault slip is a known failure mechanism that releases strain energy from the subsurface [Kanamori (1994), Mulders (2003)]. As outlined in the previous sections, the released energy originates from formations that undergo stress unloading. It is therefore important to understand the stress loading and unloading behavior of formations. Energy dissipated by creep and other irrecoverable deformation processes in subsurface formations limits the available energy for release during a potential seismic event. The stress carrying capacity of faults at the onset of slip and their post-failure behavior determine what equilibrium conditions are possible and thereby the associated stored energy levels of adjacent formations.

At present, it is assumed that the earthquakes in the Groningen field are induced by gas production in the depleting reservoir and not by fault slip outside the depletion area. The left-hand side of Figure 9.5 shows the principle of seismicity by fault slip away from the depleting reservoir, whereas the right-hand shows reservoir depletion-induced seismicity, in which a growing Mohr circle touches the shear failure line. The assumption of reservoir depletion-induced seismicity is based on observations from other fields like Roswinkel (down-hole geophone trial, ABB, 2001) and the Bergermeer UGS (down hole geophone, pers. com. TAQA, KNMI, TNO). Both fields show seismicity mainly at reservoir depth. Also it is observed that a producing gas field records the first earthquake only after a certain pressure drop (van Eijs et al. 2006). This indicates that the normal faults in the Dutch subsurface are not critically stressed initially.
Based on currently available data, it cannot be ruled out that the seismic events originate from fault slip occurring above or below the depleting reservoir units.

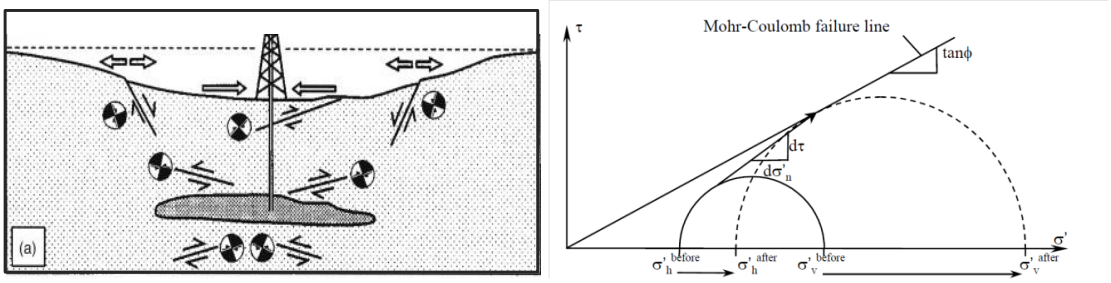

Figure 9.5 Principle of seismicity occurring outside the reservoir (left, taken from Segall, 1989) and depletion-induced seismicity (right, taken from Mulders, 2003)

A large number of faults have been interpreted in the Groningen field. The location of 707 major faults relative to the recorded seismic events is shown in Figure 9.6. This subset has been used for the construction of static, dynamic and geomechanical models. The subset of approximately 1000 minor faults has been disregarded for practical reasons. (Note that the extent to which these small faults, and even smaller sub-seismic faults, play a role in the geomechanical behavior of the reservoir rock is yet to be established). The faults in Figure 9.6 Are color-coded based on the number of seismic events within 500 meter distance. This implies that individual seismic events may be assigned to multiple faults. The range of 500 meter is based on the approximate accuracy of the current seismic monitoring network. Seismicity by slip along existing geological faults is a plausible explanation, although other failure mechanisms cannot be ruled out based on available field data.

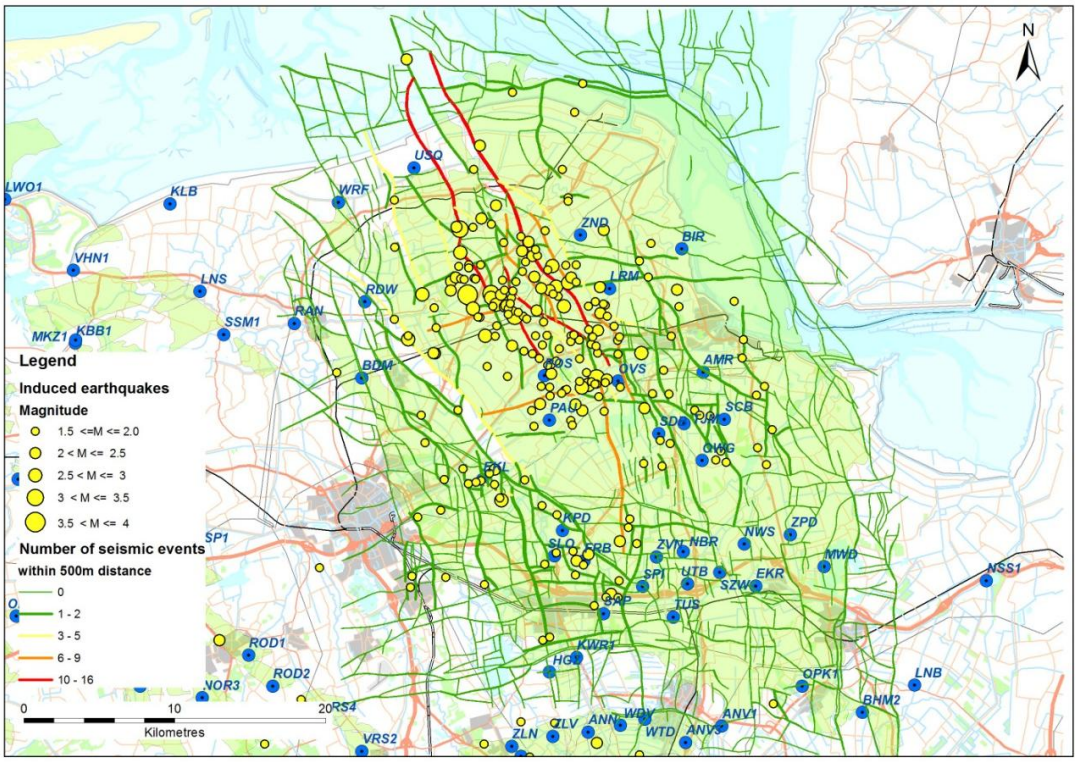

Figure 9.6 Groningen fault map with epicenters of recorded seismic events > 1.5. Color of faults indicates the number of events within 500 m distance from each fault. A selection of wells drilled in the area is indicated by the blue dots. Faults shown are at Top_Rotliegend level

9.3 What we know and what we don't know (yet)

In this section, an attempt is made to outline what is known and what is not known in terms of the geomechanical evaluation framework. Virtually all modeling elements of the framework need substantial improvement to make a step forward in the understanding of seismicity. At the same time many of these elements are difficult to constrain by field data. In principle the same strategy is followed that has lead in the past to successful approaches in the prevention of borehole instability and the management of sand production. In each section possible field monitoring options are identified to test modeling assumptions and constrain uncertainties. Subsequently, the following topics are discussed:

A. equilibrium of forces (stress), either statically or dynamically,
B. the (subsurface) structure that ensures that equilibrium is satisfied,
C. the material behavior of various components of the subsurface structure
D. the (depletion) loading on the subsurface structure

9.3.1 Equilibrium of forces (stress), either statically or dynamically

Seismic events are characterized by acceleration and deceleration of mass (material points). The conventional approach in geomechanical modeling is to assume static equilibrium, which is appropriate to simulate the onset of failure (such as fault slip) and even post-failure behavior as long as stable equilibrium can be demonstrated. Possibly, also the static stress distribution after a seismic event could be assessed. However, the internal stresses induced by acceleration require a vibration (dynamic) analysis.

Vibration analysis considers the forces associated with mass velocity and accelerations measured during seismic events. In theory, vibration analysis can address triggering of fault slip induced by slippage of neighboring faults if incorporated in a single dynamic system. However, industry experience in conducting this type of evaluation is very limited. Vibration analysis requires validation of additional modeling assumptions as well as calibrations of its parameters by dedicated field data, while modeling static equilibrium is already challenging.

A pilot study is scheduled for late 2013 to investigate how vibration analysis can contribute to a better understanding of the seismic events in the Groningen field. The pilot study is conducted on a 2-dimensional model and aims to reveal the importance of inertia effects on the stress distribution and the onset of fault slip. The pilot study should provide directions for this line of investigation.

9.3.2 Subsurface structure

A recently updated static subsurface model is available [Visser, 2012]. The static model determines the production-induced stress re-distribution in the subsurface in a geomechanical analysis. Formation layers that have a similar constitutive model may be joined together for geomechanical assessment. Up-scaling is applied to eliminate geometrical detail that is irrelevant to the risk under consideration, while maintaining the geomechanical response at large. More than 1700 faults have been interpreted in the Groningen field, of which 707 have been used to construct the static and dynamic reservoir model. Currently, geomechanical evaluation of all 707 faults in a single geomechanical model cannot be conducted realistically. Therefore, simplifications are incorporated in ongoing 3D modeling efforts, and dedicated studies are being conducted to reduce the modeling uncertainties (see section 9.4).

Key geometrical parameters, such as fault location, dip and azimuth angle are available in 3D. Also depth and thickness of adjacent formations and the throw across the fault can be obtained from the static subsurface model. These geometrical aspects have been found important in the determination of the onset of fault slip [Mulders, 2003], and are being used in detailed 2D analysis (see section 9.4.2). However, the available level of detail cannot be satisfied to the same level in 3-dimensional evaluations.

In general, geometrical detail that is not captured by seismic acquisition is not available. This includes sub-seismic faults, and formation offset along known and unknown faults. Also, other asperities that may induce local stress disturbances, and could trigger the onset of failure, are not captured.

An important factor in modeling the geomechanical response of the Groningen field is the required level of geometrical detail. Fault orientation and other geometrical aspects (asperities) are known to be very important in the prediction of slip onset, while the static model accuracy may be too limited due to the seismic resolution. On the other hand, computer capacity is also too limited to include all detail required for appropriate assessment. In summary, it is assumed that sufficient field detail is available for practically geomechanical evaluation, but more detail may improve assessment potential fault slip areas in the future. Seismic field monitoring needs to demonstrate the validity of the simplifications made, and whether or not the Groningen earthquakes can be associated with the current fault set. The uncertainty in the hypocenter locations with the current monitoring network is simply too large to draw that conclusion now. The down hole geophones will hopefully reveal whether the present model accuracy is at its right level of detail. The fault model can be considered to be appropriate if most earthquakes can be mapped.

9.3.3 Material behavior

The pre- and post-failure behavior of all formations is important for estimating the subsurface response to pressure depletion resulting from production (see section 9.2). In general, the mechanical contribution to the response reduces with the distance from the depletion area. The following models and parameters are relevant:

- Elastic response by Young's modulus (or compressibility) and Poisson's ratio. This is relatively well established for the Slochteren Sandstone from numerous experiments aimed at predicting compaction and subsidence in the field. However, these tests were done at relatively high loading rates. Lower loading rates normally lead to more strain (see also the description of the Isotach model in section 4). Furthermore, stiffness contrasts are less well understood due to the lack of measurements and the complex interaction of fluid dynamics with mechanical behavior (drained versus un-drained)
- Onset of failure in subsurface formations (the tensile, shear and compressive failure model and their associated parameters). Various lab experiments have shown that the onset of (shear) failure in the Slochteren Sandstone occurs at a high stress level (Holt, 2011), higher than expected stress paths in the Groningen field during the full production cycle. It is realized that there uncertainties related to the upscaling of lab test results to field-scale, and the impact of pre-existing defects within the rock mass.

- The post-failure behavior of the Slochteren Sandstone and Ten Boer Claystone has not been investigated.
- Unloading and cyclic behavior of the Slochteren Sandstone and Ten Boer Claystone in particular. Cyclic loading was studied in detail as part of an investigation to the Norg underground gas storage. A total of 70 cyclic loading tests were carried out on 5 core samples. The first cyclic loading resulted in a significant reduction of pore compressibility and compaction coefficient. This may partly be attributed to core damage. A further slight reduction in pore compressibility was recorded over cycle 2 to 5. A very small amount of un-recoverable strain was measured after each cycle, and attributed to creep behavior. After the fifth cycle the samples behave near elastic over the full reservoir pressure operational range between 33 and 10 MPa with a compaction coefficient of around $6*10^{-5}MPa^{-1}$.
- The shear stress carrying capacity of faults and their post-failure behavior. Some models have been proposed in which slip velocity is incorporated, such as rate and state slip models. The conversion of strain energy into thermal energy needs further attention. However, this is a fundamental uncertainty that depends on details of the dynamic rupture process and might be a limitation to further constitutive modelling.
- The variability of the constitutive behavior of formations and fault properties over the field. It is assumed that the behavior varies as a function of lithology and stress history. In particular the shear stress carrying capacity of faults is considered an important parameter. The quantification of this variability is not possible at this stage.

The main objective of additional constitutive modeling is to improve the accuracy and distribution of production-induced strain energy in the reservoir. The most important improvement step may arise from a long term compaction study with a particular focus to time-dependent subsidence behavior conducted by NAM and supervised by the "Waddenacademie (KNAW, 2013)".

9.3.4 Loading conditions, initial and production-induced

A distinction is made between initial loading and production-induced loading. The initial loading includes the determination of the virgin in-situ stress direction and magnitude in the field, as well as the pore pressure. The production-induced loading comprises the change of pore pressure and in-situ stress condition.

Initial Stress field direction and magnitude

The available stress data in the Netherlands suggest a normal faulting stress regime, with the assumption that the maximum principal stress is parallel to the vertical or overburden stress, and the minimum and maximum principal stress components are both in a horizontal direction. Principal stress values and their directions are key parameters for the analysis of possible reactivation of faults at the reservoir level in the Groningen Field. This section describes the interpretation of available data and the recently acquired data from the Borgsweer-5 well.

The vertical total stress is considered well established, and has been derived from the integration of the density log with depth. More than ten wells have an almost complete coverage of the density from surface to end depth. The variation in stress gradient at the reservoir is limited and mainly caused by thickness variations in the overlying Zechstein salt.

The minimum horizontal stress is not properly established for the Groningen field. The fracture closure pressure that can be interpreted from a rock strength test is the closest approximation of the value of the total minimum horizontal stress, which in our case is assumed to be the minimum horizontal stress or Sh. Stress values from rock strength test data were reported by Bouts (2000) and Hettema et al. (2000). The best estimate of the values including uncertainties is given in Hettema (2000). A thorough investigation concluded that the three data points that have been used in previous reports and publication are not reliable and should not be used in any subsequent study. Consequently, the only reliable information available from the Groningen rock strength tests was obtained during depletion. The rejection of the initial data points makes an assessment of an initial value of the Sh cumbersome. The extrapolated value from a straight line through only two data points yields a value for the initial stress of 1.6 bar/10m at an initial

pore pressure of 350 bar with a depletion constant of 0.6 (Figure 9.7). These values were used as the best guess values in the subsequent finite element models described further on, but are highly uncertain.

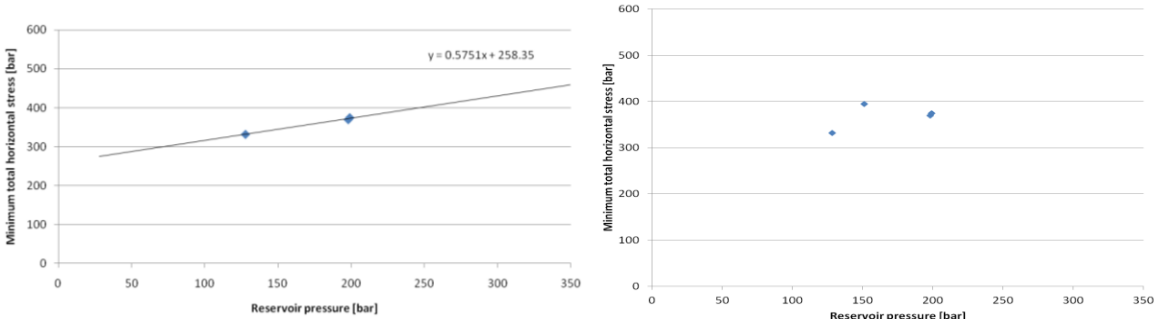

Figure 9.7 *Left: Historical rock strength tests from wells in the Groningen field and the trend line used to derive values for the initial stress and depletion constant for further studies. Right, same figure with the inclusion of the new Borgsweer-5 data point.*

The new rock strength test in Borgsweer-5 adds a new data point to this plot (van der Bas, 2013) visible in the right plot in Figure 9.9. It confirms the hypothesis that the stress and/or depletion constant is likely to be variable in the field, but makes a proper choice of a general value for the minimum total stress in further modeling attempts difficult. Therefore, the future acquisition of more data is an absolute necessity.

Multiple sources suggest a value for the maximum horizontal stress between 1.05 and 1.15 times the minimum horizontal stress. In the previous section the main focus was on the derivation of the magnitude and direction of the minimum principal stress. The value for the intermediate stress, which in our case is equivalent to the maximum horizontal stress or SH, cannot be measured directly. It can be obtained by finding a value for the stress ratios and then, by knowing the value of the minimum stress, calculate a value for the intermediate stress. Stress ratios can be derived from Differential Strain Analysis (DSA), breakout inversion and circumferential sonic logging tools like the sonic scanner that was run in the recently drilled Borgsweer-5 well. The results from these analyses were consistently showing a weak anisotropy where the SH is 5 to 15% higher with respect to the Sh. An average value of 10% will be used in subsequent studies.

The maximum horizontal stress direction is relatively well constrained from image logs. Image logs in a near vertical well can reveal information on a possible horizontal anisotropic stress field (e.g. Brudy and Kjørholt, 2001) when it is assumed that one of the principal stress directions is aligned parallel to the vertical axis. This approach has been pursued in an earlier study by van Eijs and van Dalfsen (2004) where stress directions have been mapped for the available data in the Netherlands. Additional data was found in the NAM data and interpreted. Six wells in the Groningen area (Wildervank-4, Rysum-Z-1, Rodewolt-1, Oude Pekela-2, Kiel Windeweer-1, Bierum-13) have image log data. Only two of them (Rodewolt-1 and Kiel Windeweer-1) contain clear expressions of breakouts. Kiel Windeweer -1 has a good quality image and shows breakouts over multiple sections (Figure 9.8).

The average direction for the SH derived from this data is 160°-340°. The Rodewolt-1 well contains poor breakout data for only three sections of breakouts. An estimated direction for the SH in this well is 155°-335°. An overview of the interpreted available data is given Figure 9.9.

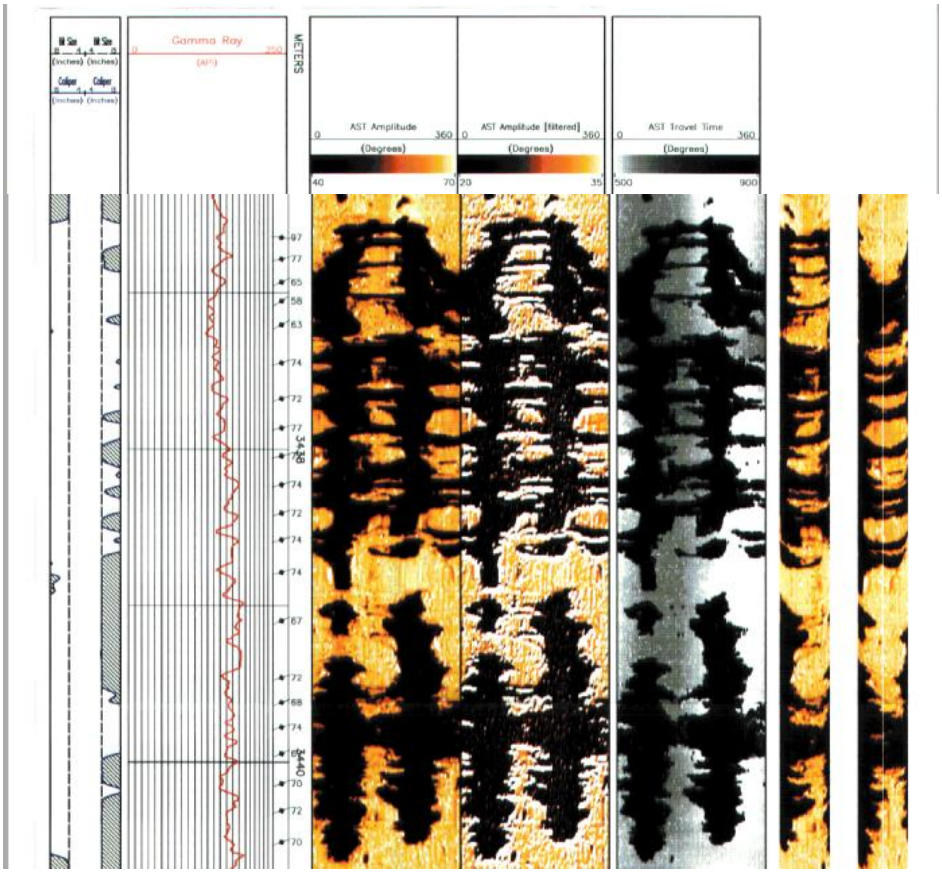

Figure 9.8 Part of the Kiel Windeer-1 image log showing a consistent pattern of breakouts

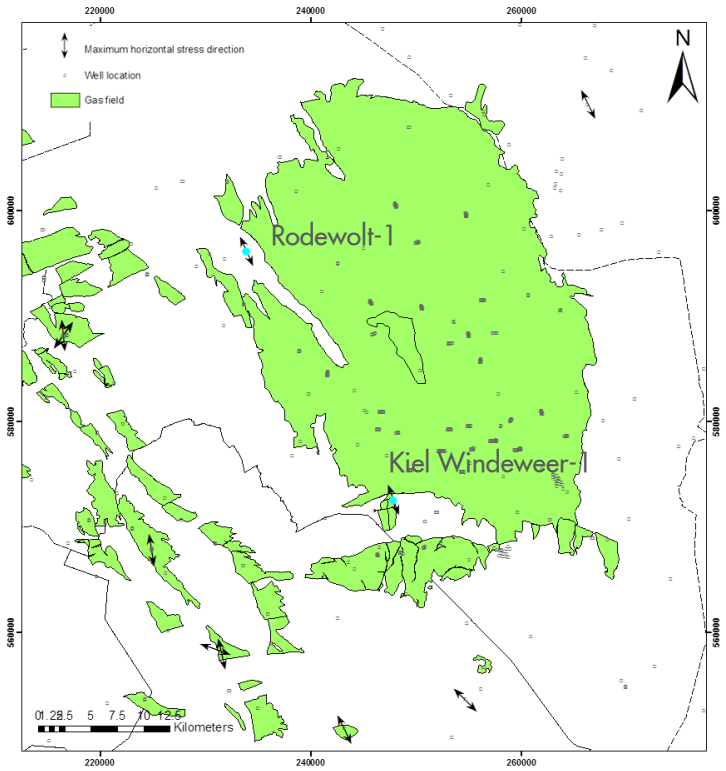

Figure 9.9 SH directions for the Groningen area. The new data (with labels and a blue dot in the middle) have been combined with information from the world stress map database

Production induced stress changes

The rock strength tests illustrated in Figure 9.7 show the dependence of the Sh on the depletion. Usually an average value for the depletion constant can be derived from this type of data, but currently the number of data points is too limited. For subsequent geomechanical modeling it was suggested to use a best estimate value of 0.6 or a stress-depletion relation based on the Poisson's ratio and Biot- alpha. The latter method is followed by Exxon-Mobil in their 3D finite element approach. The impact of the depletion on the Sv has not been investigated but is expected to be negligible. The gas production has been history matched to the reservoir engineering model by allowing a high transmissibility for the faults, but it cannot be excluded that gas or water is trapped within faults. This high pressure in the faults could increase the possibility of fault slippage. The same process may also play a role where water from the underlying aquifer preferentially flows into highly permeable faults.

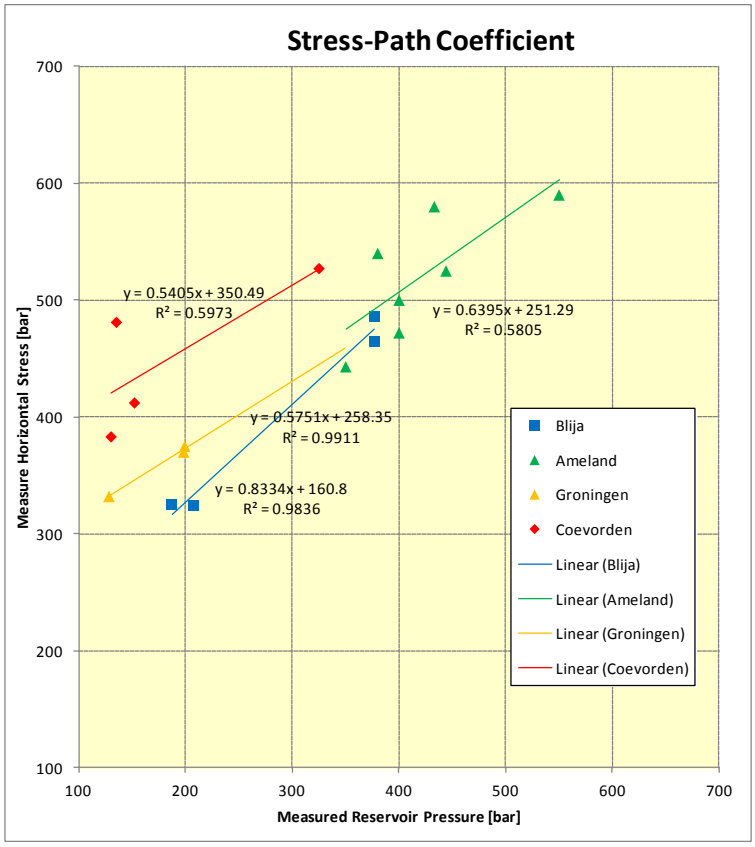

Figure 9.10 The (minimum) horizontal stress measured in different fields in The Netherlands at various levels of reservoir depletion and the derived stress-path coefficient (gradient of the linear trend lines).

9.3.5 Monitoring activities and further investigations

To test the hypothesis that seismicity occurs at the reservoir and at the faults as a result of poro-elastic stress changes, NAM will install two down hole arrays in the Zeerijp and Stedum monitoring wells (Figure 9.11). Based on modeling, these arrays will be able to detect and locate events in the micro-seismic domain M>-3 with a location accuracy of around 50m for a M=-1.5 event at an occurrence distance of around 500m. This is a very critical step in the assessment of the concept of induced seismicity that also forms the foundation of our current 2D and 3D finite element (FE) models.

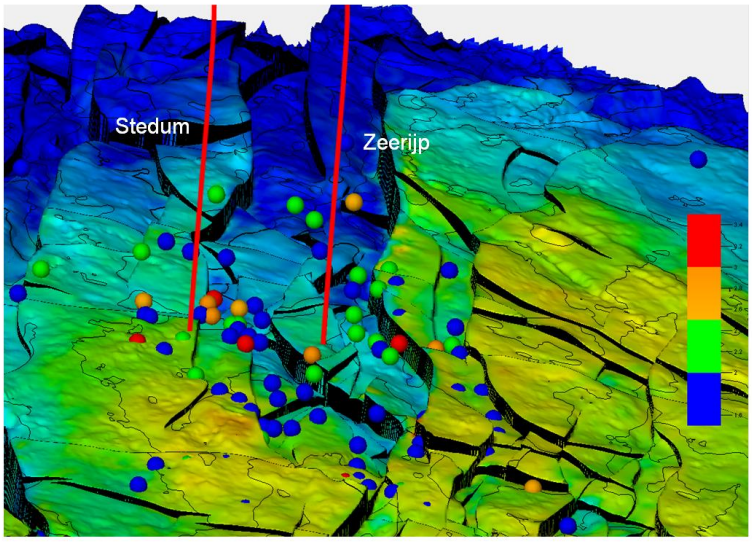

Figure 9.11 3D view towards the north of the top reservoir structure map with the subsurface position of the Stedum and Zeerijp wells where a temporary seismic array will be installed in autumn 2013.

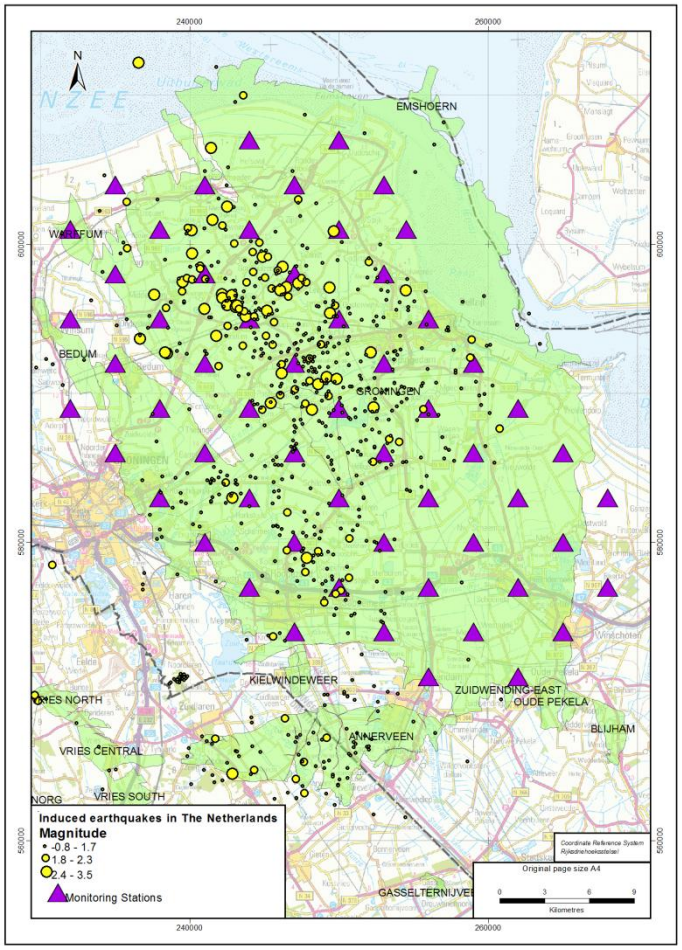

Figure 9.12 Proposed improved shallow geophone network

The planned extension of the shallow geophone network (Figure 9.12) also aims to significantly reduce the uncertainty in the position of the hypocenter. Moreover, it reduces the monitoring threshold for the whole Groningen field to a M=0.5 level. More details on the geophone monitoring are provided in section 10.2.

9.4 Geomechanical modeling

Currently, two types of modeling are on-going. One type has the objective to capture and represent the 3D field conditions as good as possible. The other type evaluates the parameters to be incorporated in more advanced modeling stages in the future. The first type is covered by the 3D modeling effort discussed in the next section. The second type comprises 2D modeling studies that address the impact of the geometrical configuration and the constitutive behavior of formations and faults on the onset of fault slip.

9.4.1 Full 3D modeling

The objective of the 3D geomechanical modeling approach is twofold:

- Create a load-and-resistance modeling approach that characterizes Groningen subsurface behavior related to production-induced fault reactivation
- Evaluate how alternative production strategies may help to manage subsurface stresses, in order to reduce fault slippage

The word "may" underlines the complexity of earthquake physics as well as the complexity of the subsurface and its relevant parameters. This is discussed more thoroughly in section 9.1. Reactivation of faults is linked to the 3D stress evolution in and around the producing field while it is being produced. Both Baker Hughes and Exxon Mobil (XoM) were asked to build 3D models for the full field. In addition, XoM also builds two zoom-in models that both capture more geological detail and a better mechanical description for fault behavior. The location of the two zoom-in models is indicated in Figure 9.13.

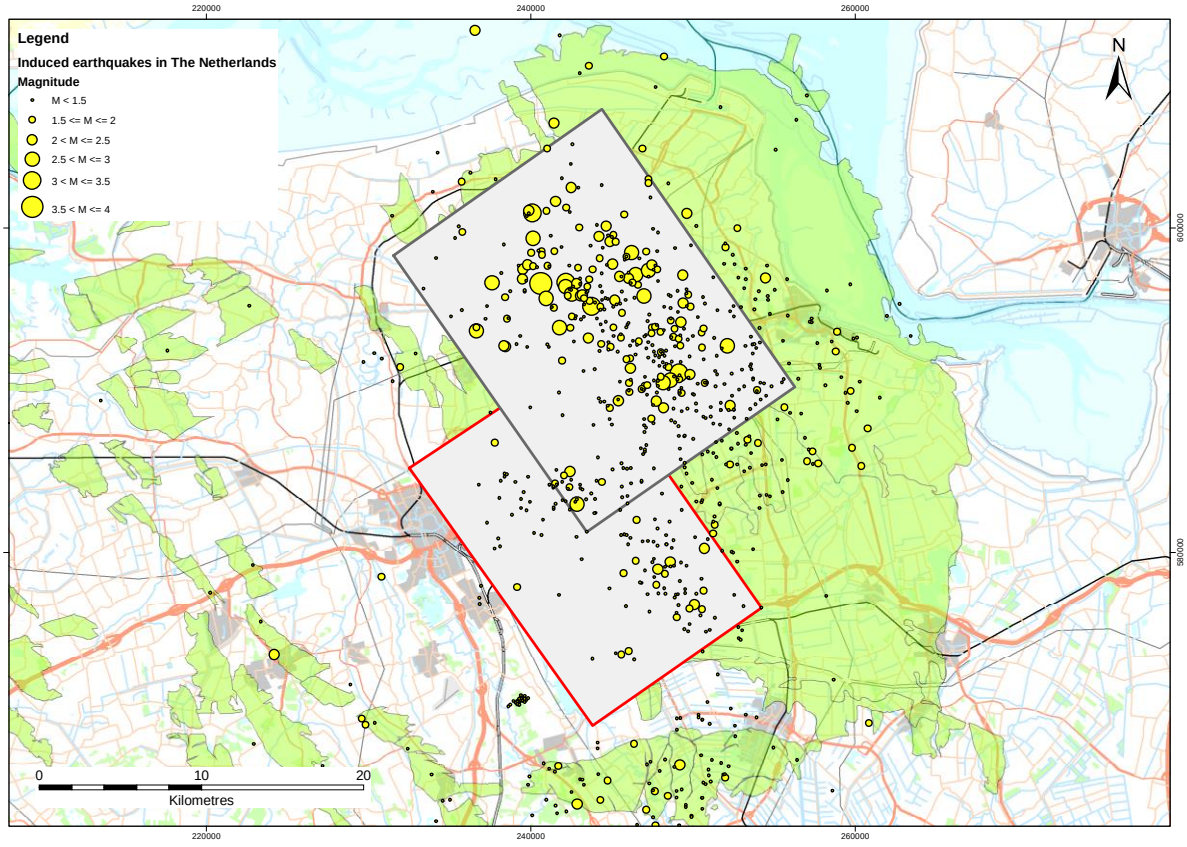

Figure 9.13 Location (red and grey rectangles) of the zoom-models from XoM.

The 3D modeling results are described in section 9.16 (3D modeling results). Figure 9.14 conceptually illustrates how the geomechanical modeling may fit into a more comprehensive subsurface stress management / risk management framework, also including lab measurements, field measurements and surveillance.

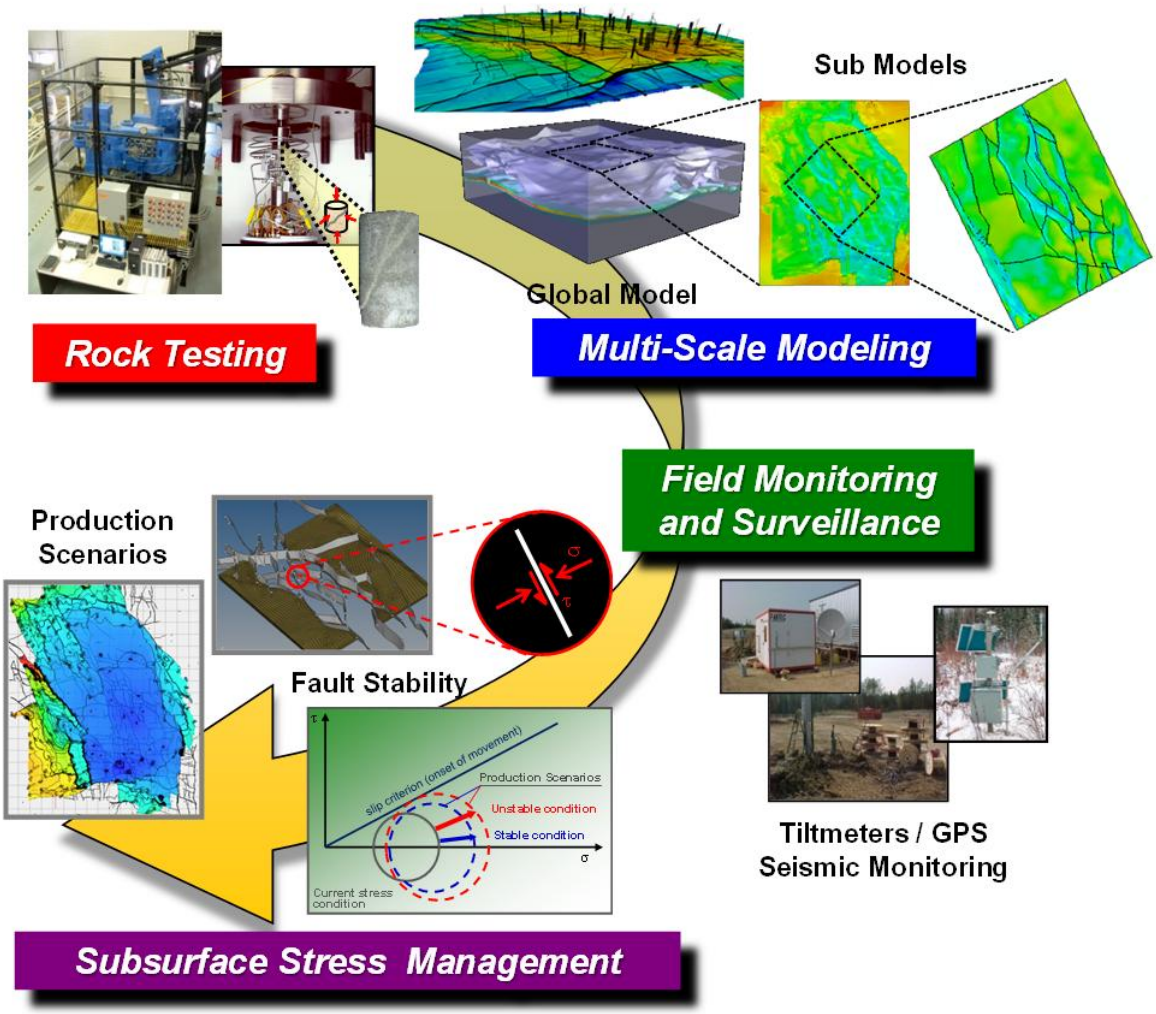

Figure 9.14 Geomechanical modeling as part of a subsurface stress management / risk management framework.

9.4.2 2-Dimensional modeling of fault slip

A 2-dimensional model generator is being developed to address some of the modeling uncertainties highlighted in Section 9.2 above. This line of investigation builds on previous work by Roest (1993), Mulder (2003) and Orlic (2012) among others. Main difference is the focus on the Groningen field conditions. Both static and dynamic equilibrium conditions are being evaluated.

The main objective of the static evaluations is to develop a better understanding of the impact of geometrical and constitutive modeling assumptions on the onset of fault slip for different depletion conditions. In particular, the throw of formations with different thickness across a dipping fault is addressed (Figure 9.15). The model allows incorporation of a different in-situ stress and pore pressure condition in each formation on both sides of the straight fault plane. Also, the formation properties can be assigned independently. Initially, the only failure mechanism incorporated is slippage along the fault plane assuming no post-failure hardening or softening behavior. Subsequent evaluations will include more complex, non-linear and time-dependent (creep) behavior for the fault as well as for the formations.

The dynamic (vibration) analysis is aimed to reveal the importance of inertia effects on the stress distribution and the onset of fault slip.

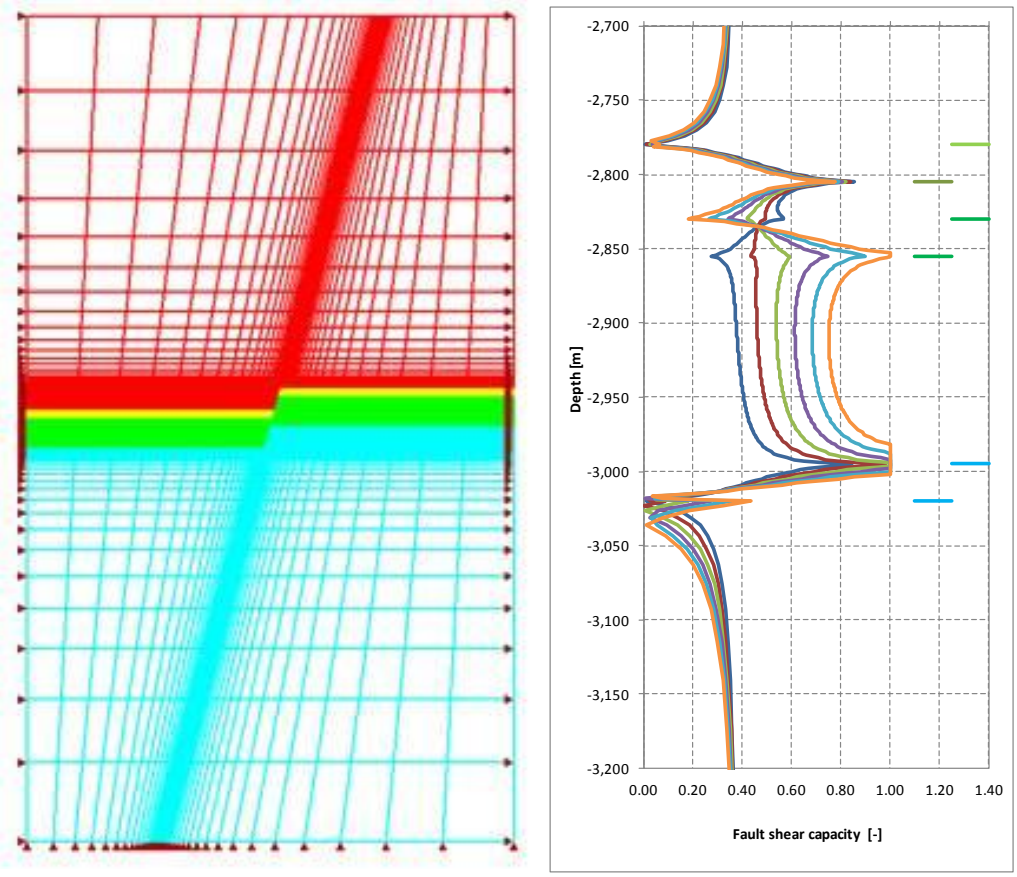

Figure 9.15 Example of a 2D finite-element model (left) and the Shear Capacity Utilisation (SCU) along a fault plane (right) under increasing pressure depletion conditions. The fault is slipping where SCU=1.

9.5 2D Geomechanical investigation of the potential causes of fault slip and seismic events

The objective of the work reported in this section is to identify potential fault slip mechanisms and the impact of various modelling options and their associated parameters on the simulated geomechanical response. Knowledge of the potential fault slip mechanisms and slip geometries can help to focus the field data acquisition programme and possibly test the actual occurrence of particular mechanisms in seismic events. Knowledge about the simulated geomechanical response is expected to help selecting the most appropriate modelling option for the observed behaviour. A two-dimensional modelling environment is chosen to allow for a wide range of modelling options and parameters to be evaluated relatively quickly. These modelling options comprise all main elements of the geomechanical evaluation framework as outlined in Research study 5 (2013), namely geometrical modelling, constitutive modelling, in-situ stress and depletion modelling, and also dynamic equilibrium modelling aspects.

This chapter reports the initial results of the 2D studies addressing the impact of formation offset on the onset and post-failure behaviour of fault slip. Previous work by Roest & Kuilman (1994), Glab & van Eijs (2001), Mulder (2003) and Orlic & Wassing (2012) has revealed that geometrical parameters and in particular the offset along faults influences the onset of fault slip. Therefore, this study focuses on this specific modelling aspect first. It differs from previous work in its evaluation of the depletion level at the onset of fault slip for various offsets, but also the post-failure behaviour in terms of the development of total length of the fault slip sections, the maximum Relative Shear Displacement and the dissipated energy level as a function of depletion and fault offset. In addition to the fault throw aspect, also other geometrical, constitutive and in-situ stress parameters will be investigated.

The main features of the newly developed 2D model generator are described, followed by a presentation of the parameters used in this initial study. The geometrical parameters and in-situ stress conditions reflect the Groningen field conditions as good as possible given the limited available data. The formation and fault properties have been selected in such a way that fault slip is triggered within the depletion range applied

(0-20 MPa), and such that the impact of fault throw is revealed without unnecessary influence of other modelling aspects. Consequently, the reported values are not representative for the Groningen field conditions at this stage, but are aimed to develop a qualitative insight into the impact of formation throw on the onset of fault slip and slip behaviour.

9.5.1 Model features

A model generator has been built to evaluate the geometrical configuration outlined in Figure 9.16 using finite-element techniques. The configuration comprises a dipping fault plane and 2 sets of horizontal formation layers, 4 in the foot wall and 4 in the hanging wall. The most shallow layer (1) on each side of the fault represents the overburden, layer 2 is a stiff anhydrite/carbonate interval, layer 3 represents a potential reservoir unit that can be assigned a change of pore pressure, and the deepest layer (4) is the underburden. Note that layer 2 represents the Basal Zechstein stratigraphic interval, and all Rotliegend stratigraphic intervals (Ten Boer, Upper Slochteren, Ameland and Lower Slochteren) are grouped into layer 3. The thickness of each of the constituent model layers can be specified independently. The vertical throw over the fault is defined by the difference in thickness of the overburden layer (1) in the hanging wall and the foot wall. Furthermore, the dip angle and dip azimuth of the fault relative to North, as well as the maximum horizontal stress azimuth is specified to set the desired initial stress conditions.

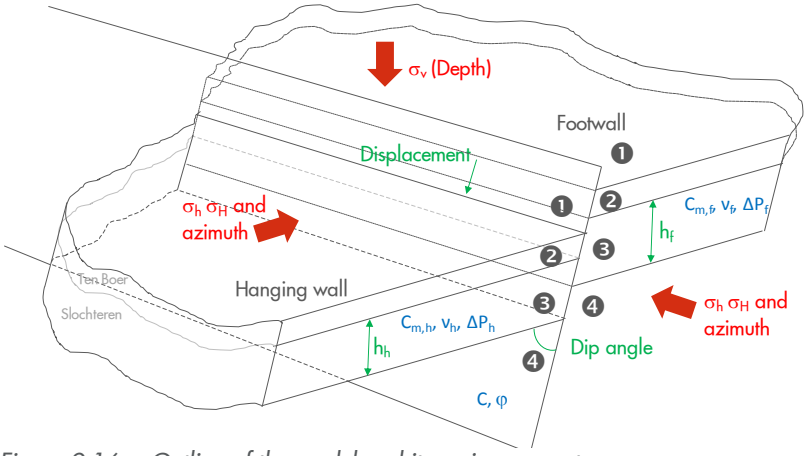

Figure 9.16 Outline of the model and its main parameters.

The material properties, in-situ stress and pore pressure can be specified for each of the 8 layers independently. The current model generator supports linear-elastic material behaviour, specified by Young's modulus and Poisson's ratio. The total vertical stress is given by the density of each formation layer, whereas both horizontal total stress components are specified through a k0 ratio with the total vertical stress. The pore pressure is specified by a depth gradients from a given reference pressure and reference depth. An independent change of pore pressure can be specified to 4 formation layers, namely layers 2 and 3 on the hanging and foot wall side of the fault. This change of pore pressure is assumed to be uniform within the 4 formation layers. The pore pressure in the fault can be assigned equal to the formation pore pressure at either the left or right side of the fault.

The fault behaviour is described by a Mohr-Coulomb slip criterion, which is specified by a cohesion and friction angle. The post-failure behaviour is assumed "ideal plastic", which means that the shear stress carrying capacity of the fault remains constant after onset of slip. A dilatancy angle is specified to describe the post-failure behaviour in the fault [TNO-DIANA, 2011].

Fault slip behaviour is evaluated by a 2-dimensional (DIANA) plain strain finite-element model (Figure 9.17). One-dimensional interface elements simulate the behaviour of fault slip. The size of the interface elements is restricted to 1 m in order to appropriately describe the development of critical stress conditions in the presence of fault offset. The quadrilateral continuum elements next to the interface elements have a similar size and increase towards the boundaries of the model. The fault zone and the four formations on each side are recognised by the small element region in the middle of the model in Figure 9.17.

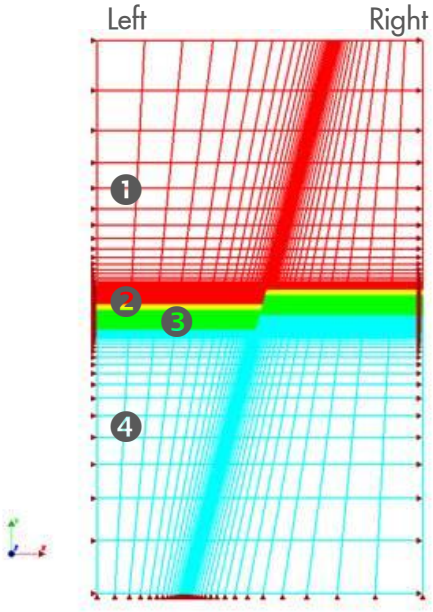

Figure 9.17 Example a generated finite-element mesh with down-thrown (positive offset) model layers on the left-hand side of the fault.

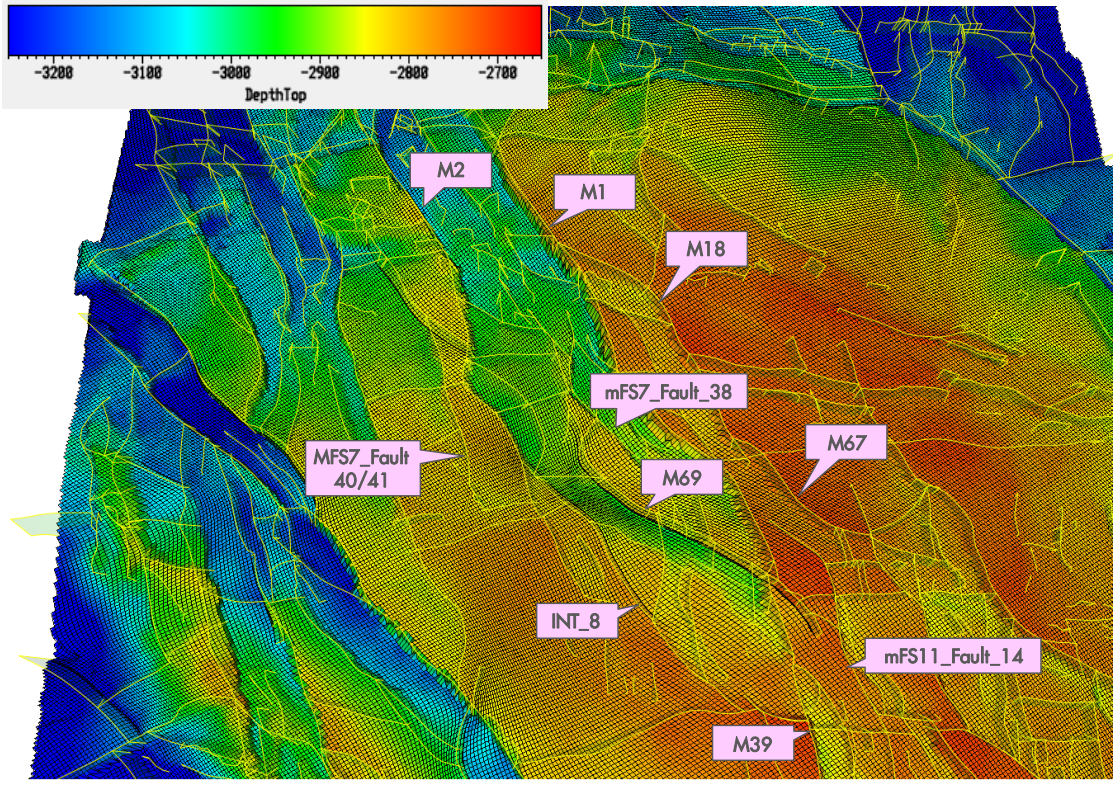

Figure 9.18 Top Rotliegend depth map and the interpreted fault planes [2] in the North-Western part of the Groningen field. A selection of faults in the vicinity of the largest recorded seismic events has been indicated.

Geometrical setting

The analysis results reported in this study have been obtained from a model with a total width of 2000 m and a depth between 0 and 6000 m. The thickness of layers 2 and 3 as described above has been derived from the Groningen subsurface model.

The fault configuration of fault M1 (Figure 9.18) has been used to determine the ranges for various geometrical parameters in the current study. The various relevant parameters are summarised in Table 9.1. The thicknesses of all model layers have been kept constant in the current study, except for the overburden thickness on the left-hand side of the fault (see Figure 9.17). In this way, throw magnitudes between -300 and +500 meter have been prescribed (Note that only normal faulting - i.e. positive throw - is seen in the Groningen field). The fault dip has been set to 65 degree with the horizontal (25 degrees with the vertical). This configuration generates a modelling cross-section perpendicular to fault M1 and looking in North-North-Western direction.

	Unit	Value
Rotliegend depth	[m]	2780
Basal Zechstein thickness	[m]	50
Rotliegend thickness	[m]	215
Vertical throw	[m]	Between -300 and +400
Fault dip with horizontal	[deg]	65
Fault sip azimuth North to East	[deg]	240 (60)

Table 9.1 Formation thickness, throw and other geometrical properties along Fault M1.

9.5.2 In-situ stress and formation properties

The in-situ stress has been taken from [Van den Bogert et al., 2013]. The stress gradients have been converted into a formation density and a maximum and minimum total horizontal stress ratio to the total vertical stress (k0-max and k0-min respectively) to facilitate incorporation into the 2D model. The results of the conversion are given in Table 9.2.

Identical values for Young's modulus and Poisson's ratio have been used for all model layers in order to remove any influence of stiffness contrast on the onset of fault slip. The impact of stiffness contrasts is to be addressed in further studies to better represent the actual values in the field.

Table 9.2 Formation thickness, throw and other geometrical properties along Fault M1.

	Density	K0-max	K0-min	Young's modulus	Poisson's ratio
Unit	[kg/m^3]	[-]	[-]	[GPa]	[-]
Layer 1 – Overburden	2172	0.795	0.748	10	0.25
Layer 2 – Basal Zechstein	2450	0.795	0.748	10	0.25
Layer 3 – Rotliegend	2450	0.795	0.748	10	0.25
Layer 4 – Underburden	2700	0.795	0.748	10	0.25

The initial pore pressure in the overburden layer 1 is hydrostatic with a pressure gradient of 10 kPa/m (1.0 bar/10m). Also, layer 2 has been assigned this initial pressure gradient. The more saline aquifer in the underburden layer (4) causes a somewhat elevated pressure gradient at 11.66 kPa/m. In model layer 3 a gas density of 1.8 g/cm^3 has been applied. Furthermore, the Gas-Water Contact has been set at 2995 m TVD at a pressure 35.2 MPa (352 bar). This pressure regime has been applied to layers 3 and 4.

Finally, cohesion and friction angle for the interface elements that describe the fault behaviour are set to 7 MPa and 13 degrees, respectively. These values have been used in a previous study to ensure that onset of fault slip is predicted in a wide range of values for Poisson's ratio that strongly influences the change of the horizontal stress in uniaxial compaction conditions under reservoir depletion.

Reservoir depletion conditions

Uniform reservoir depletion has been simulated by lowering the pore pressure in model layer 3 on both sides of the fault. That is, the fault has been assumed to transmit and to equilibrate any pressure difference that might occur in the course of production. The pore pressure in the fault follows the depletion along those parts that are in contact with a depleting layer and maintains the virgin pressure in all other parts. Depletion has been increased in 20 steps of 1 MPa (10 bar). This is the depletion level that is encountered in large part of the field, and has also been used in a previous assessment [Van den Bogert et al., 2013]. No pressure depletion is prescribed in any of the other model layers.

9.5.3 Model results

The model described in the section 9.5.1 has been used to evaluate the onset of fault slip and subsequent slip behaviour under increasing reservoir depletion conditions for a throw between -300 (up-thrown) and +500 m. About 40 analyses have been conducted with throw increments of 20 meter.

The results of the two-dimensional analyses are discussed in detail for the case with a (downward) throw of 80 meter. The results include the prescribed pore pressure, the calculated effective normal and shear stress, the Shear Capacity Utilisation (SCU) and the Relative Shear Displacement (RSD) along the fault plane as a function of depth and depletion level. Furthermore, the strain-energy level in the model is tracked as well as the energy dissipated by fault slip. It is emphasised that none of the mentioned results are representative for the Groningen field conditions at this stage. The analyses are aimed to develop a qualitative insight into the impact of formation throw on the onset of fault slip and slip behaviour. Various modelling parameters have been selected such that fault slip would be triggered.

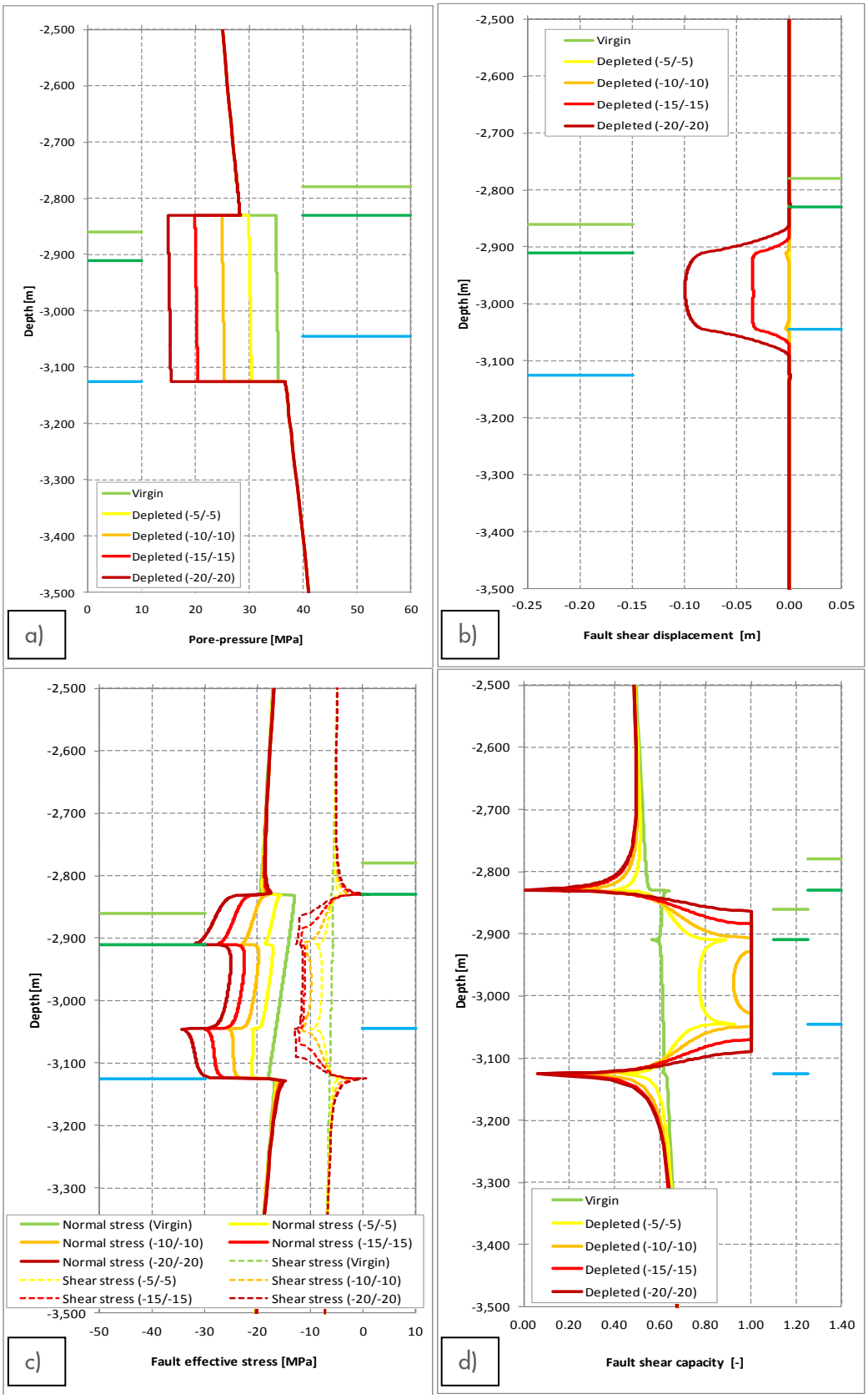

Figure 9.19 a) Pore pressure, b) Relative Fault Shear Displacement (RSD), c) Effective normal and shear stress, and d) the Fault Shear Capacity Utilisation as a function of the depth for a throw of 80 meter, under virgin and 5, 10, 15 and 20 MPa depletion conditions.

Figure 9.19a shows the applied pressure profile as a function of depth for 5, 10, 15 and 20 MPa (50, 100, 150 and 200 bar) reservoir depletions. The location of the interfaces between formation layers 1, 2, 3 and 4 on both sides of the fault are indicated by horizontal (green and blue) marker lines. The gas gradient in the reservoir formations is steeper than the water gradients in over- and underburden.

Figure 9.19b shows the Relative Shear Displacement (RDS) along the fault plane as a function of depth for the same depletion levels. Negative values indicate that the left-hand side of the fault is displaced downwards relative to the right-hand side of the fault. For a throw of 80m a maximum RSD of 0.10 meter is calculated under 20 MPa depletion, whereas the slip is negligible for a depletion level of 10 MPa and lower.

Figure 9.19c shows the effective normal and shear stress distribution and Figure 9.19d shows the derived Shear Capacity Utilisation (SCU) as a function of depth. This is the ratio of the actual shear stress τ and the shear stress carrying capacity τ_{max} according to a Coulomb friction law, with a cohesion of 7 MPa and a friction angle of 13 degree. An SCU of 1 means that the maximum shear stress has been reached and that the fault is slipping. Values larger than 1 are not possible. The total length of the interface elements for which SCU=1 is defined as the slip section. Two slip sections are found under 5, 10 and 15 MPa depletion, whereas one larger slip section is found under 20 MPa reservoir depletion.

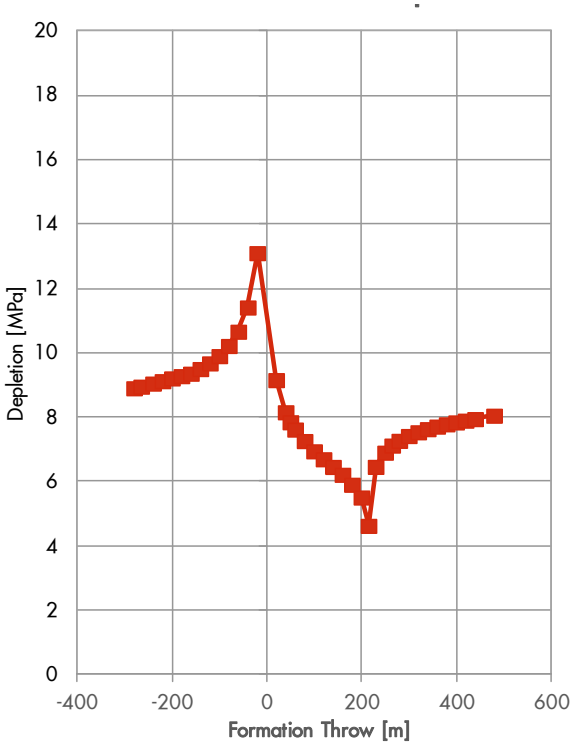

Figure 9.20 Onset of fault slip as a function of fault throw in the formation

The onset of fault slip is determined by the occurrence of an interface element with an SCU of 1, and is given as a function of fault throw in Figure 9.20. The depletion level is calculated by interpolation between depletion step results. It is seen that a fault with zero throw requires the largest depletion level for the onset of fault slip, whereas a fault with a throw that is equal to the reservoir thickness (215 m in this case) starts to slip at the smallest depletion level. Furthermore, it is found that extremely large positive or negative throws converge to the same depletion level for the onset of slip. These cases describe a model configuration with depletion on one side of the fault only. The offset of the depleting reservoir layer is so large that peak stresses do not interfere with each other. Finally, it is noted that fault slip is not initiated under 20 MPa depletion in the case of 0 m offset. In this case, the maximum SCU is 0.97 under 20 MPa depletion.

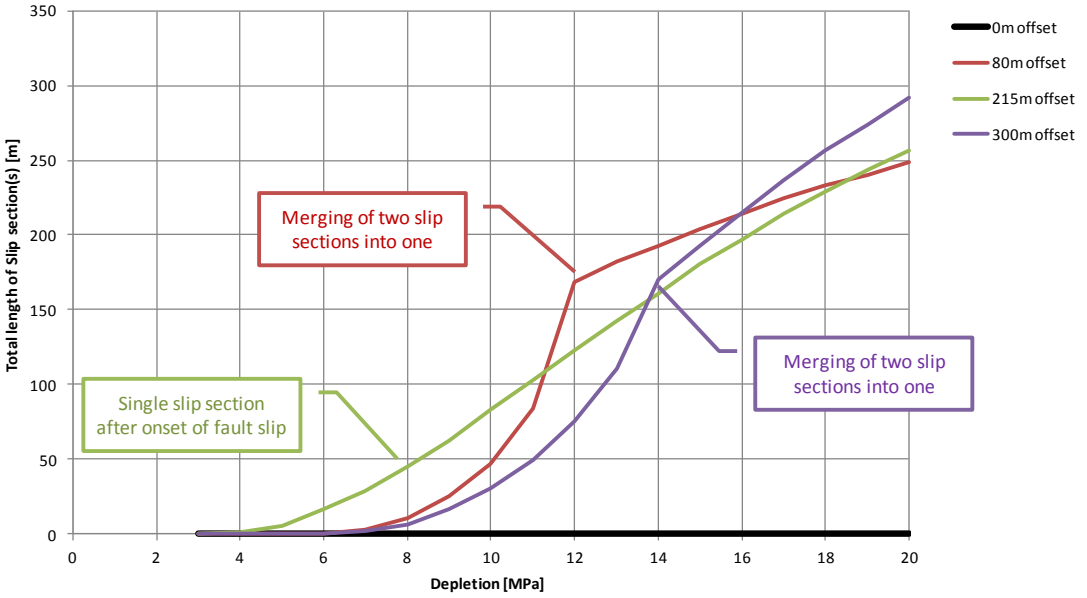

Figure 9.21 Development of the slip section [m] as a function of the depletion level for different throws (offset) along the fault plane.

The development of the slip section with increasing reservoir depletion is plotted in Figure 9.21 for the cases of 0, 80, 215 and 300 m throw along the fault. No fault slip is developed with zero throw up to 20 MPa depletion, while the slip section gradually grows starting after a depletion slightly over 4 MPa in the case of 215 m fault throw. This case features only one slip section that initiates at the top of the down-thrown block. The case of 80 m fault throw, shown in detail in Figure 9.19, features two slip sections up to 12 MPa depletion when both merge into a single slip section. Figure 9.21 shows that the growth of the two slip sections accelerates with depletion, until they merge and continue to grow in a stable rate upon further depletion. The same fault slip geometry is found for a fault throw larger than the thickness of the depleting reservoir formation, in which case two slip sections merge into a one larger section under increased depletion.

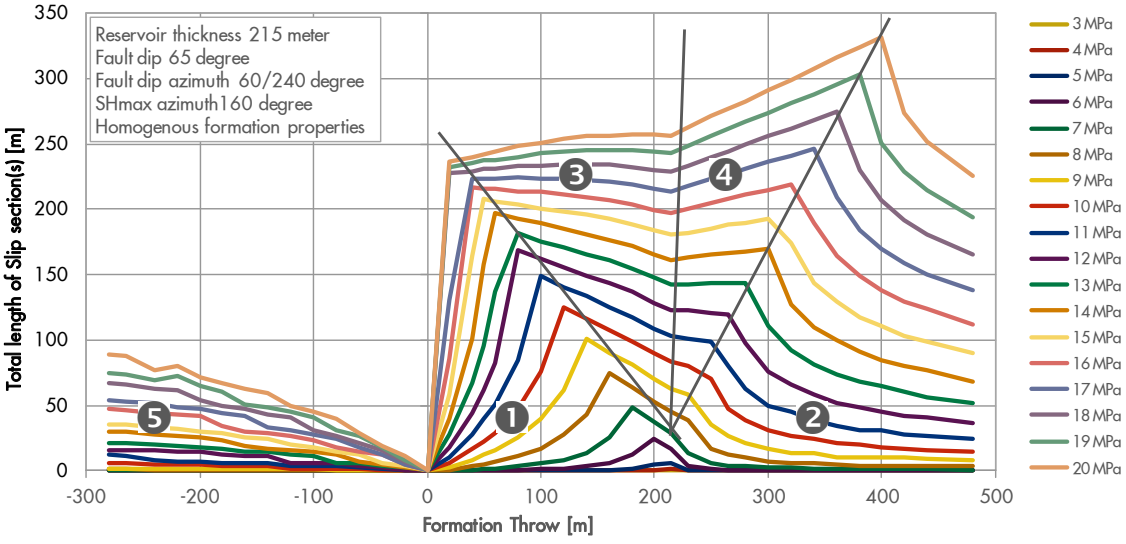

Figure 9.22 Total length of slip sections as a function of fault throw and reservoir depletion.

Figure 9.22 shows the total slip length for all evaluated depletion levels (starting at 3 MPa) and a throw between -300 and +500 m. Three fault slip conditions can be identified based on throw and depletion level:

1. Two slip sections are found in case of a positive reservoir offset and under low to moderate depletion levels, labelled 1 and 2.

2. A single, merged fault slip section is found under in case of a positive reservoir offset and under elevated depletion levels, labelled 3 and 4.
3. Two slip sections that do not merge even under elevated reservoir pressure in case of a negative reservoir offset, labelled 5.

The merging of the two slip sections into one is dependent on the offset along the fault. The transition from slip condition 1 with two slip sections to slip condition 3 with one slip section is somewhat different for a throw smaller than the depleting formation thickness (215 m in this case) than the transition from slip condition 2 to 4 for larger throws. In the latter case, the slip section length grows more rapidly with depletion. This is also seen in Figure 9.21, where the merged slip section for a throw of 300m increases faster (after 14 MPa depletion) compared to the case of a throw of 80 m (depletion larger than 12 MPa).

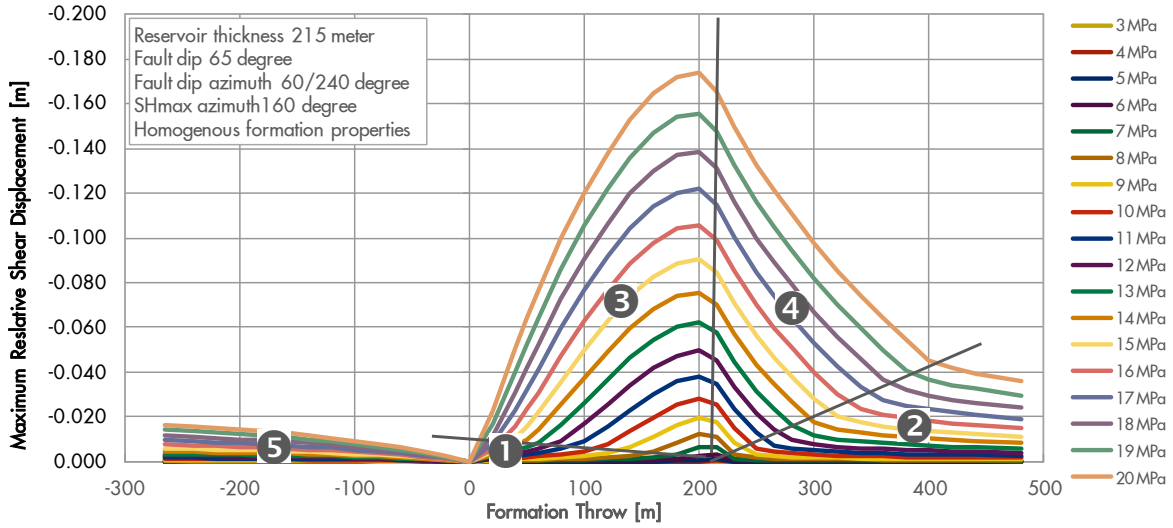

Figure 9.23 Maximum Relative Shear Displacement [m] as a function of throw and reservoir depletion

The maximum Relative Shear Displacement (RSD, Figure 9.23) shows an extreme value at an offset slightly smaller than the depleting formation thickness for all depletion levels. The five different fault slip conditions indicated in the figure highlight that the RSD accelerates with depletion after the slip sections have merged. This particularly holds for fault throws smaller than the thickness of the depleting reservoir: the maximum RSD in slip condition 1 is smaller than in condition 2 under the same depletion level, while the maximum RSD in 3 is comparable to, or larger than, in 4.

In sum, it is seen that fault configurations with an offset smaller than the thickness of the depleting reservoir layer develop a larger slip displacement over a shorter slip length than configurations with an offset larger than the thickness of the depleting reservoir layer.

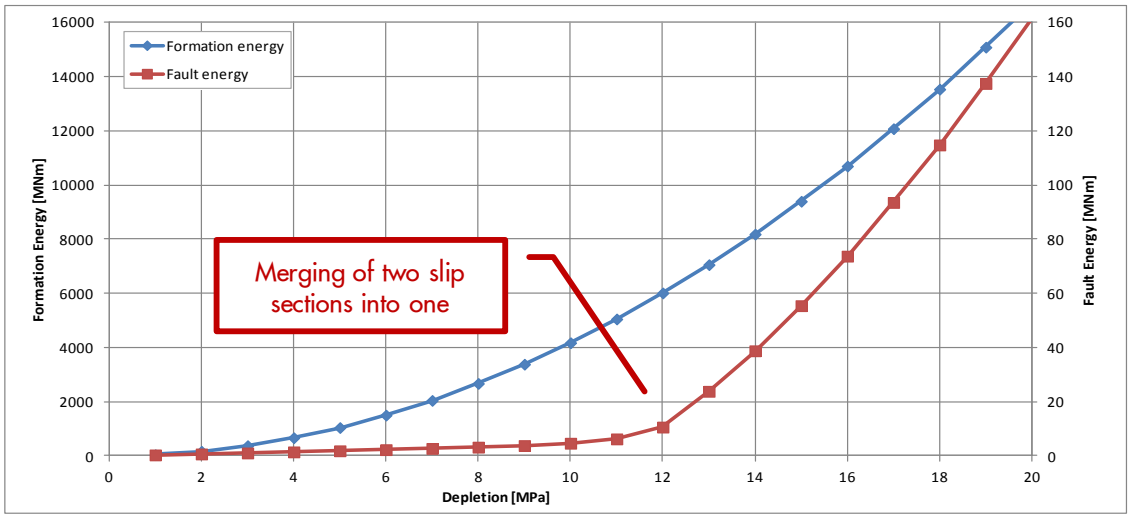

Figure 9.24 Formation and fault energy as a function of depletion level for a throw of 80 m.

The dissipated energy by fault slip is calculated as the product of the shear stress, the slip displacement and the area of each interface element. The dissipated fault energy (Figure 9.24) shows an acceleration with increased depletion after the two slip sections have merged. Note that the onset of fault slip, which occurs at 7.3 MPa depletion in the case of 80 m throw, is not visible on the scale used in Figure 9.24, while the merging of the two slip sections is. The energy dissipated in the fault up to onset of slip is elastic and recoverable, whereas the incremental energy after onset of slip is not. However, the dissipated energy level remains limited as long as two slip sections exist.

The strain energy in the formation increases nonlinearly with depletion and is several orders of magnitude larger than the energy dissipated by fault slip. The strain energy is calculated by integration of the stress-strain relationship for all material points in the 2D model. A larger model (volume) will have a larger strain-energy level while the dissipated fault energy will remain the same in that case. For the linear-elastic stress-strain relation employed here, the incremental strain-energy stored in the model by an incremental depletion of the reservoir pressure increases with the depletion level and causes the nonlinear curve in Figure 9.24 for the formation energy.

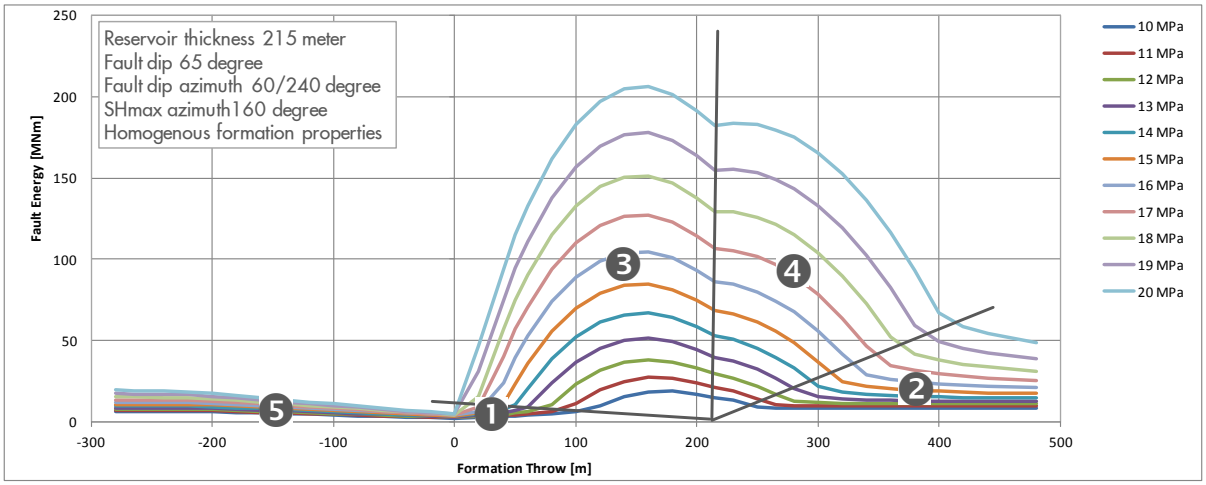

Figure 9.25 Fault energy dissipated by fault slip as a function of throw and depletion level

The five different fault slip conditions indicated in Figure 9.25 highlight the limited energy dissipation for conditions 1, 2 and 5. For slip conditions 1 and 2, the energy dissipation in the latter is substantially larger for offsets larger than the thickness of the depleting layer. In both cases 1 and 2, the energy dissipated by fault slip becomes more significant when the two slip sections have merged into one slip section, indicated by the labels 3 and 4 in the figure. It is seen that most energy is dissipated in slip condition 3, which is in general characterised by the larger RSD and smaller slip section length than in slip condition 4.

9.5.4 Summary of findings 2D modeling

In the previous section, different fault slip geometries have been identified based on fault throw and depletion level under the assumptions given in section 9.5.1. It is found that offset of depleting reservoir layers along existing faults highly impacts the geomechanical response in terms of

- The depletion level at the onset of fault slip
- The number of slip sections
- The total length of the slip sections
- The maximum Relative Shear Displacement
- The energy dissipated by fault slip.

The following cases can be identified in terms of throw:

1. The throw is smaller than the thickness of the depleting reservoir layer
2. The throw is larger than the thickness of the depleting reservoir layer
3. Negative throw (reverse faulting).

Fault slip generally starts with two slip sections at a relatively low depletion level in all three cases. They differ in the merging of the two slip sections at an elevated depletion level for cases 1 and 2, which is not found for the evaluated condition in case 3. The merging of the two slip sections has different characteristics in Case 1 than in Case 2. Generally, in Case 2 a smaller slip displacement is developed over a larger slip length compared to Case 1. Also, the energy dissipation varies. The two slip sections in Case 2 dissipate more energy than the two slip sections in Case 1 under the same depletion level, while this is the other way around for most throws in Case 1.

Two exceptions to the above are identified, where a single (merged) slip section occurs directly after the onset of fault slip, namely

1. Zero throw:
   a single slip section is predicted over the entire thickness of the depleting reservoir layer just after the onset of fault slip.
2. The throw is equal to the thickness of the depleting reservoir layer, in which case the slip section gradually increases with depletion at the location where the two depleting layers connect.

These two exceptions also provide the upper and lower limit of depletion at the onset of fault slip. Exception case 1 can hold the highest depletion level before the onset of fault slip takes place, while Exception case 2 starts to slip at the lowest depletion level. Hence, onset of fault slip is found to be strongly dependent on throw.

Under the current modelling assumptions, the development of the slip section after the onset of fault slip occurs most gradually with depletion for a fault throw equal to the thickness of the depleting reservoir layer. For all other cases with normal faulting, the development of the slip section accelerates with depletion until the two sections merge into a single slip section (Figure 9.21). In the extreme case, in the absence of throw, the slip section develops abruptly at the onset of fault slip. So, fault slip in the two extreme cases occurs either abruptly over the thickness of the depleting layer at an elevated depletion level, or gradually with depletion starting at a low depletion level.

The assumption of ideal plastic fault slip behaviour causes a stable propagation of the slip sections in all cases evaluated so far. Faults with zero offset show the most rapid development of the slip section, but also in this case a stable equilibrium condition is found. This implies that incremental reservoir depletion is required to propagate the slip section and, as a result of the time-scale of this process, that this occurs in an a-seismic fashion. So, it is found that an ideal plastic fault slip model in combination with the fault configurations evaluated so far, does not lead to seismogenic fault slip.

The current results are in line with those reported earlier by Mulder (2003) and Orlic & Wassing (2012). The calculated Relative Shear Displacement (RSD) shows a similar distribution as a function of depth, specific fault throw cases are recognised, and the maximum RSD is in the same range as in Mulder (between 0.15 and 0.20 m). A more comprehensive insight is obtained in the development of merged slip sections at elevated depletion levels and their dependence on fault throw. Furthermore, a relationship is observed between reservoir depletion, fault throw, number of slip sections and the total length of the slip section, the maximum RSD, and the dissipated energy.

Although only one parameter has been evaluated so far, it is clear that the structural geometry is an important element in the geomechanical explanation of fault slip. Further analysis of sensitivities to other geometrical factors, such as reservoir thickness, fault dip and dip azimuth angle, and formation and fault properties should reveal their relative importance. The available structural model [Visser, 2012] provides a basis for further constraining the geometrical parameters. More accurate determination of the hypocentre location of future seismic events may also help to constrain the modelling parameters for formation and fault behaviour.

9.5.5 Next steps 2D modeling

Despite the two-dimensional nature of the model, some relevant insights have been gained into the potential fault slip geometries that might be responsible for the recorded seismic events in the Groningen field. It is expected that the various fault slip responses found in the current study will occur under different depletion levels, or may be suppressed or emphasised by other factors not considered here. Also, other

responses may be found when considering other modelling options. Nevertheless, the study shows that different fault slip geometries are conceivable, and that each of these is characterised by a different depletion triggering level, a different slip section length, maximum RSD and different fault slip energy dissipation. This opens up the opportunity to look for seismic fingerprints to

1. Determine if slip along existing faults is indeed the root cause of the recorded seismic events, and
2. Discriminate between different slip geometries, constrained by available structural information and the analysis of focal mechanisms from recorded events.

Further studies will be aimed at developing a more comprehensive overview of potential fault slip mechanisms and geometries and their characteristics under various modelling assumptions. Initial focus will be on other geometrical aspects, such as reservoir thickness, fault dip angle and dip azimuth angle, because these parameters are relatively easy to quantify. Furthermore, the impact of fault slip softening will be addressed to investigate under which conditions potentially unstable seismogenic fault slip conditions can be developed. Finally, the impact of stiffness and (horizontal) in-situ stress contrasts will be addressed using the current 2D-model.

Based on the results of these additional studies, an attempt could be made to incorporate the 2D configurations in the 3D structural model of the Groningen field. Also, an update of the probabilistic hazard assessment and the 3D geomechanical field model could be considered. How exactly, and to what extent, is best decided after completion of the 2D modelling studies indicated above.

The current linear-elastic formation behaviour in the 2D model generator can be extended to include nonlinear and time-dependent behaviour. This would allow more appropriate modelling of salt behaviour and the impact on onset and post-failure behaviour of fault slip.

In an ideal case, the relevance of identified slip geometries and associated modelling assumptions and parameter values will be confirmed by field data. Whether or not future monitoring and data acquisition will provide sufficient information to do so will remain uncertain.

9.6 Three-dimensional modelling results

9.6.1 Geomechanical assessment of seismicity with full field geomechanical model (URC)

Full-field 3D finite element models are utilized to improve the understanding of geomechanical aspects during seismic events in the Groningen field and evaluate alternate producing strategies that may help manage subsurface stresses to reduce fault slippage. This multi-scale modeling framework includes a "global model" to capture full-field phenomena and "sub-models" which honor conditions of the global model, but also include explicit modeling of selected faults to understand production-induced fault slippage. Two key sub-model regions are considered in this study (Figure 9.26).

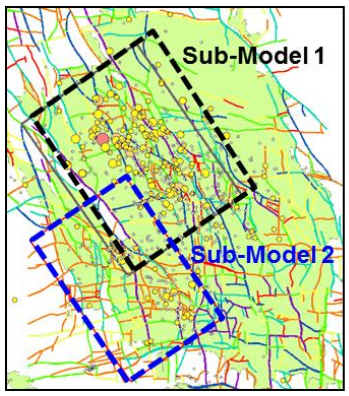

Figure 9.26 Site location showing epicenters of registered earthquakes and location of sub-models (dashed rectangles); sub-models were developed for regions with varying levels of historical seismicity

This modeling framework requires the use of state-of-the art computational mechanics implicit algorithms to capture fault slip behavior with non-linear contact mechanics. The modeling framework is illustrated in Figure 9.27.

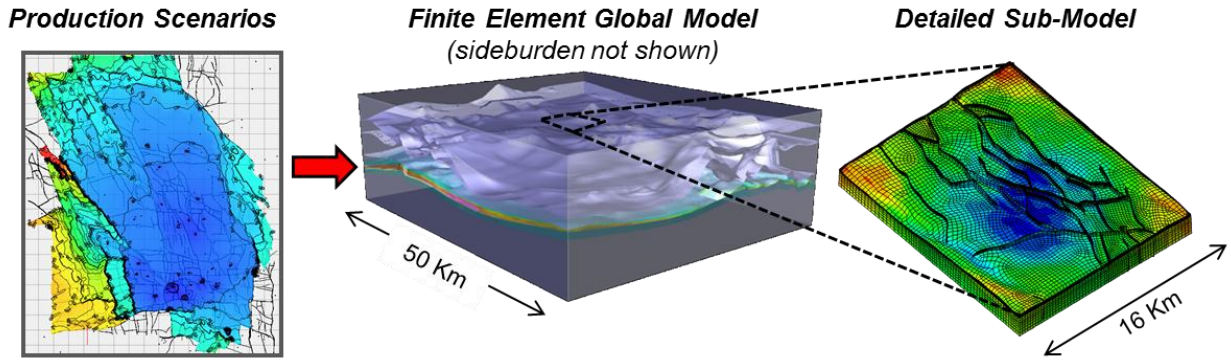

Figure 9.27 Multi-scale geomechanical modeling framework. Reservoir pressures from reservoir simulator output are mapped into geomechanical models as boundary conditions; deformation of sub-model boundaries is driven by deformation of the global model. Global model is 182.8 km x 190.5 km in plan view; additional details are discussed in section ***Error! Reference source not found.****.*

The geomechanical models integrate geologic, geomechanics, drilling, and production data to simulate field deformation from the start of production. These advanced models consider irregular geologic layering and fault surfaces, variable rock properties including Biot's coefficient effects for reservoir layers, a rate-dependent salt model to capture creep and stress relaxation effects before and during production, poro-mechanics elements to capture non-uniform pressure changes throughout the field over time, a frictional law to model slip behavior along faults, and other input data such as initial stresses to represent the virgin in-situ stress condition. Additional information is provided in Section 11 Appendix A.

Results from the global model provide a reasonably good match to field measurements of surface subsidence and downhole strains (De Hond well) as shown in Figure 9.28.

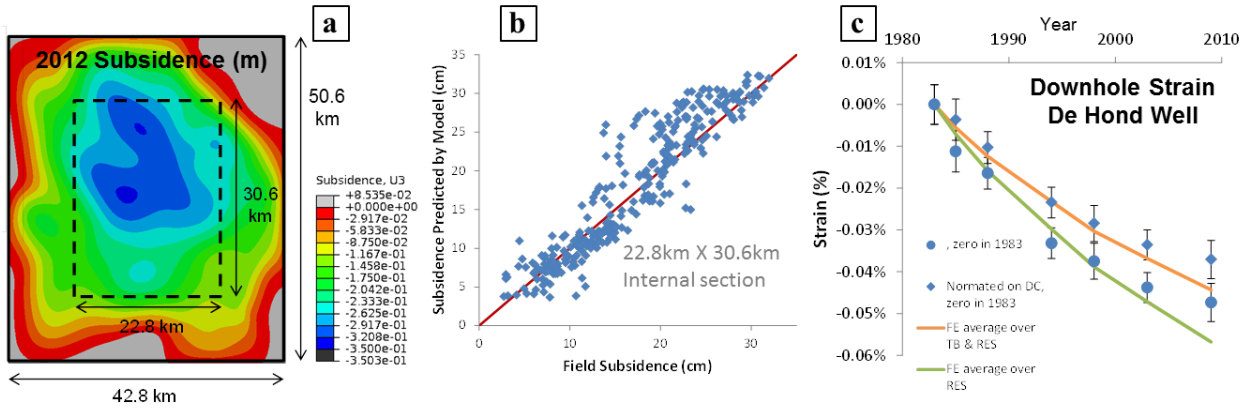

Figure 9.28.

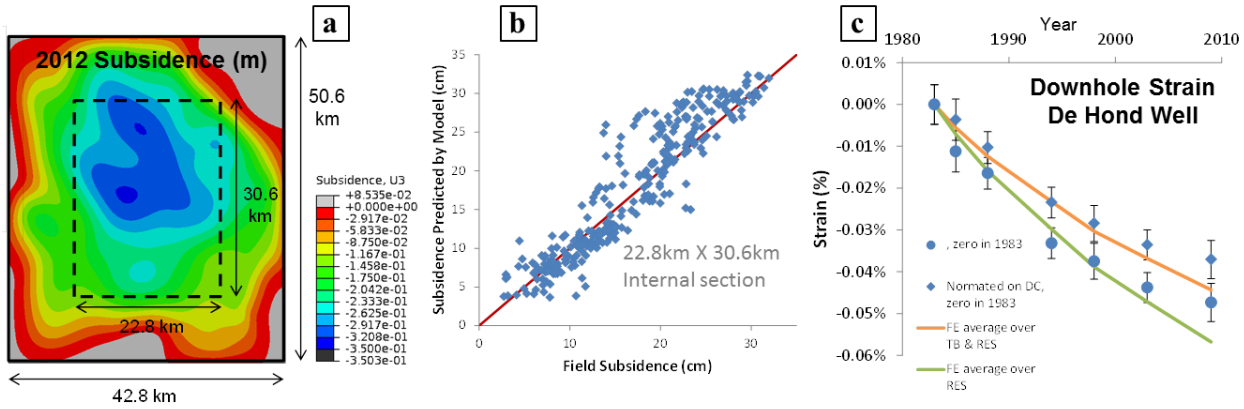

Figure 9.28 Validation of geomechanical model: a) 2012 subsidence in meters (m), b) Predicted subsidence vs. field measurement; subsidence measured between the year of first leveling measurement (different for different locations) and 2012, and c) Strain predictions compared to downhole strain measurements derived from radioactive bullets at De Hond well.

Deformation of the models is driven by reservoir pressure changes and salt creep behavior. Displacements from the global model are mapped into the boundaries of the sub-models to enable calculations of stresses on faults and resulting slip at different faults and at different points in time (Figure 9.29).

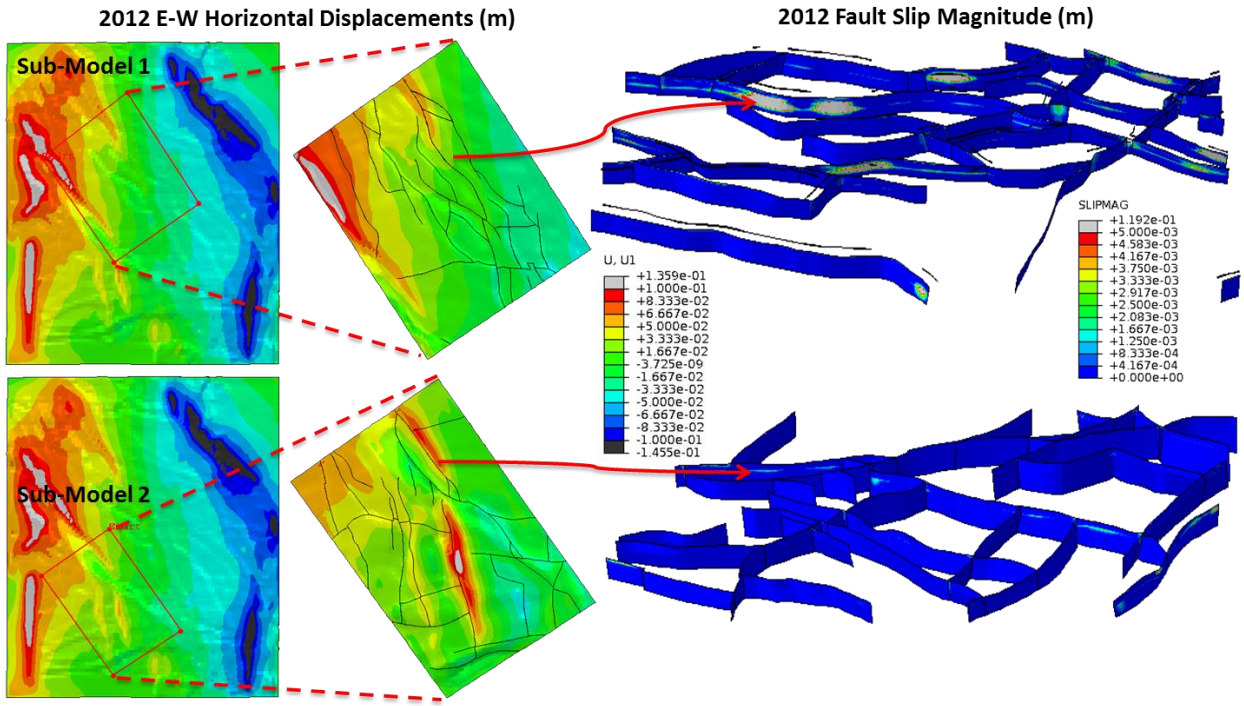

Figure 9.29 Example results for global model and sub-models 1 and 2; year 2012. East-West horizontal displacement contours (U1) are shown for top of Unit 14 (USS_2_Res). Predicted fault slippage is significantly more in sub-model 1 than in sub-model 2.

Seismicity at Groningen has been linked to production-induced reactivation of existing faults at the reservoir level [Dost et al, 2012]. The fault slip predicted in the sub-models, may in reality occur aseismically, as a seismic event, or as a combination of the two. Aseismic fault slip does not contribute to the generation of seismic waves and therefore to radiated energy. This modeling framework presents significant improvements over analytical or numerical models that cannot predict relative displacement along fault surface, but they are still limited to a quasi-static setting with the consequence that radiated energy cannot be explicitly accounted for. Still, the onset of aseismic and seismic slip can be captured by the same frictional slip criterion. For this reason it is critical to understand and manage subsurface stresses to reduce fault slippage that may lead to seismic events.

Different quantities may be used to evaluate subsurface stress conditions and fault activity for different production scenarios. The Shear Capacity Utilization (SCU) is a scalar quantity which expresses the criticalness of fault stress state relative to the fault strength. This quantity is particularly useful for a quick stability analysis in the absence of slip information. However, since it does not contain slip or post-failure information, it cannot discriminate between significant and small slip events. Fault slippage, which is defined as the relative shear displacement on a fault surface, may provide relevant information. Slip data at a single location is of limited use as this information does not indicate whether the slip is restricted to a narrow or wide area. Analyzing fault slip at different locations and points in time can become rather complex and have limited usefulness. The calculated dissipated energy during frictional sliding is a scalar quantity that provides a representative measure of fault activity for a given area of interest and can be used to identify production scenarios that reduce fault loading. This quantity integrates key geomechanical information: fault shear stress and strength, fault slippage, and the area undergoing frictional sliding.

While these geomechanical models cannot explicitly predict radiated energy, model results show that a fraction of the cumulative dissipated energy correlates well with the cumulative radiated energy from observed seismic events for sub-model 1 and 2 regions (Figure 9.30). Hence, the calculated dissipated energy from fault slippage appears to be a suitable indicator of overall seismic activity. Sub-model results are in agreement with field observations, indicating that total dissipated fault energy in sub-model 1 region is significantly greater than the one predicted for sub-model 2 region (Figure 9.30). The Gutenberg and Richter (1956) relation log_10⁡E=1.5M+4.8 is used to estimate the radiated or seismic energy E in Joules during earthquake events based on the magnitudes M published by KNMI.

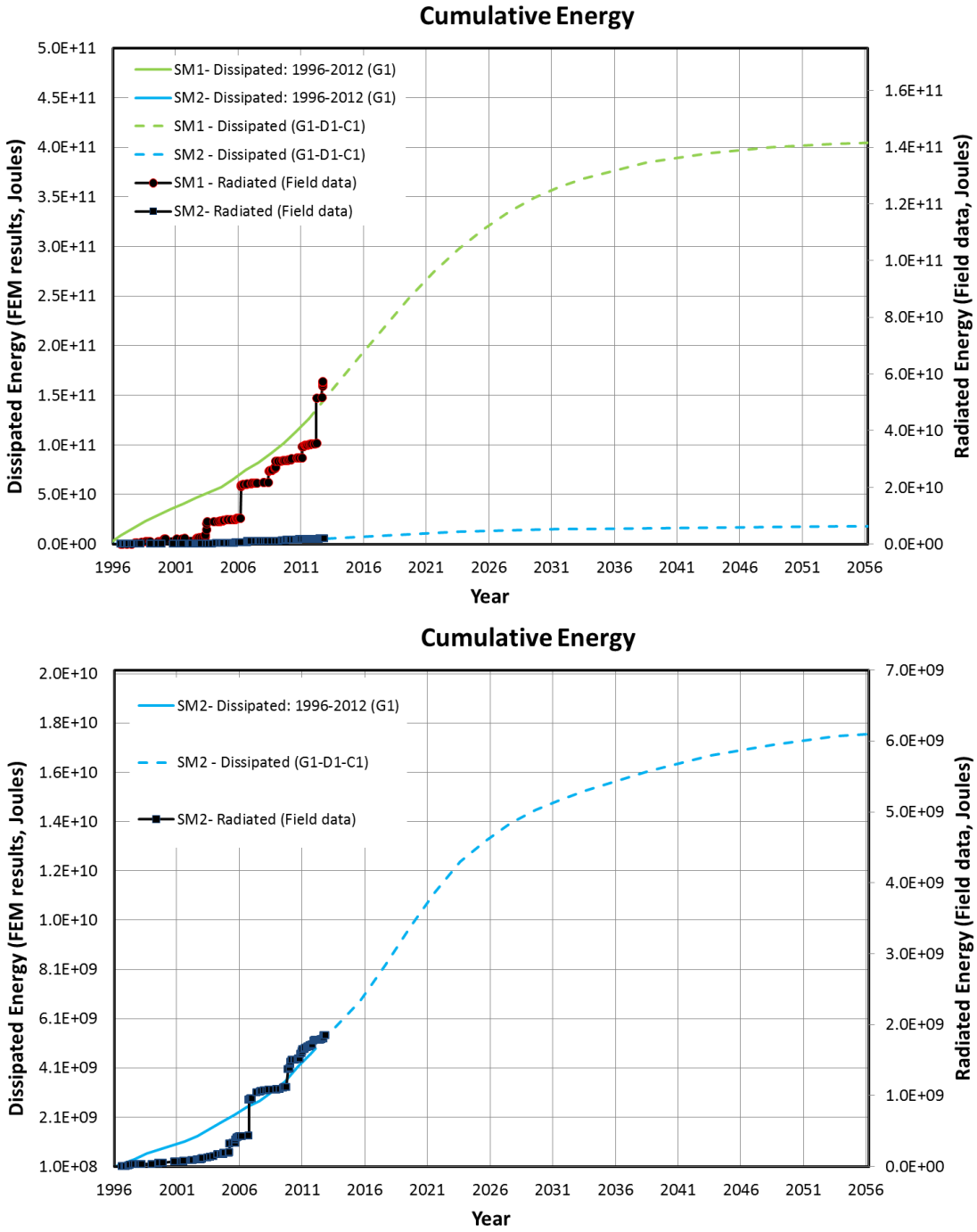

Figure 9.30 *Cumulative dissipated fault energy (sub-model results) vs. cumulative radiated energy (field data) for sub-models 1 and 2 (SM1 and SM2) as a function of time. Results are normalized to 1996 representing the first year with a complete earthquake catalog. Left vertical axis corresponds to dissipated energy and right vertical axis to radiated energy; vertical axes are related through the same scaling factor for both plots.*

Moreover, the scaling factor between radiated and dissipated energy considered in Figure 9.30 is the same for both, sub-model 1 (SM1) and sub-model 2 (SM2). These results indicate that advanced geomechanical models are a powerful tool that can provide valuable insight into the overall trend of cumulative radiated energy. It is important to note that it is not possible to translate dissipated energy from fault slip into earthquake magnitudes, because of the quasi-static nature of the models. Fault slip may or may not be accommodated in a seismic event. Here, it is found that this ratio is similar between two areas with a different seismic activity level. Even though there is no reliable predictor for individual earthquake events, this full field geomechanical modeling approach should be useful in understanding Groningen

seismic activity and to identify production scenarios that reduce fault loading and therefore mitigate seismic activity.

Several depletion scenarios have been developed (see Table 3.2) and are being evaluated with the modeling framework discussed herein (Figure 9.31 and Figure 9.32). The production scenarios consider two geologic interpretations: i) moderate NW aquifer support (G1), and ii) and weak NW aquifer support (G2). Three development scenarios: i) KHM1 hook-up, 2nd and 3rd stage compression (D1), ii) D1 + NW periphery development (D2), and iii) D2 + SW periphery development (D3). And the following curtailment conditions: i) market demand (C1), ii) 40 bcm/year cap (C2), and iii) 30 bcm/year cap (C3). Depletion scenarios considered in this section pertain to geologic interpretation G1.

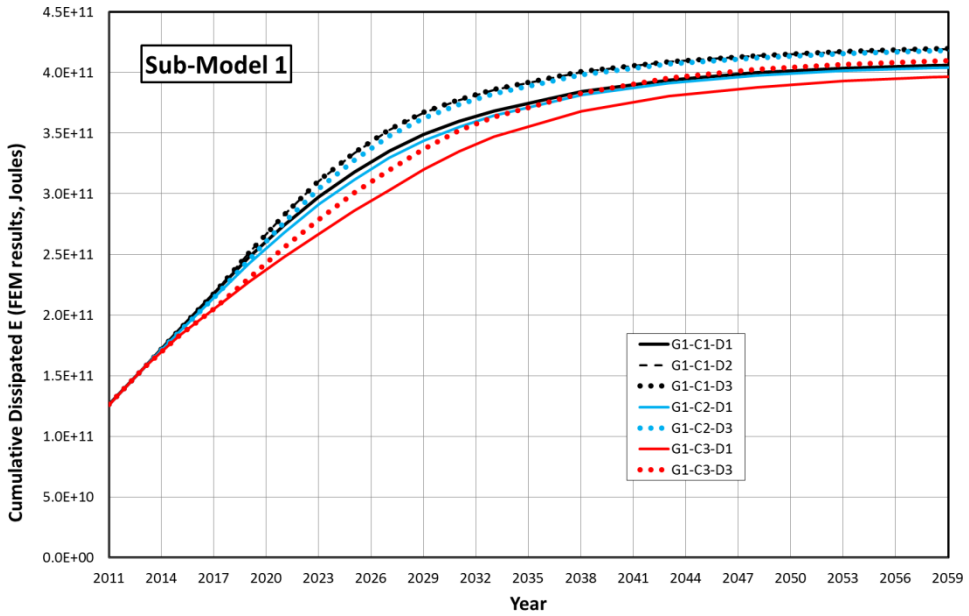

Figure 9.31 Cumulative dissipated fault energy vs. time for selected production scenarios in SM1 region. Curtailing production (C2 and C3) has a limited effect in the total dissipated energy; additional development in the SW (C1-D3) has a limited effect in the SM1 region compared to C1-D2; production curtailment to 30 bcm/yr (C3-D1) reduces dissipated energy, however additional development in the northwest region (C3-D3) increases dissipated energy closer to the base case (C1-D1).

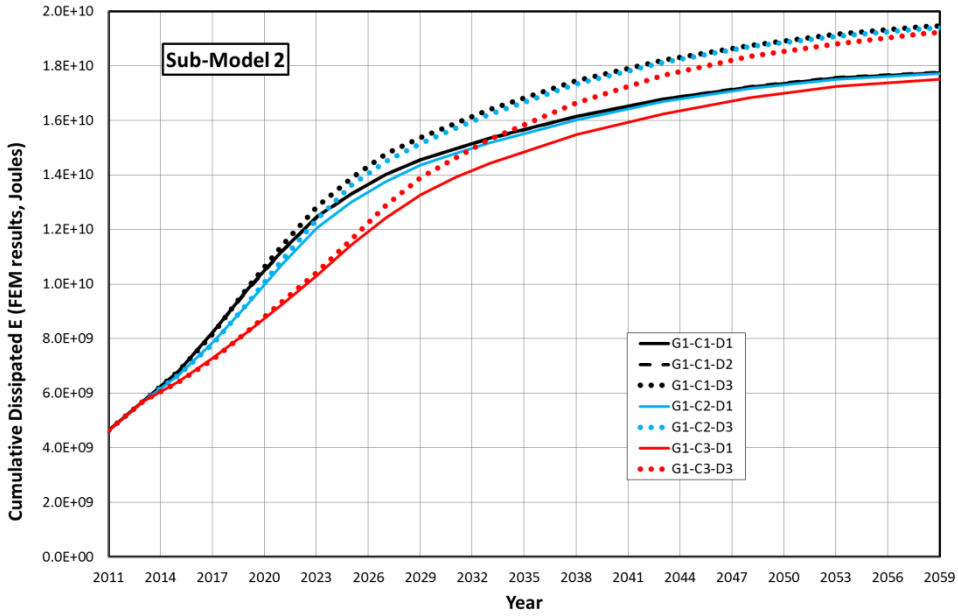

Figure 9.32 Cumulative dissipated fault energy vs. time for selected production scenarios in SM2 region. Additional development in the NW (C1-D2) has no practical effect in SM2 region. Additional development in the

SW (D3) has a moderate effect in SM2 region. Curtailment scenario C2 shows a minor decrease on dissipated energy relative to market demand case C1.

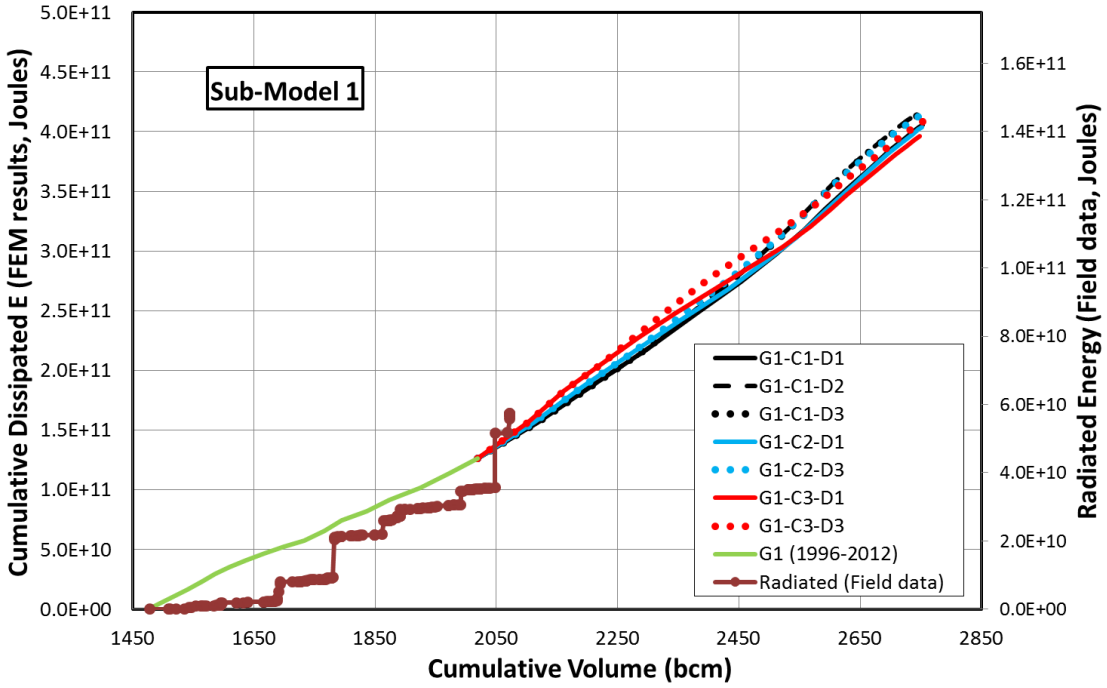

Figure 9.33 Cumulative dissipated energy vs. volume for selected production scenarios in SM1 region. Minor cumulative dissipated energy differences are observed across the investigated depletion scenarios. Right vertical axis corresponds to cumulative radiated energy by year. Results are normalized to 1996.

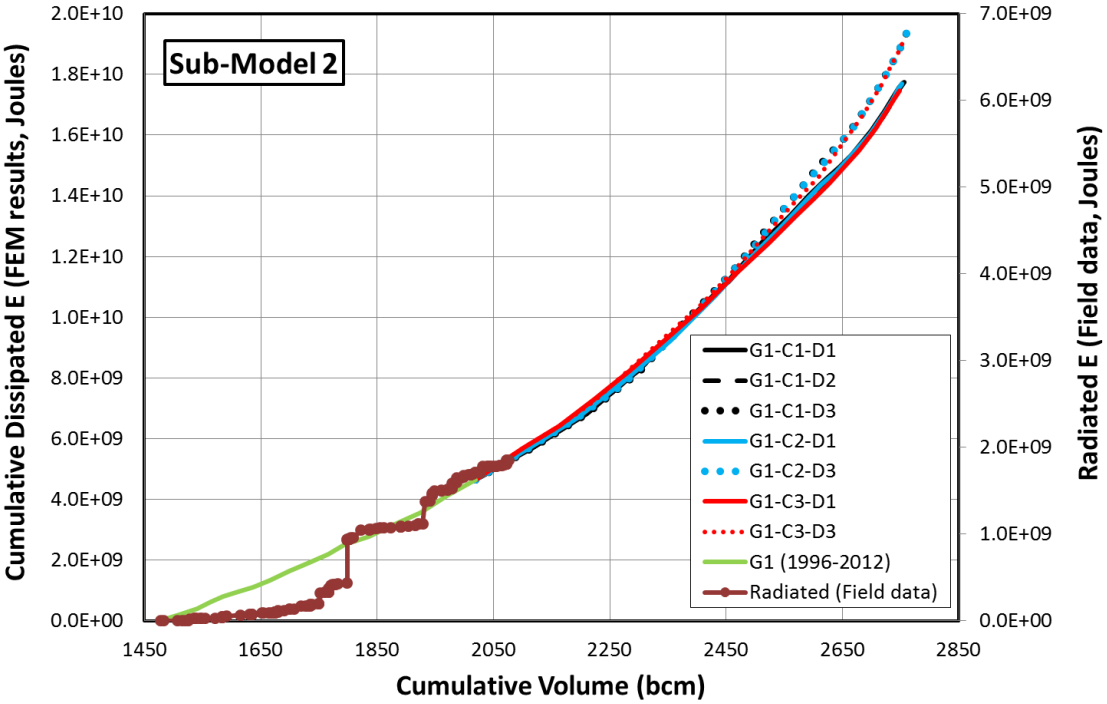

Figure 9.34 dissipated fault energy vs. volume for selected production scenarios in SM2 region. Dissipated energy is greater for depletion scenarios D3 (additional development in the SW periphery) when total production is more than 2,500 bcm. Right vertical axis corresponds to cumulative radiated energy by year. Results are normalized to 1996.

Figure 9.33 and Figure 9.34 show dissipated energy evolution as a function of total produced volumes for both sub-model regions. The production alternatives investigated so far do not show significant changes in the dissipated energy relative to the base case (G1-C1-D1). Model results indicate that curtailment of

production is not an effective alternative for mitigating fault energy dissipation and related fault activity in sub-model 1 and 2 regions (Figure 9.33 and Figure 9.34).

So far we have considered creep behavior for the irregular Zechstein salt section located above the reservoir. To better understand the effect of salt creep behavior in the reservoir faults, we also model the stress-strain response of the salt section with a linear elastic rate-independent constitutive model. This sensitivity analysis indicates that salt creep behavior reduces overall fault loading in SM1 and SM2 regions (Figure 9.35). Rate-dependent salt behavior affects nearby stresses and deformation mainly due to two mechanisms: i) the inability of creeping salt to sustain deviatoric stresses with time affects the stresses in the surrounding sediments according to the global salt geometry and local irregular configuration, and ii) the more compliant viscous salt behavior reduces the constraint on the lateral deformation of compacting/contracting rocks subjected to depletion. Note that the constant scaling factor between radiated and dissipated energy for the two sub-model regions was developed using the results with salt creep included. This factor may be different if salt creep effects are not considered.

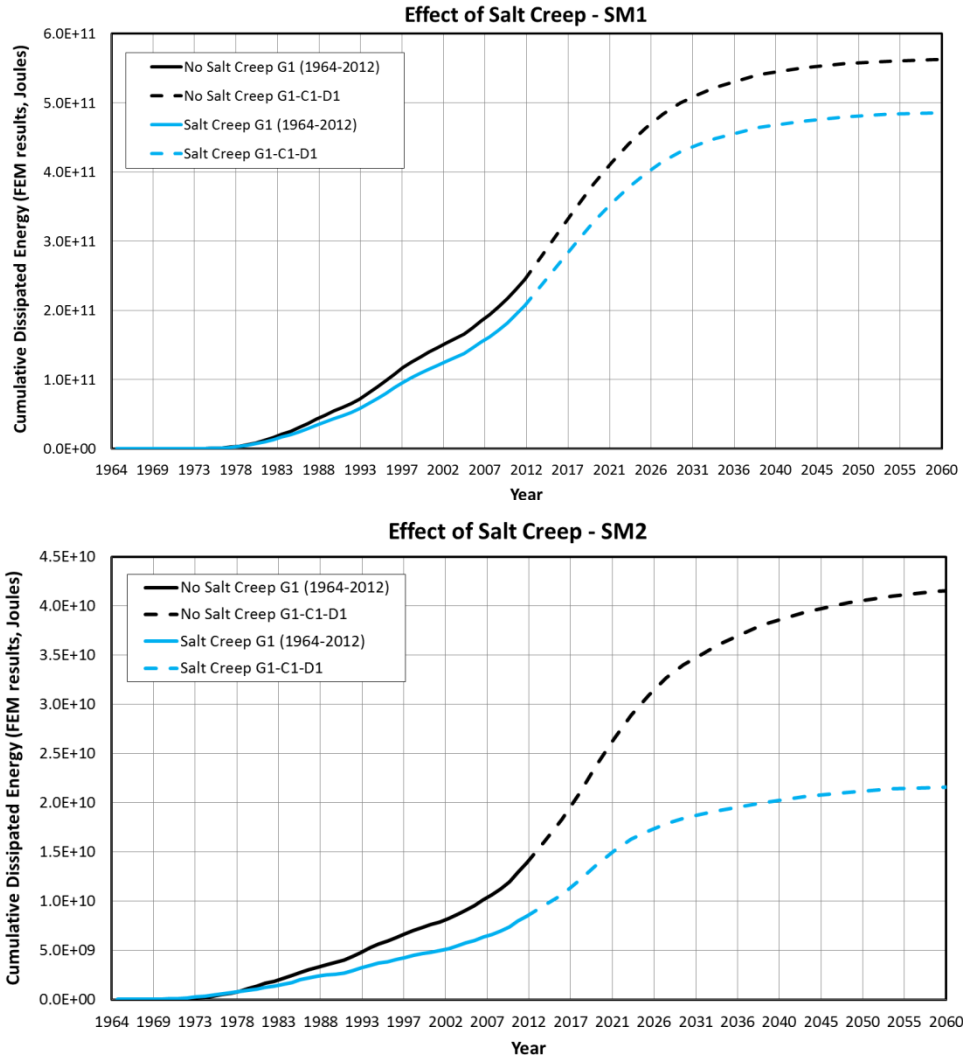

Figure 9.35 Cumulative dissipated fault energy as a function of time for SM1 and SM2 showing the effect of creep behavior in the Zechstein salt section. Total fault dissipated energy is reduced when salt creep behavior is considered.

Results presented in this section demonstrate that an advanced understanding of fault reactivation and related seismicity at Groningen is achieved with an improved modeling framework. At the same time, the findings given here leave room for extension, both in analysis and in modeling. Enhancements to the Coulomb friction law are required to explain other specific features of faulting mechanics such as slip and velocity weakening. However, this potential extension would require additional data that is not currently available, and would result in more complex models, making the analysis even more difficult. Additional

geologic and geomechanical information could also be incorporated into the model. Some of these improvements may be considered in future work based on Groningen Project needs and feasibility constraints imposed by current computational capacity. Finally, our models should be further validated as additional seismic field monitoring data becomes available.

In summary, detailed finite element models provide significant insight into the mechanics of a very complex problem. The mechanics of fault behavior considered in the models described above can only be investigated by numerical modeling of a complex non-linear boundary-value problem that captures discontinuous displacement fields across fault surfaces. Additional sub-models may be developed to cover the entire field region to capture the full impact of alternative production scenarios. These models are currently being used to test a range of production scenarios that may potentially be implemented to better manage subsurface stresses that could lead to fault slippage and seismicity. They may also be used to help in optimizing the design of surveillance programs. The expectation is that insight gained from advanced geomechanical modeling is used to create alternative production scenarios to effectively reduce fault instability, and that the capability to test alternate producing strategies is used to provide an actionable dimension to an overall Risk Management Framework for Groningen.

9.6.2 Geomechanical assessment of seismicity with full field geomechanical model

Production-induced pore pressure changes are responsible for rock stress variations which can trigger fault slip and radiate seismic energy. Pressure maintenance is proposed as an alternative measure to mitigate fault reactivation and related seismicity. The multi-scale geomechanical framework presented in section 9.6.1 is utilized herein to evaluate the fault energy dissipation of sub-model 1 and 2 regions (NW-central and SW central regions respectively) when subjected to a production scenario involving Nitrogen injection.

The predicted dissipated energy for this injection case is compared to selected production depletion cases for SM1 and SM2 regions in Figure 9.36 and Figure 9.37 respectively. This particular injection scenario provides enough pressure support in SM1 region to practically stop fault energy dissipation after 2019. Fault energy dissipation resulting from this injection test case is slowed in SM2 region but not stopped, indicating partial pressure support.

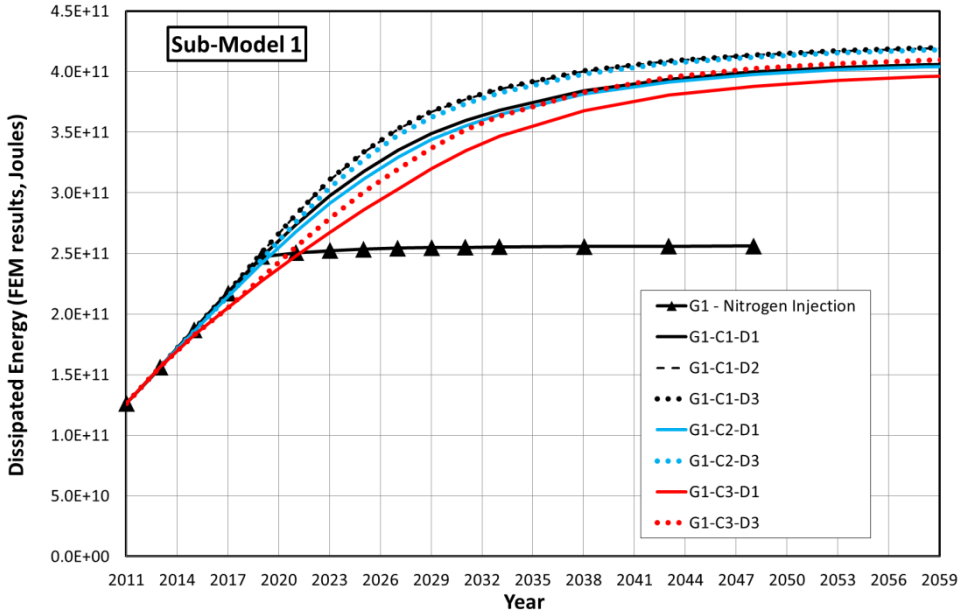

Figure 9.36 Cumulative dissipated fault energy vs. time for selected production scenarios in SM1 region. Depletion cases show a monotonic increase in dissipated energy with time. The Nitrogen injection case (triangular symbols) considered in this analysis provides sufficient pressure support in SM1 region to stop energy dissipation after 2019.

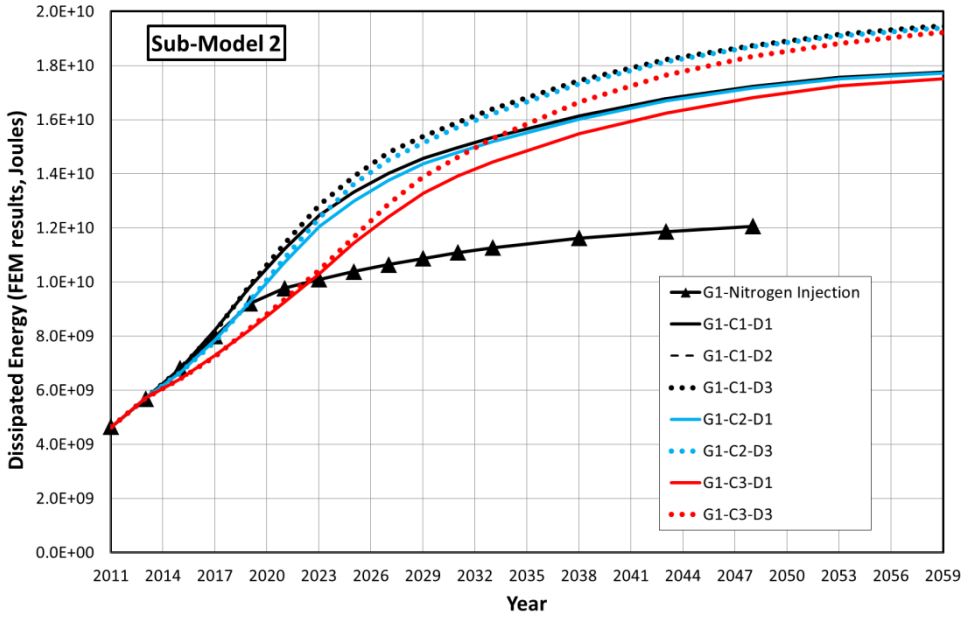

Figure 9.37 Cumulative dissipated fault energy vs. time for selected production scenarios in SM2 region. The Nitrogen injection case (triangular symbols) reduces fault loading and mitigates fault energy dissipation after 2019. Note that pressure support from this injection scenario in SM2 is not as effective as in SM1 region.

The dissipated energy plotted vs. cumulative production volumes are shown in Figure 9.39 and Figure 9.40. Note that the injection-driven pressure support in SM1 region results in a negligible increase in surface subsidence (predicted by global model analysis, shown in Figure 9.38 once injection is implemented. This test case, injection for pressure support, once implemented and assuming it's implemented consistently across the field, could arrest compaction and therefore arrest seismicity. Other production strategies short of full injection support may also balance stresses on faults and arrest seismicity, even if compaction is not fully arrested. Such opportunities, represented by the "working space" in Figure 9.39 and Figure 9.40 wherein the dissipated energy vs. production volume lies between the level in 2012 and the forecast for case without any curtailment, are being explored via 3D geomechanical modeling. Further modeling may help in developing production scenarios with best combination of uncurtailed production and seismicity reduction.

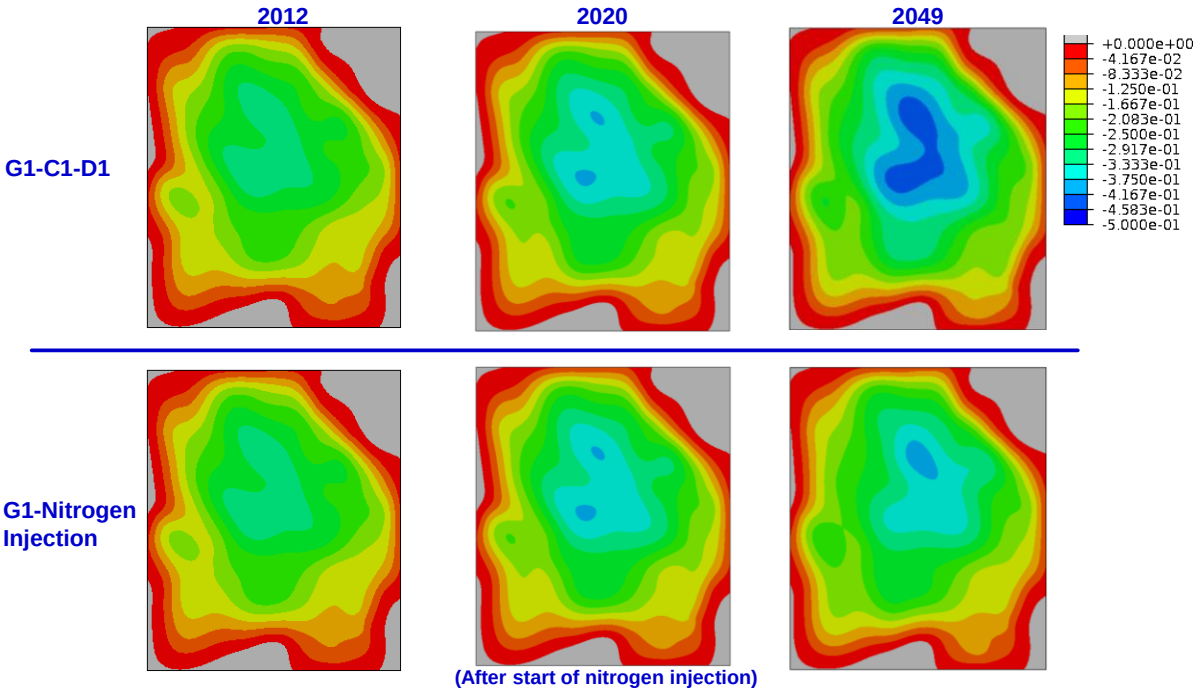

Figure 9.38 *Comparison of surface subsidence (m) for base case G1-C1-D1 with that for nitrogen injection; note negligible change in surface subsidence for nitrogen injection case after start of injection compared to the subsidence for base case over the same period*

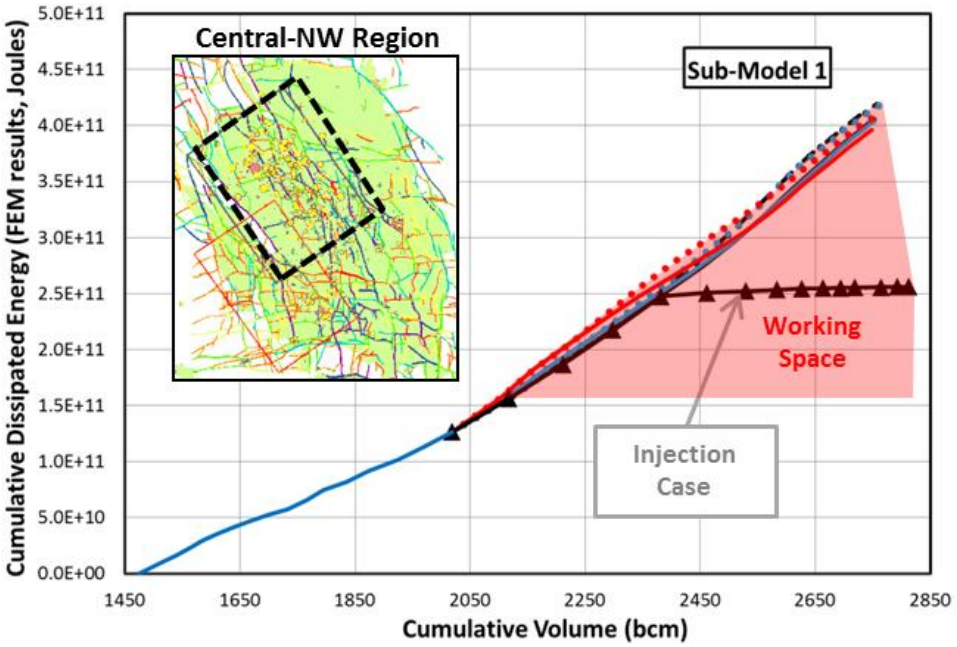

Figure 9.39 *Cumulative dissipated fault energy vs. cumulative production volume for selected depletion scenarios and a Nitrogen injection case (triangular symbols); SM1 region. "Working space" denote region bounded by uncurtailed depletion and full pressure support end members. Results correspond to a fault friction coefficient of 0.48. Results are normalized to 1996 representing the first year with a complete earthquake catalog.*

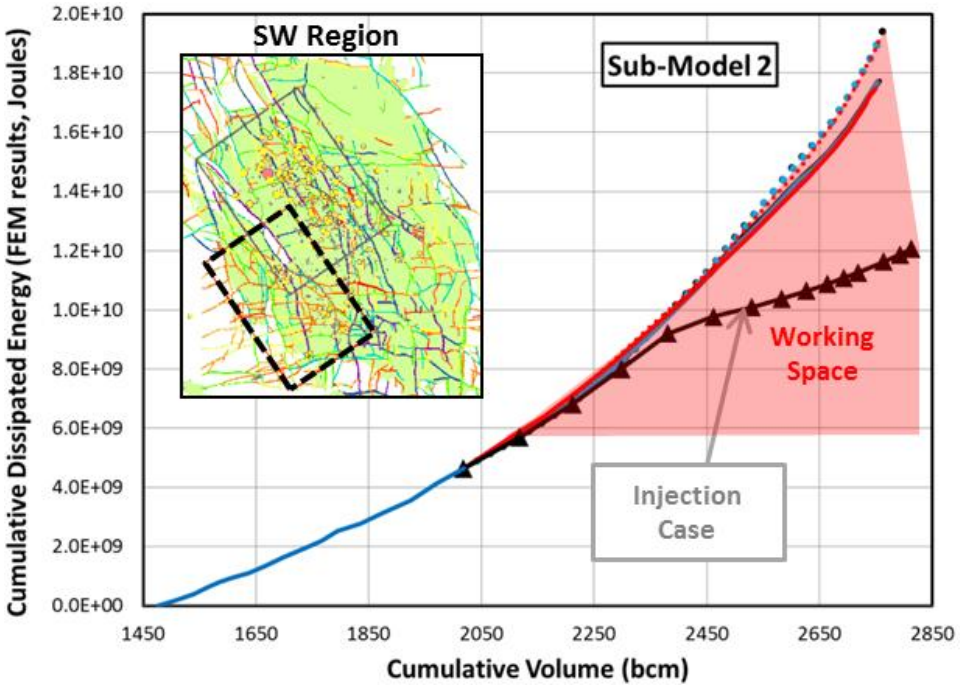

Figure 9.40 *Cumulative dissipated fault energy vs. cumulative production volume for selected depletion scenarios and a Nitrogen injection case (triangular symbols); SM2 region. "Working space" denote region bounded by uncurtailed depletion and full pressure support end members. Results correspond to a fault friction coefficient of 0.48. Results are normalized to 1996 representing the first year with a complete earthquake catalog.*

9.7 Conclusions

Our understanding of seismicity and the geomechanical behavior of faults in the Groningen area and their relation to seismic events is hampered by the dimensions and complexity of the Groningen structure and the scarcity of quantitative data on key geomechanical parameters. A twofold approach is taken to overcome these limitations. First, the acquisition of new data has been intensified (see Chapter 10.2). Second, new insights will be gained through the application of advanced 2D and 3D geomechanical modeling techniques. Both approaches are ongoing, as discussed elsewhere in this document.

In summary, the following modeling uncertainties need to be further addressed, and associated monitoring and measurement activities to be carried out:

- The minimum horizontal stress is poorly constrained. No reliable data is available from the time before production started, while limited data is available under depleted reservoir conditions. Stress anisotropy is expected between different formations, but is not well established (except for the Zechstein formation). Both initial value and stress development as a consequence of depletion should be measured when having the opportunity (drilling of new wells, workovers).
- Reservoir pore pressure in the Rotliegend reservoir is well established from production and observation wells, but there are areas in the field with poor well coverage. The main area of uncertainty is the pressure field over time in the underlying aquifer and in the overlying Ten Boer Claystone. Data acquisition is needed to reduce these uncertainties.
- Pore pressure evolution within faults is not known and cannot be measured in the subsurface. However, the impact of this process can be evaluated through modeling. This is the objective of the ongoing vibration analysis study (2D evaluations).
- The accuracy of determining hypocenter locations needs to be improved to differentiate between possible failure mechanisms. Both the installation of down hole geophones and additional shallow geophones fulfill this objective.
- Time-delayed compaction and other irreversible deformations that could delay or reduce fault slippage is the subject of ongoing research (KNAW, 2013).
- Advanced 3D geomechanical modeling is carried out to investigate the stress evolution in and around the producing Groningen field and its relation to the reactivation of faults. The models also serve to evaluate the effects of different production scenarios in the framework of TBO research topic 6.

More options for additional data gathering are being reviewed. These include:

- Post failure behavior and unloading (cyclic) behavior of reservoir and cap rock could be investigated by laboratory experiments. Also, monitoring and associated modeling studies in other fields could be considered to gain a better understanding of the formation behavior.
- Onset of fault slip and subsequent post-failure behavior can also be studied through fundamental lab experiments.

9.8 References

Brudy, M., Kjørholt, H. (2001) *Stress orientation on the Norwegian continental shelf derived from borehole failures observed in high-resolution borehole imaging logs*. Tectonophysics 337, pp. 65-84.

Davison, J.M., Ita, J., Hofman, R.A., Seli, P. and Ong, P., (2010), *Ensuring Production in the Malaysian F6 Field Using Field Monitoring and Geomechanical Forecasting*, SPE 132195, Int. Oil & Gas Conf. and Exhibition, 8-10 June 2010, Beijing, China.

Glab, M. and Van Eijs. R (2001), *Localisation of Sensitive Reservoir Settings for Induced Seismicity using FEM*, Report TNO-NITG 00-320-A

Hettema, M.H.H., Schutjens, P.M.T.M., Verboom B.J.M., Gussinklo, H.J., (2000) *Production-Induced Compaction of a Sandstone Reservoir: The Strong Influence of Stress Path.* SPE Reservoir Eval. & Eng. 3 (4) PP. 342-347.

Kanamori, H. (1994), *Mechanics of Earthquakes*. Annual Rev. Earth Planet Sci., 22, p207-237.

KNAW (2013) *Resolution inauguration the scientific steering committee for the long-term subsidence study in the Wadden Sea region with a brief description of its tasks.*

Mulders, F.M.M. (2003*), Modeling of stress development and fault slip in and around producing gas reservoirs*, Ph.D. thesis, Delft University of Technology.

Orlic, B. and Wassing, B.B.T. (2012), *Modeling stress development and fault slip in producing hydrocarbon reservoirs overlain by rock salt caprocks*, ARMA 12-145, 46th US Rock Mechanics / Geomechanics Symposium, Chicago, USA, 24-27 June 2012.

Roest, J.P.A., Kuilman, W. (1993). *Geomechanische Analyse van de lichte aardschokken in het Eleveld reservoir*, TU-Delft.

Segall, P. (1989). *Earthquakes triggered by fluid extraction*. Geology, Vol. 17, pp. 942-946.

TNO-DIANA bv, DIANA: *Finite-Element Program and User Documentation*, version 9.4.3, 2011

Van den Bogert, P. Van Eijs, R., van der Wal, O (2013) *Groningen Fault Stability Assessment*

Van Eijs R., van Dalfsen, W. (2004) *Borehole observations of maximum horizontal stress orientations in the Dutch upper crust.* TNO-NITG – Information, December 2004.

Van Eijs, R.M.H.E., Mulders, F.M.M., Nepveu, M., Kenter, C.J., Scheffers, B.C. (2006) *Correlation between hydrocarbon reservoir properties and induced seismicity in the Netherlands.* Eng. Geology, 84, p99-111.

Van Thienen-Visser, K., Nepveu, M., Hettelaar, J. (2012) *Deterministische hazard analyse voor geinduceerde seismiciteit in Nederland* (in Dutch). TNO report R10198.

Visser, C. (edt.), *Groningen Field Review 2012, Static Modelling and Hydrocarbon Volume Determination*, Document number: EP201203204663

10 Reducing the Remaining Uncertainty in the Hazard

10.1 Introduction

This report and the previous report issued to the TBO [Ref. 1], describe the results of the study program into induced earthquakes in the Groningen field, coordinated by NAM and carried out in the second half of 2012 and 2013. A Study and Data Acquisition Plan was issued October 2012 and has since then been regularly updated during 2013 [Ref. 2 and 3]. This study work carried out over 2012 and 2013 forms the technical basis for the seismic hazard analysis of the Groningen Winningsplan 2013. Despite the progress made, some technical questions remain unresolved, while uncertainties in the geomechanical parameters and in the estimated seismic hazard are large.

Some of the remaining uncertainty stems from lack of knowledge (epistemic uncertainty) and is therefore liable to be further constrained with increasing data acquisition and analysis.

10.2 Data acquisition activities

10.2.1 Introduction

Objectives of the research on induced seismicity in the Groningen Field are to increase our understanding of the mechanism inducing the earthquakes and the resulting hazard of damage (e.g. to buildings) and if possible to define measures to minimize this hazard.

High resolution mapping of seismicity and lowering the current detection and location magnitude threshold is expected to be essential in a better geomechanical understanding of the earthquake hazard. The improved determination of the locations of the hypocenters of the earthquakes will allow better tie-in with the structural model of the Groningen Field.

To improve the resolution over the whole Groningen field an extension of the (existing) passive seismic monitoring network will be implemented with installation of additional seismometers and accelerometers (Figure 10.1. Installation of two subsurface installed vertical arrays in the Loppersum area will improve the determination of earthquake hypocenters.

10.2.2 Extension passive seismic network

The current configuration of the Groningen monitoring network has provided field-wide coverage since 1995 for the detection and location of all events with a magnitude bigger of equal to 1.5 (M>=1.5 events). The network consist of 14 borehole stations, 8 installed in 1995 and extended in 2010 with an additional 6 stations, plus 12 accelerometers.

This network recorded a catalogue of 188 M>=1.5 events between 1995 and 2012 and is the primary basis for current earthquake hazard assessment within the field. The horizontal location uncertainties are typically about 0.5 km and the events are assumed to be at a depth of 3km.

Extension of the monitoring network would have two key advantages over the existing network, more sensitivity and more accuracy.

More sensitive as more reliable detection and locate more of the M<1.5 events within the field to allow more robust statistical analysis of the relationship between the number of earthquakes and gas production.

More accurate as measure earthquake locations with sufficient accuracy to reveal their relationship with mapped faults and their depth distribution relative to the reservoir to understand what causes these earthquakes.

To deliver the earthquake data necessary to realize these objectives, the performance criteria for the network are considered to be:

- Detect 10 events for every M>=1.5 event. Given the existing earthquake population has a b-value of 1, this means reducing the magnitude of completeness from the current M=1.5 to M=0.5.

- Locate all detected events with a standard horizontal error of less than 200 m and a standard vertical error of less than 500 m.

To improve resolution the network will be extended with 60 boreholes, spread in 6x6km grid covering the whole Groningen Field (Figure 9.12). Each 200m deep borehole will be equipped with 4 levels of geophones, one accelerometer at surface including required electronics for data-transmission, pre-amplifiers and communication means.

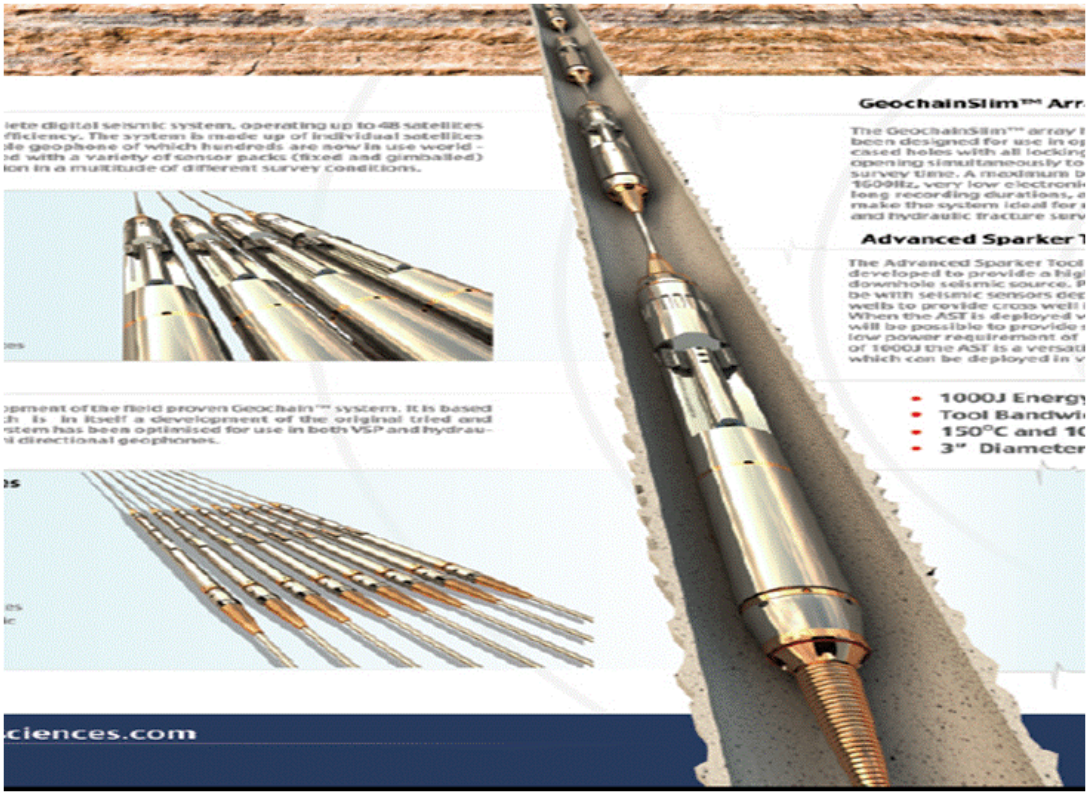

Figure 10.1 Extension of the shallow borehole geophone network.

Additionally 4 boreholes equipped with strong motion sensors (low frequency geophones) will be realized in order to faithfully record the signals for the very largest events without clipping and enable ongoing recalibration/updating of the ground motion attenuation relations measure high range earthquakes.

10.2.3 Subsurface vertical seismic arrays

Down hole seismic monitoring allows monitoring at substantially reduced noise conditions thereby improving signal-to-noise ratio, magnitude detection threshold and precision of the hypocenter determination. From the surface installed seismic network the vertical location of earthquakes are assumed to be at a depth of 3km. Implementation of a subsurface seismic array would lead to accuracy in horizontal and vertical location of events.

Challenges in borehole seismology are a secure deployment of sensors, safe date transmission to surface, formation temperature and pressure and reservoir fluids. Thereby drilling is expensive, risky and logistically difficult and requires preparation time. As down hole instruments need to operate at elevated pressure and temperature conditions proper engineering is essential.

Objective is to have two subsurface installed vertical arrays in the Loppersum area with sensors covering Zechstein down to Carbonferious. The sensors should be suited to a target event magnitude range of M=-

2.5 to M=+1 over the distance range 500m to 10 km, and a system minimum sampling frequency 2KHz (0.5ms data) or higher.

10.2.4 Temporary vertical seismic arrays

With the objective to implement subsurface measurements as soon as feasible two existing observations wells in the Loppersum area (Stedum-1 and Zeerijp-1) where selected to be modified into seismic observation wells. As these wells have been drilled more than 35 years ago, and not initially designed as seismic observations wells it was proposed to temporary install vertical seismic arrays without performing a workover. Advantage of this solution would be deployment on short notice, disadvantage vertical coverage is limited to the reservoir section only.

Based on the experience gained over the last 3 years in Bergermeer (Taqa) a system has been designed which will be installed in October 2013. Two arrays with respectively 8 and 11 levels, with 30m station spacing will be installed. The installation requires well killing, installation of additional pressure control equipment, and communication and data collection equipment. Objective is to have the equipments operational until the permanent monitoring wells are in place (about a year). Continuous monitoring will start immediately after installation; and data will be made available via GSM connection to KNMI and Magnitude for further analyze.

10.2.5 Permanent vertical seismic arrays

For the permanent vertical seismic arrays it has been advised to realize newly drilled dedicated observation wells. In a Request for Information contractors have been invited by NAM to propose their solution for permanent seismic monitoring systems. It is the objective to have an operational permanent seismic recording system in the fourth quarter of 2014.

10.3 The 2014 Study and Data Acquisition program on Induced earthquakes in the Groningen field

During 2014 NAM will continue the research program to gain further insights in the processes leading to earthquakes and the size of the resulting hazard. The analysis of the contributions to the epistemic uncertainty in the hazard using the logic tree approach, showed four factors to be important: the strain partitioning factor describing the coupling between compaction strain and seismicity, the ground motion prediction equation, the compaction and to a lesser extent the b-value.

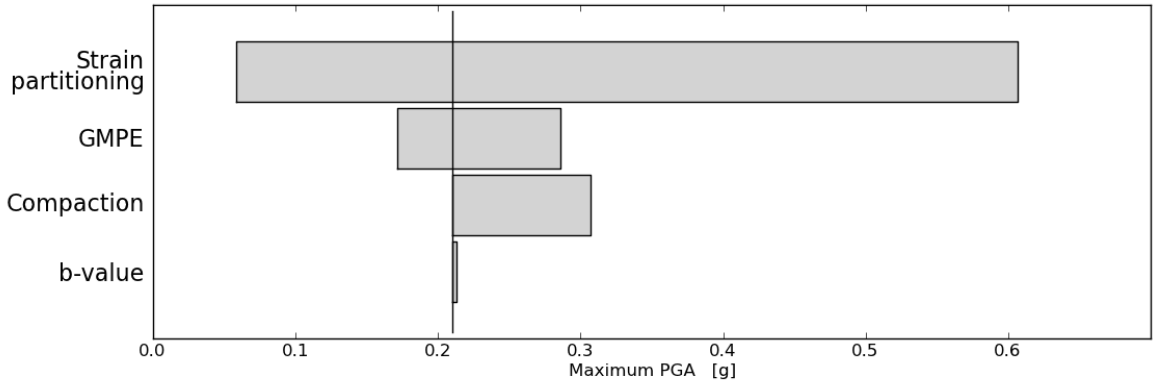

Figure 10.1 Variation in the maximum PGA found within the Groningen Field with a 2% chance of exceedance over the period 2013 to 2023, due to epistemic uncertainties represented in the logic tree.

The partitioning factor has the largest impact on the uncertainty in the seismic hazard. Insights and limits to the partitioning factor will most likely have to come from outside the current hazard framework. Both attempts to gain insights from analogy with tectonic earthquakes and further geomechanical investigations are elements of the study program to improve the understanding of process inducing the earthquakes and the partitioning factor. Table 10.1 shows the main activities in the research program into induced earthquakes in the Groningen field for 2014.

10.3.1 Geomechanical discussion to reduce uncertainty in the partitioning factor

A seismologic model developed to characterize future seismicity (ref Report to the Technical Guidance Committee (TBO) on Subsurface Aspects of Induced Earthquakes in the Groningen Field) is based on the concept of induced earthquakes accommodating depletion-induced strains. A relationship developed between historical seismicity and reservoir compaction is used as a framework for assessing future seismicity based on future compaction induced by planned gas production. This relationship (partitioning factor) has previously been inferred by comparing total seismic moment (from measured data) with calculated values of compaction (from geomechanical/compaction models which are well constrained by measured subsidence data). Significant variability has been observed in these comparisons.

To better understand this variability, it should be considered that the relationship between compaction and seismicity should depend on the characteristics of faults in the vicinity of the compacting region(s). Geomechanical/compaction models used in current seismological analysis have treated faults only in an implicit, statistical manner. At present there is no field evidence that seismicity in the Groningen field is governed by regions with different fault characteristics (e.g., presence or absence of faults, fault geometry and orientation, stress exerted on faults, etc.) and as such, the model does not distinguish between regions that may have similar compaction characteristics, but different fault characteristics. Because the true distributions of fault characteristics are unknown, multiple factors are being "lumped together", resulting in variability that may be greater than the true physical uncertainty in partitioning factors.

The geomechanical / fault movement FEA models described in section 9.6.1 and section 9.6.2 may provide the capability to reduce the uncertainty in partitioning factor calculations, even prior to collection of additional field data. A number of these models have shown good agreement with field measurements and because they explicitly account for faults (a subset of faults interpreted from seismic data was included in the model), this is a promising approach to provide a physically meaningful basis for relating compaction strain energy with energy exerted during fault slip (labeled dissipated energy in prior Figures).

Results shown on Figure 10.2 illustrates the potential advantages of this approach:

- Temporal evolution of fault energy dissipation from geomechanical models correlates reasonably well with observed radiated energy from seismic events
- As a first step the partitioning or scaling factor that relates radiated energy with dissipated energy was assumed to stay constant within the analyzed period (1996-2012).
- Predicted energy dissipation is significantly greater in SM1 than SM2 regions; in agreement with observed seismicity

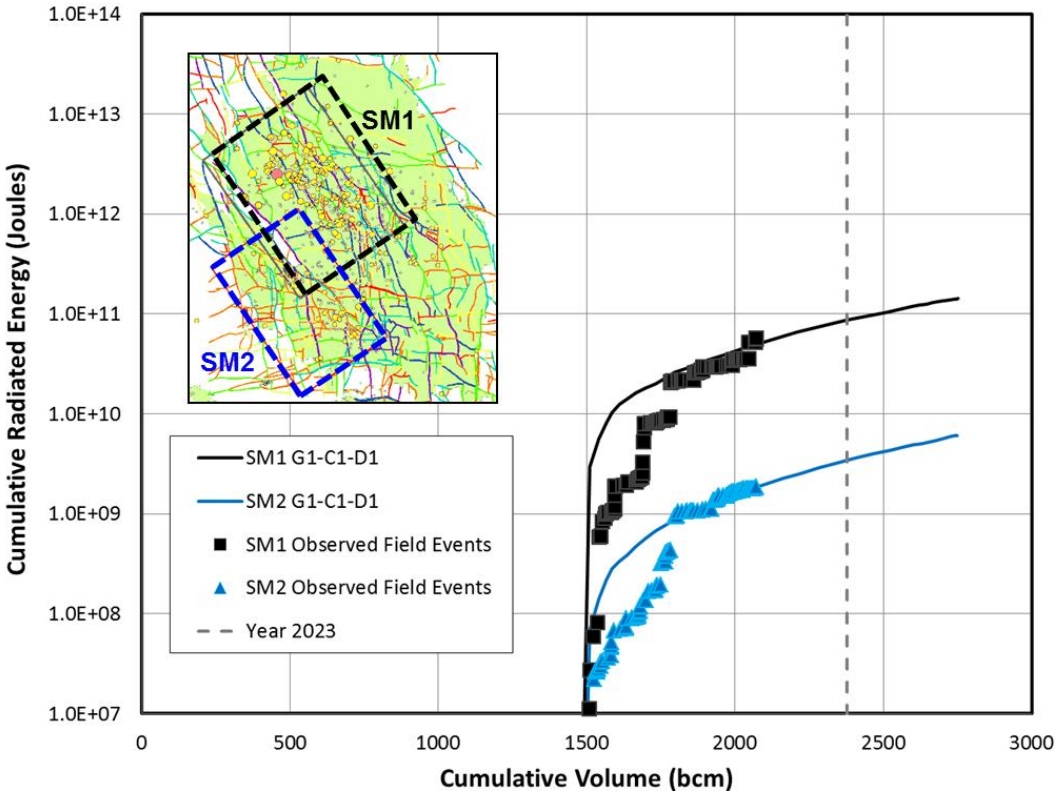

Figure 10.2 Total observed (square symbols) and modeled (blue line) radiated energy since 1996 as a function of gas production for sub-model regions 1 and 2. The modeled radiated energy is determined from the fault dissipated energy (calculated from the FEA models) by applying a single valued, constant partitioning factor. Observed radiated energy is calculated from M≥1.5 events.

While the comparisons in Figure 10.2 are encouraging, further improvement may be established by enhancing the representation in the FEA models of the faults, fault behaviors (e.g., slip / velocity weakening), compaction physics (e.g., non-linear, rate-dependent compaction), etc. Also the full range of models consistent with the historic seismicity data accounting for the stochastic variability due to finite sample effects within the earthquake catalogue should be assessed.

By providing a "physics-based" constraint on the relationship between compaction strain energy and fault dissipated energy, these models could reduce the variability in partitioning factors that had previously been calculated based on models without explicit consideration of faults.

10.3.2 Continuation of the Study Program

Main Uncertainty	Study and Data Collection to reduce Uncertainty
Compaction	■ Update of the porosity model for the Groningen field in view of new measured subsidence data. ■ Geodetic analysis of the measured subsidence data, using SURE (software package to derive subsidence from all available geodetic measurements in an integrated manner over time and space) to obtain a best estimate of the full subsidence field. ■ Improved matching of the models with measurements, based on a formal minimum acceptance criteria test to better assess the validity of the different compaction models. ■ Rock measurements on core samples and theoretical investigations to improve models of the time-dependent compaction behavior.

Partitioning Factor & Improved Geomechanical understanding of the rupture process	■ Review with group of external experts to look for possible avenues of research, which may enable us to constrain the value of the partitioning factor at the upper end. These may include a literature search for the partitioning factors and the fault aspect ratios seen elsewhere.
	■ The pre- and post-failure behaviour of faults and adjacent formations determines the energy storage and release prior to and during seismic events. The following activities are foreseen:
	  ■ Experimental testing into the dynamic fault friction behavior, failure and unloading characteristics of reservoir rock, to better understand the physics of fault re-activation and rupture and the conditions which determine whether fault slip is seismic or a-seismic. Also the effect of pore fluid needs to be investigated.
	  ■ Modeling studies to evaluate experimental results and the impact of various geomechanical modeling options on the physics of fault re-activation and rupture (geometrical aspects (reservoir thickness, fault dip angle and dip azimuth angle), fault slip softening and stiffness and stress contrast).
	■ Detailed geomechanical modeling to investigate whether a rupture initiated in of below the Rotliegend reservoir section will propagate into the Zechstein salt or whether the Zechstein salt will limit rupture growth in the case of Groningen.
	■ Currently, the association of the earthquakes with identified faults in the structural model is hampered by the large uncertainty in the hypo-centre location of the earthquakes and uncertainty in the characterization of the structural model.
	Two initiatives have been initiated to address this issue by improving hypocentre location of the earthquake and characterization of the source radiation parameters:
	  ■ Extension of the field wide geophone network consisting of some 60 borehole stations each with a string of geophones with 30 meter spacing and a surface accelerometer. In addition, KNMI will install a further 4 broadband sensors.
	  ■ Placement of geophones at reservoir level in deep wells located in the Loppersum area. Over the limited region covered by these deep

	arrays the accuracy of measured event depths will be greatly enhanced. ▪ Accurate imaging of the earthquake hypocenter requires knowledge of the 3D velocity field. Measurement of the rock density and P- and S- wave velocities in the overburden well sections of Borgsweer-5 well and future wells aim to improve our knowledge of the 3D velocity field (see also GMPE). ▪ Advanced multi-scale mechanical modeling combined with a geomechanics-seismicity relationship might provide a suitable framework to better understand seismic fault slip behavior and assess future seismicity via a physically-constrained strain partitioning (i.e., partition factor). This will be the subject of future study work, which will aim to establish a workflow leading to a robust integration between 3D explicit fault modeling and the existing Seismological Modeling to reduce seismic uncertainty. ▪ Improvement of the current full field geo-mechanical modeling, to investigate the possibility of sub-surface stress management. Results of the aforementioned model selection studies are to be incorporated. Further calibration is supported by additional field measurements of: ▪ The minimum horizontal stress across the field, in particular in and around the depleting formations. ▪ The pore pressure field over time in the underlying aquifer and the overlying Ten Boer claystone.
Ground Motion Prediction Equation	▪ Surface ground motion data for further calibration of the GMPE on a much denser grid than currently possible will be obtained by the accelerometers placed in the cellars of some 60 geophone wells of the extension of the network. Data from the geophones in the 60 shallow wells will also be valuable for characterizing site response. ▪ Conduct site response analyses (based on field measurements of Vs30 and borehole geophone data) to give spatially varying site corrections and a field-specific rather than generic site amplification model. ▪ Waveform modeling and full waveform inversion (FWI) to understand the impact of spatial heterogeneity of rock properties and the role of the Zechstein interval in attenuating amplitudes from source to surface and also to give insight into possible alternative forms of GMPE. ▪ To improve the modeling of propagation of the seismic wave field through the subsurface, the velocity field in the rock overlying the reservoir section needs to be known in greater detail. If well design allows, measurement of the rock density and P- and S- wave velocities in the overburden will be acquired in future wells.
b-value	▪ The densified seismic array over the Groningen field will enable the earthquake catalogue to be extended by detection of larger numbers of smaller events (M≥0.5) distributed across the field. The overall b-value for the catalogue is already well constrained and we have found that variations in b have a limited impact on the predicted hazard. Nevertheless, the new data from the densified array should improve our ability to calculate b-values for subsets of the data catalogue and so better identify variations in b with location and compaction.

Table 10.1 Main components of the 2014 Study and Data Acquisition program on Induced earthquakes in the Groningen field.

Apart from study and data acquisition work to better understand and assess the seismic hazard, NAM will also continue investigating options into measures to reduce seismicity. Table 10.2 lists these studies.

Measures	Study Identify and Assess the effectiveness of Measures
Pressure Maintenance	▪ The study on pressure maintenance options for Groningen field provides an outline for an nitrogen injection development of the Groningen field. Feasibility of this has yet to be demonstrated and implementation of such a development has a relatively long timeline. A follow-up feasibility study into pressure maintenance is planned to be started early 2014. This will address the main technical feasibility of the sub-surface gas recovery process and the required facility infrastructure aspects of such a pressure maintenance development. The assessment of the large impact of such major development on the Groningen community, integration and identification of potential synergies with other industrial activities will also be part of this study.
Stress Management	▪ Using sub-models of the field, geomechanical studies on fault stability will be continued. Based on this study effort the potential for active stress management of the reservoir will be investigated. ▪ Impact of pressure management of the blocks in the western periphery of the field will be assessed using a full-field or sector geomechanical model ▪ Optimisation of off-take from the clusters based on reservoir stress management.

Table 10.2 Main components of the 2014 Study and Data Acquisition program on identification and assessment of effectiveness of measures to reduce the impact of seismicity.

10.4 References

[1] Report to the Technical Guidance Committee (TBO) on Subsurface Aspects of Induced Earthquakes in the Groningen Field, October 2013, NAM.

[2] Study and Data Acquisition Plan for Induced Seismicity in Groningen Planning Report, November 2012, Jan van Elk and Dirk Doornhof

[3] Study and Data Acquisition Plan for Induced Seismicity in Groningen Planning Report, August 2013, Jan van Elk and Dirk Doornhof

11 Appendix A: Full 3D geomechanical modeling methodology

11.1 Introduction

Full 3D geomechanical modeling approach integrates geologic, geomechanics, and production data to simulate field deformation from the start of production. Due to the large scale of the field, and significant number of faults, a multi-scale approach that combines large scale model to characterize field wide behavior, and finer scale sub-models to understand production-induced fault slippage is used. A *global* model of the entire field, without faults modeled explicitly, is developed to characterize the stress states in the entire regions and model the surface subsidence. Two *sub-models*, with selected faults included, for smaller regions in areas of observed seismic activity were developed to study production induced fault slippage.

The full 3D geomechanical modeling methodology is based on the load-resistance approach to fault reactivation, wherein reservoir pressure changes due to depletion lead to deviation of the stress state from initial conditions (*load*) and that may consequently lead to fault slippage governed by the frictional strength of the fault (*resistance*). This methodology is summarized in Figure 11.1.

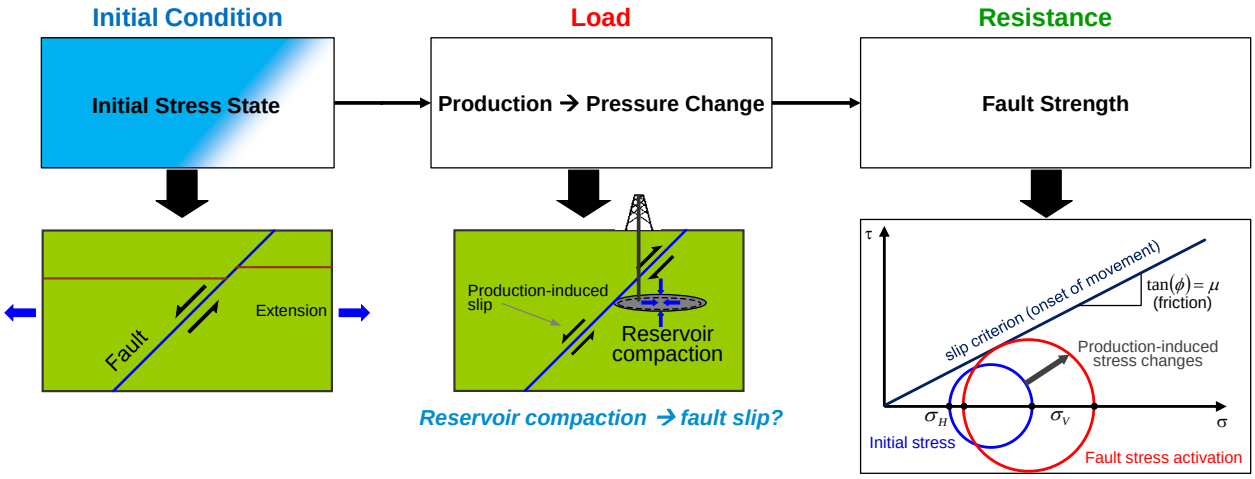

Figure 11.1 Load-resistance (production induced stress changes and frictional strength of faults respectively) based approach to fault slippage modeling

The global model will be used to study effect of reservoir depletion on stress changes on the entire field scale, and smaller scale sub-models with detailed fault modeling will be used to predict fault slippage and the frictional dissipated energy. Various production scenarios may be ranked based on these predictions.

The details of the geological, material and stress input data used to initialize the model, and brief description of the global and sub-modeling methodology are included in the following subsections.

11.2 Geological model input

The finite element model honors NAM-derived GFR2012 static modeling framework from Petrel for reservoir zonation. The model contains 22 structural horizons from ground surface to base of model, and contains 12 reservoir model units from base of Zechstein to base of lower Slochteren.

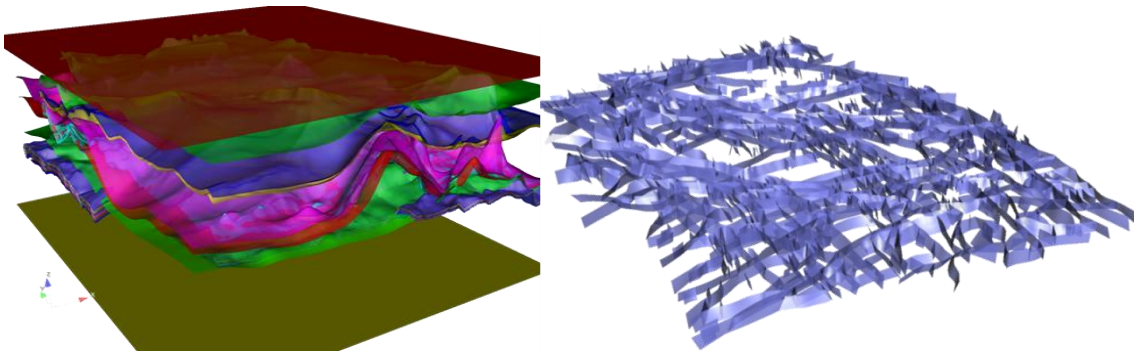

Figure 11.2 Geological model structural horizons and fault framework

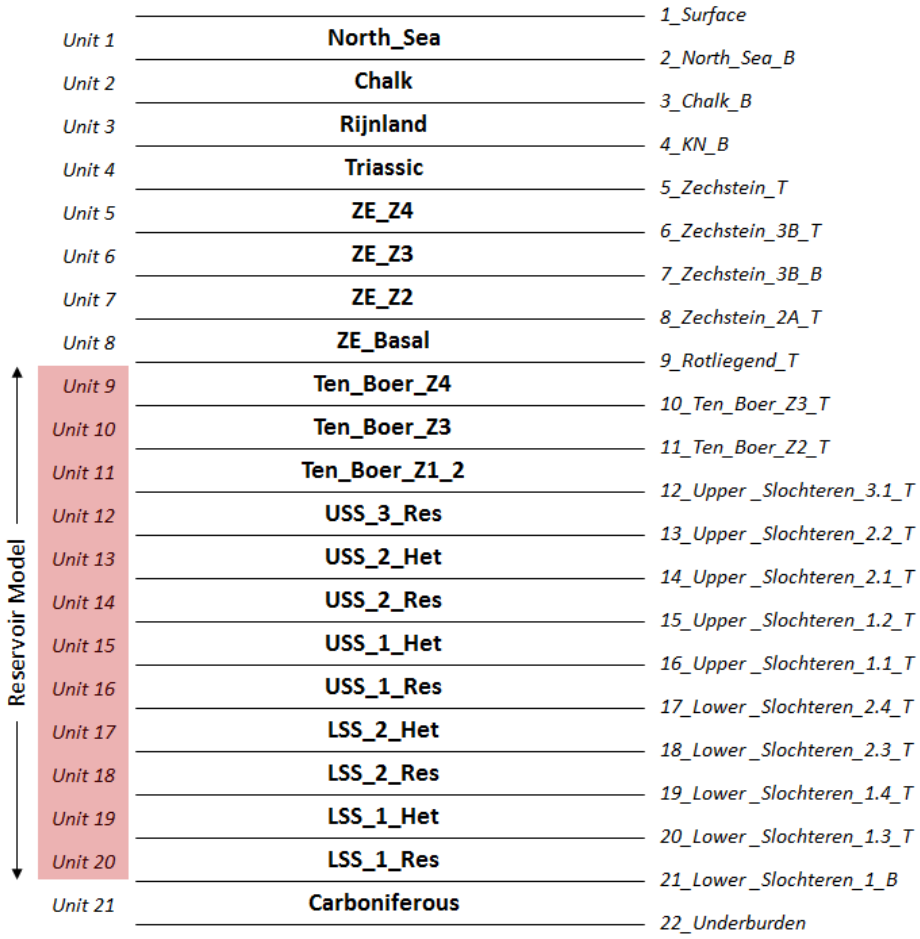

Figure 11.3 Geological layers included in finite element model

The global finite element model includes 21 layers as indicated in Figure 11.3. Names of the horizons and layers in geologic model and the unit numbers used in NAM reservoir simulator analyses are included in the figure. The global model includes all these layers up to depth of 20km (the Carboniferous layer is extended to reduce effect of boundary conditions). The sub-models include all layers from salt layer ZE_Z2 to Carboniferous up to depth of 4km.

11.3 Material properties

The material properties for reservoir layers are based on test data provided by NAM. Properties for all other layers except Anhydrite are provided by NAM. The Anhydrite properties are based on data from literature since no field specific tests or data are available. The elastic properties, densities and the source of the data are summarized on Table 11.1.

Table 11.1 Elastic material properties and densities for soil layers

Unit		Young's Modulus (GPa)	Poisson's Ratio	Density (kg/m^3)	Data Source
North Sea		2	0.3	2150	NAM
Chalk		10	0.25	2350	NAM
Rijnland		16	0.25	2350	NAM
Triassic		16	0.25	2350	NAM
Zechstein	Halite	30	0.35	2100	NAM
	Andydrite	70	0.25	2900	Literature
Ten Boer		40	0.2	2300	NAM
Slochteren	Heterolithic	36	0.2	2300	NAM
	Reservoir	Porosity-Dependent			Core Data
Carboniferous		40	0.2	2300	NAM

The Young's modulus, Poisson's ratio, density and the Biot coefficient of the reservoir layer are dependent on porosity. This dependence is captured in the finite element model by defining porosity as a field variable and these properties to be a function of this field variable. The plots of these properties vs. porosity and the fit used in the model are shown in Figure 11.4 through Figure 11.7. The data for Young's modulus, Poisson's ratio and Biot coefficient from different well locations is indicated by different colored symbols as indicated by plot legends.

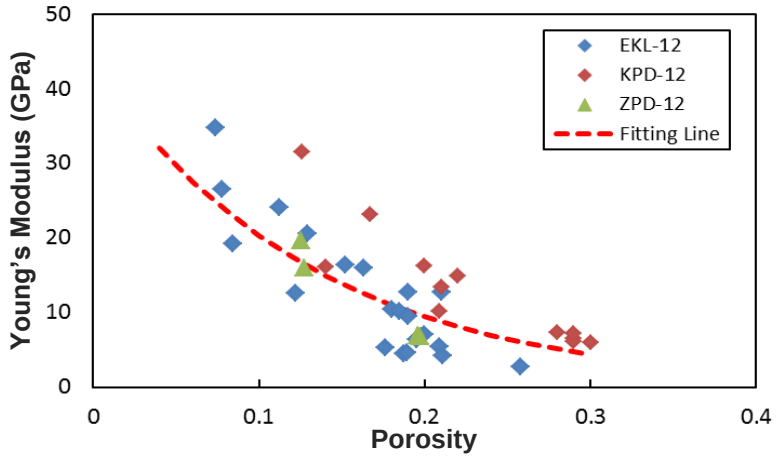

Figure 11.4 Young's modulus vs. porosity of reservoir rock

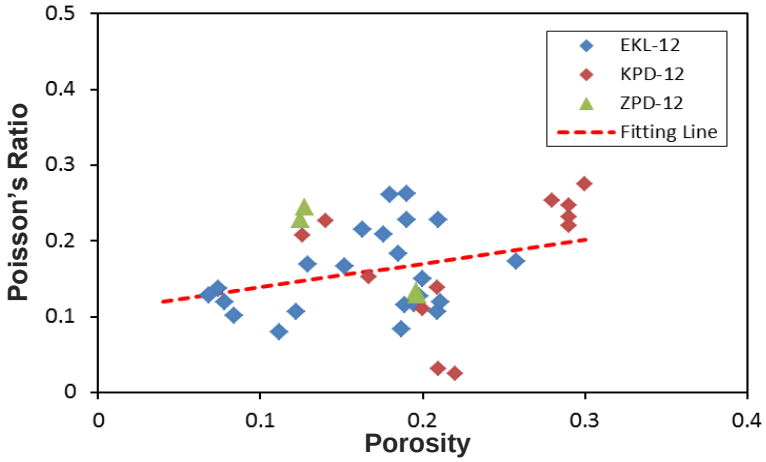

Figure 11.5 Poisson's ratio vs. porosity of the reservoir rock

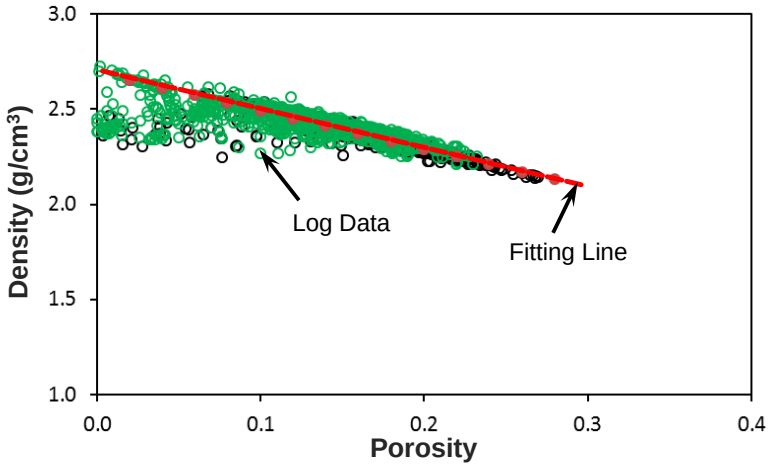

Figure 11.6 Density vs. porosity of the reservoir rock

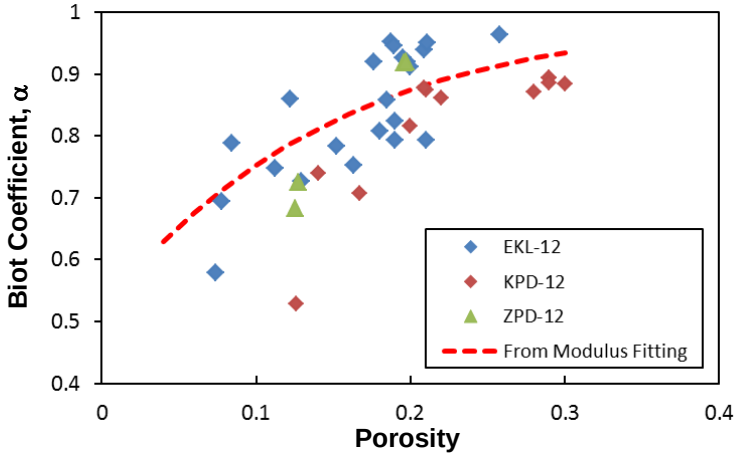

Figure 11.7 Biot coefficient vs. porosity for the reservoir rock

The plasticity properties for reservoir layers are based on core sample triaxial test data provided by NAM. The data fit and parameters for Drucker-Prager material model are shown in Figure 11.8.

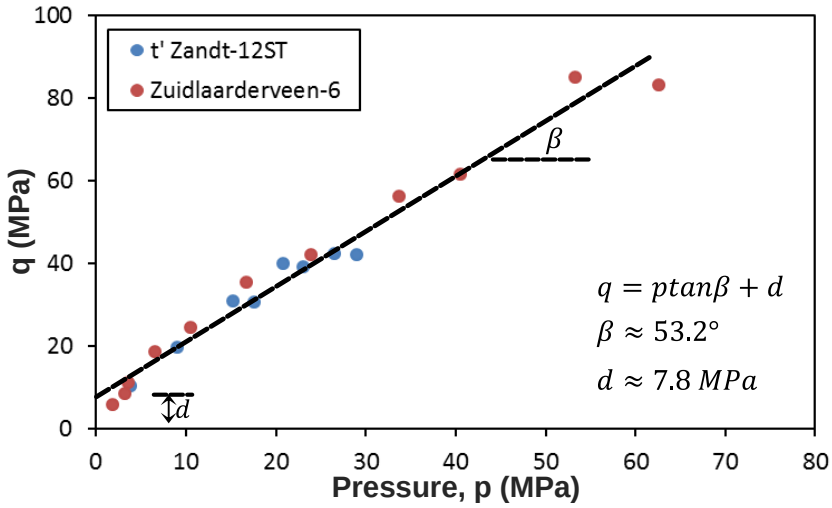

Figure 11.8 Peak shear failure envelope of reservoir rock and fitted Drucker-Prager model parameters

The faults are modeled using Coulomb friction model with the friction coefficient based on the residual strength of reservoir rock. The plot of residudal strength (shear stress) vs. normal stress in triaxial tests in included in Figure 11.9. The slope of the fitting line indicates an upper bound for coefficient of friction for the faults; however, the actual strength of the fault is likely to be lower. Sensitivity studies using the sub-models indicated that a friction coefficient of 0.48 provides a good match for predicted slip magnitude and dissipated energies with field data for production history (1964-2012).

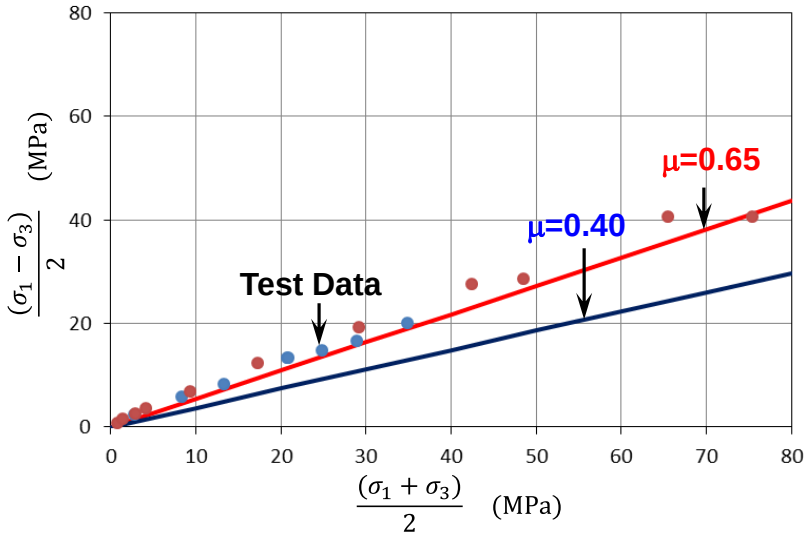

Figure 11.9 Residual strength of the reservoir rock

11.4 Initial stress state

The initial stresses in the soil layers are defined using the following gradients provided by NAM:

- Vertical stress: 2.14 bar/10m
- Maximum horizontal stress: 1.71 bar/10m
- Minimum horizontal stress: 1.60 bar/10m

The maximum horizontal stress azimuth is 160° from North. The stresses in the two halite layers are isotropic, i.e. both the horizontal stresses are equal to the vertical stresses. The horizontal stresses in anhydrite layers are also close to the vertical stress; however, the stress state need not be perfectly isotropic. A separate "salt-creep" step is run prior to production pressure history/forecast analysis to ensure isotropic stress state in halite layers, and higher stresses in anhydrite layers.

The reservoir pore pressure values in finite element model are interpolated and mapped from the pressure values from NAM reservoir simulator analyses, and are applied as initial and boundary conditions for all pore pressure degrees of freedom in the finite element model.

11.5 Global model analysis methodology

The global model includes the entire Groningen field region, with additional sideburden added on all sides to reduce the effect of boundary conditions. This model does not explicitly include faults. The Groningen field region in the global model is 42.8km x 50.6km. Overall horizontal dimensions of the model are 182.8 km x 190.5 km x 20km depth. The depth of 20km, much larger than reservoir layer depth of approximately 3km, is similarly used to reduce the effect of the bottom boundary. A vertical cross-section of the global model mesh is shown in Figure 11.10. The average thickness of various soil layers, number of element layers within soil layers and average element thicknesses are summarized in Table 11.2. The mesh includes approximately 800,000 elements.

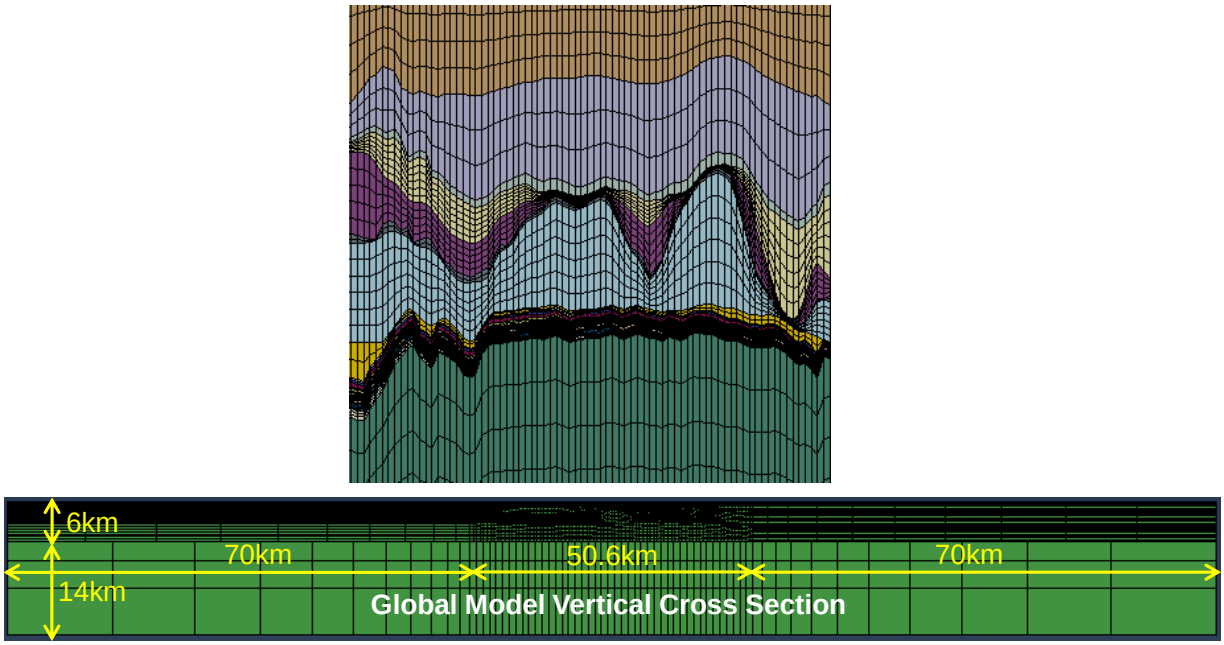

Figure 11.10 Groningen field region with modeled rock layers (top figure); vertical dimensions scaled by factor of 10; sideburden not included. Global model vertical cross-sections (bottom figure) showing Groningen field region and entire model with sideburden.

Reservoir Model

Layer	Elems across layer	Avg elem thk	Avg layer thk	max TVD	min TVD
CARBONIFEROUS	8	343.40	2747.20	6000.00	2721.17
LSS_1_RES	3	10.80	32.40	4242.21	2718.17
LSS_1_HET	2	2.07	4.14	4195.93	2716.17
LSS_2_RES	4	10.34	41.34	4193.93	2703.30
LSS_2_HET	2	2.84	5.68	4157.85	2700.68
USS_1_RES	3	10.65	31.94	4155.85	2678.66
USS_1_HET	4	1.59	6.37	4152.85	2672.40
USS_2_RES	3	10.59	31.77	4127.49	2632.82
USS_2_HET	2	2.08	4.17	4092.10	2629.49
USS_3_RES	2	10.23	20.46	4090.10	2612.21
TEN_BOER_Z1_2	1	25.62	25.62	4056.85	2595.23
TEN_BOER_Z3	1	14.23	14.23	4026.36	2582.21
TEN_BOER_Z4	1	12.57	12.57	4003.46	2569.98
ZE_BASAL	2	31.42	62.83	4000.57	2510.62
ZE_Z2	6	78.64	471.83	3693.78	1100.85
ZE_Z3	2	29.14	58.28	3531.04	986.00
ZE_Z4	5	44.30	221.49	3529.04	436.68
TRIASSIC	6	77.65	465.91	3442.23	378.85
RIJNLAND	1	82.43	82.43	2317.98	376.89
CHALK	3	263.95	791.85	2219.47	190.83
NORTH_SEA	4	216.87	867.48	1431.42	0.00

Table 11.2 Soil layer mesh details

The global model analysis includes three steps: (i) initial geostatic stress initialization, (ii) salt-creep step to ensure isotropic stress state in halite layers and higher horizontal stresses in anhydrite layers, and (iii) production pressure history/forecast analysis. The effect of salt creep was also included during the production analyses. The analysis takes approximately 50 hours to run on 256 cpus.

The first two steps above, geostatic initialization and salt-creep are required to ensure correct initial stress state, as described in above subsection, before start of production pressure history/forecast analysis. This stress initialization was verified by plotting stresses along 100 vertical lines in a 10x10 grid pattern over the Groningen field region, and at 70 locations within the sub-model- 1 region as indicated in Figure 11.11.

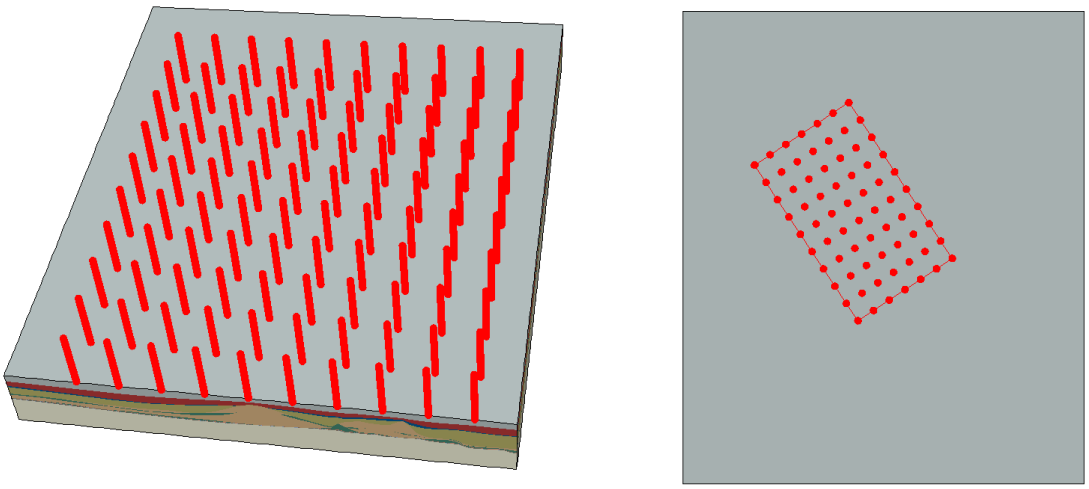

Figure 11.11 Locations for stress vs. depth plots for verification of initial stress state

The initial stresses along these vertical lines are plotted in Figure 11.12 through Figure 11.15. Note that the stresses are approximately aligned around the specified gradient for all soil layers except halite and anhydrite. There are deviations from the specified gradient due to the effect of salt-creep (isotropic stress state in salt also modifies stresses in surrounding region). Additionally, there are some deviations due to

numerical limitations of the model. However, note that these numerical errors are mainly present for regions near the boundary of the Groningen field region. The stress plots for the sub-model-1 region are significantly smoother.

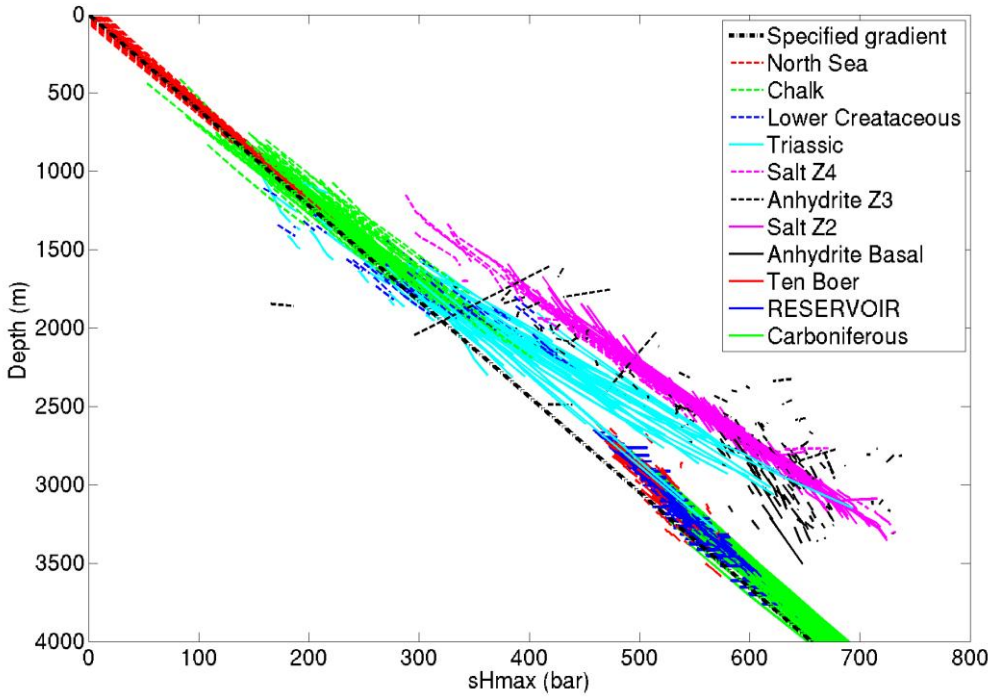

Figure 11.12 Global model sHmax at the 100 locations after salt-creep step

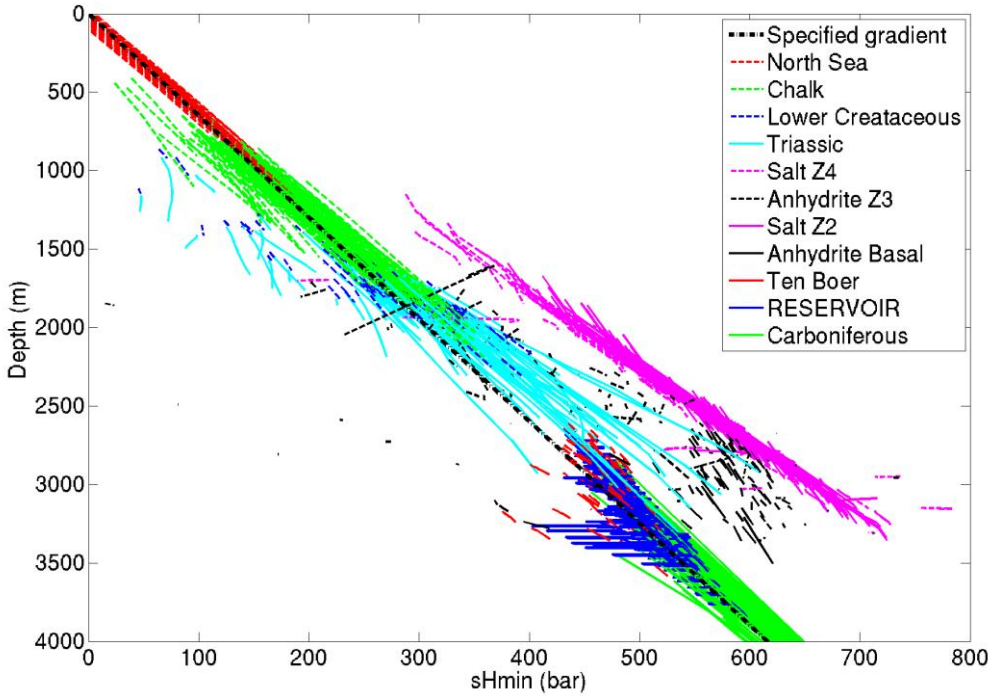

Figure 11.13 Global model sHmin at the 100 locations after salt-creep step

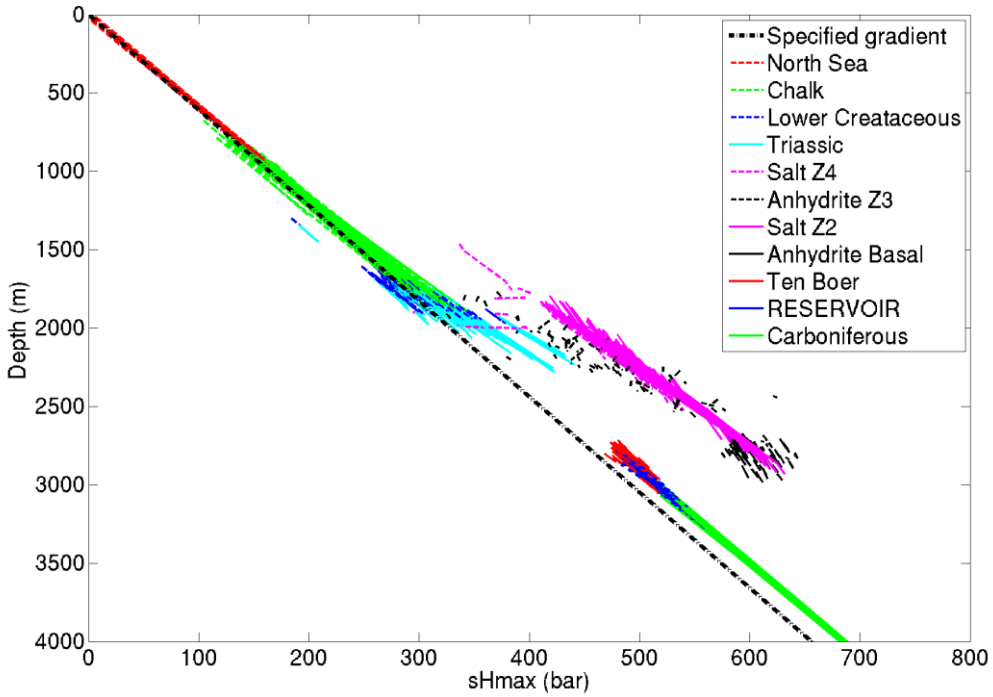

Figure 11.14 sHmax stress in the sub-model-1 region (output from global model analysis)

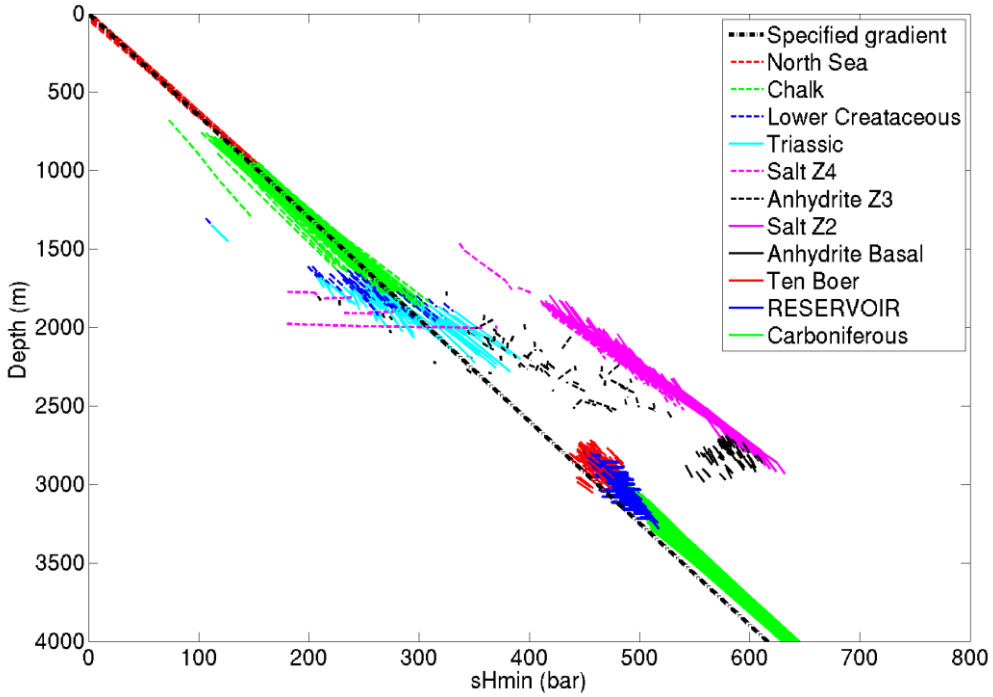

Figure 11.15 sHmin stress in the sub-model-1 region (output from global model analysis)

The production history analysis for years 1964-2012 based on geological model realization G1 with moderate strong northern aquifer was used to predict surface subsidence and reservoir strains. The contour plot of predicted surface subsidence in 2012 and comparison with field data is shown in (a) (b)

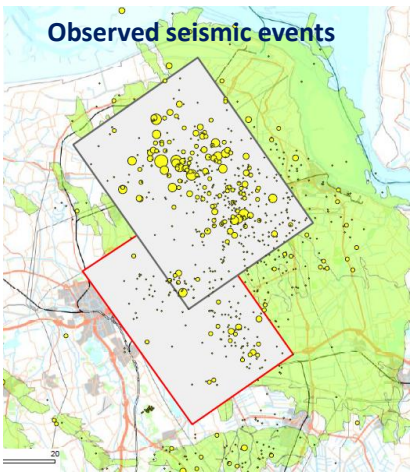

(c)

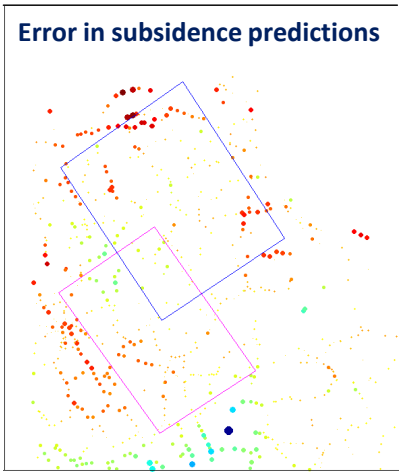

(d)

Size of circles indicates magnitude of error

Blue-green colors: prediction lower than field data

Orange-red: predictions higher

Note that errors are towards edges of sub-model regions; away from observed seismic event locations

Figure 11.16. (a) and (b). A map of error between model predictions and field data is included in (d), which indicates that errors in subsidence predictions are very low in areas of significant seismicity shown in (c).

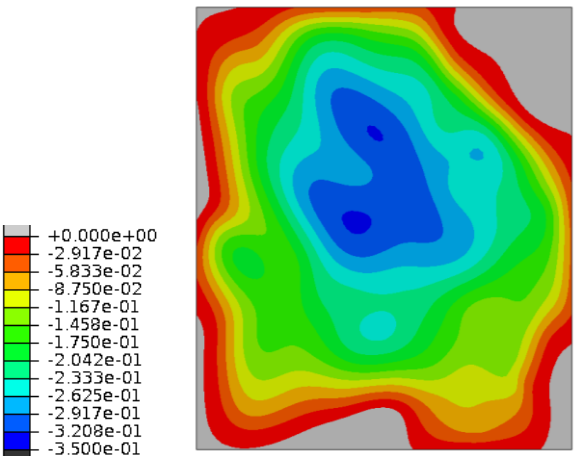

(a)

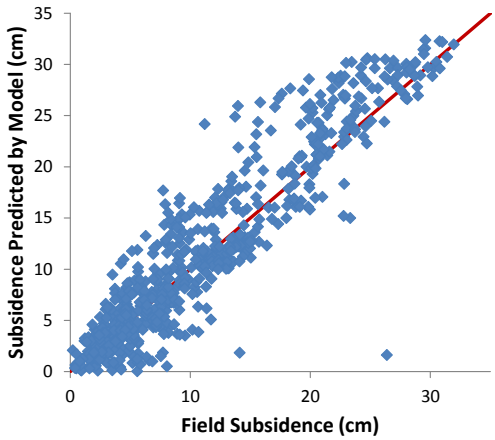

(b)

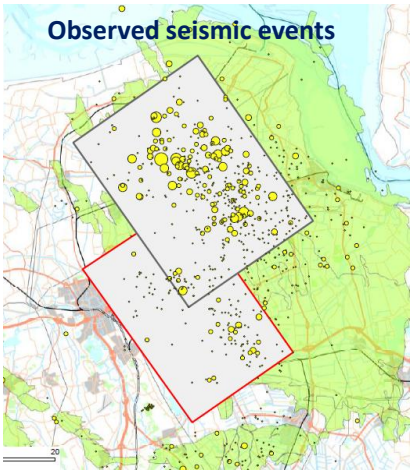

(c)

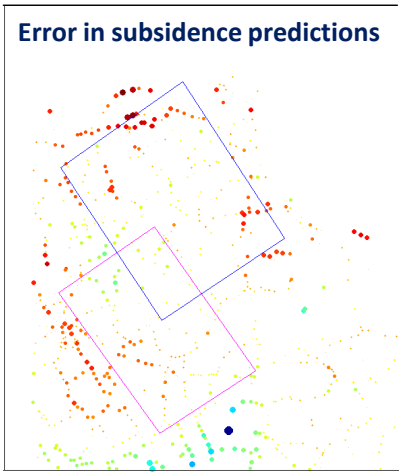

(d)

Size of circles indicates magnitude of error

Blue-green colors: prediction lower than field data

Orange-red: predictions higher

Note that errors are towards edges of sub-model regions; away from observed seismic event locations

Figure 11.16 (a) Contour plot of predicted surface subsidence (m) in 2012, (b) comparison with field data, (c) locations of seismic events from NAM, and (d) map of error between model subsidence predictions and field data

The predicted average strain in the reservoir layers is compared with available field data. The comparison for one well location, De Hond, is shown in Figure 11.17. The average strain is computed over reservoir (reservoir rock and heterolithic layers) only and over reservoir and ten boer layers combined, since the averaging interval for the field data is not known.

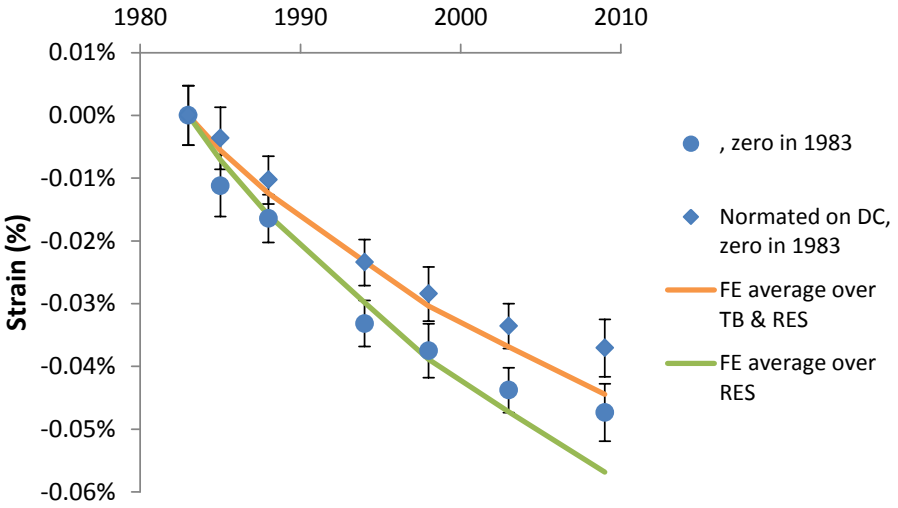

Figure 11.17 Comparison of predicted reservoir layer strains vs. field data (De Hond well location)

11.6 Sub-model analysis methodology

Two sub-models have been developed to model the regions of seismic activity in greater detail, including detailed modeling of faults as contact surfaces that permit slippage. The sub-models include soil layers from ZE_Z2 halite to the Carboniferous up to depth of 4 km. The dimension of sub-model-1 and -2 are 16.3km x 20.0km and 12.7km x 19.2km respectively.

More than 1700 faults have been interpreted in the Groningen field, of which 707 have been used to construct the static and dynamic reservoir model. Due to extreme complexity of meshing with faults, a selected number of faults were included in the sub-models. The fault selection was based on: (i) faults along major/compartment boundary, (ii) fault throw, (iii) shear capacity utilization from NAM analysis, and (iv) the proximity to seismic events. The first step in fault selection process is to include the faults along major/compartment boundaries. Additional faults according to each additional criteria area added in subsequent steps. This process for sub-model-1, with faults added in each step, is shown in Figure 11.19. Sub-model-1 includes 40 faults and sub-model-2 includes 37 faults. Both meshes include approximately 250,000 elements, with over 99.7% hexahedral (brick) elements to ensure accuracy of the solution. The three-step analysis (same as global model) takes approximately 30 hours to run on 128 cpus. The locations of these two sub-models relative to the Groningen field region in the global model are shown in Figure 11.18.

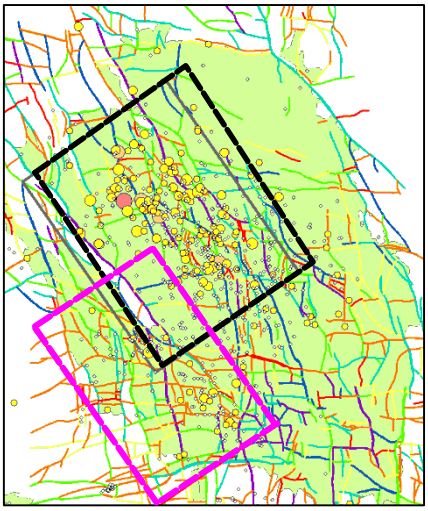

Figure 11.18 Location of sub-models; sub-model-1 indicated by black lines, sub-model-2 indicated by magenta lines

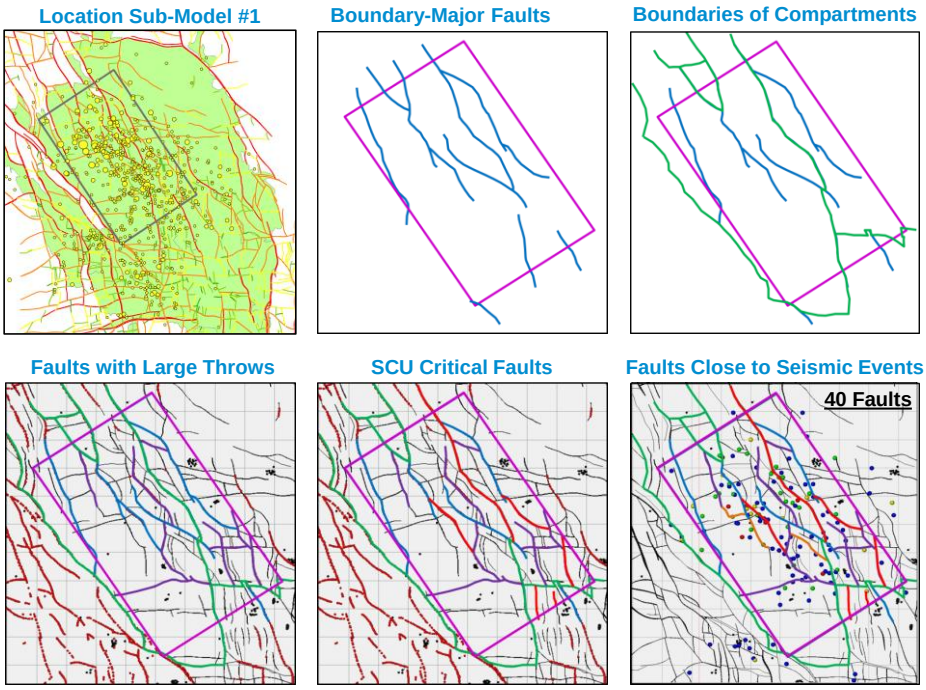

Figure 11.19. Fault selection for sub-model-1; total of 40 faults included after final step

The meshes for the two submodels, with faults highlighted, are shown in Figure 11.20.

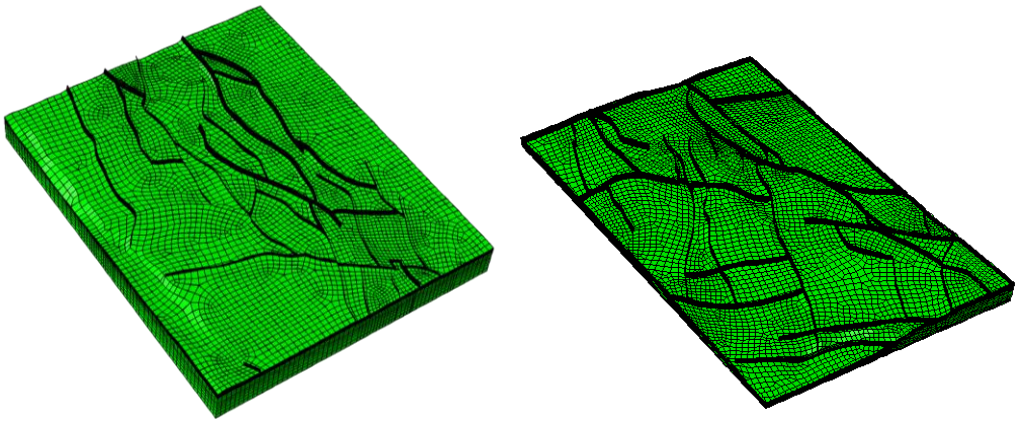

Figure 11.20 Sub-model-1 and 2 meshes with faults highlighted

The sub-model analyses are run separately from the global model, with the exterior node boundary conditions driven by displacements in the corresponding global model analysis. Figure 11.21 through Figure 11.24 show the comparison of stresses, displacements and pore pressures in the top reservoir layer of the sub-models with those in global model to verify consistency of sub-models with the global model.

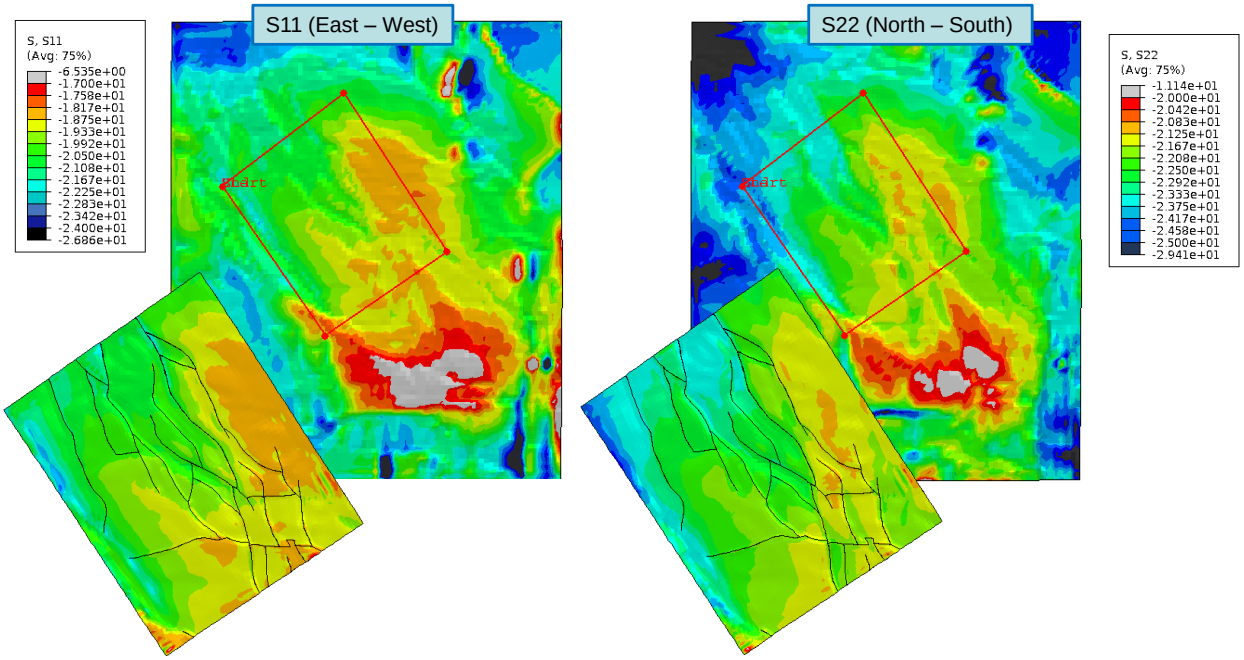

Figure 11.21 Initial stresses (in MPa) in sub-model-1 top of reservoir layer USS_2_Res compared with the global model stress field

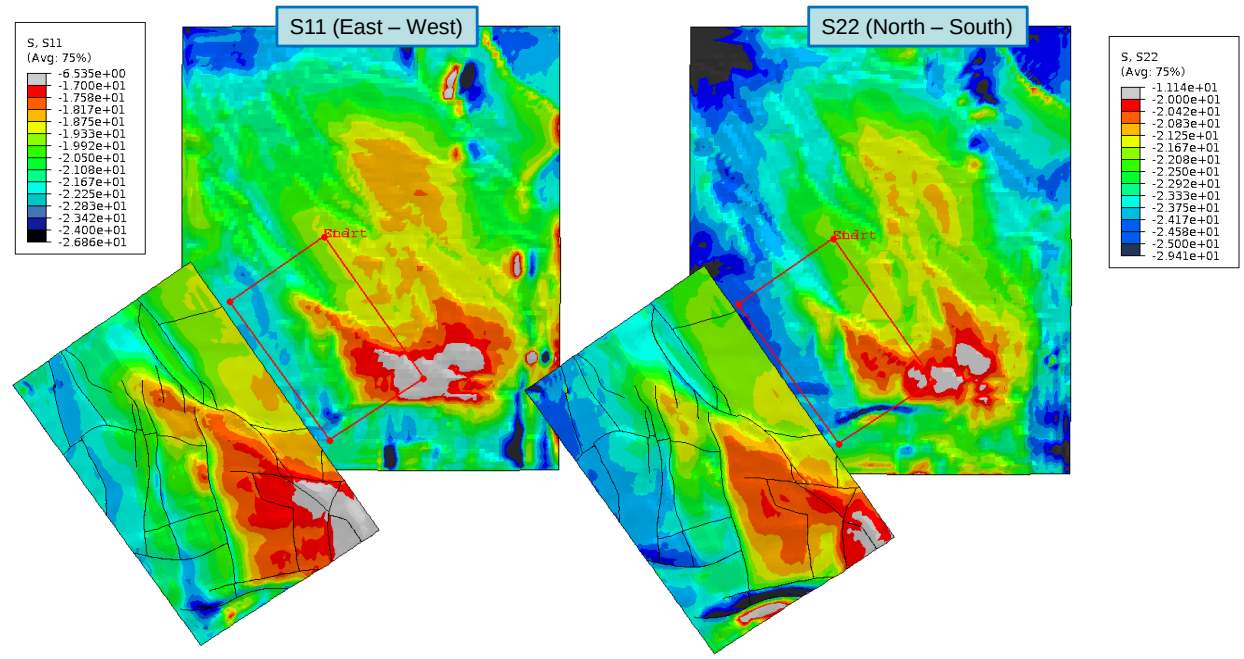

Figure 11.22 Initial stresses (in MPa) in sub-model-2 top of reservoir layer USS_2_Res compared with the global model stress field

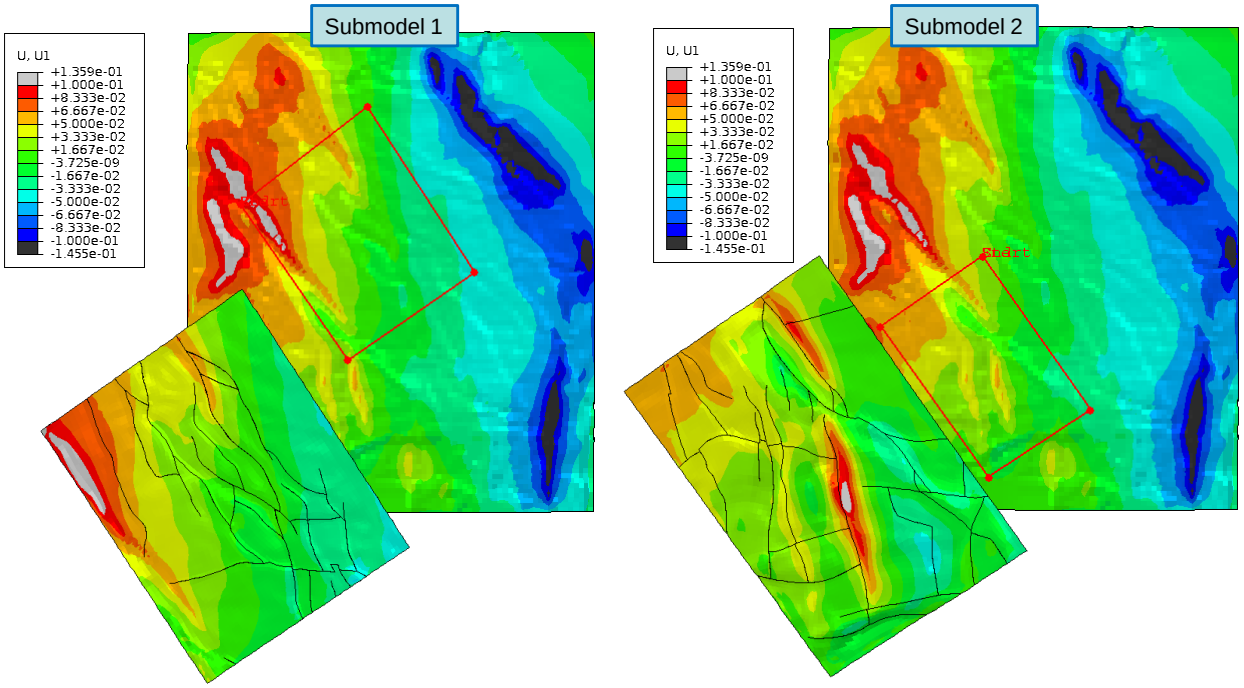

Figure 11.23 Horizontal displacement (East-West, in meters) for top of layer USS_2_Res in sub-model-1 and -2 in year 2012 compared with global model; comparisons for other two displacement components indicate similar match

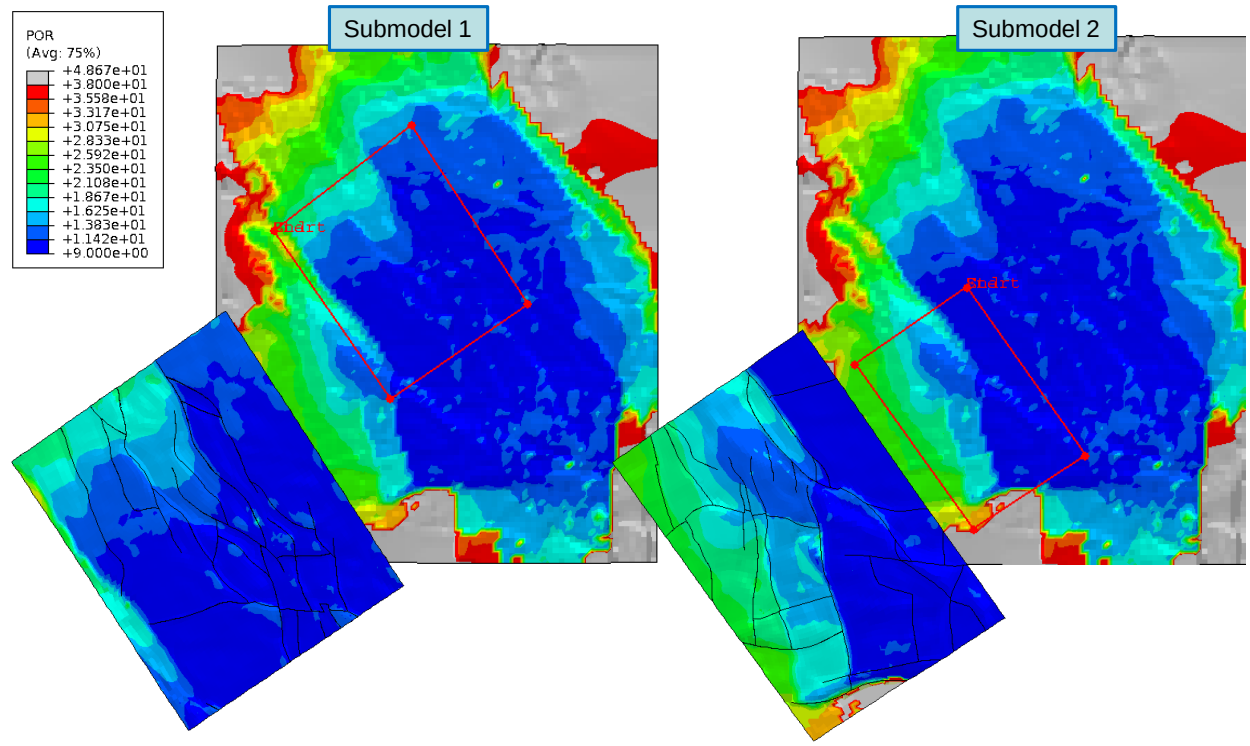

Figure 11.24 Comparison for 2012 pore pressure (in MPa) for top of reservoir layer USS_2_Res

The sub-model analyses are used to predict production induced fault slippage and the energy dissipated due to this slippage. Fault slip is predicted at different locations and at different points in time. The contour plot of slip magnitudes along faults for sub-model-1 analysis for base case development scenario (D1) based on Geological model realization G1 is shown in Figure 11.25. The predictions for dissipated energies for various cases are compared in the main text of this report.

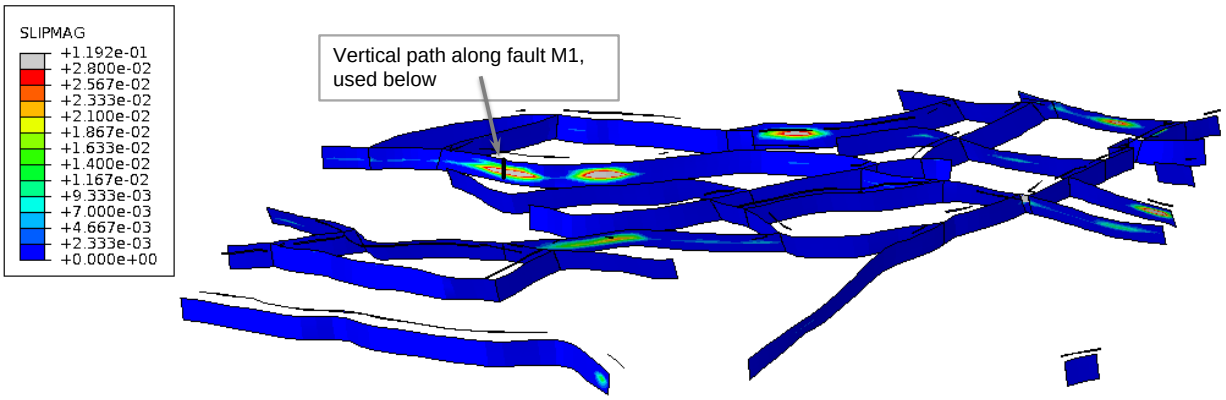

Figure 11.25 Contour plot of slip magnitudes in 2059 along faults of sub-model-1 for the base case production scenario

Evolution of slip along the vertical path shown in Figure 11.25 with time is shown in Figure 11.26. This path is located at the region with maximum slip magnitude along fault M1.

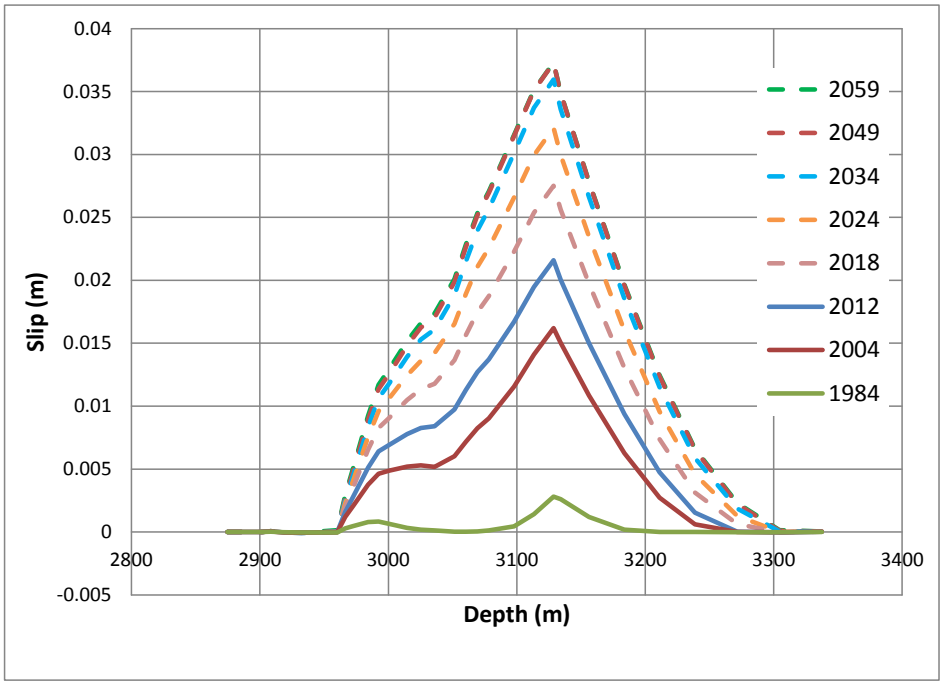

Figure 11.26 Evolution of slip magnitude along vertical path shown in Fig. A1.24 for the base case production scenario

The slip magnitudes and the extent of the vertical section of the fault that is slipping both increase with time. However, note that the slip is zero near top and bottom in anhydrite and carboniferous layers respectively. This indicates that the slip magnitudes have not "saturated" due to zero-slip boundary conditions at top and bottom. Additionally, as shown in Figure 11.26, the slip magnitudes do not increase significantly beyond approximately year 2050, since there is significantly less depletion beyond this year compared to earlier years.

The predicted dissipated energy is very sensitive to the friction coefficient used to model faults. Predictions for evolution of dissipated energy for various friction coefficients for sub-model 1 are compared in Figure 11.27. This sensitivity study was used to identify the friction coefficient value of 0.48 for use in the sub-models. This value was used consistently to model all production scenarios so that the predicted energies for different scenarios can be compared directly.

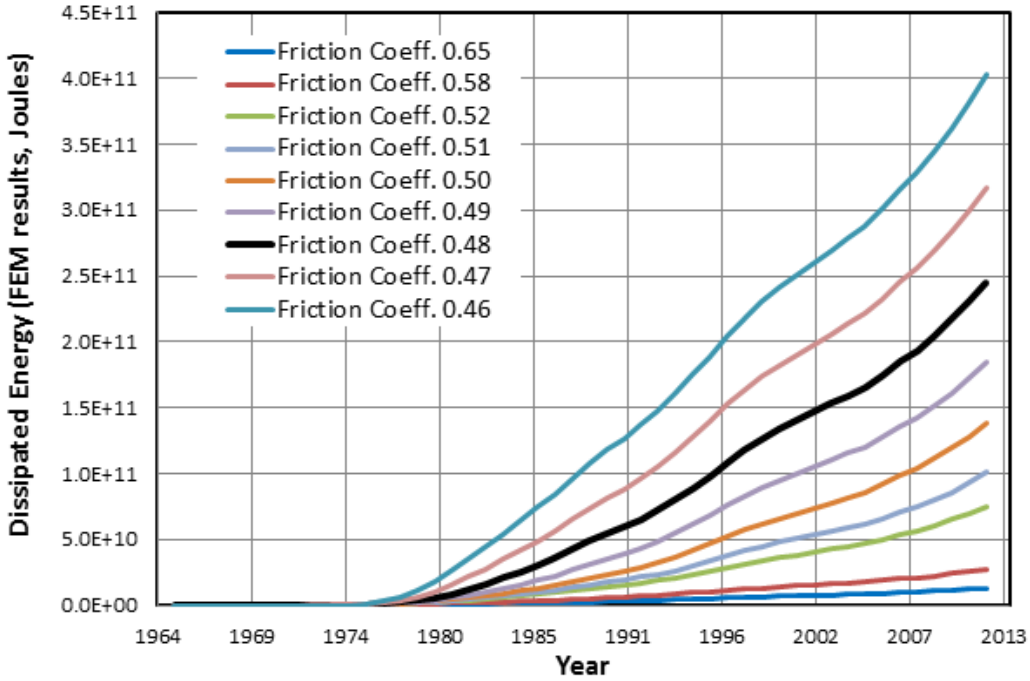

Figure 11.27 Dissipated energy for different coefficients of friction for production history (1964-2012) analysis; geological model realization G1; sub-model 1

The sub-models include a limited number of faults that are selected according the prioritization criteria described above. This prioritization process ensures that faults that are most critical to seismic activity are included. Results from sub-models predict that nearly 90% of dissipated energy is due to only 10% of the faults that are included. A plot of the contribution to dissipated energy by individual faults is included in Figure 11.28. This comparison indicates that the assumption that critical faults are captured by the prioritization process is reasonable. Adding more faults, either those that are currently excluded or others that have not been imaged by seismic surveys, are not expected to change the predicted dissipated energy significantly.

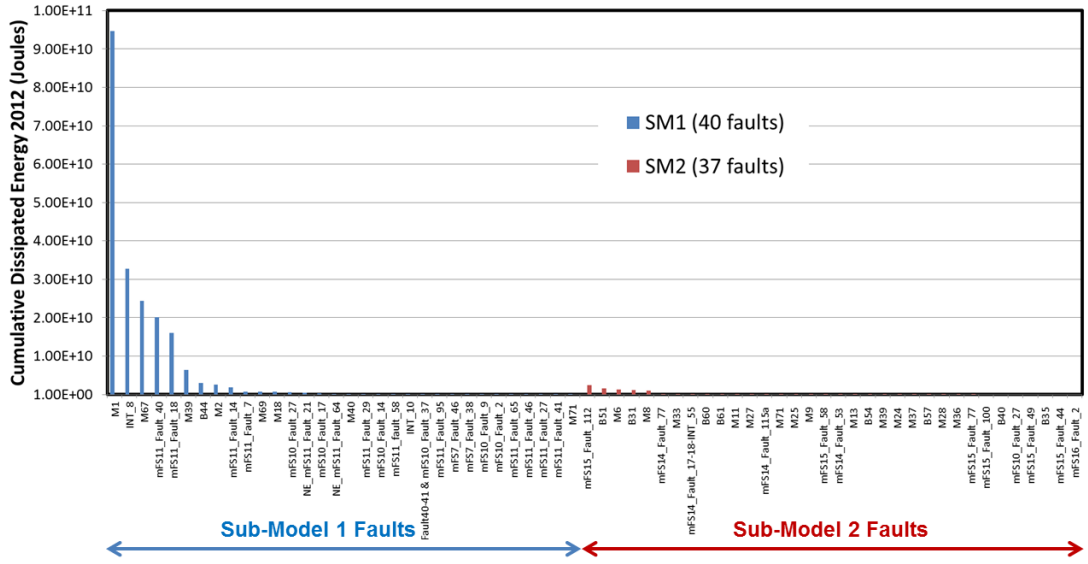

Figure 11.28 Contribution to dissipated energy by individual faults; 10% faults contribute 90% of energy

12 Appendix B: Pressure Maintenance

12.1 Introduction

In a letter to parliament (11 February 2013 reference TK 2012-2013 33529, no. 2), the Minister of Economic Affairs initiated a number of studies on induced earthquakes in the Groningen area. The Minister also installed and confirmed the TBO (Technische Begeleidingscommissie Ondergrond; Technical Guidance Commission Subsurface), to oversee the study work done by NAM and to provide independent assurance. One of the studies (number 6) relates to the subsurface operation of the field and addresses the question: "Are there alternative gas recovery methods that result in a reduction of the seismic activity"?

Study number 5 has been addressed in the; "Report to the Technical Guidance Committee (TBO) on Subsurface Aspects of Induced Earthquakes in the Groningen Field", which has been issued previously. It describes the technical studies carried out by NAM and reports the gained insights to the TBO.

Study number 6 is a continuation of this work. It consists of two parts. Part 1 addresses the impact of different depletion scenarios on seismicity, and has been issued separately. The current document reports on part 2, which addresses development options for the Groningen field based on pressure maintenance by injection of fluids.

Part 2 consists of 5 sections, including this introductory section. The other sections are briefly introduced below.

2. This section describes the selection of the injection medium for pressure maintenance. Several fluids are considered, but nitrogen is selected as the most suitable option.
3. This section describes the modelling of the displacement and mixing of the injected nitrogen and the indigenous natural gas. Production forecasts and reserves estimates are prepared for a basecase development concept. Several alternative development scenarios are evaluated in parallel.
4. This section describes the surface facilities required for a field development on the basis of pressure maintenance through nitrogen injection.
5. This section briefly describes the effectiveness of using water as an injection medium to achieve reduced seismicity through pressure maintenance.

Pressure maintenance is expected to arrest reservoir compaction, and hence to reduce the seismic hazard. However, to what extent is yet to be established through further geomechanical modelling. This work is documented in a separate report (Ref. 1) and was carried out by URC Houston (XoM) and NAM/Shell. Another area of further study is the impact on seismicity when injecting into or close to a fault.

12.2 References:

1. Report to the Technical Guidance Committee (TBO) on Production Measures Part 1: Depletion Scenarios and Hazard Analysis, NAM, November 2013.

12.3 Selection of the injection medium

Pressure maintenance as a general concept is based on reinjection of a volume equal to the gas volume production from the reservoir. By balancing the injected and produced volume, the pressure in the gas reservoir can be stabilised. With the stabilised reservoir pressure, compaction of the reservoir rock will halt after some time. Since compaction is thought to be a key factor in the creation of seismicity, this would also reduce seismic activity in the Groningen area.

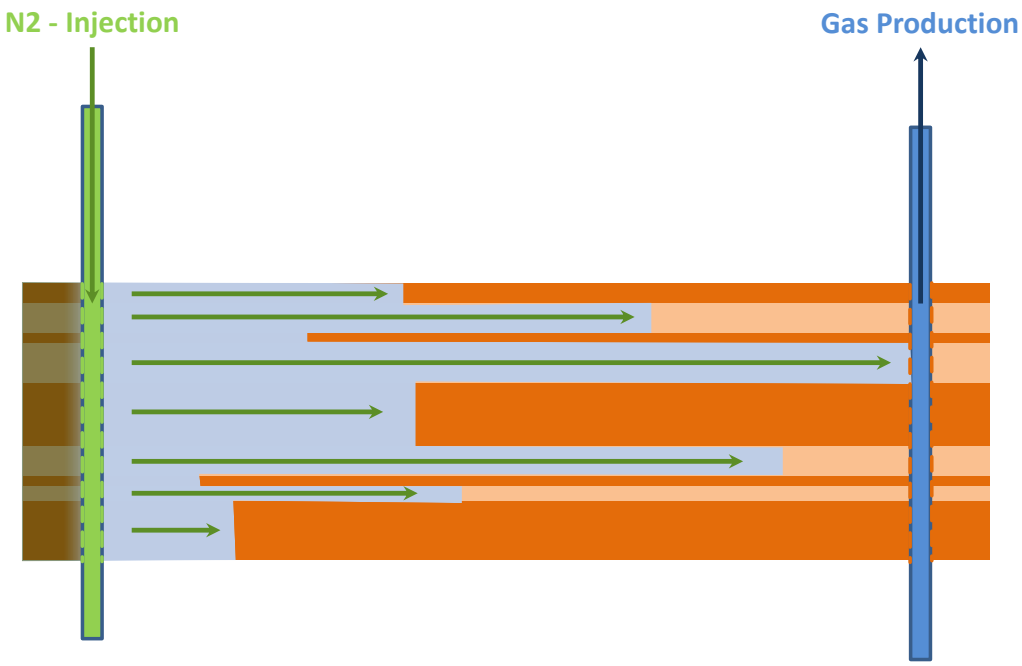

Figure 12.1 Principle of pressure maintenance by injection.

The medium to be injected needs to meet several criteria. First, this substance either needs to be a liquid or a gas to allow injection into the reservoir rock. Second, it should be available in large quantities at acceptable cost to warrant an economically feasible development scenario.

An initial screening of injection media showed that water is the only liquid available in sufficiently large quantities. The use of water injection for pressure maintenance is discussed in Section 5 of this report.

Several gases can in principle be used as an injection agent for pressure maintenance. These are either natural components of the air or products from combustion processes:

- Nitrogen (N_2),
- Carbon dioxide (CO_2),
- Flue gas
- Air

Each of these gases has its advantages and disadvantages. An initial screening of these gases for the Groningen field is provided below.

12.4 Nitrogen (N_2)

Nitrogen (N_2) is a colourless gas which constitutes around 78% of the volume of the Earth's atmosphere. The gas is mostly inert and non-corrosive. Therefore no special metallurgy measures are required to avoid corrosion of pipelines, wells and facilities. In fact, nitrogen is already present in small quantities (14%) in the Groningen gas.

Nitrogen can, in principle, be sourced in large quantities from the air using a cryogenic process. This will require industrial size facilities described in Section 3. The non-corrosive nature of nitrogen helps in achieving an efficient production and relatively safe operation process.

As nitrogen is less compressible than Groningen gas and other injection media, it provides a higher reservoir displacement volume per standard volume of nitrogen injected than any of the other injection gases. Therefore it has the lowest volume requirement for pressure maintenance. A first calculation shows that some 23 wells are required for nitrogen injection. This number is based on the total amount of gas to be replaced, the injection capacity of a Norg big-bore well, and of specific gas properties such as compressibility and corrosion potential. Additional surfaces facilities include a dedicated nitrogen pipeline network to transport the gas from the production plant to the injection wells

After breakthrough of the nitrogen in the production wells, it needs to be removed again to bring the produced gas back to sales specification. This requires a cryogenic process of a smaller scale, but on each of the production clusters instead of a centralized plant. Compressors and flowlines are required to evacuate the produced nitrogen to the injection wells.

12.5 Carbon dioxide (CO_2)

Carbon dioxide (CO_2) can be sourced from the combustion of coal or natural gas (from electricity generation or other processes) using air separation prior to burning. This is similar to the clean coal technology. However, the annual carbon dioxide volume required for injection compares well with the total volume generated by all current power generation facilities in The Netherlands. It is not realistic to assume that this total volume can be made available for injection. Furthermore, the carbon dioxide needs to be cleaned to remove remaining impurities.

The corrosive nature of carbon dioxide (in combination with water vapour) requires gas to be removed from the production stream. This can be done with a knock out drum to take out the liquids followed by an electric heater (or membrane pre-treatment). Gas is then routed to membranes, followed by an amine polishing unit.

The injection facilities are similar to the nitrogen case. Field distribution requires a dedicated carbon dioxide distribution pipeline network and a pipeline to a source. The pipeline network and completions in the injection and (after breakthrough) 295 production wells needs to consist of special corrosion resistant materials. Alternatively, the gas can be dried in which case carbon steel pipe is suitable. Based on its specific properties, the injection of carbon dioxide requires more wells than for nitrogen.

In the US, some experience was gained with carbon dioxide used for enhanced oil recovery. However, the gas is in this case sourced from carbon dioxide fields which are not available in North-Western Europe.

12.6 Flue Gas and Air

Flue gas is exhaust gas from power plants, gas turbines, gas engines or heaters. It can also be sourced from the combustion of coal or natural gas. The flue gas volumes generated are considerably larger than that of carbondioxide and no air separation is required. However it is very corrosive since it contains NO_x, SO_x, CO, CO_2, H_2O, and O_2. Therefore, after breakthrough in the production wells, the flue gas will need to be removed from the production stream before sales. Especially for oxygen the sales specification is very tight making it difficult to reach the required levels. Other projects using flue gas have experienced problems related to the corrosive nature of the gas.

Once passed through the reservoir and having been in contact with water, the wet flue gas will become even more corrosive. Therefore, it needs to be removed from the production stream which requires a cryogenic unit Injection facilities are similar to the nitrogen case. Field wide distribution requires a dedicated flue gas pipeline network and a flowline from the production cluster into the network. Also in this case, the pipelines and completions in the injection and (after breakthrough) production wells need to have a special corrosion resistant materials. The complex composition of the gas makes the selection of the corrosion resistant material much more difficult than in the case of carbon dioxide.

The corrosive nature of the flue gas may lead to a longer term safety issues. Additional explosion risks associated with the presence of high pressure oxygen in the pipeline system will also need to be addressed.

In case of air injection, an additional risk is the reaction between the gas and oxygen in the reservoir (internal combustion). This is sometimes used as an EOR method in oil reservoirs. Here the heat generated by the internal combustion helps to reduce the oil viscosity.

12.7 Conclusion

Table 12.1 Lists the main selection criteria of the injection medium discussed above. It is clear that nitrogen has advantages above all the other options. These include availability, non-corrosive nature, cost, handling infrastructure and environmental and safety issues. For the same reasons, nitrogen has been chosen and

successfully applied for more than 20 years in pressure maintenance and enhancing reservoir-drive mechanisms for both miscible and immiscible oil recovery projects

Table 12.1 Options table for selection of the injection medium.

	Nitrogen	Carbon-dioxide	Flue gas and Oxygen	Air
Abundance				
Relative cost of generation in large quantities				
Corrosiveness				
Reaction with reservoir and internal combustion with the reservoir gas.				

12.8 Gas recovery with nitrogen injection.

12.9 Introduction

There is considerable experience in the petroleum industry around the world and within Shell with the injection of nitrogen in reservoirs. However, it is mostly injected for Enhanced Oil Recovery or for pressure maintenance purposes of gas condensate fields. The De Wijk field in the Netherlands is one of the few examples where nitrogen is injected into a gas reservoir for Enhanced Gas Recovery, but this project is still in its early days.

The largest nitrogen production unit in the world is located in the Cantarell Field in Mexico (ref. 1 to 9). This is the fifth largest oil field in the world. Gas is injected to stabilise the pressure in the gas cap and thereby increase the oil recovery from the field. The scope of the pressure maintenance case in the Groningen field is different, but the Air Separation Units of the Cantarell project may serve as a good analogue for what is required in the northern Netherlands.

A first estimate is that the capacity of Air Separation Units for pressure maintenance in the Groningen field needs to be 5 to 7 times larger than the capacity of the Cantarell facilities.

Figure 12.2 The fifth largest producing field in the world is the Cantarell complex in Mexico. It lies 85 km from Ciudad del Carmen and is operated by Pemex. The facilities in the Groningen field need to be 5-7 times larger.

12.10 Objectives of the subsurface study

A screening and early feasibility study has been carried out on nitrogen injection and pressure maintenance in the Groningen field. The existing Groningen history matched dynamic model was used for this purpose, and the experience gained in simulating multiple composition gases in modelling of the Norg and Grijpskerk underground gas storages was incorporated. Additional experience is being gained in the De Wijk nitrogen injection project.

The impact on field reservoir pressure distribution and economic recovery was assessed. To date, the Groningen reservoir has demonstrated "tank like" behaviour, which means that analytical methods such as material balance models can be applied. However, since a history matched model of the Groningen field is already available, it was chosen to take a simulation model approach. This has the following advantages:

- Geological (local heterogeneity) and structural (faults) features of the reservoir can be taken into account,
- The number of required wells, their locations and the surface facilitiescan be optomized,
- A more accurate representation of the gas-gas mixing PVT behaviour can be incorporated.

12.11 Basis for modelling

Modelling of a gas injection production mechanism is challenging, especially because historically the field has been produced under depletion drive. Thermodynamically, miscibility is defined as the condition when two fluids are mixed in any proportion and resulting mixture is a single phase. Therefore by injecting in the reservoir, a first contact miscible displacement process of the natural gas by the nitrogen will take place, since both fluids are in gaseous phase in reservoir conditions. Moreover, there is already a 14% volume fraction of nitrogen in the Groningen gas composition. The effectiveness of the sweep mechanism is controlled by mixing of the two gases by diffusion, by gravity segregation and by the impact of geological heterogeneities.

Practical field observations and experience are very important to provide confidence in the predicted behaviour of the reservoir. The Groningen asset operates two underground gas storage (UGS) projects - Norg and Grijpskerk, where gas is stored in the same Rotliegend reservoir as in the Groningen field. In the underground gas storages gas is injected during the summer and produced back during cold winter days. Similar reservoir processes take place with the injection of nitrogen for pressure maintenance. Hence, the experience in modelling of gas-gas mixing in Norg and Grijpskerk can also be used for Groningen nitrogen injection. Specific aspects include:

- Matching the Grijpskerk tracer test from 1997 (Figure 12.3),
- Matching the Norg tracer test from 2008,

- Modelling of the Norg Leaning Process, which is the displacement of indigenous Norg gas by injected Groningen gas using the Norg UGS model (Figure 12.4). To make this displacement process more efficient, a well was drilled in the North of the Norg field in 2012. Accurate modelling of this process is important as only the gas at Groningen specification (*i.e.* unpolluted with indigenous Norg gas) can be used as working volume for the storage.

There are two options for modelling gas injection in the reservoir simulation tool, without using a fully compositional simulator. These are passive and active tracers:

- Passive tracers-are fluid constituents which do not, in any way, influence the properties of the host fluid. Passive tracers can be considered as a colour or dye which is put into the reservoir fluids to track fluid flow. The passive tracer equations are solved by a separate solver. They have the option to reduce the numerical dispersion and take less calculation time.
- Active tracers (PVT tracking) do influence the properties of the fluid with which they travel and are used for interpolation between different PVT models. When different types of fluids mix, intermediate PVT descriptions are used, which correspond with the resulting new tracer concentration.

  The use of active tracers helps in more accurate fluid modelling.

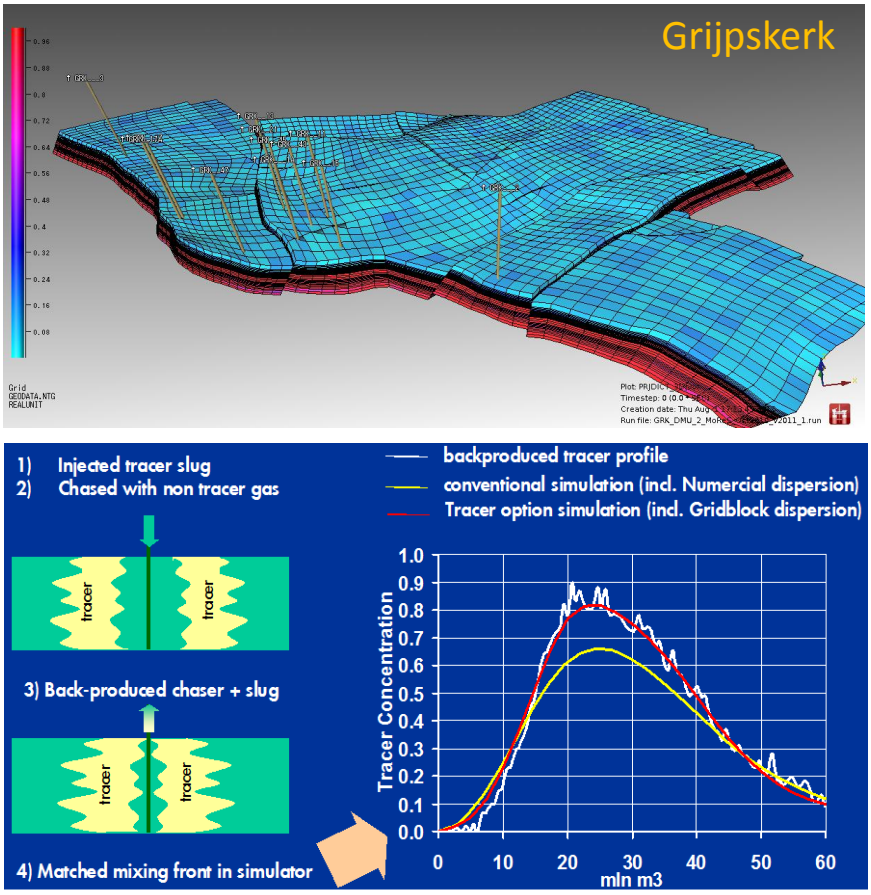

Figure 12.3 A tracer test was performed in the Grijpskerk field to investigate gas – gas mixing in the reservoir.

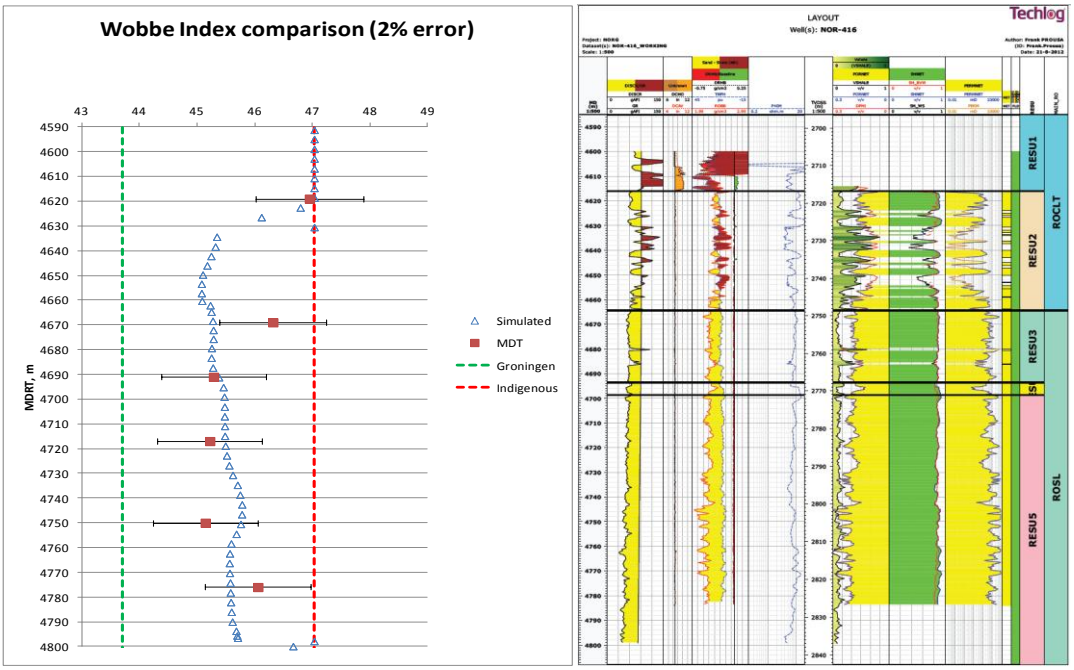

Figure 12.4 The experience with these models gives additional confidence in the modelling of the nitrogen displacement process in the Groningen field.

12.12 Simulation workflow

Simulation techniques used in the Norg UGS were applied to simple box models in order to demonstrate the strengths and weaknesses of the passive and active tracer modelling methods. Both methods were implemented on the Full Field Model (FFM) depending on the phase of the modelling process. Passive tracers were used for screening purposes and the selection of a base case. They were also used for the runs which were coupled with IPSM (Integrated Production Surface Modelling) tool. Subsequently, active tracers were implemented to capture the gas-gas mixing process.

12.12.1 Test model

A "test model" was used to review the main differences between the two tracer options, and to better understand their underlying assumptions. The following sensitivities were performed on the test model:

- Timestep and grid dimension sensitivity
- Sensitivity on the number of "intermediate" PVT models
- Numerical dispersion and diffusion factors

The test model was initialised using the Groningen PVT Model (dry gas phase). The properties of the injection fluid, i.e. nitrogen at surface and reservoir conditions, were generated using PVTSIM tool (Figure 12.5). Additionally, the properties of the synthetic mixtures of Groningen gas and nitrogen (Figure 12.5) were simulated in PVTSIM.

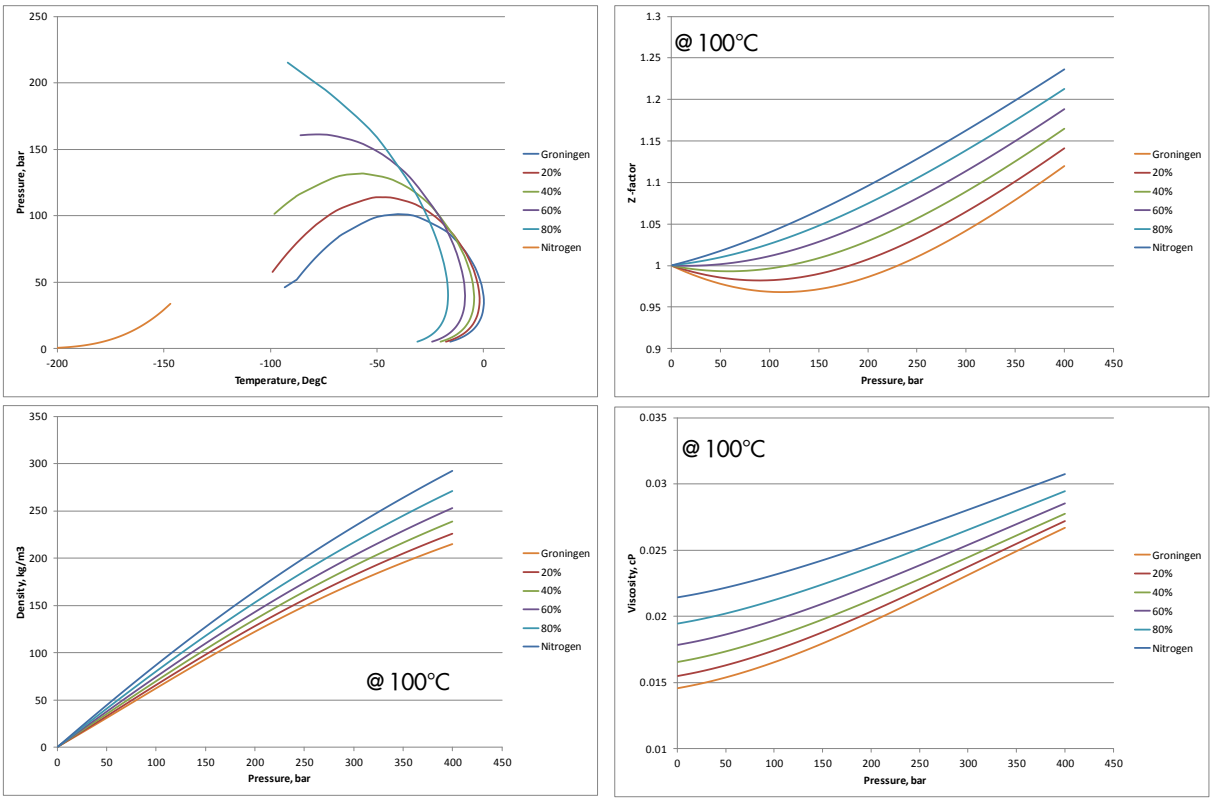

Figure 12.5 Properties of the injected and produced gas.

From Figure 12.6 it can be observed that using active tracers results in an earlier nitrogen breakthrough, because of the numerical dispersion. Numerical dispersion reduces the breakthrough time depending on the simulation grid dimensions. However, the geological detail captured in the numerical models is in most cases more homogeneous than in reality. This leads to a potential underprediction of the geological dispersion in the reservoir. These two factors might compensate one another to a certain extent. Since with passive tracers only host fluid exists, (in this case the lighter Groningen gas), it overestimates production and injection potentials to the same extent as the host and injected fluid mobility difference (Figure 12.6). The breakthrough time in both cases is a function of the grid cell and time step size. Here, the experience

gained with the calibration of the Grijpskerk and Norg models against actual observed reservoir dispersion becomes vital, even more because all three fields (Norg, Grijspkerk and Groningen) produce from the same Rotliegend sandstone reservoir.

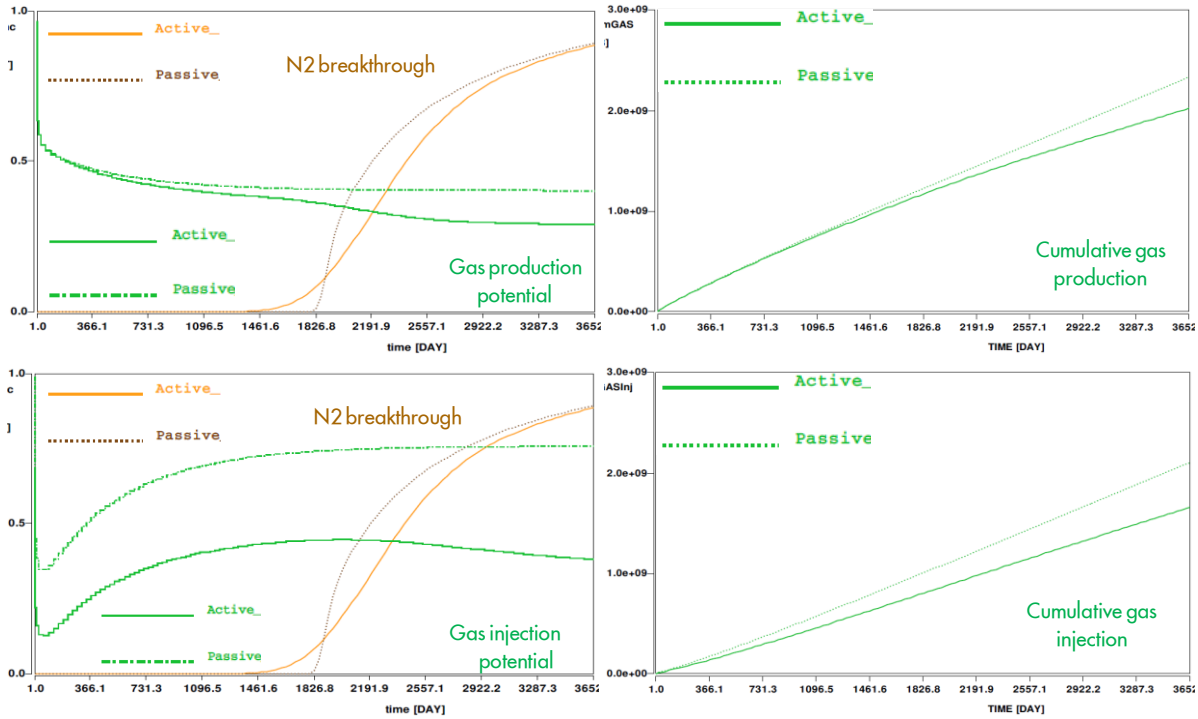

Figure 12.6 Comparison of breakthrough of injected nitrogen in test model.

The sensitivity on the number of intermediate PVT models with active tracers in Figure 12.7 shows only a minor effect on the simulation results. This is mainly due to the fact that the property changes between Groningen gas and nitrogen are linear. However, the simulator run time with higher number of PVT models increases significantly (Table 12.2). The impact of using the dispersion factors from the Grijpskerk field in the passive tracer option is shown in Figure 12.7. The default value in the simulator is already very close to the one derived from the tracer test in Grijpskerk.

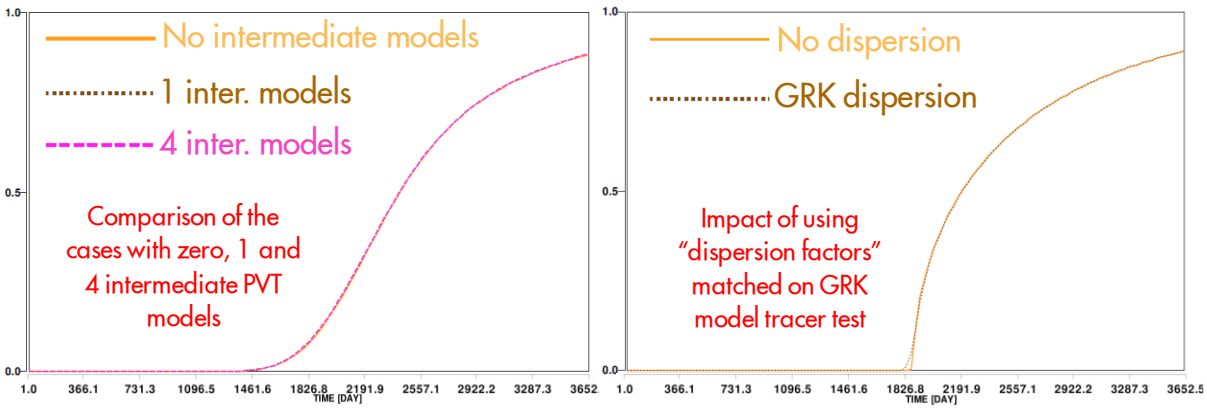

Figure 12.7 Comparison of breakthrough of injected nitrogen in test model.

Table 12.2 Simulator run time with higher number of PVT models.

Model	Active	Passive
	CPU time, sec	CPU time, sec
Test	727	625
Test (with 4 intermediate PVT models)	1101	
FFM	70877	28339

It was decided to use passive tracers for the screening phase because of the run time benefits. The active tracers were implemented after selection of the basecase.

12.12.2 Full Field Model (FFM)

The Groningen FFM was completed in 2012 and consists of more than 240 thousand active cells. The main reservoir properties are shown in Table 12.3. The well stock consists of 297 producers and 2 water disposal injectors.

Table 12.3 Main reservoir properties of the Rotliegend reservoir in the Groningen field.

Permeability (mD)	150
Porosity(%)	15
Initial P_{res} @ 2875 m (Bar)	345
Initial T_{res} @ 2875 m (°C)	100
Current P_{res} @ 2875 m (Bar)	95
Well stock, producers	297
Well stock, water disposal	2

The Groningen reservoir fluid is a dry gas with approximately 82 mol% of methane (CH_4), 0.9 mol% of carbon dioxide (CO_2) and 14.2 mol% of nitrogen (N_2). Gas density at normal conditions (0°C and 1.01 Bar) is 0.835 kg/m^3. The main properties of the Groningen gas and nitrogen are shown in Table 12.4. Density and viscosity are slightly higher for nitrogen, but the difference is marginal.

There are several PVT models in the FFM depending on the depth and the location. So called "pseudo thermal" initialisation was used, i.e. a separate PVT model for every 1°C temperature change. However, for active tracers only one PVT model was considered which corresponds to Groningen gas at 100°C.

Table 12.4 Properties of Groningen gas and Nitrogen compared.

	Groningen gas	Nitrogen
Density (@ 0°C, 1.01 Bar), kg/m^3	0.835	1.25
Density (@ 100°C, 300 Bar), kg/m^3	0.174	0.235
Viscosity (@ 0°C, 1.01 Bar), cp	0.011	0.0165
Viscosity (@ 100°C, 300 Bar), cp	0.023	0.028
Formation volume factor (@ 100°C, 300 Bar), sm^3/rm^3	0.00476	0.00531

Reservoir properties such as horizontal and vertical permeability are crucial factors for gas injection. Because gas breakthrough time and sweep efficiency are the key parameters in the field development plan, it is very important that the upscaled model is a good representation of the detailed geological model.

Several grid size sensitivities were done to assess the impact. Figure 12.8 shows a comparison of the well log versus detailed (blue line) and upscaled (red line) grid resolution from the simulation model. This comparison shows that the current simulation model is also fit for purpose for gas injection.

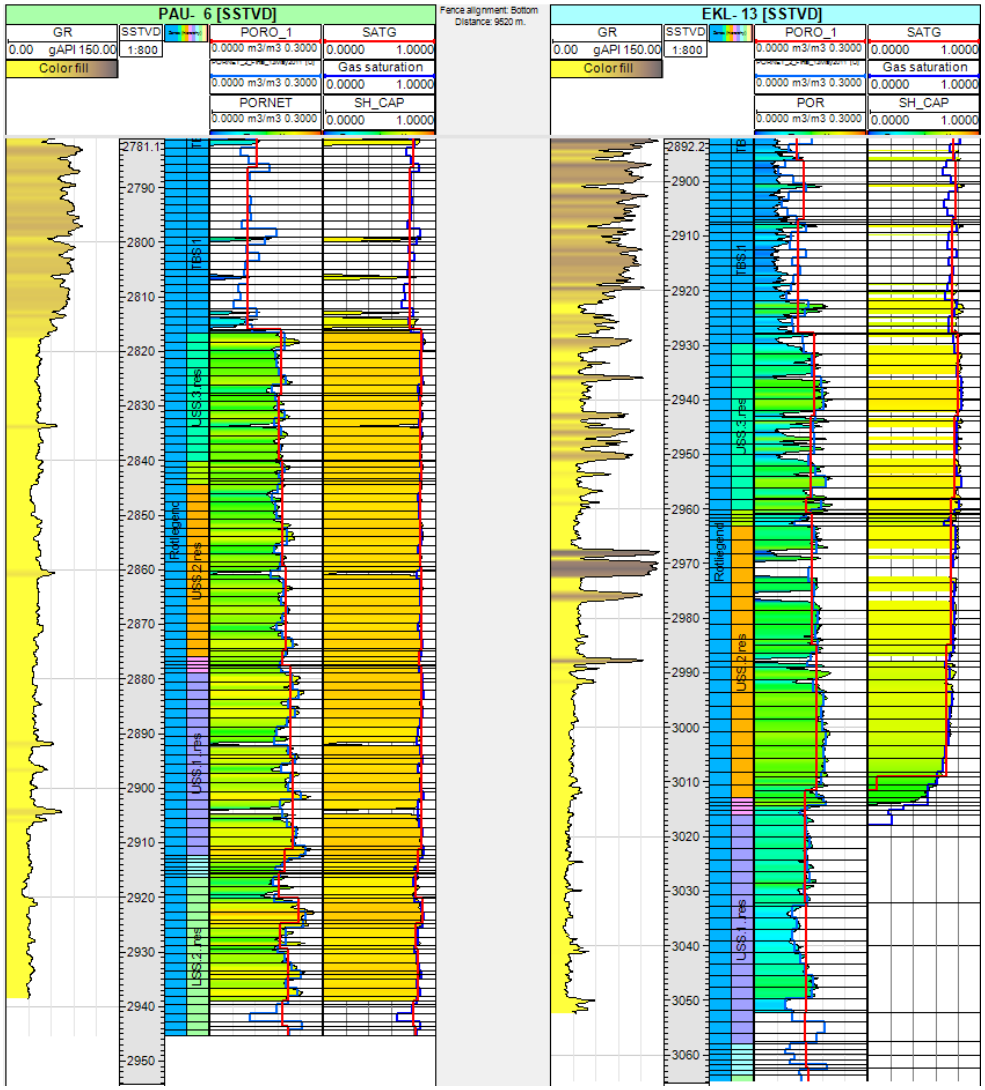

Figure 12.8 Comparison of reservoir properties measured in the wells and used in the model after upscaling.

Since the purpose of the injection is to maintain the pressure, a voidage replacement scheme was chosen as the base case development scheme. This means that the reservoir volume of the produced gas needs to be replaced by injected nitrogen.

The start of injection time was assumed to be January 2020 for the case which evaluates the effect on the reserves. (Figure 12.12) According to the Air Products report on the surface facilities required for the nitrogen injection the first gas for the injection will be available in 2018 on some of the clusters and a full injection capacity could be achieved in 2023. Therefore in the simulation model the middle of that period was chosen as a start date.

For the rest of the sensitivities the injection start date is always January 2017.

The number of required injection wells was derived by dividing the total field gas production rate by the maximum injection rate of the nitrogen injector.

Norg big bore capacity wells were taken as analogues for Groningen nitrogen injectors in terms of completion and pressure and rate constraints. Provisional injector locations are shown in Figure 12.9. These need to be optimized, but for now it has been assumed that each of the 23 injector wells will need to be drilled from a separate new location.

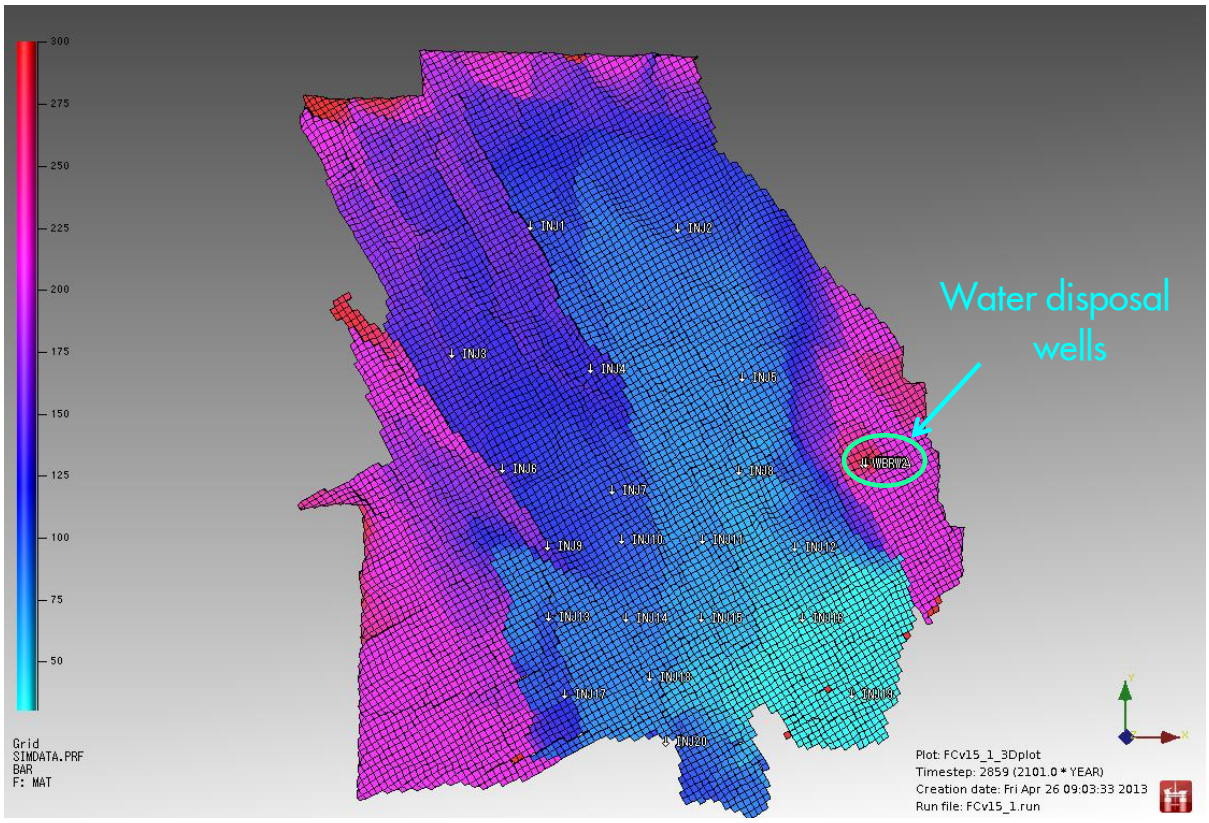

Figure 12.9 View of the Groningen model with the 23 injector wells locations indicated.

12.13 Results and observations

For the reserves evaluation, nitrogen injection was modelled using an IPSM (Integrated Production System Modelling) tool, which consist of surface network modelling tool coupled to a reservoir simulator. This was required to honour the existing and future facility constraints in the Groningen system, including:

- First stage compression
- Summer – winter gas demand variations
- Fluctuations in response to UGS activity
- Gas consumed in operation

Simulations using the IPSM tool are very time consuming and difficult to interpret. Therefore, only forecasts with the reservoir model (and without the production facility model) were used to test sensitivities, and to generate forecasts taking 2nd and 3rd stage compression into consideration. In the runs with IPSM model the passive tracer option was used, for simulation time reasons.

A comparison of the average reservoir pressure is shown in Figure 12.10. The pressure is stabilised at around 60 -70 bar in the injection case. Pressure distribution maps are shown in Figure 12.11. at different time steps. The locations of the injection wells can potentially still be further optimized.

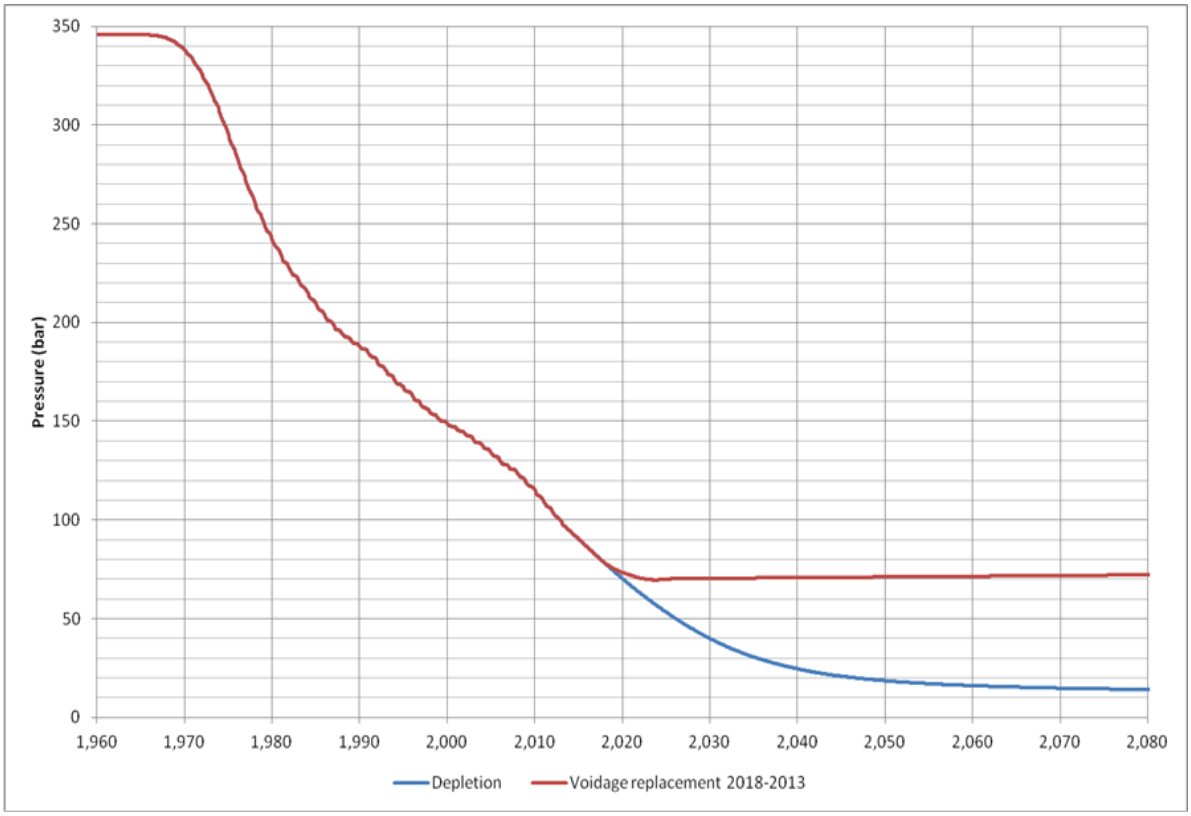

Figure 12.10 Comparison of the pressure development over time for the continued depletion drive development case and the pressure maintenance development based on nitrogen injection. The reservoir pressure for the latter case is stabilised at around 60 - 70 bar.

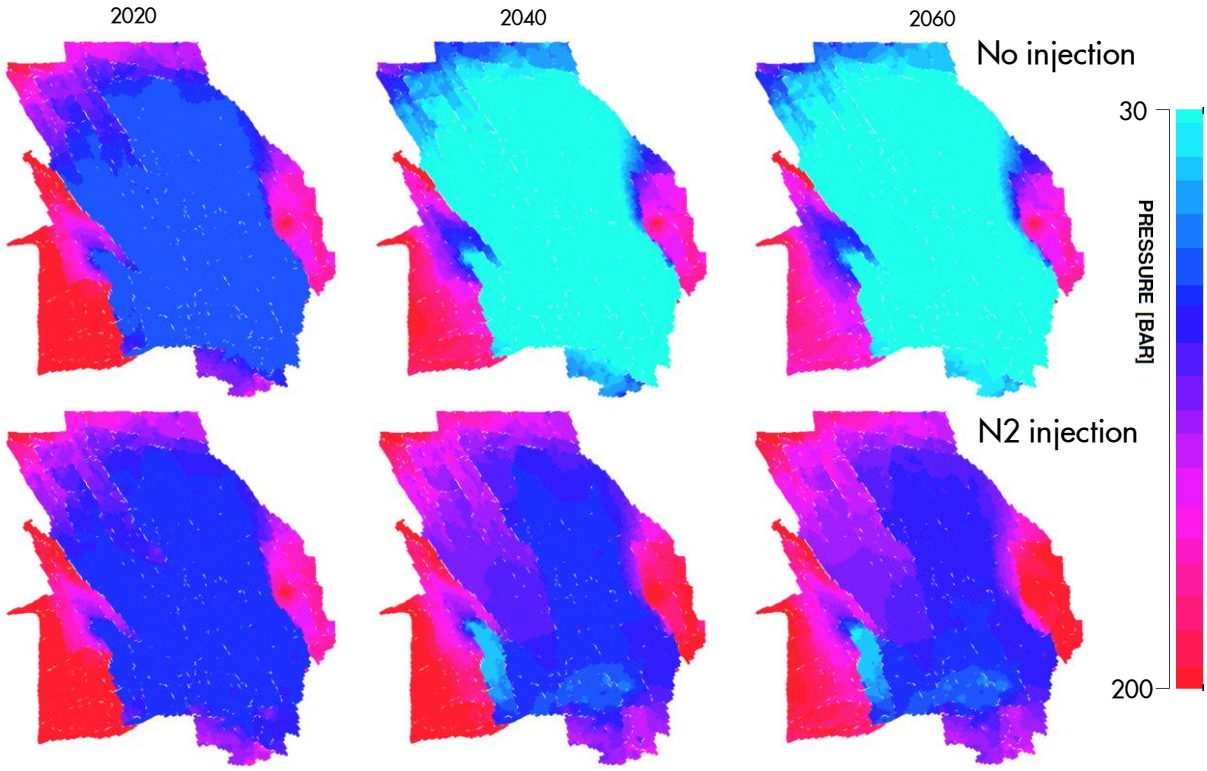

Figure 12.11 Maps of areal pressure distribution in reservoir layer 7 for three time snapshots (2020, 2040 and 2060). The reservoir pressure maps for continued depletion and pressure maintenance are shown.

Figure 12.12 shows a comparison of production profiles for the base case vand the nitrogen injection case. The economic threshold for nitrogen is calculated using De Wijk example. It is shown with an economic cut-off of 75% N2 cut the loss of reserves is around 110 BCM. An optimisation of the nitrogen injection in individual wells in response to the nitrogen breakthrough in production cluster wells may lead to a further reduction of the reserves losses.

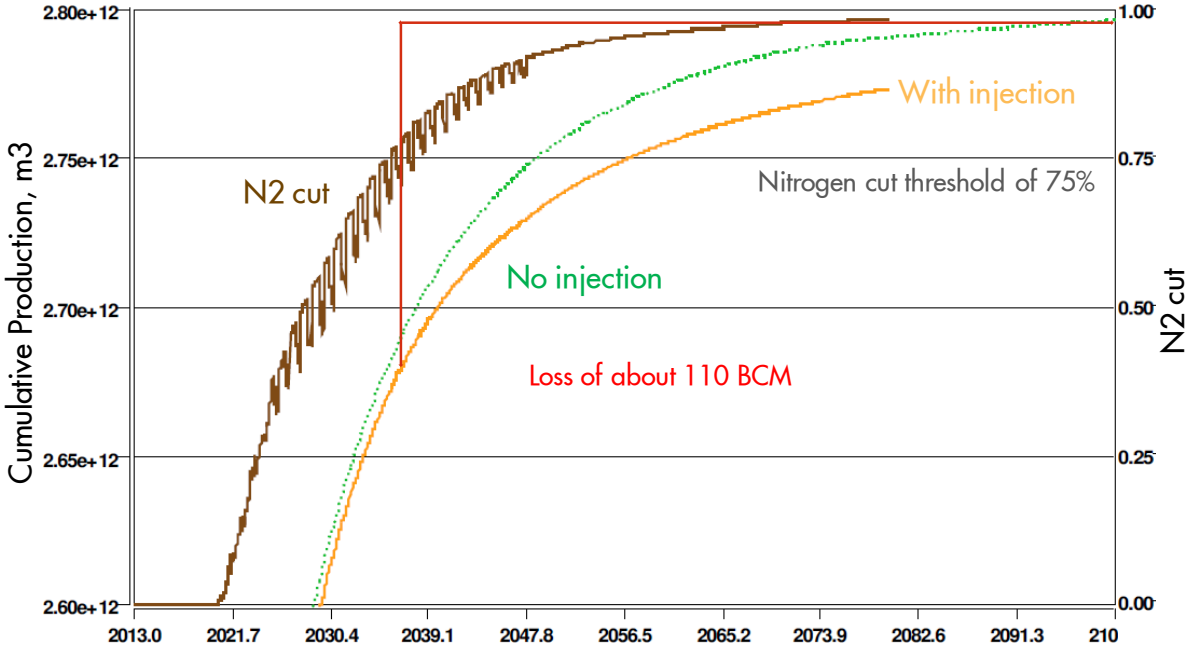

Figure 12.12 Comparison of the cumulative production profile for the depletion development (no injection) and the pressure maintenance development (with nitrogen injection). The nitrogen cut due to breakthrough of the injected nitrogen gas is also shown.

The same sensitivity on the cell dimensions as was done for the test model was also performed on the FFM. The results in Figure 12.14 show that on a large scale the difference is negligible.

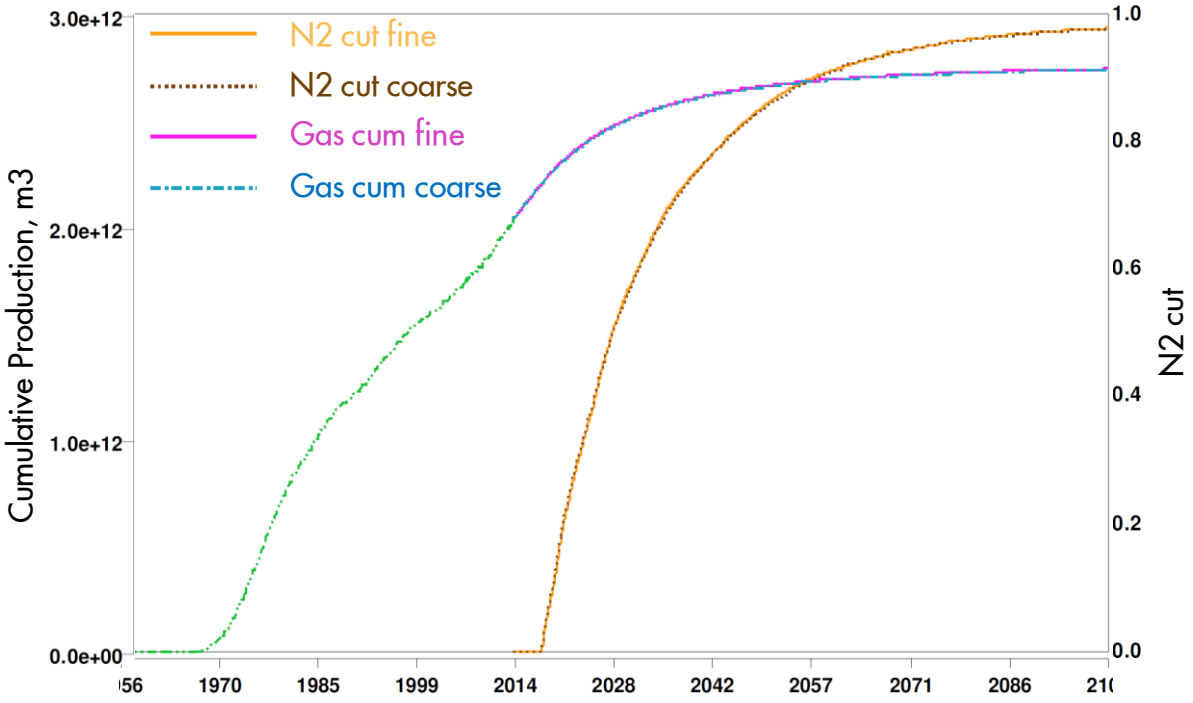

Figure 12.13 Sensitivity of nitrogen injection for the grid size used in the reservoir simulation. Both the gas production and the nitrogen cut at the producer wells are not significantly affected by the cell dimensions.

12.14 Alternative Development Options

Various sensitivities were tested in the full field model of the Groningen field to assess the merits of different development options:

- Partial voidage replacement
- Injection wells located in the northern part of the field only
- Different start up times for the injection

12.14.1 Partial Voidage Replacement

In the base case development, full voidage replacement was maintained throughout the production period. This means that the reservoir volume of injected nitrogen gas was kept equal to the volume of gas withdrawn from the reservoir. In case of partial volume replacement, only a fraction of the withdrawn reservoir gas volume is replaced by nitrogen injection. In this development option, the reservoir pressure decline is slowed down, reducing the compaction rate compared to the depletion drive scenario.

Production profiles of different partial voidage replacement cases are illustrated in Figure 12.15. Expectedly, the smallest loss of gas recovery occurs with minimum injection which is chosen to be 50% of the production. However, in this case the reservoir pressure declines more than for the other partial voidage replacement cases throughout the production period (Figure 12.16) and the impact on compaction and seismicity is therefore also reduced.

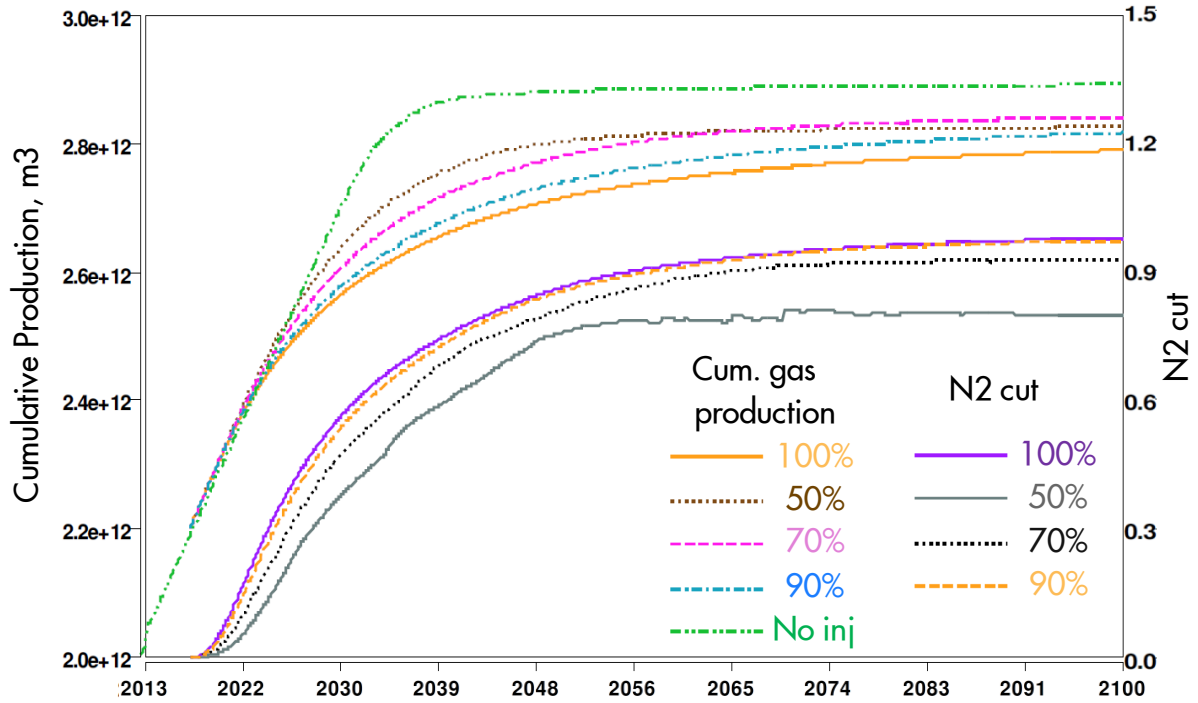

Figure 12.14 Cumulative production and nitrogen cut of the production for different partial voidage replacement development options.

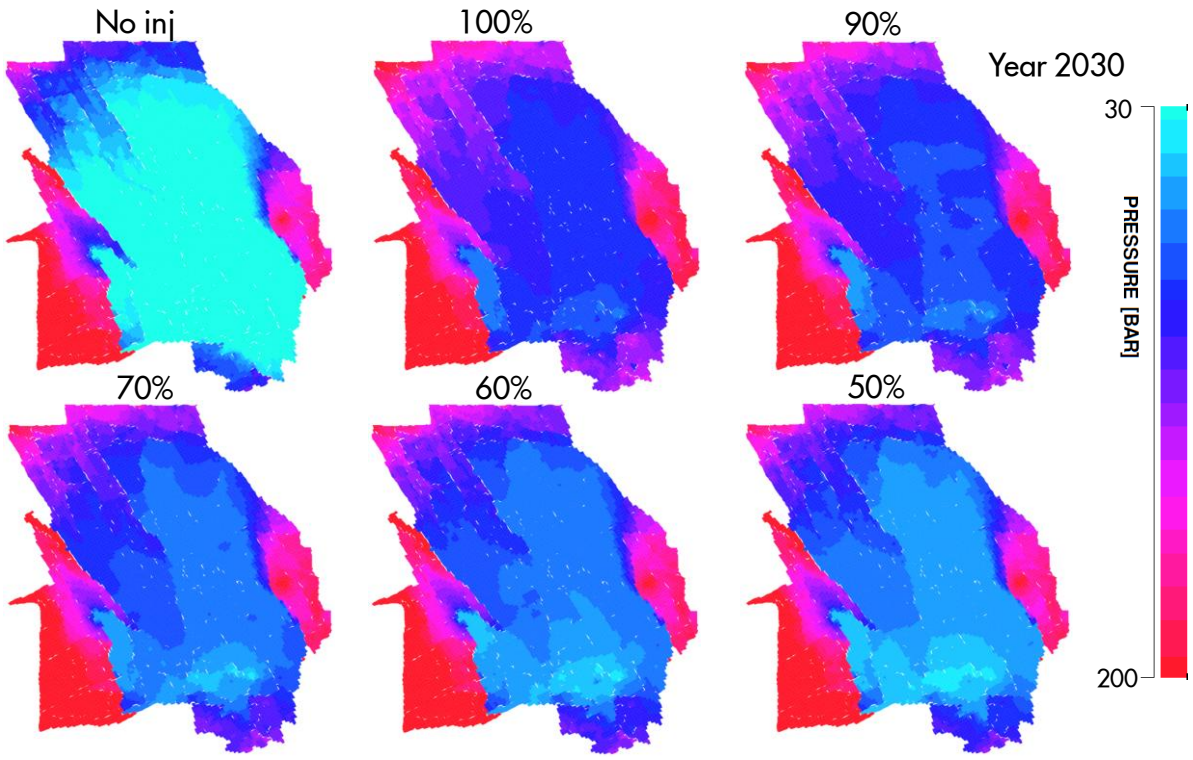

Figure 12.15 Reservoir pressure distribution (reservoir layer 7) in 2013 for different voidage replacement scenario's. The depletion scenario and voidage replacement at 100%, 90%, 70%, 60% and 50% are shown.

12.14.2Injection in the northern part of the field only

In the base development scenario, the injection wells are located throughout the field, at larger distances from the production clusters to achieve an effective displacement of the Groningen gas towards the production clusters. A streamline display shows the displacement paths from injection point to the production cluster of the gas (Figure 12.17). Initial screening showed the well placement is effective, but can be further optimised.

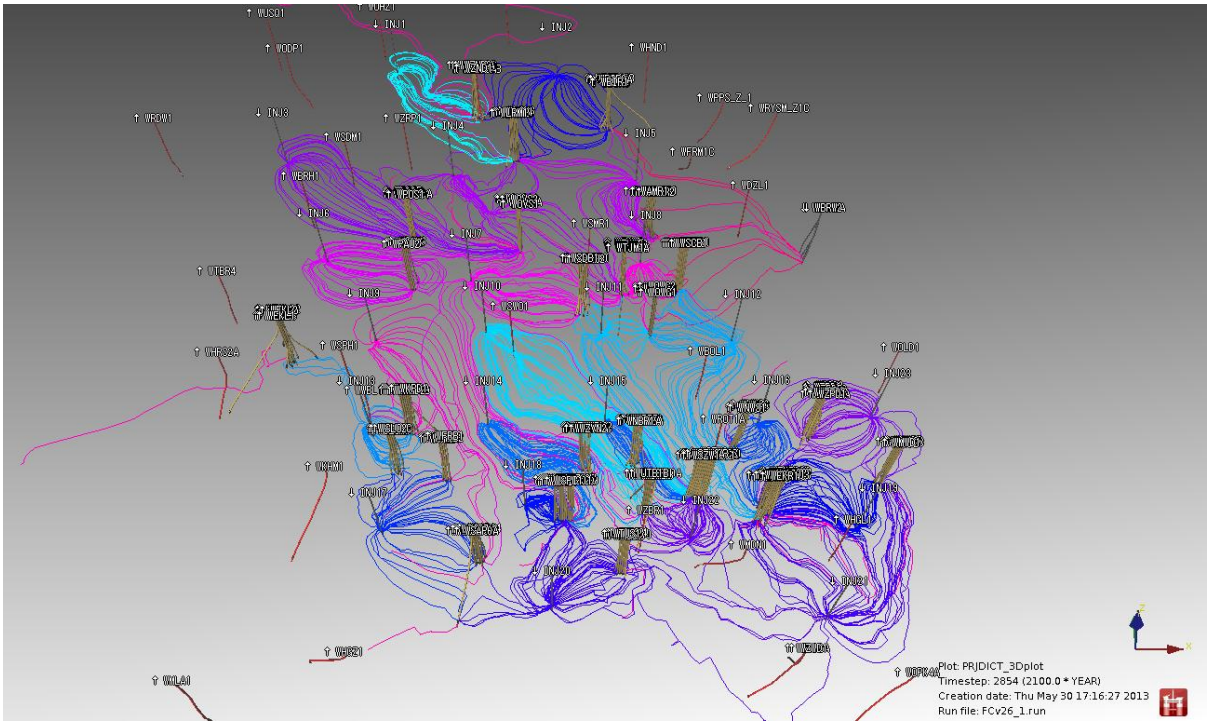

Figure 12.16 Streamlines for nitrogen from the injector wells to the production clusters. This plot has been used as a tool to optimise the injector locations.

The majority of the production clusters in the Groningen field is located in the southern part of the field. In section 3.2, the historical development of the field is discussed. The denser development of the southern area has a clear impact on the reservoir pressure while producing under depletion. This suggests an alternative development scheme for pressure maintenance, where nitrogen is injected exclusively in the north of the field and gas is swept towards the southern production clusters.

This scenario requires a less extensive nitrogen pipeline network and would results in a North to South displacement of the gas. Of course, the northern clusters would start producing mostly nitrogen early on. The scenario with northern injection wells only is shown in Figure 12.18. The pressure distribution is much less uniform between North and South. This will probably reduce the effectiveness of this option in reducing seismicity. However, the production profile looks more attractive comparing with the full injection case. (Figure 12.19). Also, the pressure decline in the north is reduced, which is the area with the largest seismic risk. This may have a positive effect on the total seismic hazard.

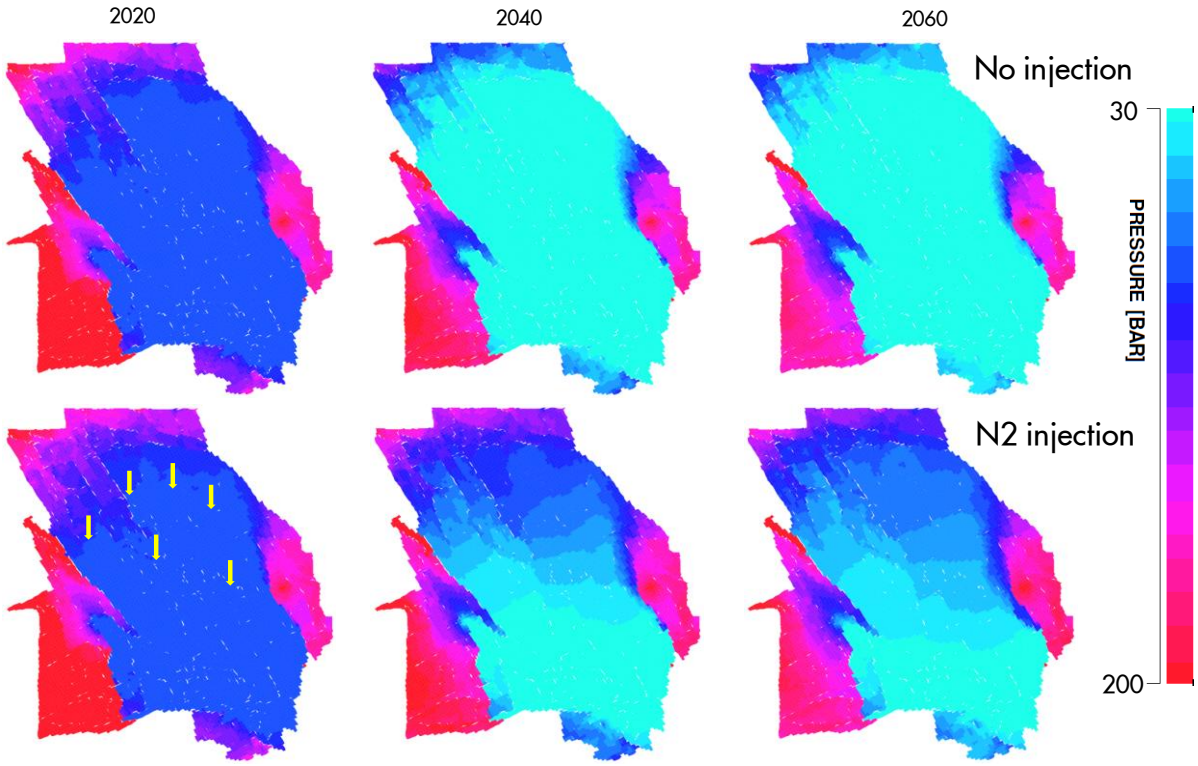

Figure 12.17 Reservoir pressure distribution (in reservoir layer 7) over the field for both the depletion case (above) and the (below) case with nitrogen injection exclusively in the north of the field (below).

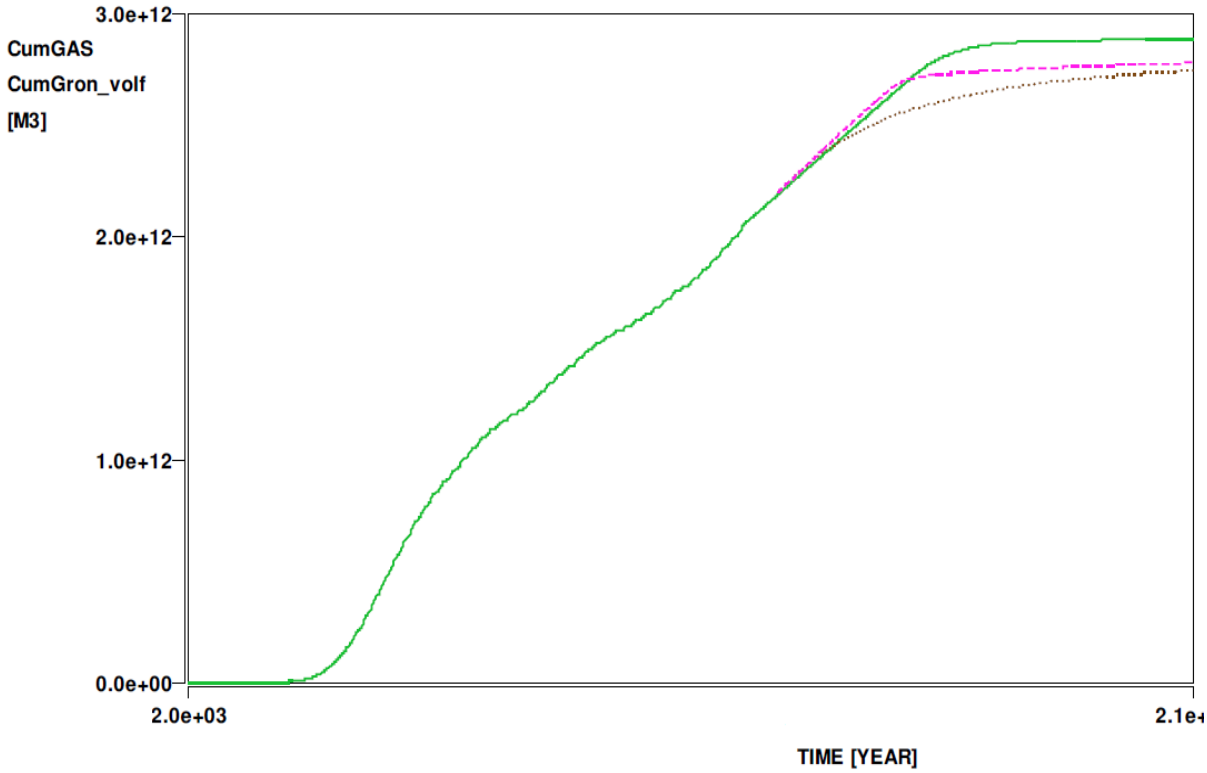

Figure 12.18 Production profiles for three development options; (1) depletion (green), (2) nitrogen injection in wells throughout the field (red) and (3) nitrogen injection wells exclusively in the North (brown).

12.14.3 Different start up times for the injection

The earliest possible start of nitrogen injection in the Groningen field is in 2018, as will be explained in section 4. The effect of a later start was also assessed. Figure 12.19 shows results for starting injection in 2017, 2019, 2021 and 2023, respectively. It is obvious that delaying the injection start results in a higher gas recovery, but also in a delay in the reduction of reservoir compaction.

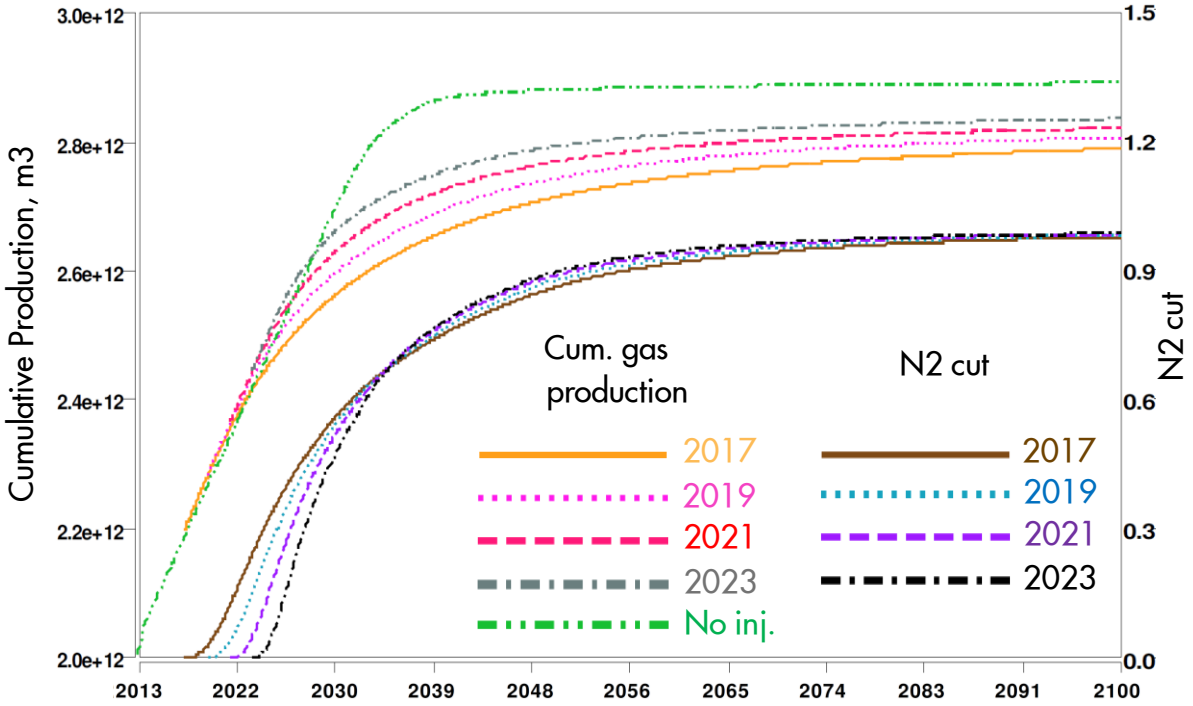

Figure 12.19 Cumulative gas production and nitrogen cut for scenarios with different start of nitrogen injection. Later start of injection leads to a reduced loss of reserves. Continuation of depletion without injection (green) results in the largest recovery from the field.

12.14.4 Summary of the development options.

During the simulation phase on the full field simulation model the following alternative development scenarios were considered:

- Partial voidage replacement options with the range from 50% to 90% reinjection of produced volume by nitrogen. The results suggest that the least voidage replacement option (50%) will have a minimum negative impact on the reserves. However, it also will have a reduced effect on the compaction i.e. more pressure decline compared to the other cases.
- A development plan based on injection exclusively in the northern part of the field results in a less uniform pressure distribution, but though it has a more attractive production profile (than the base case pressure maintenance development). Due to the different approach to areal sweep fewer injection locations in the reservoir are required. This allows the number of wells to be reduced in case of lower initial injection volumes and partial volume replacement.
- Different start-up times for the injection from 2017 to 2023 were also analyzed. The earliest injection start-up time yield in the lowest ultimate recovery, although the reservoir pressure stabilizes at higher value.

12.15 Development plan for pressure maintenance using nitrogen injection

12.16 Technical premises

This section describes the surface requirements for nitrogen injection in the Groningen field. The facility scope will be described, including a project execution strategy and the operations / maintenance of the nitrogen injection facilities.

In order to maintain the reservoir pressure in the Groningen field, new injection wells have to be drilled in the province of Groningen, in approximately the same area where the production clusters and pipeline infrastructure are located. Additional facilities are required for the production and transport of nitrogen. The new infrastructure scope consists of:

- Injection wells to be drilled from 23 new locations (see section 12.4).
- Nitrogen supply systems (so called ASU – Air Separation Units).
- Nitrogen Rejection Units (NRU; to separate excess nitrogen from the produced gas to bring the gas back to Groningen quality before delivery into the GTS pipeline system. The nitrogen from the NRU's will be used for reinjection).
- Pipeline and compression infrastructure for transporting the nitrogen from the ASU's to the injection wells and from the NRU's to the injection wells.
- Electrical infrastructure for the ASU's and NRU's.

The project execution (construction) is expected to take approximately 6 years and Front-end activities (selection of facilities and design) about 2 years. First injection could start in 2018 and full injection 2023.

12.17 Non-technical premises

The surface facilities (construction and permanent presence during operation), pipelines (construction – crossing canals/highways) and drilling of new wells will have a large impact on the landscape and therefore on local communities.

A large electrical power consumption is required, which will have a big impact on CO_2 emissions. Currently, it is assumed that the electrical power will be supplied by power plants. This can be optimized in the future using synergy with concepts having a lower carbon footprint. Potentially, the Eemshaven power plant can be utilised.

It has been assumed that seawater cooling will be used for facilities close to the coast, which can also impact the seawater temperature. This impact also has to be assessed for future development. Cooling for the NRU's is assumed to be done with air coolers.

12.18 Assumptions

The initial screening concept has been based on certain assumptions already captured in section 12.16 and section 12.17. These assumptions and others are described here with some relevant background information.

Table 12.5 Assumptions table for the pressure maintenance development plan for the Groningen field based on nitrogen injection.

Assumption	Background
Nitrogen will be produced through up-scaling of a proven technology (cryogenic process).	The cryogenic process is an established process used worldwide in different industries and also for injection in reservoirs (including Cantarell, Mexico and NAM De Wijk).

The base case is an injection rate equal to the Groningen yearly production of: 1) 42 BCM/year (base case) 2) 30 BCM/year (option) with an injection pressure of 130 bar.	The earliest start date for injection is in 2018 and full injection rate can be achieved in 2023. The Groningen production and related required injection pressure is expected to be at that level in 2023. This has to be assessed in more detail in a next phase.
23 Injection wells spread out over the field area are required.	See section 12.4
The composition of the produced gas has to remain on Groningen specification. Injected nitrogen breakthrough in the reservoir will take place and excess nitrogen has to be removed. The excess nitrogen will be re-injected in the injection wells.	No changes in the required gas composition on the European market are foreseen LoCal gas).
The ASU's will be grouped together in the vicinity of the Eemshaven.	■ The environmental impact is lower in the Eemshaven area than on the countryside. ■ Seawater cooling can be used. ■ Power plants are located in the Eemshaven.
An NRU will be located in the vicinity of each production cluster.	■ Minimal transport distance between excess nitrogen and reinjection wells. ■ The maximum height of an NRU is restricted to 25 m to limit the environmental impact.
The pipelines will be located as close to the existing infrastructure as possible.	Minimal impact on permits because of the bundling principle.
Power plants (electricity supply) and electrical infrastructure for the NRU's will be provided by utility companies. Additional connections and transformers will be included in this project.	In line with the Groningen field electrical infrastructure philosophy.

12.19 Development concept

12.19.1 Plot lay-out

The plot lay-out is given in Figure 12.19. The 23 injection wells (light blue dots) are located throughout the Groningen field. The ASU plant is located in the North of the province next to the Eemshaven. The pipeline infrastructure (light blue lines) transports the nitrogen from the ASU to the injection wells. The nitrogen distribution pipeline is split in a western and eastern section connecting the production clusters (dark blue dots) as the existing production pipeline ring. The injection wells are connected to the nitrogen distribution network (red). Next to each production cluster an NRU is located. The NRU is connected to the main pipeline via a short pipeline.

The pipelines have to cross canals and highways, which will complicate both the permits and execution.

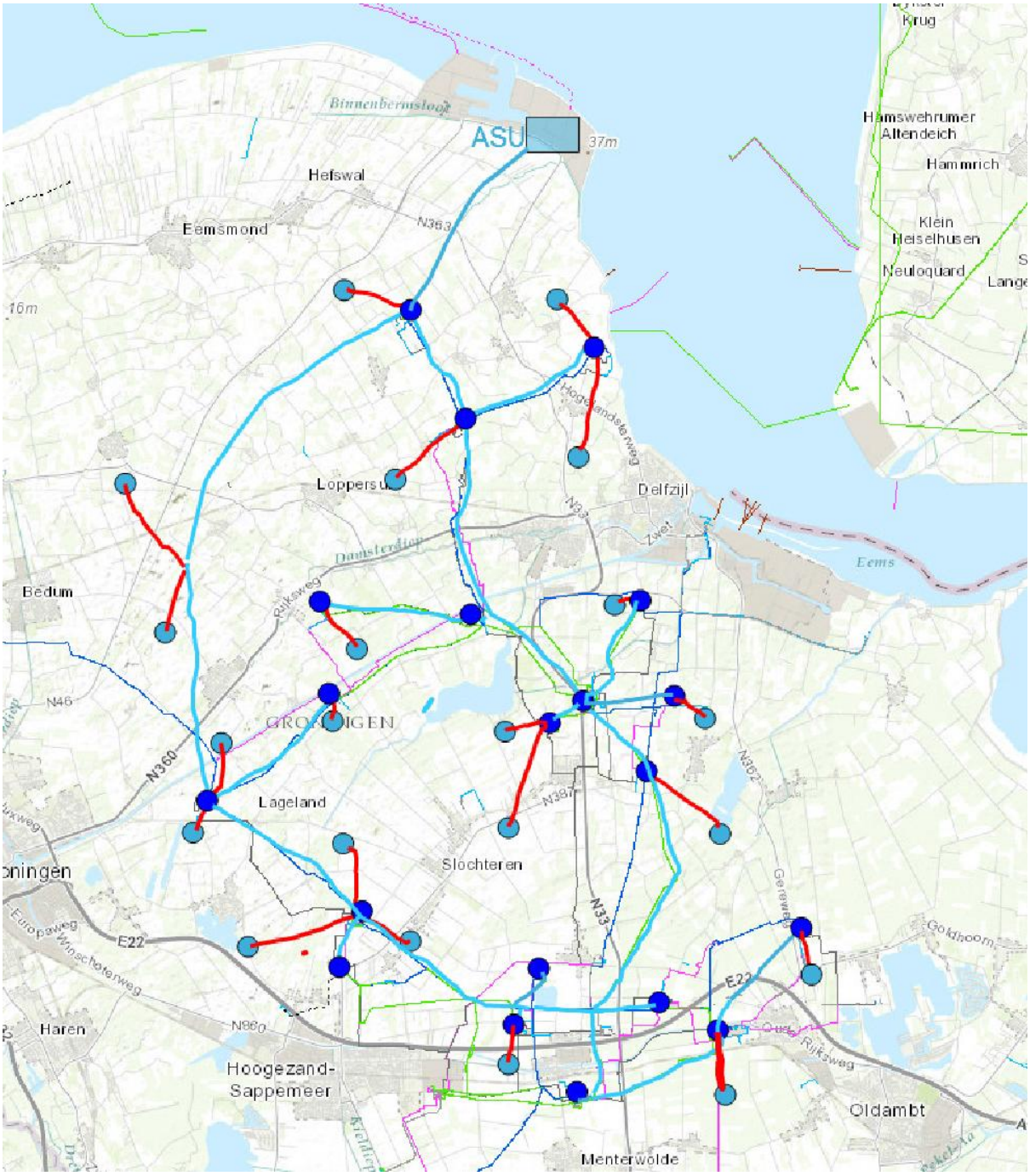

Figure 12.20 Plot lay-out of the ASU plant, N_2 injection facilities, NRU's wells and pipelines in the Groningen province

12.19.2Injection wells

The scope of the injection wells is as follows:

- The injection well designs are based on the Norg injection wells (9 $^5/_8$" tubing). A large rig is required to drill these wells.
- New land has to be leased for each injection well.
- Civil/electrical infrastructure and hook-up to the pipeline. The hook-up concept is based on De Wijk, up-scaled to the required flow rate.

12.19.3 Air Separation Units (ASU)

The ASU concept has been developed by a large supplier of ASU's. The ASU comprises the following scope:

- The nitrogen production rate will start with 30 to42 BCM/year declining in the future as excess nitrogen from the produced gas will be re-injected.
- The plant consists of 9 to12 parallel ASU's (for the 30 and 42 BCM/y case, respectively), which requires a flexible production rate. Compressors for separation of nitrogen/oxygen and for compression to the distribution pipelines are provided with a housing to comply with noise regulations.
- All ASU's are located on single plot space (450 x 270 m) with a maximum height of 62 m (cold boxes). This land has to be leased.
- The maximum power requirement is 1000 to1416 MW (30 and 42 BCM/year cases), which is in the range of powerplants at the Eemshaven. A 380 kV connection to Eemshaven Oudeschip (utility company connection point) is required.

Artist impressions of the ASU plant can be found below (Figure 12.21 to Figure 12.23). This gives an idea of the size of the ASU plants. The power plant shown depicts the one already present at Eemshaven industrial area (without power lines) in relation to potential ASU installation. The power plant shown provides an example and is similar to the one already present in the Eemshaven industrial area. Note the exact ASU complex location will be subject to change. Also the power cable poles are not shown and therefore the exact location of the ASU plant will probably change.

Figure 12.21 ASU plant view from the south

Figure 12.22 ASU plant aerial view

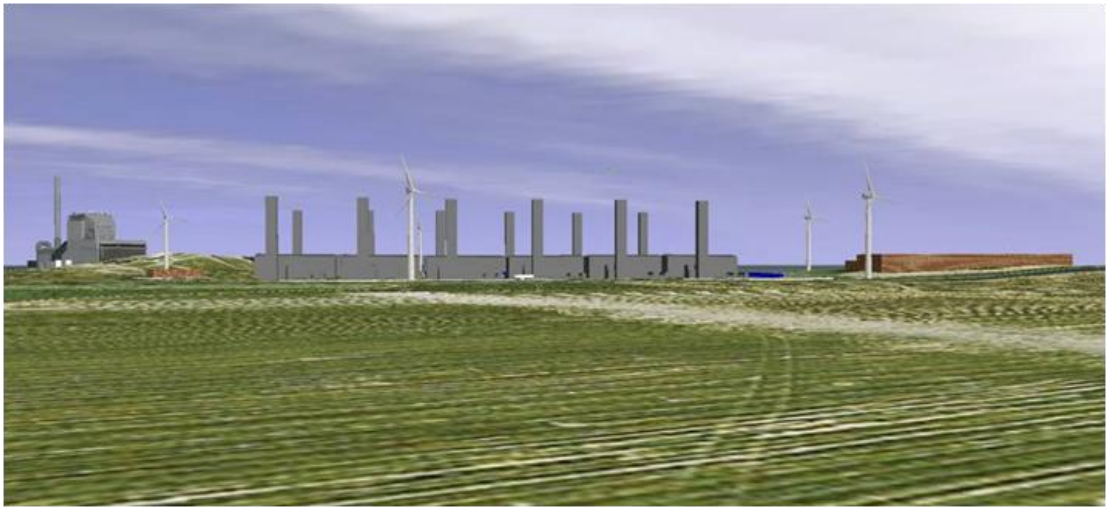

Figure 12.23 ASU plant side view (with existing power plant to the left)

12.19.4Nitrogen Rejection Unit (NRU)

- The NRU concept has also been developed by a service company. An NRU is required for each gas processing unit and therefore 20 NRU's are required. Each NRU comprises the following scope:
- The nitrogen breakthrough in the produced gas is limited at the start of injection but will increase with time. Therefore, the NRU concept will be able to process a variable nitrogen content and flow rate.
- Pre-treatment (removal of mercury, carbon dioxide, water, solids).
- The plot space of an NRU is 200 x 100 m and the maximum height (cold box) is 25 m. This land has to be leased.
- The maximum power requirement is 32 MW per NRU. Additional 110 kV rings to substations and new transformers are required.
- Compressors for the separation of nitrogen and natural gas and for compression to the distribution pipelines are provided with a housing to comply with noise regulations.
- Air coolers are used for cooling similar to the De Wijk ASU design.

Note: The nitrogen facilities study was based on the removal of maximum 50 mass% nitrogen. Latest study work indicates that this should be maximum 80 mass%. Cost and energy use have been scaled to reflect this.

An artist impression is shown in Figure 12.24.

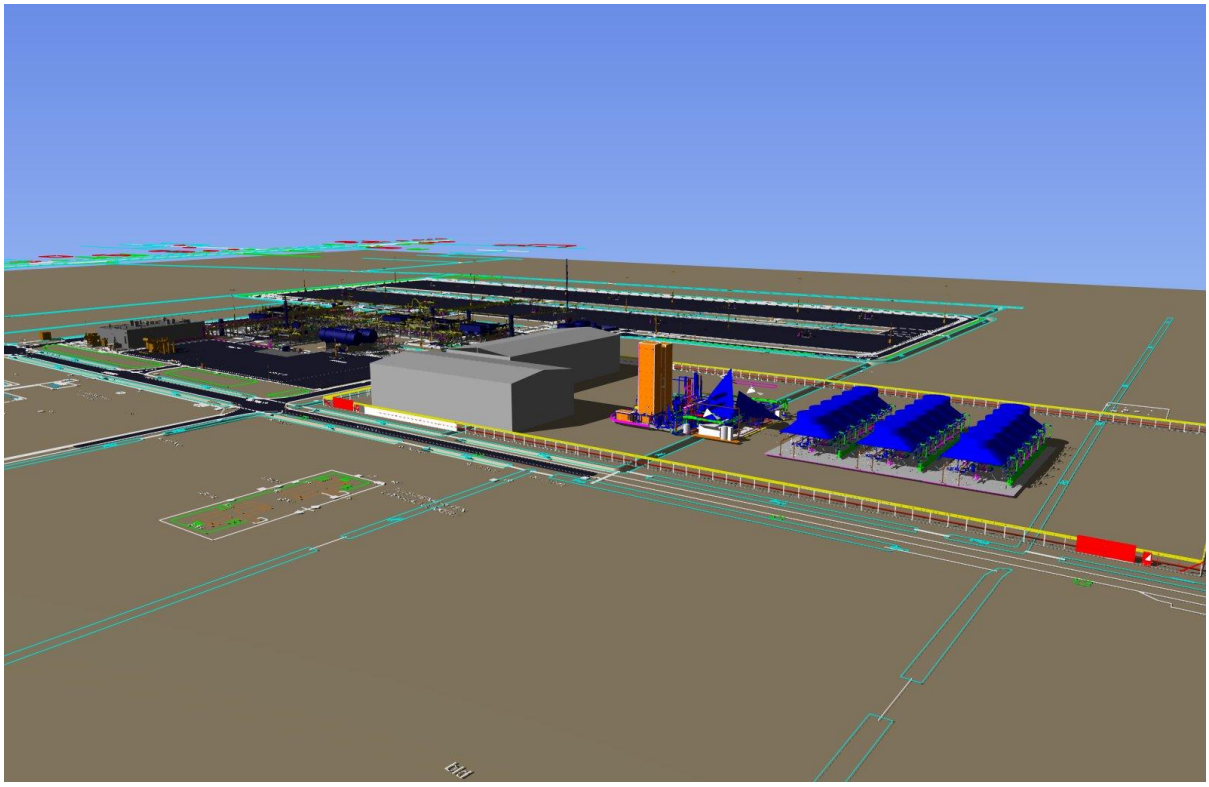

Figure 12.24 NRU plant aerial view (with existing production facility to the left)

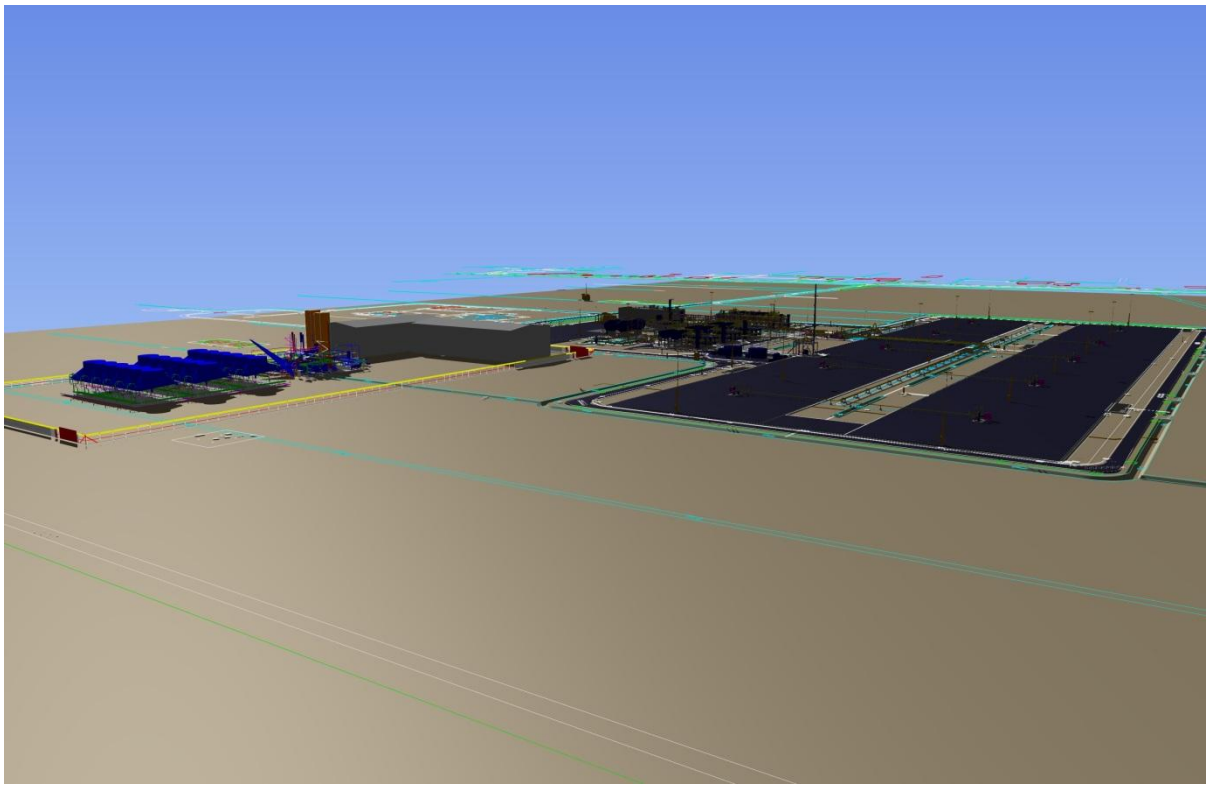

Figure 12.25 NRU plant aerial view (with existing production facility to the right)

12.19.5Pipeline infrastructure

The pipeline infrastructure is divided in a western and an eastern line, which connect in the south to form a ring. The east and west lines do not individually need to transport the full capacity as a 100% availability is not assumed to be required. The dimensions of the pipelines are based on that assumption. The total

length of the pipeline ring is around 120 km with side connections to the injection wells and NRU's. Carbon steel has been selected as material for the pipelines.

12.19.6 Project Execution planning

At least 2 years are required to investigate several concepts, select the final concept and design. The execution (construction) could start earliest in 2016 and is expected to take 6 years to complete. Injection of nitrogen could start earliest in 2018 and is expected to reach full injection rate of 30 to 42 BCM/year by 2023.

The project execution planning can be found in the Table 12.6 below:

Table 12.6 Notional high level Project schedule. Indicated is the number of completed units (cumulative). For example, 3 wells are drilled and hooked-up in 2017, 11 in 2019 and the 23 wells are all finished in 2022.

	2014	2015	2016	2017	2018	2019	2020	2021	2022
Feasibility, Concept Select and FEED									
Final Investment Decision									
Injection wells drilling				3	7	11	15	19	23
Injection wells civil				3	7	11	15	19	23
Injection wells hook-up				3	7	11	15	19	23
Pipeline infrastructure									
ASU AP				1	3	6	8	10	12
ASU civil									
NRU				1	4	8	12	16	20
NRU civil									
NRU hook-up									
Electrical infrastructure									

12.19.7 Operations and maintenance

The ASU's and NRU's typically have an expected lifetime of 15 years and need a 4-yearly maintenance shutdown. There is an option for the ASU's and NRU's to be owned, operated and maintained by the vendor.

The electricity power requirement is:

ASU's: 1416 MW (42 BCM/year) or 1000 MW (30 BCM/year) at maximum use

NRU's: 640 MW at maximum usage

An important aspect is the flexibility requirement for the NRU plants. The export gas has to be maintained at Groningen quality specifications for delivery into the GTS pipeline system. Changes and disturbances can be caused by trips/maintenance/start-up of the upstream production facility, start-up/ramp-up of the NRU itself and the change in the nitrogen content of the produced gas. This requires further in-depth study of the concept, taking into account control and automation requirements and optimising the concept of the NRU's in combination with the ASU plant.

12.19.8 High level development cost estimate (screening level)

The cost estimate is preliminary and subject to a large potential variation, due to unforeseen scope growth, complexity and/or permit requirements.

The CAPEX cost estimates are given below for the 30 BCM/year and 42 BCM/year cases:

30 BCM/year case	
CAPEX (nominal)	bln EUR MOD
Injection wells drilling	11%
Pipeline infrastructure	15%
ASU, incl. water intake	25%
NRU	45%
Electrical infrastructure	3%
Total	5.7 – 8.5

42 BCM/year case	
CAPEX (nominal)	bln EUR MOD
Injection wells drilling	11%
Pipeline infrastructure	16%
ASU, incl. water intake	30%
NRU	40%
Electrical infrastructure	3%
Total	6.5 - 10

Table 12.7 Nominal Capex estimates

The OPEX cost estimate is based on operations, maintenance and electricity costs. The electricity costs are based on electricity consumption estimates by Air Products and on 2013 electricity market prices in the Netherlands. The electricity costs will be highest in 2023 as a maximum of 30 or 42 BCM is injected. The maximum electricity demand will be in 2018 when the injection will start. From 2023, nitrogen from the produced gas can be reused for injection. The NRU's require less power. The increased fuel gas consumption to generate electricity results in a further reducing of sales gas.

The OPEX cost estimates are given below:

30 BCM/year case	
OPEX (nominal)	mln EUR/y
Electricity	686
Ops & Maintenance	58
Total	744

42 BCM/year case	
OPEX (nominal)	mln EUR/y
Electricity	858
Ops & Maintenance	72
Total	930

Table 12.8 Nominal Opex estimates.

12.20 Project uncertainty

This early feasibility study aims to establish the total scope of a pressure maintenance project. Therefore, large uncertainties remain to be addressed which requires further investigation. These uncertainties include:

- Geological complexity of the reservoir may affect the nitrogen breakthrough times differently than assumed.
- Gas-gas mixing and displacement behaviour in the reservoir might be different from that observed in the UGS fields, which were used as an analogue.
- The current engineering concept is based on vast upscaling of existing concepts. Its feasibility is yet to be demonstrated. Both timing and costs will be affected by the uncertainty in the upscaling.
- Non-technical uncertainties pertain to the environmental and societal footprint associated with the project. This is treated in section 4.7.

12.21 Project optimisation

Further optimisation of the injection well locations may result in a higher efficiency of the displacement process in the reservoir.

- The research team in Rijswijk working on Optimised Decision Making under Uncertainty (ODMUU) has analysed the scope for further optimisation of the nitrogen injection balance and identified various optimisation trade-offs. For instance, nitrogen breakthrough could be delayed and nitrogen production could be reduced at the expense of lower production rates and gas recovery losses. Detailed economic evaluation will be required to find the preferred optimum for this trade-off.
- Optimisation of injection well locations has the potential to improve the efficiency of the displacement process.
- The development scheme used in this report can potentially be optimised. For instance, as an alternative for the Eemshaven location of the ASU, Delfzijl could be considered.
- Different scenarios with full and partial voidage replacement schemes and various injection start-up times could be considered.
- Chasing of the nitrogen with cheaper flue gas from the ASU's or power plants in the Eemshaven industrial area. This would need to be done with care to avoid breakthrough of the flue gas in the production wells which at that point will be lost for production.
- Scaling of the various elements of the project, particularly the nitrogen plant, could be further optimised. Cost estimates have been prepared both for a 40 Bcm/yr production case and a 30 Bcm/yr production case. Currently, these indicate that the larger scheme is more attractive on a unit nitrogen cost basis, but detailed engineering analysis needs to confirm this.

12.22 Environmental and societal impact

A nitrogen injection project will carry a significant environmental footprint:

- Significant acreage will be required to locate the facilities.
  - The nitrogen generation plant will be located at a large site at Eemshaven.
  - The 23 injector wells will need to be drilled from new locations.
  - Additionally, substantial extension of current production cluster locations will be required to place the nitrogen rejection units.
- The dimensions of the required industrial complex at Eemshaven and the 20 NRU's at gas processing facilities throughout Groningen will result in horizon pollution in the wide Groningen landscape and may prove to be an unacceptable visual impact for the local community and nation at large..
- The compression required for producing nitrogen from air and for removal of nitrogen from the produced gas will cause noise pollution. Gas transport may cause additional noise issues.
- Installing 200 km of large diameter pipeline with crossing of roads, highways and canals will cause significant disturbance.
- The production of nitrogen and its removal from the produced gas requires significant amounts of electrical power.
- This power consumption is associated with a large carbon dioxide footprint.
- Seawater cooling at Eemshaven may increase water temperatures in the Eems-Dollard estuary. This may constitute an undesirable impact and may impact the feasibility of the project.
- Nitrogen removal limits the operational flexibility in production capacity.

Due to these environmental impacts, the societal support for such a large-scale project needs to be tested and explored.

12.23 Gas recovery with water injection

Water injection for Enhanced Oil Recovery purposes and for the Pressure maintenance is widely used in the world. However, it is very rare that water is injected in dry gas reservoirs. There are a number of reasons for this:

- Dry gas recovery is already quite high without any enhancing methods, because of its compressibility (Figure 12.26).
- The mobility difference between gas and water is large, so displacement would be unfavourable and leads to trapping of significant amounts of unrecoverable hydrocarbons. 25%, 50% and 100% lines in Figure 12.26 are combined from the sweep efficiency effect and the economic cut-off of water production. This is just a conceptual representation of the driving mechanism and for the more accurate results the detailed simulation study is required.
- The process of gas displacement by water is immiscible. Gas will be trapped as residual saturation behind the water front.

There are additional reasons why water injection is not attractive for the Groningen field:

- The impact of water injection on seismicity is difficult to predict,. In fact it may introduce more earthquakes because of the large pressure gradients in the field, fraccing due to thermal effects and injection into fault planes.
- Injection of sea water may result in souring of the reservoir i.e. through the formation of H_2S.
- Possible fault weakening due to lubrication of the fault interface which may cause a fault sliding.
- The amount of water required to inject in Groningen for pressure maintenance is between 1.3 and 1.8 mln res m^3/day. This volume requires between 250 and 400 injector wells. The surface facilities required are 30 times bigger than Shell's largest water injection asset in Bonga, Nigeria.

It can be concluded that the combination of project size, costs and potential negative impact on seismicity makes water injection an unattractive development option for pressure maintenance in the Groningen field.

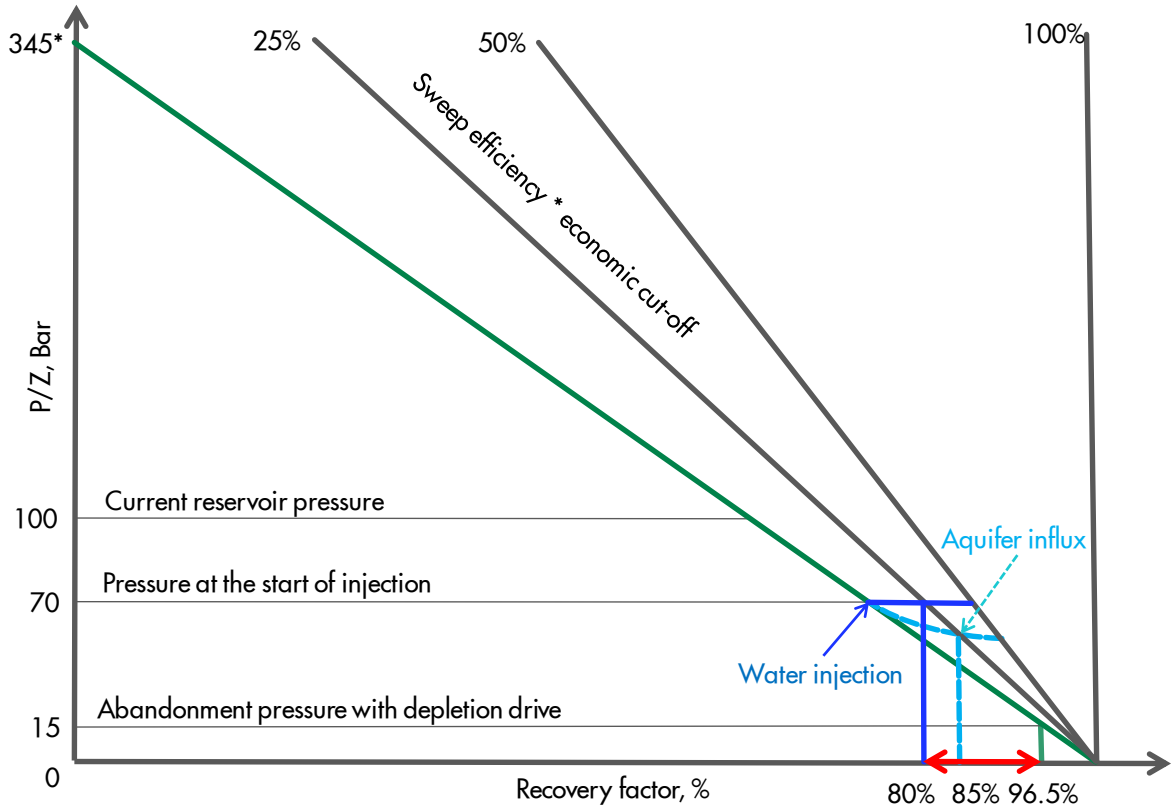

Figure 12.26 The effect of water injection on the gas recovery. Also the natural aquifer influx effect is shown for comparison sake.

12.24 Conclusions

- Maintaining the reservoir pressure in the Groningen field at a level above the abandonment pressure will after a delay period halt compaction and subsidence.
- Although pressure maintenance will arrest reservoir compaction, further geomechanical modelling is required to confirm and assess the impact on the seismic hazard. This is currently being addressed by URC Houston (XoM) and NAM/Shell. Especially the impact on seismicity of injection into or close to a fault is a concern (Report to the Technical Guidance Committee (TBO) on Production Measures Part 1: Depletion Scenarios and Hazard Analysis, NAM, November 2013).
- Pressure maintenance using injection of nitrogen has been studied, supported by a base case development concept and production forecasts.
- Based on its abundant presence, relatively inert behaviour and tolerance for presence in the sales gas, nitrogen was chosen as the optimal injection medium.
- Analyses have been based on the Groningen reservoir model, and on the experience in modelling of gas–gas displacement and mixing in the reservoir in the underground storage projects of Norg and Grijpskerk, but the remaining uncertainty in the production forecasts and recovery is large.
- Breakthrough of nitrogen in producer wells as a consequence of pressure maintenance is expected to significantly reduce Groningen gas reserves compared to continued depletion of the reservoir.
- Large electricity consumption further reduces the gas volume available for sales.
- The scope of the project is far beyond the scale of current global experience (5 – 7 times larger than the largest similar project ever installed).
- Although the contours and main dimensions of a Pressure Maintenance Project have been sketched, technical feasibility of the project has not yet been established.
- Installation of nitrogen injection takes at least 5 years to first injection and some 9 years to ramp up to full capacity.

- Cost of the project is estimated at 6 to 10 bln EUR.
- The project carries a material environmental footprint, with significant land use and electricity consumption. Societal support for a large-scale nitrogen injection project is expected to be a key risk.
- This study is in an early stage assessment of the recovery concept. Optimization is still possible for a number of aspects.
- Injection of water is not considered a feasible and reliable pressure maintenance option to reduce seismic activity.

12.25 References

Reservoir Management Issues in the Cantarell Nitrogen Injection Project, F. Rodríguez, G. Ortega, J.L. Sánchez, O. Jiménez, PEMEX Exploración y Producción, 2001 13178-MS OTC Conference Paper

Nitrogen from Cryogenic Air Separation Process To Be Used for Pressure Maintenance and To Enhance Recovery at Cantarell Complex in Campeche Bay, Mexico, John R. Kirtley, Bechtel, 1999 10864-MS OTC Conference Paper

Nitrogen Injection in the Cantarell Complex: Results After Four Years of Operation, J.L. Sánchez, SPE, A. Astudillo, F. Rodríguez, SPE, J. Morales, and A. Rodríguez, PEMEX E&P, 2005 97385-MS SPE Conference Paper

Implementing Convection in a Reservoir Simulator: A Key Feature in Adequately Modeling the Exploitation of the Cantarell Complex, E. Manceau, E. Delamaide, J.C. Sabathier, S. Jullian, F. Kalaydjian, IFP; J.E. Ladron De Guevara, J.M. Sanchez Bujanos, F.D. Rodriguez, PEMEX, 2000 59044-MS SPE Conference Paper

Implementing Convection in a Reservoir Simulator: A Key Feature in Adequately Modeling the Exploitation of the Cantarell Complex, E. Manceau, E. Delamaide, J.C. Sabathier, S. Jullian, F. Kalaydjian, IFP; J.E. Ladron De Guevara, J.L. Sanchez Bujanos, F.D. Rodriguez, Pemex, 2001 71303-PA SPE Journal Paper

Overview of the Cantarell Field Development Program, T. Limón-Hernández, G. De-la-Fuente, G. Garza-Ponce, Pemex Exploracion y Produccion; M. Monroy-Hernandez, Bechtel, Corp., 1999 10860-MS OTC Conference Paper

Status of the Cantarell Field Development Program: An Overview, T. Limón-Hernández, G. Garza-Ponce and C. Lechuga-Aguiñaga, Petroleos Mexicano (Pemex) Exploración y Producción, 2001 13175-MS OTC Conference Paper

Mechanisms and Main Parameters Affecting Nitrogen Distribution in the Gas Cap of the Supergiant Akal Reservoir in the Cantarell Complex, Fernando Rodr guez, PEMEX-UNAM; Jose L. Sanchez, Agustin Galindo-Nava, PEMEX, 2004 90288-MS SPE Conference Paper

Cantarell Field: Modernization and Expansion of the Pipeline Network, J. B. de León; A. Argüelles, R.M. Morales, Petroleos Mexicano (Pemex) Exploración Y Producción, 2001 13176-MS OTC Conference Paper

13 Appendix C: Conclusions / Insights

The strength of an earthquake may be characterized according to the magnitude, or moment, of the earthquake in the subsurface which is characterized by the amount and area of slip that occurs on faults during the earthquake. Alternatively the strength of an earthquake may be measured as the magnitude of ground motion experienced at the surface during an earthquake which is typically characterized by the peak ground velocity (PGV) or the peak ground acceleration (PGA).

Establishing the future maximum strength of earthquakes in the Groningen gas field depends on the method chosen to assess the maximum magnitude as well as on some remaining technical uncertainties. The key assessment choices concern with 1) how to express the strength of an earthquake, 2) the time interval for which the maximum magnitude is to be assessed, and 3) the appropriate statistical definition for maximum strength.

The time interval for assessment matters for two reasons. First, a longer time interval means more earthquakes and hence a greater chance of experiencing a higher magnitude earthquake. Second, unlike natural earthquakes, induced seismicity has a beginning, middle, and end. This means statistics describing the average annual number or moment of observed earthquakes is not constant in time but will vary with gas production. For these reasons the maximum strength of a future earthquake depends on the exposure time considered and the start time of this exposure interval relative to the cumulative gas production.

Several different definitions for the maximum strength of a future earthquake exist; each appropriate for different purposes. These include the maximum possible magnitude, the maximum expected magnitude, *i.e.* the magnitude with a 50% chance of exceedance, or the maximum magnitude with some other chance of exceedance, e.g. a 10% chance of exceedance over 10 or 50 years are commonly seen in international conventions adopted for reporting hazard assessments for natural seismicity.

The following sections summarise the findings of the NAM studies conducted in response to the fifth study described in the Letter to Parliament (Kamp, 2013).

13.1 Maximum possible magnitude

Previous seismic hazard assessments considered relevant for the Groningen gas field were all influenced by an estimate for the maximum possible magnitude of 3.9 (Crook et al., 1995; Crook, Haak, & Dost, 1998; van Eck et al., 2006; Muntendam-Bos et al., 2008; Dost et al., 2012). Two main methods were used to estimate this maximum possible magnitude. First, frequency-magnitude statistics of historic earthquakes were used to estimate a cut-off magnitude for which it was considered impossible for a larger magnitude event to ever occur regardless of exposure time. Second, compaction models and mapped fault geometries were used to estimate the maximum possible slip and slip area. Based on the insights of the work done in the previous months these estimates are now recognised to be unreliable due to shortcomings in the applications of these methods. The estimates based on the frequency-magnitude statistics do not take full account of the observational uncertainties associated with a limited number of recorded earthquakes. The estimates based on geomechanical models do not take full account of the maximum possible area of pre-existing faults given the resolution limits of reflection seismic surveys.

The recent studies reported here demonstrate that the frequency-magnitude data provide no reliable estimate for the maximum possible magnitude due to the limitations associated with the small number of recorded earthquakes in Groningen in accordance with a recent independent study (Muntendam-Bos & Waal, 2013). Other methods were also investigated based on the physical limitations imposed by the finite amount of strain energy or the finite area of pre-existing faults or from global analogues. These indicate the maximum possible magnitude might be as large as 6.5. This does not mean that earthquakes up to this magnitude are expected, it only illustrates that there is a physical upper limit to induced earthquake magnitudes in the Groningen Field. If the partitioning factor were invariant with production, the maximum magnitude of a future event is expected to be M=4.5 with a 95% upper bound of M=5.5. However the fraction of induced strain accommodated by earthquakes is likely increasing with on-going reservoir compaction and this explains the observed distribution of earthquakes in time and over the Groningen area. If future seismicity follows the same trend observed in the historic earthquake catalogue, then based

on the current analysis there is a 1 in 2 chance of M>4.2, a 1 in 10 chance of M>4.9, and a 1 in 100 chance of M>5.4 before the end of 2023.

This significantly revised estimate means that the maximum possible earthquake magnitude is unsuitable for characterising the seismic hazard associated with future induced earthquakes as it has little or no connection with the credible range of future seismicity. Instead, future seismicity is more appropriately characterised by probabilistic assessments that yield estimates for the earthquake magnitude or the ground motion with a certain probability of exceedance over a certain exposure period. Such probabilistic estimates of seismic hazard are necessary to appropriately assess the resilience of buildings and infrastructure within the vicinity of the Groningen gas field.

13.2 Probabilistic seismological assessment

Reservoir pressure depletion induces reservoir compaction, and together they induce stress changes within and around the reservoir. In some places the stress changes experienced by a pre-existing fault may be sufficient to equal its resistance to slip. Under these conditions the fault is vulnerable to experiencing earthquakes. During an earthquake, abrupt slip on a fault releases elastic strain energy stored in the surrounding region by localizing anelastic strain along the fault.

Geomechanical models for reservoir compaction within the Groningen field are constrained by subsidence measurements to provide estimates for the induced elastic strains that are available to induce earthquakes. The fraction of induced strain accommodated by seismogenic fault slip cannot yet be predicted by geomechanical models – but it can be measured in the field by comparing historic seismicity and subsidence observations. These data indicate the historic strain fraction associated with earthquakes is very small (0.1%) but possibly increasing with reservoir compaction. A probabilistic model for this compaction-dependent strain fraction was developed and includes a wide range of uncertainty due to the limited number of recorded earthquakes.

Over the next 10 years (2013-2023), based on a linear-elastic reservoir compaction model and the current production plan (BP12), the expected maximum magnitude (50% chance of exceedance) is 4.2. Over the same period there is also a 10% chance of exceeding a magnitude 4.9, and a 1% chance of exceeding a magnitude 5.4. Subsequent 10-year periods exhibit different seismicity rates due to the changing balance between the possible seismicity increases with further compaction and the expected seismicity decreases with the natural decline in future production rates. All these estimates include allowances for the known aleatory uncertainties (random variations). However, they are also contingent on the assumption that the statistics of historic seismicity will provide a guide to the statistics of future seismicity. This epistemic uncertainty is not trivial and motivates significant further data gathering.

13.3 Probabilistic seismic hazard assessment

Probabilistic Seismic Hazard Analysis (PSHA) was performed using two independent implementations of standard Monte-Carlo techniques adapted to account for time variant seismicity. Taking Eurocode 8 as a guide, these assessments focused on mapping the ground motion with a 0.2% average annual chance of exceedance over the next 10 years (2013 to 2023). This is equivalent to the 10% chance of exceedance within 50 years stated in Eurocode 8 for time-invariant natural seismicity, but for a reduced assessment period of 10 years to ensure a sufficiently reliable assessment of the time-variant induced seismicity observed within the Groningen Field.

Predicted maximum ground motions with an average annual 0.2% chance of exceedance, for the 10 years of production from 2013 to 2023, are 22 cm/s (PGV) and 5.6 m/s^2 or 0.57g (PGA), located above the region of greatest reservoir compaction. These values were obtained using the linear compaction model, the Akkar et al (2013) ground motion prediction equation (GMPE) modified to be consistent with ground motion data from the Groningen Field, and by including all earthquakes of at least magnitude 1.5. Direct comparisons with hazard maps published for other regions are to be avoided because these generally only include M≥5 earthquakes, *e.g.* California or M≥4.5 earthquakes, *e.g.* Europe. Disaggregation of the seismic hazard into its component parts show that only intermediate magnitude earthquakes (4 to 5) influence the result. Earthquakes less than magnitude 4 are too small and earthquakes greater than magnitude 5 are too rare to influence the hazard.

13.4 Remaining technical uncertainties

Results from recent NAM studies indicate there are at least four key sources of epistemic uncertainties. These all may be amenable to reduction in time given sufficient gathering of reliable new information.

First, the current seismic hazard assessment excludes the possibility of any triggered earthquakes that release compaction-induced elastic strains as well as naturally occurring elastic strains due to tectonics or some other natural process. The lack of any earthquakes in recorded human history within the vicinity of the Groningen field prior to gas production supports this choice.

Second, the detailed mechanics of reservoir compaction and subsidence remain subject to uncertainty due to the limited sensitivity and time sampling of historic subsidence measurements and due to the limited length-scales and time-scales of laboratory measurements. Consequently a range of linear and non-linear constitutive models for compaction in the Groningen field are presently consistent with the known history of gas production and subsidence. These different models differ in their long term predictions for reservoir compaction but only show limited variability in the next 10 years.

Third, the role of faults and the future evolution of the fraction of the elastic strain released by earthquakes (strain partitioning factor) remain subject to uncertainties due to the relatively limited duration of historic earthquake monitoring and the performance capabilities of the current monitoring network. The historic earthquakes do not always occur on mapped faults; this might be due to the current level of earthquake location uncertainty, or because the earthquakes also occurred on smaller faults below the resolution limit of reflection seismic surveys, or because earthquakes did not always occur on pre-existing faults. The current seismological model allows for all three possibilities – however it is possible that new information gained from further and improved earthquake monitoring will reveal just one of these mechanisms as dominant. Equally, the wide uncertainty range about the future strain fraction released by earthquakes may require revision given subsequent new information about the mechanism or the rate of seismic moment release with further reservoir compaction. The benefit of geomechanical models for predicting the future slip behaviour of mapped faults is uncertain due to limited knowledge of the number, location, geometry and strength of pre-existing faults that may host intermediate magnitude earthquakes. Nonetheless, such models do offer opportunities for investigating possible scenarios for compaction-induced fault slip to aid further understanding of the process.

More detailed geomechanical modeling with emphasis on the role of faults is in progress, but is currently hampered by the paucity of relevant field data. which leaves room for multiple geomechanical explanations (models). A higher resolution of more field parameters is required to make a step forward in a better understanding of the geomechanical behavior. A data acquisition campaign is in progress, including logging of geomechanical rock properties (Borgsweer) and installation of geophones in two deep observation wells. Additionally, the existing monitoring network of shallow geophones and accelerometers will be extended.

The geomechanical modeling combined with the new field data will be used to improve the understanding of the fault slip behavior and when validated by the observed seismicity, this has the potential to reduce the currently large epistemic uncertainties. A full field geomechanical modeling exercise is in progress showing promising results. This should lead to a geomechanical workflow used in the seismic hazard analysis to enable subsurface stress management as a tool to reduce the hazard.

Fourth, the relationship between an earthquake and the strength of the associated ground motions experienced throughout the region of the Groningen field remains uncertain due to the limited number of ground motion measurements for earthquakes of at least magnitude 3 that are necessary to constrain current uncertainties in the scaling of ground motion with earthquake magnitude and the variability in ground motion between different earthquakes and between different surface locations.

13.5 Future data gathering designed to reduce uncertainties

Since 1995, the current configuration of the Groningen monitoring network has provided field-wide coverage for the detection and location of all earthquakes of at least magnitude 1.5: standard horizontal location uncertainties are about 500 m, but typically earthquakes depths cannot be estimated and they are then assumed to be at a depth of 3 km (see Kraaijpoel et al. 2008). Plans are now in place to increase the

density of the Groningen seismic monitoring network to an array of some 60 stations complemented by two down-hole arrays of geophones located within and just above the reservoir. At each of these locations it is planned to deploy borehole geophones to improve depth estimates and broadband accelerometers at the surface to improve magnitude estimates and ground motion measurements.

The motivation for this densification is to significantly increase the precision of earthquake locations and to increase the sensitivity of earthquake detection with the aim to identify all earthquakes of at least magnitude 0.5 within the Groningen Field. These enhancements should enable better characterisation of seismically active regions and improve statistical constraints on the seismological model. This enhanced monitoring network is expected to reveal if earthquakes initiate within, above, or below the reservoir and provides opportunities to identify any localised seismicity on mapped faults.

Additional opportunities for improved acquisition of complementary seismic and geodetic data and the application of recent developments in waveform-based earthquake data processing methods are also under development.

13.6 References

Kamp, H.G.J. Brief van De Minister Van Economische Zaken. Kamerstukken (Tweede Kamer der Staten-Generaal, www.overheid.nl), Vergaderjaar 2012–2013, Kamerstuk 33529, nr. 2.

Muntendam-Bos, A. G., & Waal, J. A. de. (2013). Reassessment of the probability of higher magnitude earthquakes in the Groningen gas field: Including a position statement by KNMI. Retrieved from http://www.sodm.nl/sites/default/files/redactie/20130116 Groningen seismicity report final.pdf